

# Chelation as a strategy with the potential to overcome multidrug resistance in cancer

Dissertation  
zur Erlangung des Doktorgrades (Dr. rer. nat.)  
der  
Mathematisch-Naturwissenschaftlichen Fakultät  
der  
Rheinischen Friedrich-Wilhelms-Universität Bonn

vorgelegt von

Dipl. Chem. Veronika Friederike Sophia Pape

aus Unna

Bonn, 2015

Angefertigt mit Genehmigung der Mathematisch-Naturwissenschaftlichen Fakultät der  
Rheinischen Friedrich-Wilhelms-Universität Bonn

1. Gutachter: Prof. Dr. M. Wiese

2. Gutachter: Prof. Dr. G. Bendas

Tag der Promotion: 17.06.2016

Erscheinungsjahr: 2016

für meine Familie  
und für die Freunde, die wie Familie für mich sind

*for my family  
and for those friends, who are like family for me*

*mind a hivatalos,  
mind a közeli barátokból álló választott családomnak*

I HAVE LEARNT THAT ALL OUR THEORIES ARE NOT TRUTH ITSELF, BUT  
RESTING PLACES OR STAGES ON THE WAY TO THE CONQUEST OF  
TRUTH, AND THAT WE MUST BE CONTENTED TO HAVE OBTAINED FOR  
THE STRIVERS AFTER TRUTH SUCH A RESTING PLACE WHICH,  
IF IT IS ON A MOUNTAIN, PERMITS US TO VIEW  
THE PROVINCES ALREADY WON AND THOSE STILL TO BE CONQUERED.

— *Justus von Liebig* (in a letter to Joseph Henry Gilbert, 25<sup>th</sup> of December 1870)



## Chelation as a strategy with the potential to overcome multidrug resistance in cancer

1.	Introduction	
1.1.	MDR – making Cancer invulnerable?	1
1.2.	ABC-transporters – stories from a family album	2
1.3.	Attempts to overcome MDR	6
1.4.	Collateral sensitivity – in search for the Achilles' heel	8
1.5.	Putting the bite on metals – Role of Chelation in (MDR) Cancer therapy	17
1.6.	Keeping the balance on a double edged sword – ROS	22
2.	Objective	29
3.	Results and discussion	
3.1.	Critical evaluation of literature reports	
3.1.1.	Serendipitous findings	31
3.1.2.	Pharmacogenomic approach	35
3.2.	Development of new compounds – Design of a focused library	40
3.2.1.	Thiosemicarbazones – Compound classes I/II/III	48
3.2.2.	Arylhydrazones – Compound class IV	54
3.2.3.	Hydrazino-benzothiazoles – Compound classes V/VI	55
3.2.4.	Combination of chemical entities – Compound class VII	58
3.2.5.	Structure activity relationships in the focused library and beyond	59
3.3.	Having a closer look at the 8-hydroxyquinoline scaffold	69
3.4.	Elucidation of putative mechanism(s) of action	
3.4.1.	Impact of ROS	78
3.4.2.	Impact of metals – co-incubation with FeCl <sub>3</sub> and CuCl <sub>2</sub>	80
3.4.3.	Investigation of Fe(III) and Cu(II) complexes – stabilities and stoichiometries	84
3.4.4.	In vitro testing of preformed complexes – and the impact of P-gp on their toxicity	94
3.4.5.	Redox activity of complexes	
3.4.5.1.	Cyclic voltammetry	98
3.4.5.2.	Reactivity with antioxidants	101
3.4.6.	Relevance of redox activity of the complexes for toxicity	105

3.5.	Establishing techniques to measure ROS	
3.5.1.	DCFDA	108
3.5.2.	HyPer fluorescent protein	117
4.	Summary	127
5.	Tumor models and biological methods	
5.1.	Cell lines, media and buffer	136
5.2.	Cell culturing	137
5.3.	Determination of cell numbers	138
5.4.	Cryo-conservation and revitalization of cells	139
5.5.	Test for Mycoplasma infections	139
5.6.	Measurement of cell viability	
5.6.1.	MTT viability assay	141
5.6.2.	Presto Blue viability assay	142
5.6.3.	mCherry, eGFP, DsRed fluorescence assays	143
5.6.4.	Evaluation of dose response curves	144
5.7.	Verification of MDR phenotype	
5.7.1.	Toxicity of P-gp substrates	145
5.7.2.	Calcein AM assay	146
5.8.	ROS determination	
5.8.1.	DCFDA	149
5.8.2.	HyPer	
5.8.2.1.	Preparation of stably HyPer-expressing cells	151
5.8.2.1.1.	Transformation into Top10 competent E.coli cells	152
5.8.2.1.2.	Isolation and Purification of amplified plasmid DNA	153
5.8.2.1.3.	Quantification of DNA	153
5.8.2.1.4.	Transient expression and selection in neomycin G418	154
5.8.2.1.5.	Lentiviral transfection	155
5.8.2.2.	Real time measurement of intracellular H <sub>2</sub> O <sub>2</sub> -levels	155
6.	Synthesis and analytical chemical methods	
6.1.	Synthesis of a focused library	157
6.2.	UV-Vis spectrophotometric measurements for complex stability evaluation	178

6.3.	Electrochemical Studies	
6.3.1.	Cyclic voltammetry_____	181
6.3.2.	Oxidation of ascorbic acid (ASC) and glutathione (GSH)_____	185
7.	List of Abbreviations_____	187
8.	Bibliography_____	191
9.	Appendix_____	221
10.	Acknowledgement_____	229
11.	Verfassererklärung_____	232
12.	List of Publications_____	233
13.	Conference Presentations_____	234





## 1. Introduction

### 1.1. MDR – making Cancer invulnerable?

Cancer is the second highest cause of death in industrialized countries [1,2]. A broad range of diverse compounds with distinct mechanisms of anticancer activity has been developed and become available for treatment and is used in the clinical practice. Approved drugs include *Vinca* alkaloids (like *vincristine*), which depolymerize microtubules, Anthracyclines (like *doxorubicin*), that intercalate into DNA and inhibit DNA topoisomerase II, antimetabolites like *methotrexate*, DNA intercalating agents like *cisplatin* and several others [3]. Despite the diversity of drugs used for the treatment of cancer the development of drug resistance is a frequent reason for the failure of cancer chemotherapy [1,2]. Moreover, cells that are resistant to a certain cytotoxic agent can build up cross-resistance to other structurally and mechanistically unrelated drugs, leading to the phenotype of Multidrug Resistance (MDR) [3].

Resistance can emerge as a result of genetic changes, whereby targets are overexpressed or structurally modified in a manner that the binding of cytostatic agents is reduced [3–6]. An adaption can also consist of increased repair of damage caused by the applied drug, as for example in the case of DNA repair [3–5]. Signaling pathways can be modified, in order to overcome the dependence on the drug target [7]. An altered cellular metabolism can furthermore lead to an increased inactivation or decreased activation of a cytotoxic agent [3–6]. The cellular response to drugs can also be altered as a result of decreased availability of the agent. This can be achieved by sequestering of drugs within cellular compartments, a reduced inward- or mostly active outward transport (efflux) of cytotoxic agents [3–5].

This efflux is energy dependent and mediated by transport proteins of the ATP-binding-cassette (ABC) family. The human genome contains 48 genes that encode ABC transporters. The gene product of ABCB1, P-glycoprotein (P-gp), stands out among ABC transporters by conferring the strongest resistance to the widest variety of compounds [3–5,8–10].

Since the development of MDR is a multifactorial process, additionally to the increased expression of drug efflux pumps (which will be covered in detail in the next chapter), many other genetic changes are implicated with the MDR phenotype [3].

In the 1920ies Warburg discovered that the cellular energy metabolism of cancer cells is shifted from oxidative phosphorylation to (aerobic) glycolysis [11]. MDR cancer cells are reported to undergo a further metabolic shift, which results in an even higher rate of cytosolic glycolysis and oxygen consumption accompanied with an increased utilization of fat as a fuel source for the mitochondria [12,13]. As a consequence of this metabolic shift, the

mitochondrial membrane potential as well as the proton transfer against the gradient of the mitochondria are smaller in MDR cancer cells as compared to their parental cell lines [13]. The metabolic changes that occur during the development of resistance render the cells less susceptible for reactive oxygen species (ROS), DNA damage and apoptosis [13].

Since the transport of xenobiotic or endogenous substrates imposes a considerable cost in energy on a cell, metabolic changes and ABC transporter mediated drug resistance are interconnected [14,15]. As a result of increased glycolysis the production of lactic acid is increased. As evidenced by drug induced increase in lactate production and extracellular acidification rates (ECAR) of MDR cells, the energy consumption caused by the interaction of a substrate with P-gp is compensated for by increased glycolysis [15–17]. Inhibition of P-gp decreased the measured ECAR values, which furthermore correlated well with activation profiles of the transporter obtained by means of phosphate release measurements in inverted membrane vesicles for the same drugs [16,17].

Further metabolic enzymes like the methylglyoxal detoxifying glyoxalase system, might confer resistance to antitumor agents [18]. Numerous metabolic changes are mediated by Hypoxia inducible factor HIF-1 $\alpha$ , as a result of PI3K/AKT/mTOR pathway stimulation [19,20]. Disclosing a further connectivity between metabolic changes and ABC transporters, this pathway is furthermore reported to upregulate the expression of P-gp either via activation of NF $\kappa$ B [21] or via HIF-1 $\alpha$  [19,22,23].

The lysosomal accumulation of drugs has been suggested to differ in parental and MDR cells. Proton pumps like the vacuolar type H<sup>+</sup>-ATPase mediate intracellular pH gradients, which drive the lysosomal sequestration [24]. Recently the presence of P-gp in lysosomal membranes has been suggested as an additional mediator of the sequestration of drugs into the lysosome [25].

## ***1.2. ABC transporters – stories from a family album***

The superfamily of ATP-binding cassette (ABC) transport proteins consists of seven subfamilies, which are classified on the basis of sequence homology and domain organization. They are encoded by the ABCA1-10/12/13, ABCB1-11, ABCC1-12, ABCD1-4, ABCE1, ABCF1-3 and ABCG1/2/4/5/8 genes [26].

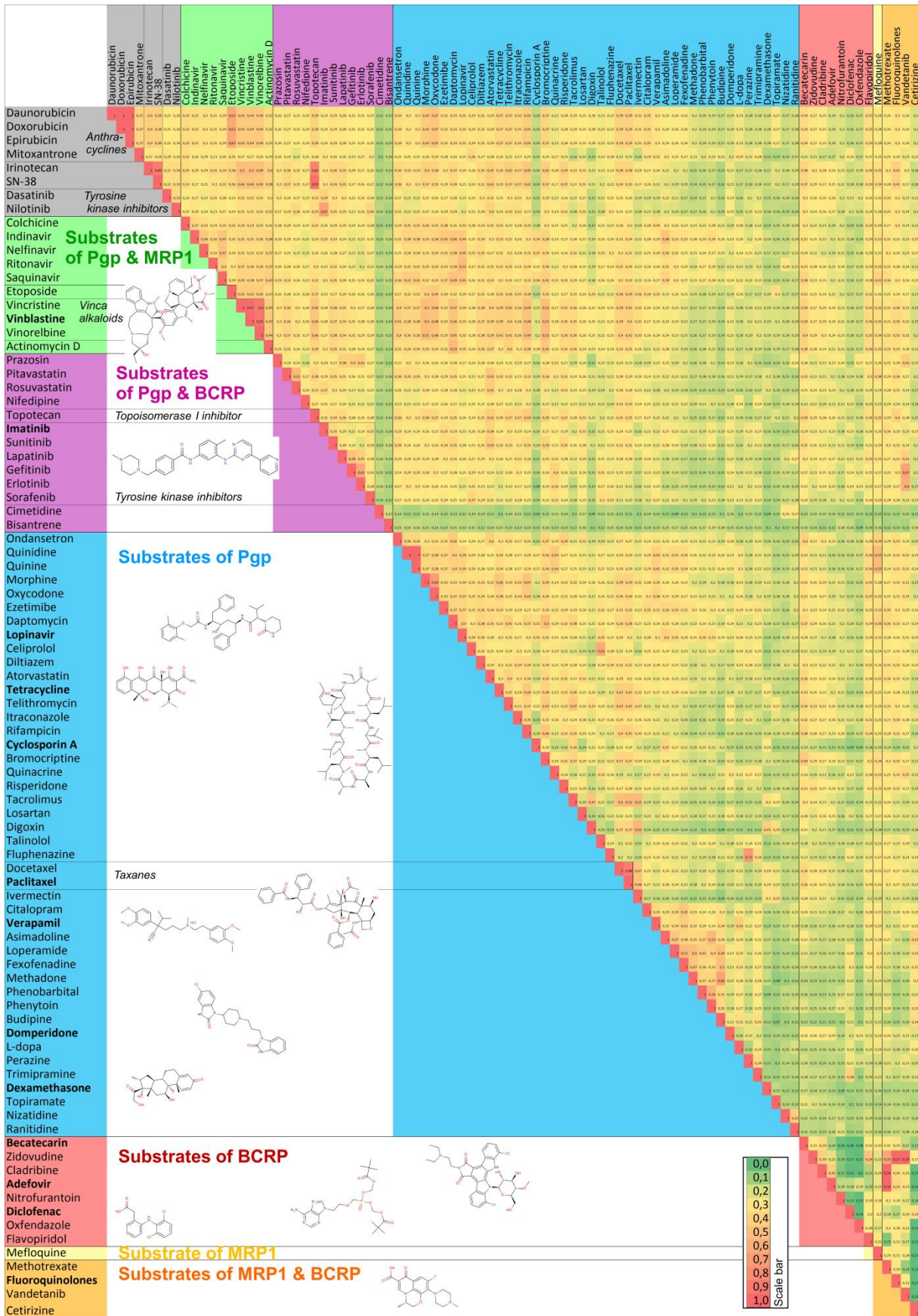
In the context of MDR, the first discovered ABC transporter was P-glycoprotein (P-gp, encoded by the ABCB1 gene). Investigating Ehrlich ascites tumor cells in 1973 *Dano* was the

first to observe the active, energy dependent outward transport of the cytotoxic agent Daunorubicin [27]. Only three years later *Juliano* and *Ling* ascertained connectivity between MDR and the ABC transporter P-gp [28]. In 1992 a further ABC transporter, the Multidrug Resistance associated Protein, MRP1 (encoded by the *ABCC1* gene), was identified to be linked to MDR and altering intracellular GSH levels [29,30]. As the third important transporter involved in MDR the Breast Cancer Resistance Protein BCRP (encoded by the *ABCG2* gene) was discovered in 1998 [31]. These three transporters are the most important efflux transporters conferring MDR.

In their structural composition they share the presence of two nucleotide binding domains (NBD), which are responsible for the ATP binding and hydrolysis that drives drug transport, and two transmembrane domains (TMD), which contain the drug-binding sites [32,33]. The TMDs are built by six membrane-spanning  $\alpha$ -helices. In case of MRP1 an additional 5-helical TMD is present at the N-terminus of the protein, while BCRP is a half-transporter, that needs to dimerize (or even oligomerize [34]) in order to function [33,35].

The wide substrate spectrum of compounds that is translocated across cellular membranes by the three presented transporters is partially overlapping. The heat-map in Figure 1 illustrates the structural similarity between the particular substrates. Compounds highlighted in grey are transported by all three transporters. Compounds that are transported by a single protein only are highlighted by primary colors: P-gp substrates are indicated in blue, BCRP substrates in red and MRP1 substrates in yellow. Substrates of two of these transport proteins are indicated by the mixed color, therefore compounds transported by P-gp and BCRP are highlighted in violet, substrates of P-gp and MRP1 in green, and BCRP and MRP1 substrates in orange.

**Figure 1:** Heat-map of substrates transported by the three MDR transporters P-gp, MRP1 and BCRP. The coloring on the upper half illustrates the structural similarity between the compounds as calculated from Tanimoto coefficients with the help of the InstantJChem software [36] (as shown in the scale bar in the right lower corner, red indicates a coefficient of 1, which is 100% identity, while green indicates a coefficient of 0 with no detectable similarity). Due to the symmetry of the heat-map, in the lower half of the figure is indicated by which transporter the respective compound is recognized and transported: grey: P-gp, MRP1 and BCRP; blue: P-gp, red: BCRP; yellow: MRP1; violet: P-gp and BCRP, green: P-gp and MRP1, orange: MRP1 and BCRP. Data on substrate specificity were collected from [10,37–40].



A model for a putative transport mechanism is exemplified for P-gp and illustrated in Figure 2. Substrates of P-gp are recognized in the context of the plasma membrane due to their hydrophobic character and enter the inward-facing drug binding cavity of the transporter [41–43]. Upon ATP binding, or ATP binding and hydrolysis, the transporter changes its conformation in a manner, that the drug binding domain is facing outward, enabling the release of the substrate [43–46]. While for most substrates, P-gp is able to establish a concentration gradient against the membrane, for lipophilic substrates, a renewed entry of the same molecule is possible, resulting in a cycle of constant efflux. This so-called “futile cycling” elevates the energy demand of the cell but can also inhibit the efflux of other (lower affinity) substrates from the pump [14,41].

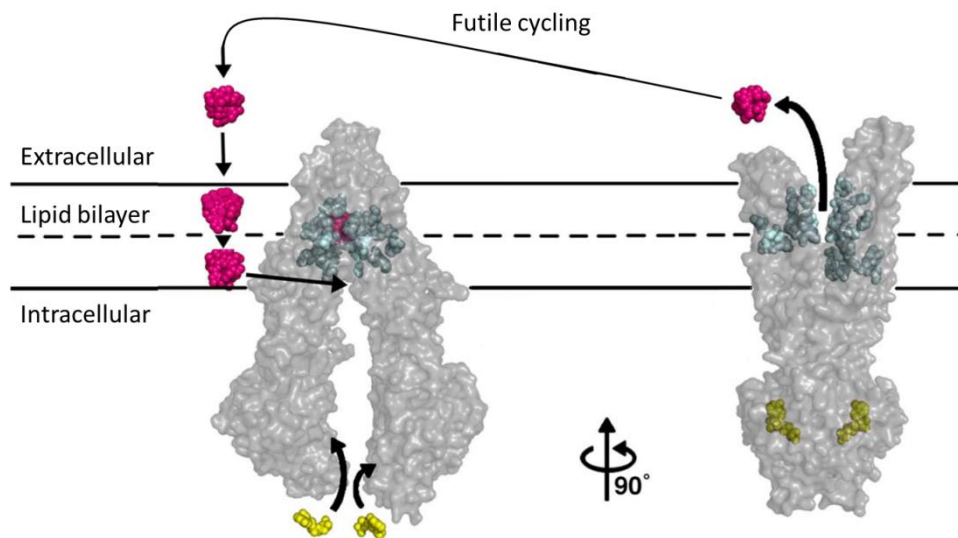


**Figure 2:** P-gp acts as a “hydrophobic vacuum cleaner” of the membrane, preventing the entry of substrates into the cell – modified from [41,43]. The substrate (magenta) enters the membrane and diffuses into the drug binding pocket (blue) of the transporter. Upon binding and hydrolysis of two ATP molecules (yellow) the conformation of the transporter changes from an inward- to an outward facing conformation, following release of the substrate.

### ***1.3. Attempts to overcome MDR***

In order to circumvent the transporter mediated resistance, inhibiting the transporters appeared to be a valuable approach. The first report following this idea was published in 1981 with the discovery of P-gp inhibitory potential of the Ca<sup>2+</sup>-channel blocker Verapamil [47]. Together with further drugs, which were already approved for other medical purposes (Quinine and Cyclosporine A), the “first generation” of P-gp-inhibitors was born [9,48]. The low efficacy of these compounds together with their toxic side effects led to the development of “second generation” inhibitors, which were modified in a way to decrease the side effects caused by the interaction with the original targets of the first generation [9,48]. Despite the achieved improvement, second generation inhibitors like Dexverapamil and Valspodar (PSC-833) showed pharmacokinetic interactions, that resulted in the failure of clinical trials [9,48,49]. In contrast, “third generation” inhibitors, like Tariquidar, Elacridar and many others, have been specifically designed for the interaction with the ABC transporter, and therefore possess P-gp inhibitory potential at low concentrations [9,48,49]. Figure 3 gives an overview over some reported ABC transporter inhibitors.

Despite promising *in vitro* results, successful translation of MDR transporter inhibition to the clinic remains elusive [35,37,50–53]. Several factors might explain the failure in the clinical trials, such as the intrinsic toxicity of the modulators and the unwelcome inhibition of transporters residing in pharmacological barriers (blood brain barrier, placenta, GI-tract, liver), resulting in an altered distribution of the simultaneously administered chemotherapy [35,51,52]. Furthermore, many P-gp inhibitors are reported to interact with Cytochrome P450 [35,52]. Genetic polymorphisms of ABC transporter genes, as represented by single-nucleotide polymorphisms (SNPs), may have prevented optimal results from the clinical evaluation of their inhibitors [35,37]. A poor outcome and marginal benefit in the clinical trials can also be explained by insufficient preclinical evaluation [35] as well as the inadequate selection of patients for the enrolment of the trials: The proof that P-gp or other ABC transporters were the main reason for resistance of treated patients was missing [37,50]. The development of imaging tools to ensure that patients involved into clinical trials of ABC transporter inhibitors really express the transporters as main mechanisms of resistance, rather than as a marker of a more aggressive phenotype, is needed before the resumption of clinical trials [37,53].

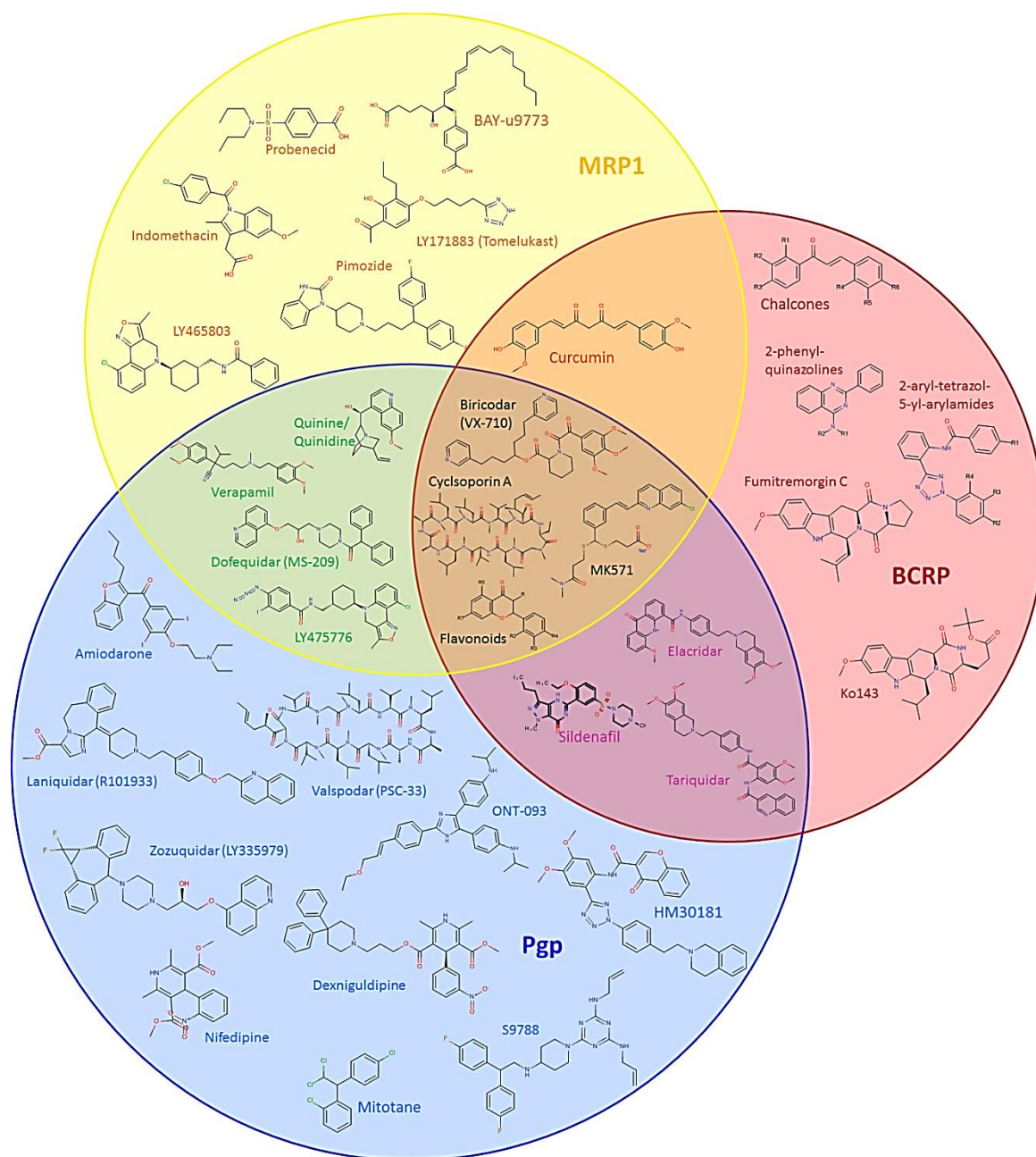


**Figure 3:** Inhibitors of ABC transport proteins, reported in the literature [35,37–39,52,54–64]. Applying the color code used in Figure 1, compounds inhibiting P-gp are marked in blue, inhibitors of BCRP in red, and MRP1 inhibitors in yellow. Compounds inhibiting more than one transporter are located in the intersections.

As summarized in Figure 4, further strategies to overcome ABC-transporter mediated MDR exist next to the inhibition of the transporters, which might “engage” the transporter. Another approach is, to develop compounds that do not interact with the transport protein and therefore “evade” it. The third strategy employs compounds, which selectively kill the MDR cells, “exploiting” vulnerabilities that are connected to the MDR phenotype.

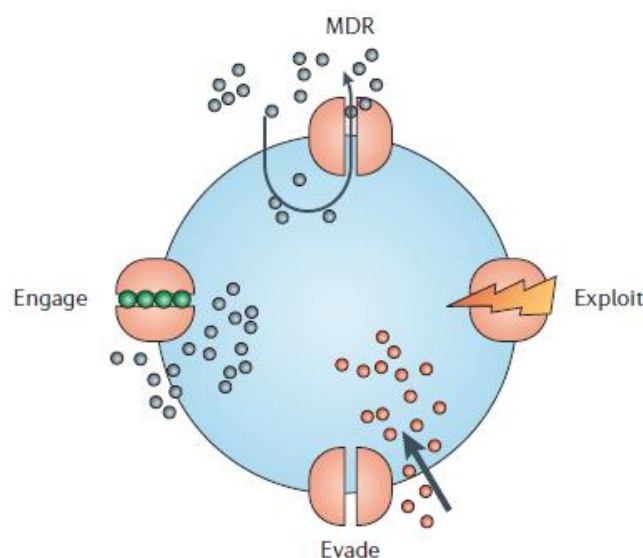


**Figure 4:** Strategies to overcome ABC transporter mediated MDR (top) include “engaging” the protein with the use of inhibitors (left), “evading” the transporter by the development of compounds which are not recognized (down), and “exploiting” it, by application of collateral sensitivity [9].

#### ***1.4. Collateral sensitivity – in search for the Achilles’ heel***

The term “collateral sensitivity” (CS) was first used by Szybalski and Bryson in 1952 to describe the increased sensitivity of *Escherichia coli* bacteria strains treated with a certain chemotherapeutic agent toward other, unrelated antibiotics [65].

Similarly, many reports can be found on MDR cancer cells exhibiting an – compared to their parental cell lines – enhanced sensitivity toward diverse compounds with distinct putative mechanisms of action [41,42,66]. As insinuated in chapter 1.1. the adaption processes that occur during the development of the MDR phenotype comprise numerous cellular changes, which, next to the benefit of survival in the presence of chemotherapeutic agents, may also provide vulnerable target points for the selective elimination of MDR cells [42]. For example, an increased drug metabolizing activity of MDR cells might result in a higher activation of xenobiotics, as observed for the natural product *austocystin D*. It has been shown, that the



enhanced P-gp expression in cell lines collateral sensitive to *austocystin D* is rather coincidental, since the selective toxicity of the compound toward MDR cell lines arises from its selective activation by cytochrome P450 (CYP) enzymes in specific cancer cell lines [67]. In contrast, in many cases ABC transporters have been reported to mediate paradoxical hypersensitivity by different mechanisms. One possible explanation could be that an MDR selective agent **facilitates or stimulates the extrusion of an endogenous essential molecule** by the transporter [66]. In case of MRP1 mediated collateral sensitivity, an enhanced toxicity of compounds might be explained by the (co-)transport of glutathione and glutathione-drug conjugates by the transporter: an enhanced export of this antioxidant will disturb the intracellular redox-homeostasis to a higher extent in the transporter expressing cells as compared to the parental cell lines, causing a higher extent of oxidative stress and cellular damage [68]. Since GSH is not a substrate of P-gp, this mechanism might not apply for the multiple cases of reported collateral sensitivity in cells, in which P-gp is responsible for the MDR phenotype of investigated cells [69].

The first reports on collateral sensitivity in P-gp expressing cells cover compounds that **disrupt the plasma membrane**, like the detergent Triton X-100 [70]. Similarly, several opiates induced collateral sensitivity that was related to fluidizing effects on membrane biophysical properties of P-gp expressing cells [71]. Since P-gp requires interaction with phospholipids for continuous drug-mediated ATPase activity and interaction with the substrate, a disruption of the plasma membrane will also affect the activity of the transport protein [72,73]. Even though differences in the biophysical properties of plasma membranes of drug-sensitive and MDR cells could be confirmed on a panel of cell lines, the increased toxic effect of Triton-X-100 on P-gp expressing cells could not be verified in a tetracycline-repressible (tet-off) plasmid system, in which P-gp expression was repressed upon treatment with tetracycline [74]. A further example of membrane perturbing agents causing collateral sensitivity is given by the block-copolymers Pluronic P85 and P105. A possible interaction of such a polymer with the lipid raft region, the micro domain of the cellular membrane surrounding P-gp, is shown in Figure 5. As stated above, this interaction will inhibit the function of P-gp, and therefore sensitize MDR cell lines toward cytotoxic drugs [73].

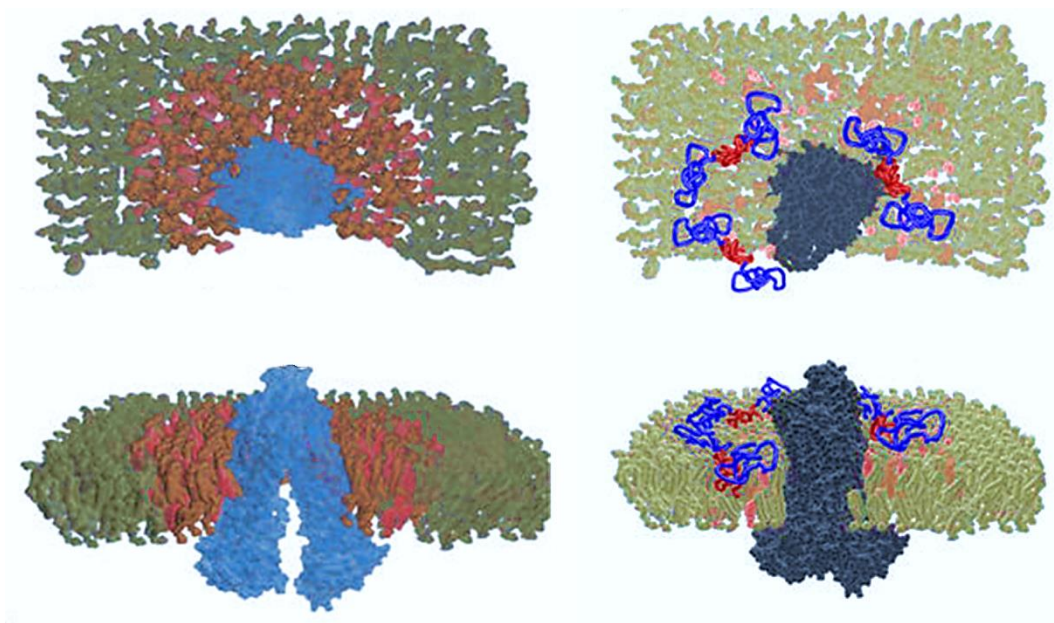


**Figure 5:** Cellular membrane with incorporated P-gp in the absence (left) and presence (right) of a Pluronic block-copolymer (blue / intense red). The intracellular lumen is located below the membrane, which is shown in Top (top) and side angle (below) view. P-gp (blue) is embedded in the membrane containing phospholipids with mainly unsaturated fatty acids (grey) in a micro domain called lipid raft. Lipid rafts contain cholesterol (red) and sphingomyelin (orange) – modified from [73].

In addition to the effect on the cellular membrane, Pluronic co-polymers P85 and P105 have been reported to decrease cellular ATP pools in MDR cells, but not in their parental counterparts [75,76]. The resulting sensitizing effect of Pluronics toward cytotoxic agents could be abolished by ATP supplementation [75]. It has been described that the block co-polymers differentially affect the mitochondrial functions in MDR and non-MDR cells, evoking an increased toxicity in P-gp expressing cells [76]. Even though the lower mitochondrial membrane potential found in MDR cells as compared to parental cells might explain the intrinsically increased sensitivity of the MDR cells toward the co-polymers, two evidences suggest a role of P-gp in this effect [13,76]: the higher responsiveness of the respiratory chain of MDR cells is not only abrogated in the presence of the P-gp inhibitor Elacridar, but also not only observed in drug-selected MDR cells, but also in cells transfected with P-gp [76].

Due to the energy dependence of the efflux by ABC transporters, P-gp-expressing cells might be more sensitive to compounds that interfere with cellular metabolic pathways and therefore cause changes in energy utilization [66]. Yet, the interaction of a compound with the cellular metabolic pathways does not necessarily require its interaction with P-gp. An **increased sensitivity to changes in energy levels** of MDR cells might explain the preferentially killing

of MDR cells by the antimetabolites, like 2-deoxy-d-glucose, and the electron transport chain inhibitors rotenone and antimycin A [66,77,78].

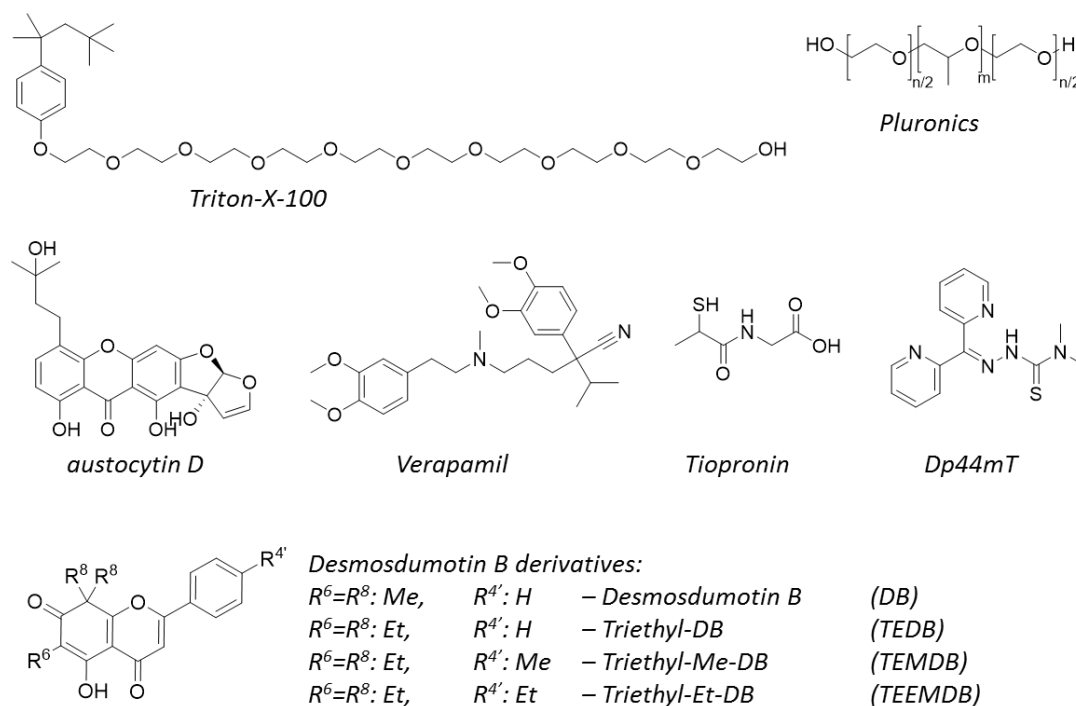


**Figure 6:** Structures of compounds with reports on CS (for details, see text).

Since the first reports about application in MDR cancer cells due to the interaction with P-gp in 1981 [47], the  $\text{Ca}^{2+}$ -channel blocker Verapamil has received a lot of attention. At lower concentrations Verapamil is a (“nontransported”) P-gp substrate, which has an ATP depleting effect on MDR cells due to a rapid cyclical efflux, re-entry and efflux (“futile cycling”, Figure 6) [14,15,41,79]. This elevated **energy depletion in P-gp expressing cells** might be a possible explanation for the differential effect on cell viability of MDR and non MDR Chinese Hamster ovary (CHO) cells, which was already reported as early as 1986 [80]. Also in other cell line models Verapamil preferentially induced apoptosis in MDR cells compared to drug-sensitive cells [81,82]. A biphasic effect was observed for the effect of Verapamil on P-gp ATPase activity and cell viability: while at lower concentrations the ATPase activity was stimulated (in agreement with Verapamil being transported out of the cell), at higher concentrations it was inhibited. Similarly the induction of apoptosis followed a biphasic trend [82,83]. Even though increased glycolysis has been suggested as the compensation of higher

energy demands due to the “**futile cycling**” [15–17], **reactive oxygen species (ROS)**, which might occur as side products of oxidative phosphorylation, have been suggested to be involved in the apoptosis induction by Verapamil [82]. An increased production of ROS is a further suggested putative mechanism of increased toxicity toward MDR cell lines [42,66].

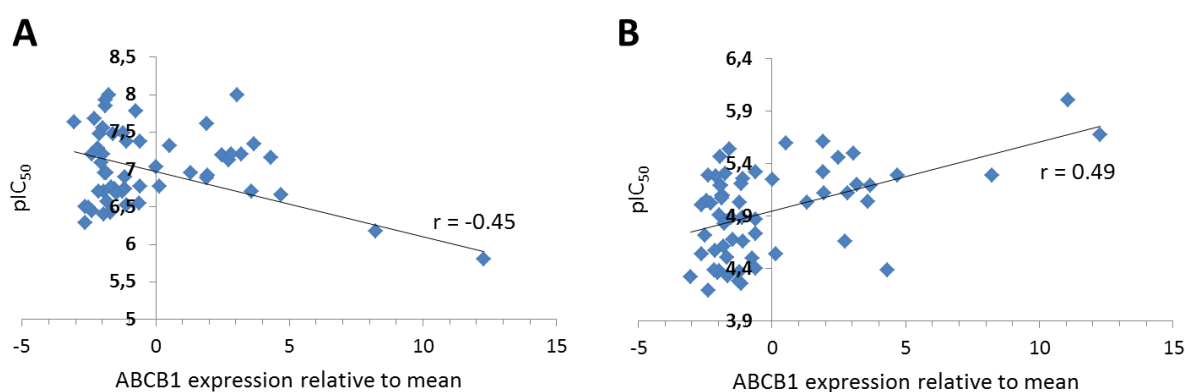
ROS might also have other sources and causes than futile cycling of P-gp substrates. For example the *N*-(2-mercaptopropionyl)glycine Tiopronin has been reported to possess enhanced (but still not very high) toxicity toward a subset of (but not all investigated) MDR cell lines expressing P-gp and MRP1 [84]. While inhibiting MRP1, Tiopronin has no impact on the function of P-gp [84]. In case of P-gp expressing cell lines, inhibition of the transporter by Tariquidar did not alter the activity of the compound [84]. Together with the cell line specificity of the effect this suggests, that the collateral sensitivity of MDR cells toward Tiopronin might be linked to other factors than P-gp. Follow up studies revealed, that the enhanced toxicity toward certain MDR cell lines is indeed linked to the inhibition of glutathione peroxidase (GPx), to which Tiopronin covalently binds [85]. In agreement with this, the addition of the ROS scavenger *N*-acetylcysteine (NAC) protected the investigated cells from Tiopronin induced toxicity [85].

Likewise, chelators might induce ROS upon formation of redox active metal complexes [86–89]. A paradoxical hypertoxicity against the Vinblastine selected P-gp-overexpressing cervix carcinoma cell line KB-V1 as compared to its parental cell line KB-3-1 has been reported for the thiosemicarbazone metal chelator di-2-pyridylketone-4,4,-dimethyl-3-thiosemicarbazone (Dp44mT) [86,90]. The lysosomal accumulation of the redox active copper complex of the ligand might be involved in the mechanism of toxicity of this ligand [87]. It has been suggested, that lysosomal P-gp might contribute to this mechanism, explaining a potential hypersensitivity [90]. Yet, experiments performed on different cell lines suggested, that this effect might not be generalized, as only a weak correlation could be found between the sensitivity of investigated cell lines toward the P-gp substrate Doxorubicin and Dp44mT (based on data of Supplement from [86]).

Further compounds with remarkably enhanced toxicity toward a P-gp expressing cell line, namely the Vincristine selected KB-VIN cell line, are derivatives of the natural product Desmosdumotin B, which was isolated from the root *Desmos dumosus* [91]. While the parent compound 5-hydroxy-7-one-6,8,8-trimethylflavone, already showed a 20-fold higher activity in KB-VIN cells, than in KB-3-1 cells [92], derivatives were designed in order to increase the selectivity. The three 6,8,8-triethyl analogues proved to be especially promising, with 4' alkylated derivatives possessing up to 460-fold higher toxicity in the MDR cell line [93,94].

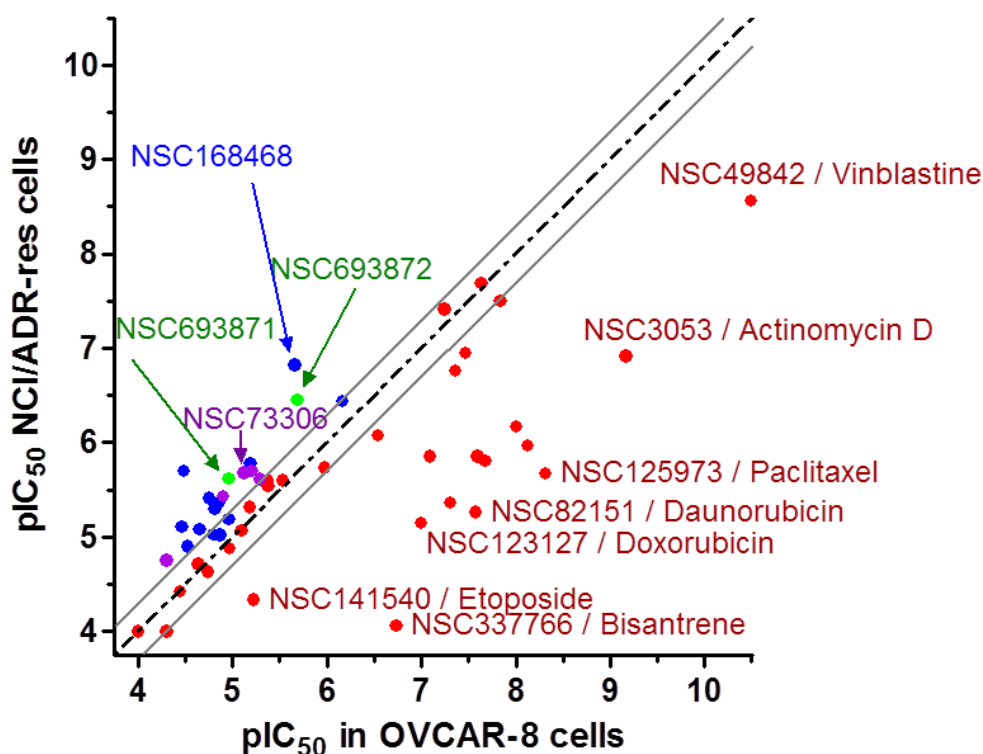
The P-gp dependence of this effect was investigated by co-administration of Verapamil, which partially reversed the selectivity of Desmosdumotin B and the triethyl-derivative (TEDB). Despite this promising data, the effect was stated to be not generally linked to P-gp, but rather restricted to only a few cell lines [93,94].

A promising strategy to find compounds that might exploit MDR in a P-gp dependent manner is based on a pharmacogenomic approach which utilizes publically available data from the Developmental Therapeutics Program (DTP) of the National Cancer Institute (NCI) [95–97]. With the help of this tool, the gene expression profiles of human ABC transporters were correlated with patterns of drug activity within the NCI60 cell line panel [95,96]. These 60 cell lines represent tumor types from different origin, including leukemia, colon, lung, central nervous system, renal, melanoma, ovarian, breast and prostate cancer [97].



**Figure 7:** Correlating publically available toxicity data (as pIC<sub>50</sub> values) against the NCI60 cell panel with P-gp expression (mean centered data displayed) of the investigated cell lines for the P-gp substrate Doxorubicin (A; NSC123127), and the MDR selective compound NSC73306 (B).

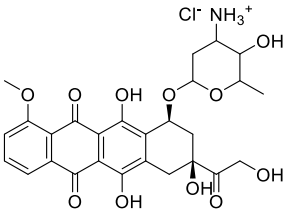
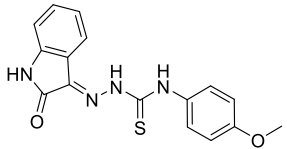
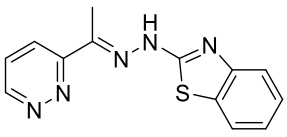
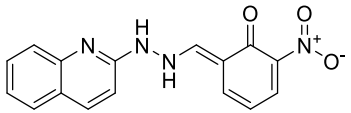
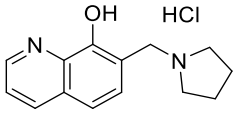
As illustrated in Figure 7, the toxicity of P-gp substrates show a negative correlation with transporter expression (Pearson correlation coefficient  $< -0.4$ ), due to the efflux of the compounds. Panel B of the figure shows, that this approach also identified compounds toward which P-gp expressing cells show a paradoxical hypersensitivity (Pearson correlation coefficient  $\geq 0.4$ ) [95,98].



**Figure 8:** Extracted data from the drug screening against the NCI60 panel data, comparing the activity of known P-gp substrates (red), and reported MDR selective agents (blue) [98] in P-gp-positive NCI/ADR-res and P-gp-negative OVCAR-8 cells. Additionally, MDR selective Thiosemicarbazones, like NSC73306, are highlighted in purple, 8-hydroxyquinoline derived Mannich bases like NSC693871 in green.

Within the 60 cell lines, a cell line pair with discriminative resistance status can be found, as the multidrug resistant NCI/ADR-res cells are derived from OVCAR-8 ovarian adenocarcinoma cells [99]. While the 60 cell lines in the panel are quite dissimilar to each other, this cell line pair shows some commonalities. Therefore comparing the activity toward these two related cell lines gives a further impression on the impact of MDR on the activity of compounds. Assuming, that P-gp expression is a major characteristic of the MDR phenotype in the investigated cell line (which is in agreement with the available expression data), a plot of activity toward the MDR cell line on the y-axis, vs. activity of the same compound against the parental cell line (X-axis), as exemplified in Figure 8, will show substrates of the transporter under the bisecting line. Compounds, selectively targeting MDR cells can be found above the bisecting line.

**Table 1:** Correlation data of the drug screening against the NCI60 panel data vs. P-gp expression as illustrated in Figure 7. Data are given for example compounds identified to be putatively MDR selective based on their Pearson correlation coefficient, as reported in [98], in comparison to the P-gp substrate Doxorubicin.

NSC123127 Doxorubicin		Pearson correlation coefficient r:	-0.45
		IC <sub>50</sub> (OVCAR-8) / μM	0.12
		IC <sub>50</sub> (NCI/ADR-res) / μM	1.58
		SR (OVCAR8 / NCI/ADR-res)	0.08
NSC73306 <b>I-a</b>		Pearson correlation coefficient r:	0.49
		IC <sub>50</sub> (OVCAR-8) / μM	7.56
		IC <sub>50</sub> (NCI/ADR-res) / μM	2.09
		SR (OVCAR8 / NCI/ADR-res)	3.63
NSC693630		Pearson correlation coefficient r:	0.40
		IC <sub>50</sub> (OVCAR-8) / μM	1.66
		IC <sub>50</sub> (NCI/ADR-res) / μM	2.29
		SR (OVCAR8 / NCI/ADR-res)	0.72
NSC168468		Pearson correlation coefficient r:	0.46
		IC <sub>50</sub> (OVCAR-8) / μM	2.19
		IC <sub>50</sub> (NCI/ADR-res) / μM	0.15
		SR (OVCAR8 / NCI/ADR-res)	14.45
NSC693871		Pearson correlation coefficient r:	0.68
		IC <sub>50</sub> (OVCAR-8) / μM	10.96
		IC <sub>50</sub> (NCI/ADR-res) / μM	2.40
		SR (OVCAR8 / NCI/ADR-res)	4.57

The collateral sensitivity of diverse MDR cancer cells toward the compounds identified in this way is abrogated in the presence of a P-gp inhibitor, suggesting that in addition to the export of substrates, ABC transporters may directly sensitize MDR cells to the effect of other compounds [95,98,100]. Based on the positive correlation of activity within the cell line panel with P-gp expression *Türk et al.* reported the potential of 64 compounds to possess MDR selectivity [98]. Out of this discovery set, 35 compounds were available for verification experiments in KB-3-1 and KB-V1 (*vide supra*) cells. While three compounds were not toxic in the test system and ten provided equal toxicity toward both cell lines, 22 of the identified compounds proved to be MDR selective [98]. The fraction of IC<sub>50</sub> values obtained in P-gp negative vs. positive cells can serve as a quantification of CS, and is called selectivity ratio (SR) [41]. Table 1 gives some examples of compounds with Pearson correlation coefficients

calculated from the drug effects over the NCI60 cell panel against the P-gp expression, as well as  $IC_{50}$  and SR values comparing the toxicity toward ovarian carcinoma cells OVCAR-8 (P-gp negative) and NCI/ADR-res (P-gp positive). The well-known P-gp substrate Doxorubicin gives a negative correlation coefficient and an inverse ( $< 1$ ) SR [8,10,35,37,101], while the confirmed MDR selective agents NSC73306 [95,98,100,102,103] and NSC168468 [98] show positive correlations and a SR higher than two.

Despite of showing some degree of diversity, the compounds identified by the pharmacogenomic approach share the ability to chelate metal ions. Strikingly, an enrichment in isatin- $\beta$ -thiosemicarbazone structures like NSC73306 can be found (9 out of the 64 potentially MDR selective compounds) [95,98,100,102,103]. Several attempts have been made to identify the structural features of isatin- $\beta$ -thiosemicarbazones that are responsible for the MDR selective activity. The major findings, that resulted in a pharmacophore model are summarized in Figure 9 [102]. The thiosemicarbazone (TSC) scaffold is required for the selective toxicity toward MDR cell lines: replacement of the sulfur to oxygen significantly decreases toxicity [102,103]. Likewise, a bulky or aromatic moiety appears to be required at the N4 of the TSC moiety (counting of atoms in the TSC moiety according to green numbers) [42,102,103]. This aromatic moiety might be substituted at positions 2', 3' or 4', out of which the *para* substitution (4') was found to be optimal, while *ortho* (2') and *meta* (3') substitutions have been concluded to be not beneficial [42]. Although the available data on *ortho* and *meta* substituted aromatic rings might not be sufficiently convincing, to definitely exclude the activity of these compounds, since many of those reported compounds show multiple substitutions on the aromatic ring. For chloro-substitutions, the *meta* substituted derivative was even superior to the *para* one, in terms of toxicity, while being equally selective [103].

The isatin moiety – or at least the lactam – seems to be necessary for selective activity. An extension of the aromatic ring system disrupts activity, while substitution at the 5th position might be tolerated in case of halogens or a nitro-group, but not in case of a sulfonate, which might be explained by a reduced cell permeability of the resulting negatively charged molecule [102].



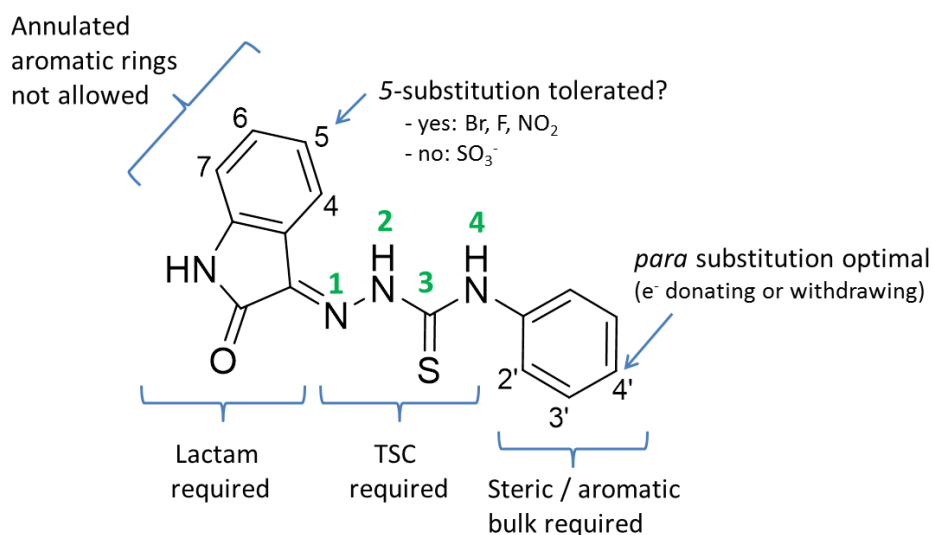


**Figure 9:** SAR / pharmacophore model on isatin- $\beta$ -TSCs, created after references [42,102,103].

### 1.5. Putting the bite on metals – Role of Chelation in (MDR) Cancer therapy

Chelators are investigated for their therapeutic potential in the treatment of diverse diseases including metal overload and diseases related to imbalanced metal homeostasis like hemochromatosis,  $\beta$ -thalassemia, Alzheimer's or Parkinson's diseases and cancer [86,88,104,105]. Several chelators display significant antitumor activity, and some were even shown to exhibit enhanced toxicity toward otherwise multidrug resistant cancer cell lines [89,95,98,100,102]. As indicated in chapter 1.4., the compounds identified by the pharmacogenomic approach to potentially overcome MDR by selectively targeting P-gp-expressing cells all share the ability to bind metal ions [98].

MDR in cancer is a highly relevant research topic, as indicated by the increasing number of publications per year (see numbers of PubMed search results in Figure 10). The numbers of publications on ABC transporter inhibition trials reflect the importance to overcome MDR. While the strategy to exploit vulnerabilities related to MDR by addressing the collateral sensitivity of cancer and the selective targeting of MDR cancer cells is relatively unconventional, and publication numbers on this topic might just start to rise, the increasing number of publications on the use of chelators as anticancer agents shows that this strategy is more frequently used. Due to their increased proliferation cancer cells have an altered metal homeostasis in order to fulfil the higher demand for metal ions that are critical for cell growth, cell-cycle progression and DNA synthesis [86,88,104]. The rate limiting step in DNA

synthesis for example is the reduction of ribonucleotides, which is catalyzed by the iron dependent enzyme ribonucleotide reductase (RR) [106,107].

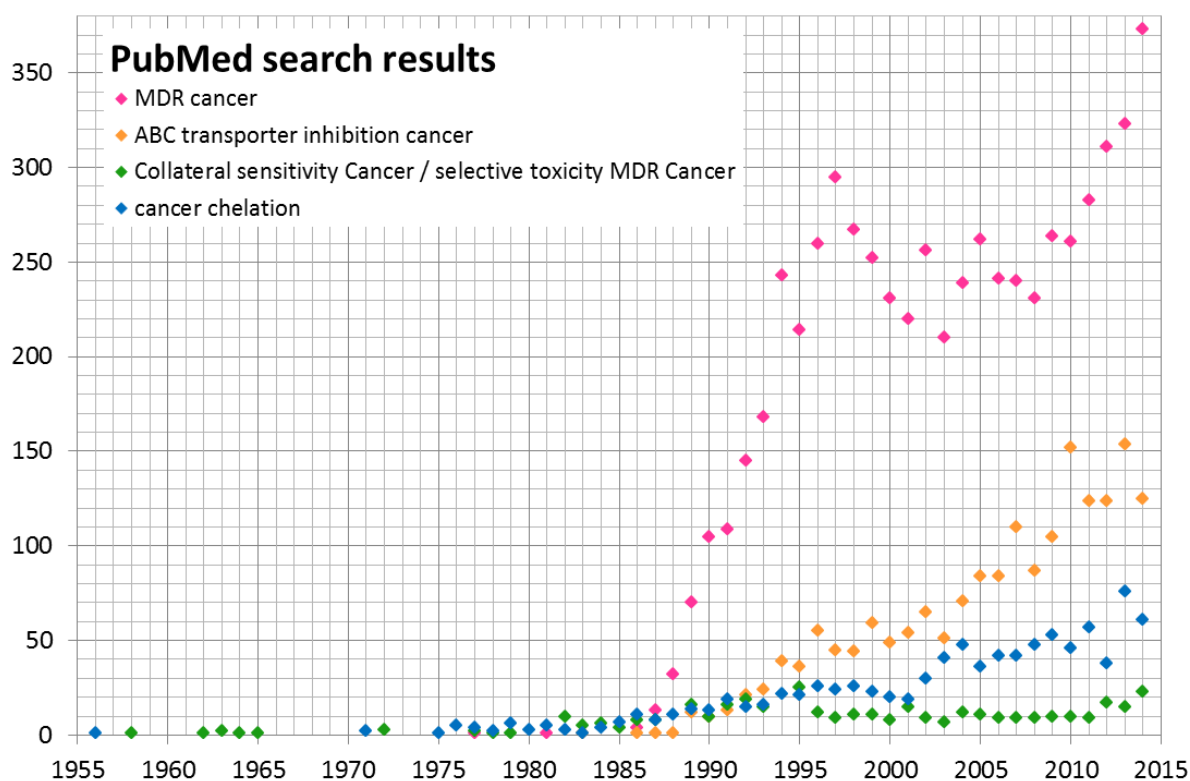


**Figure 10:** Number of articles collected in the PubMed database covering the time period from 1955 to 2014 sorted by publication date. Search results are shown for the keywords “MDR cancer” (magenta), “ABC transporter inhibition cancer” (orange), “collateral sensitivity cancer / selective toxicity MDR cancer” (green) and “cancer chelation” (blue).

Following alkali and alkaline earth metals, iron, zinc and copper are the most abundant essential metals in the human body [108]. While zinc is found to have many structure-supporting and gene regulatory roles, the ability of iron and copper to change between two stable oxidation states facilitates their utilization as cofactors with catalytic function in many enzymes. It is estimated that at least one third of the human proteome consists of metallo-proteins and many of them have been associated with a variety of diseases such as cancer, inflammatory, infectious, cardiovascular and neurodegenerative diseases [108–110]. The elevated demand of cancer cells especially for iron [111,112] and copper [113,114] provides promising target points for cancer treatment strategies [88,89,98,104,115].

The regulation of intracellular metal levels, localization and utilization is tightly regulated [116,117]. Figure 11 shows some of the key processes involved in iron and copper homeostasis (panel A) and possible interaction points of chelators (panel B).

Iron uptake is mediated by the transferrin receptor TfR. The shuttle protein transferrin (Tf) has two binding sites for ferric iron ( $\text{Fe}^{3+}$ ). Upon iron-loading, and binding of two Tf proteins to the receptor, the TfR is endocytosed together with other membrane proteins like the copper transporter CTR1, the divalent metal transporter DMT1 and the ferrireductase STEAP3 (six transmembrane epithelial antigen of the prostate 3). Within the acidic endosome ferric iron is released from Tf and reduced by STEAP3 to its ferrous form ( $\text{Fe}^{2+}$ ).  $\text{Fe}^{2+}$  is exported from the endosome by DMT1 and becomes available in the cytosol as part of the labile iron pool. Recycling of the metal free Apo-Tf bound TfR receptor is achieved via exocytosis [88,116,118–120]. Excess of iron can either be stored in the storage protein ferritin, or transported out of the cell by the transporter ferroportin (FPN1) [116,118,120]. The mitochondrial iron transporter mitoferrin-1 (MIF1) enables utilization in the mitochondria for example for iron-sulfur-cluster (ISC) and heme-synthesis, which are both incorporated in several metallo-enzymes [119–121]. The expression of proteins involved in iron-homeostasis (TfR, DMT1, ferritin, FPN1, enzymes involved in ISC and heme synthesis) is regulated on the translational level via the IRE (iron-responsive element) - IRP (iron-regulatory protein) system [119,121,122]. FPN1 is additionally regulated on a systemic level via hepcidin [88,121]. While only a minor fraction of the intracellular transition metal content is available in free ion pools, the amount of metal ions bound to, or incorporated into various proteins is much higher [117]. Metal ions serve as cofactors in a wide range of proteins and many iron-containing proteins have an equivalent copper protein with comparable function: Oxygen can be transported by the iron containing proteins hemoglobin and hemerythrin, or the copper containing hemocyanin; oxygenation reactions are catalyzed by iron containing cytochrome P-450 enzymes, or different oxygenases, as well as by the copper containing tyrosinase and quercetinase. Oxidases can be found with iron (peroxidases) and copper (amine oxidases, laccase) in their catalytic center – the same holds true for nitrite reductases. Electron transfer reactions are found to be mediated by iron containing cytochromes or blue copper proteins. Metallo proteins with antioxidative functions are iron containing peroxidases and copper containing superoxide dismutase (SOD) [108,114].

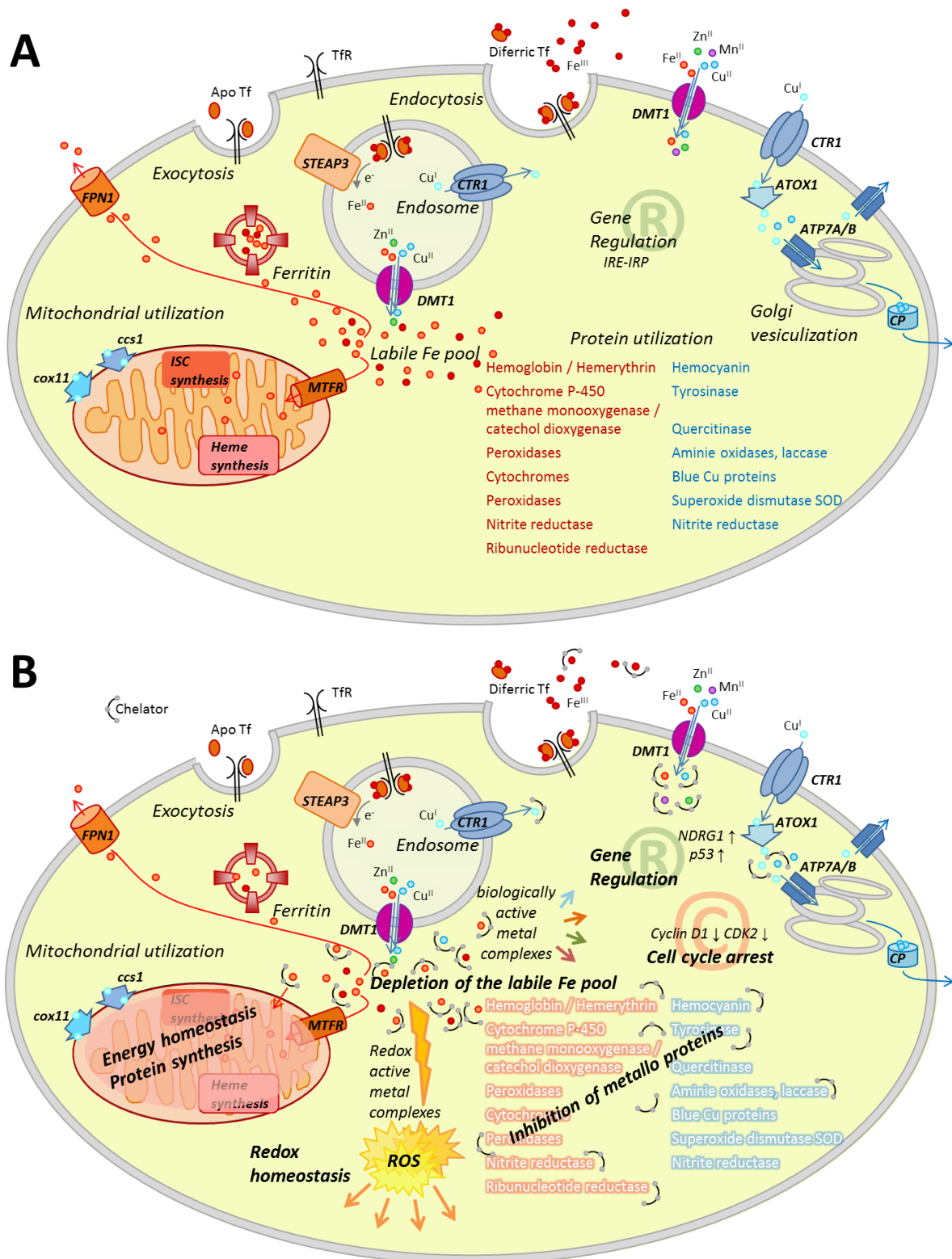


**Figure 11:** Cellular metal homeostasis (A) and possible interaction points of chelators (B). Created according to references [88,104,108,114–116,118–120,123–125], see text for details. Abbreviations: CDK2: Cyclin-dependent kinase 2; CP: ceruloplasmin; CTR1: copper transporter; DMT1: divalent metal transporter; FPN1: ferroportin; MTFR: mitotransferrin; NDRG1: N-myc downstream-regulated gene 1; IRE-IRP: iron-response element and iron-regulatory protein (1/2); ISC: iron sulfur cluster; Tf: Transferrin; TfR: transferrin receptor; STEAP3: six transmembrane epithelial antigen of the prostate 3 (ferrioreductase); ROS: reactive oxygen species.

In order to supply the cellular demands on copper, uptake of cuprous copper ( $\text{Cu}^+$ ) is regulated via the copper transporter CTR1, while cupric copper ( $\text{Cu}^{2+}$ ) is taken up by DMT1. Specific chaperones distribute copper to its target proteins: Ccs1 facilitates the incorporation of copper into SOD, Cox11 delivers copper for the synthesis of cytochrome c oxidase and ATOX1 enables transportation by the ATPases ATP7A and B out of the cells or into the secretory trans-Golgi apparatus [116,118]. In the Golgi apparatus, copper is sequestered and incorporated into ceruloplasmin and exported out of the cell, where it acts as a ferroxidase [114,116,126,127].

The incorporation of metal ions in several metallo proteins provides a broad spectrum of possible targets for chelators. Panel B of Figure 11 summarizes some general mechanisms by which chelators might interfere with the metal homeostasis. Triapine, a tridentate  $\alpha$ -N-pyridyl thiosemicarbazone, is a prominent example for a chelator, inhibiting the metallo-enzyme ribonucleotide reductase (RR). Triapine is currently undergoing different phase I and II clinical trials [128]. In its mechanism of inhibition the chelation by Triapine will not only lead to the withdrawal of the necessary iron from the enzyme, but also result in redox active complexes, which interfere with the intra-enzymatical electron transfer of the enzyme. The electron transfer from subunit R2 (which contains a tyrosyl radical and a diiron center) to subunit R1 (which harbors the catalytically active center) is pivotal for the function of the enzyme [106,129,130].

Next to their impact on DNA synthesis, chelators have been reported to result in cell cycle arrest via the down-regulation of Cyclin D1 and cyclin-dependent kinase 2 (CDK2) [88,115,131,132]. Furthermore, they regulate tumor suppressors like p53 and metastasis suppressors like the N-myc downstream regulated gene-1 (NDRG1) are down [88,115,131,133]. Iron depletion can foster apoptosis by up-regulation of the pro-apoptotic protein Bax and downregulation of the anti-apoptotic Bcl-2 [131,134]. Interfering with the IRE-IRP system, the expression of proteins involved in iron homeostasis will be regulated [119,121,122]. By chelating, ligands might deprive the cells from essential metal ions and deplete the labile iron pool [88,115]. Apart from the depleting effect, chelators might enable the transfer of metal ions through membranes, and for example shuttle additional iron into mitochondria [125]. Interfering with mitochondrial metal homeostasis, chelators might influence energy homeostasis and protein synthesis. Formed complexes might also possess biological activity, which is partially linked to their redox properties [87,124,135,136]. Copper complexes have been reported to intercalate into DNA [124,137,138], act as chemical nucleases, cleaving DNA by oxidative [124,138–140] or hydrolytic [124,141–143]

mechanisms or inhibit topoisomerase [124,144] and the proteasome [124,145,146]. Forming redox active complexes, chelators might enhance the production of reactive oxygen species, which might cause cellular damage, as addressed in detail in chapter 1.5. [88,115,116].

Several chelator classes have been described as pan assay interference compounds (PAINs). In a wide range of target-based assays, covering ion channels, enzymes, and protein-protein-interactions, these compounds have been reported to be problematic due to their reactivity, spectroscopic properties and the ability to form metal complexes as well as aggregates [147,148]. Redox active compounds might interfere with proteins, and by inactivating the target lead to false positive results [148]. Still in the areas of oncology, microbiology, and parasitology, reactive, photosensitive, and redox-active compounds may be particularly suited for therapeutic uses [147]. Often, in these areas the exact target of chelators is not known, and therefore the phenotypic drug discovery strategy is applied, where little assumptions are made concerning the participation of specific molecular targets and/or signaling pathways. Instead, compounds are investigated in complex biological systems and compound induced physiological responses or phenotypes are monitored in cells, tissues or whole organisms [149,150]. The induction of cell death upon treatment with a certain compound can be seen as a phenotypic effect [150].

### ***1.6. Keeping the balance on a double edged sword – ROS***

Reactive oxygen species (ROS) appear naturally as side products in the metabolism of aerobic organisms [113,116,151]. The main sources for cellular ROS are the complexes I and III (MCX-I, MCI-III) in the mitochondrial electron transport chain [152–155], as well as NADH cytochrome c reductase and cytochrome P-450 enzymes in the endoplasmatic reticulum (ER) [153,156], and oxidases (OX) like the membrane associated NADPH oxidases (NOX) [152,156]. The particular reactive species that can be found are oxygen containing radicals like the superoxide anion ( $O_2^{\cdot-}$ ), hydroperoxyl ( $HOO^{\cdot}$ ), or other peroxy radicals ( $ROO^{\cdot}$ ), the hydroxyl radical ( $^{\cdot}OH$ ), nitric oxide ( $^{\cdot}NO$ ), and other species like hydrogen peroxide ( $H_2O_2$ ), singlet oxygen ( $^1O_2$ ), hypochlorous acid ( $HOCl$ ) and peroxyxynitrite ( $ONOO^{\cdot}$ ) [151,157]. Also diverse radicals are formed by hydrogen abstraction ( $R^{\cdot}$ ) [151]. Out of these the three most physiologically relevant (with increasing reactivity) are hydrogen peroxide ( $H_2O_2$ ), the superoxide anion ( $O_2^{\cdot-}$ ) and the hydroxyl radical ( $^{\cdot}OH$ ) [116]. With a reduction potential of a 1-molar (oxidized and reduced form) solution at physiological pH of  $E^{\circ} = 0.32$  V,  $H_2O_2$  is

the weakest oxidizing agent of the three. Its reactivity is comparably poor, but it is highly diffusible and able to cross cellular membranes, which renders it the most efficient signal messenger and physiological regulator [113,116,153,158]. The superoxide radical  $O_2^{\cdot -}$  cannot cross cellular membranes freely, but can utilize ion channels for its translocation. It has a redox potential of  $E^{\circ'} = 0.94$  V and its inherent reactivity at physiological pH is relatively low, though it causes cellular damage mainly due to further reactions [116]. The hydroxyl radical, on the contrary is the most reactive of the three species, reacting on a diffusion limited manner [116,153,159]. With  $E^{\circ'} = 2.31$  V its reduction potential is the highest of the three species [116].

Reactive oxygen species can cause cellular damage by oxidizing biological macromolecules, namely lipids, proteins, sugars and DNA [115,151–153,157]. The oxidation of lipids mainly occurs as a consequence of reaction with the hydroxyl-radical, leading to the most common final products malondialdehyde and 4-hydroxynonenal, which can furthermore react with DNA bases, and cause mutations and DNA damage [113,155,160,161]. Since these species can be deleterious especially at high concentration, cells have developed an antioxidant system in order to disarm them [116,151,152]. Parts of the enzymatic and non-enzymatic antioxidant defense system are illustrated in Figure 12.

As indicated in chapter 1.4., metal and redox homeostasis are in tight connection [86,104,113]. Redox active metal ions or complexes can trigger oxidative stress by increased production of ROS via redox cycling [86]. On the other hand, this redox activity can be exploited for example in the antioxidant copper-containing enzyme superoxide dismutase (SOD), which catalyzes the disproportionation of superoxide ( $O_2^{\cdot -}$ ) to hydrogen peroxide ( $H_2O_2$ ) and molecular oxygen ( $O_2$ ), as indicated by the green arrows in Figure 12.

Likewise, these reactions can be catalyzed by metal ions or redox active complexes. Also the subsequent production of the reactive hydroxyl radical, which occurs via the Fenton (in case of iron) or Fenton-like (in case of other metal ions) reaction (red arrow in Figure 12), is catalyzed by metal ions or complexes, as depicted by the red arrow. The Fenton reaction is part of the so called Haber-Weiss reaction (indicated by highlighted arrows in Figure 12), that describes the metal ion catalyzed reaction of hydrogen peroxide with superoxide [86,104,113,116,121,135,151,154].

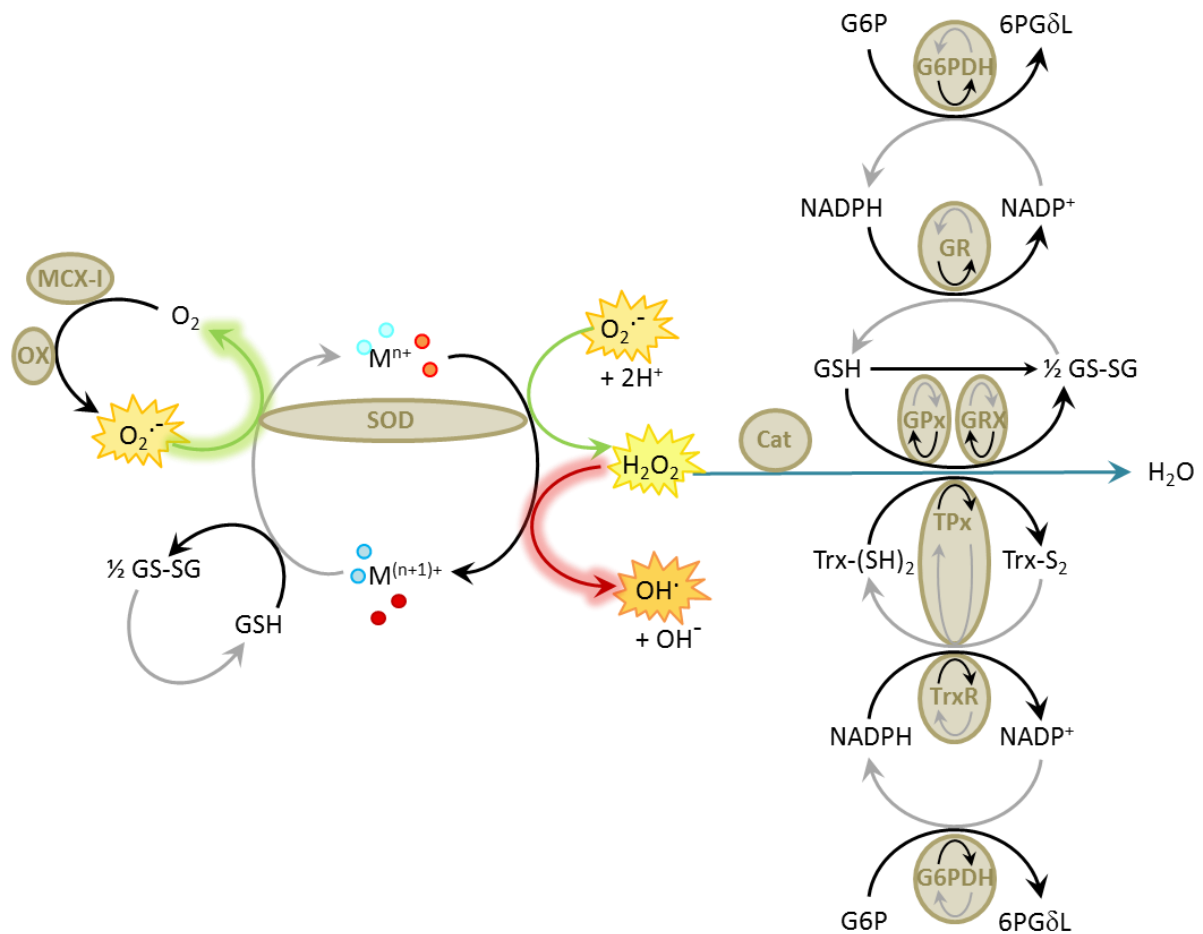


**Figure 12:** Redox homeostasis. Redox cycling of metal ions or of redox active complexes induces further reactions and responses in the cellular antioxidant system. Created according to references [116,135,151,154,89,162]. Oxidation reactions are depicted by black arrows, reduction reactions by grey arrows. Green arrows represent the reactions, which are also catalyzed by the copper-containing superoxide dismutase (SOD), the red arrow represents the Fenton (iron) / Fenton-like (other redox active metal ions) reaction. The reduction of hydrogen peroxide to water is depicted by the blue arrow. For details, see text. Abbreviations (in alphabetical order): Cat: catalase; GPx: glutathione peroxidase; G6P: glucose-6-phosphate; G6PDH: glucose-6-phosphate dehydrogenase; GR: glutathione reductase; GRX: glutaredoxin; GSH: reduced glutathione; GS-SG: oxidized glutathione; MCX-I: mitochondrial complex I; NADPH: reduced nicotinamide adenine dinucleotide phosphate; NADP<sup>+</sup>: oxidized nicotinamide adenine dinucleotide phosphate; OX: oxidases; 6PGδL: 6-phosphoglucono-δ-lactone; SOD: superoxide dismutase; TPx: thioredoxin peroxidase; TrxR: thioredoxin reductase. Trx-S<sub>2</sub>: oxidized thioredoxin; Trx-(SH)<sub>2</sub>: reduced thioredoxin.

While the reactivity of the hydroxyl radical hinders its controlled disarming, the cellular antioxidant system has several ways, to metabolize hydrogen peroxide to water (indicated by the blue arrow in Figure 12), like the enzyme catalase (cat), or the antioxidants glutathione (GSH) and thioredoxin (Trx-(SH)<sub>2</sub>). GSH is able to reduce hydrogen peroxide directly or with the help of enzymatic catalysis, namely glutathione peroxidase or glutaredoxin, which are



themselves reduced by GSH [116,151,154,162]. As a result of these reactions, GSH is oxidized to GSSG, which can be reduced by glutathione reductase (GR). The reducing power for this reduction comes from NADPH (nicotinamide adenine dinucleotide phosphate), which is itself reduced in the course of the oxidation of glucose-6-phosphate (G6P) to 6-phosphoglucono- $\delta$ -lactone (6PG $\delta$ L) by glucose-6-phosphate dehydrogenase (G6PDH) [116,151,154,163] (reactions on top of the blue arrow in Figure 12).

The thioredoxin centered reducing system works in a similar manner. The reduction of hydrogen peroxide by thioredoxin can be mediated by Trx-(SH)<sub>2</sub> directly or via catalysis through thioredoxin peroxidase (TPx). Unlike GPx, TPx can only be reduced by NADPH, like the oxidized thioredoxin (Trx-S<sub>2</sub>) [116,151,152,154].

These several redox systems enable the cell to balance between oxidant and antioxidant forces. The term “oxidative stress” therefore describes a disturbance of this balance [113,116]. While ROS at high concentrations are deleterious, their important roles in cellular functions including activation and modulation of signal transduction pathways, as well as several redox-sensitive transcription factors evidence the “two-faced” character of these species [113,116,152,155,158,159,164]. Also the duration of the oxidative stress seems to be important, as short lived redox changes, like transient and localized ROS production is involved in normal growth factor signaling, while long-lived oxidative stress often leads to cellular senescence [165].

Figure 13 illustrates some of the pathways that are activated by certain levels of reactive oxygen species. Lower levels of (or short term exposure to) ROS have mainly pro-survival effects, while increasing levels can lead to tumor promotion, proliferation and progression, and finally to apoptosis or even necrosis [113,155].

Redox regulation of the pro-survival Nrf2 pathway works via disruption of the Keap1-Nrf2 (Kelch-like ECH-associated protein 1 – Nuclear factor (erythroid-derived 2)-like 2) - complex that enables the translocation of Nrf2 to the nucleus, where it induces the transcription of antioxidant enzymes. In association with Keap1, the transcription factor is subject to ubiquitination and protein degradation [158,166,167]. Oxidative stress can furthermore induce this pathway by activation of protein kinase C (PKC), which phosphorylates Nrf2 [167]. Also the translocation of nuclear factor  $\kappa$ B (NF $\kappa$ B) is activated by ROS. The kinases I $\kappa$ B-kinase (IKK) and protein kinase D (PKD) catalyze the disruption of the complex formed by NF $\kappa$ B with its inhibitor I $\kappa$ B (inhibitor of NF $\kappa$ B), allowing the translocation of the transcription factor to the nucleus (and the degradation of I $\kappa$ B). Genes, that are regulated by NF $\kappa$ B include

anti-apoptosis factors like Bcl2, the antioxidant enzyme SOD and ABC transporters [21,152,158,166,167].

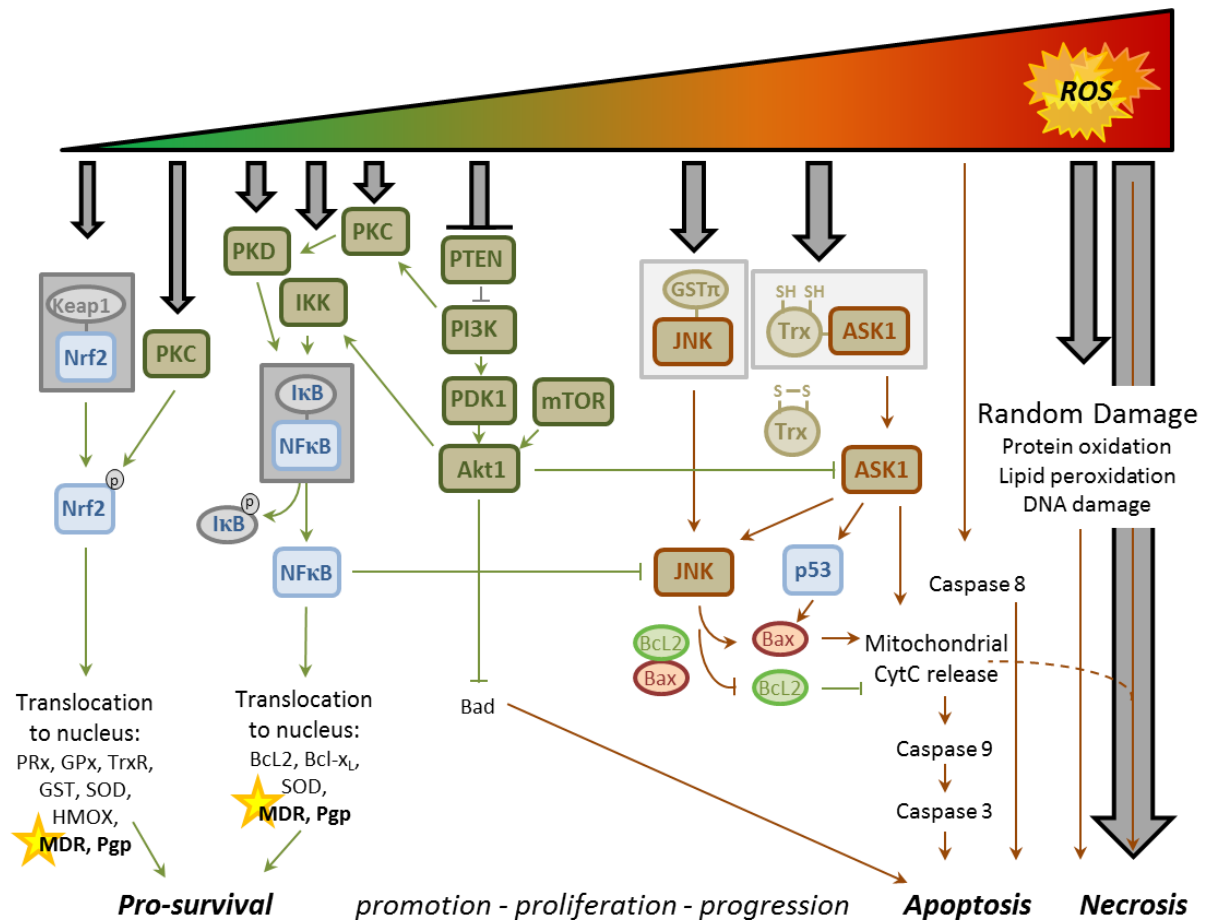


**Figure 13:** Examples for ROS-induced signaling pathways. While at low concentrations pro-survival pathways are activated, high levels lead to apoptosis, or even necrosis. Figure created according to [113,152,155,158,160,161,164,166–169]. Redox-responsive transcription factors (Nrf2, NFκB, p53) are indicated by blue boxes, kinases are shown in boxes (green for pro-survival signaling, brown for apoptotic signaling). Grey boxes surround inactive protein-complexes that are activated by kinases or ROS. Arrows indicating pathways are colored in green for pro-survival or brown for apoptotic signaling. Regulation of MDR associated genes is highlighted by a star. Abbreviations (in alphabetical order): Akt1: threonine-protein kinase (PKB); ASK1: apoptosis signal-regulating kinase-1; Bad: Bcl-2-associated death promoter; Bax: Bcl-2-associated X protein; GSTπ: Glutathione S-transferase π; IκB: inhibitor of NFκB; IKK: IκB-kinase; JNK: c-Jun N-terminal kinase; Keap1: Kelch-like ECH-associated protein 1; mTOR: mammalian target of rapamycin; NFκB: nuclear factor κB; Nrf2: Nuclear factor (erythroid-derived 2)-like 2; PDK1: 3'-phosphoinositide-dependent kinase-1; PI3K: phosphatidylinositol-3-kinase; PKC: protein kinase C; PKD: protein kinase D; PTEN: phosphatidylinositol-3,4,5-trisphosphate 3-phosphatase; Trx: thioredoxin.

Another pro-survival signaling induced by ROS is the activation of the threonine-protein kinase Akt1, which is the result of a signaling cascade starting with the oxidative inhibition of phosphatidylinositol-3,4,5-trisphosphate 3-phosphatase (PTEN) [152,166]. By activating IKK, Akt1 also induces the NF $\kappa$ B pathway, leading to an increased expression of P-gp [21]. Furthermore activation of Akt1 down-regulates pro-apoptosis factors, partially through a crosstalk to the apoptosis signal-regulating kinase ASK1 [21,152,166].

ASK1 is involved in apoptosis signaling. Under non-stress conditions it is associated to thioredoxin (Trx), which renders the protein inactive. Upon oxidation, Trx undergoes conformational changes that lead to activation of ASK1 [152,164,166,168]. As a consequence of ASK1 activation, mitochondrial cytochrome C is released, which activates caspases 9 and 3 and leads to apoptosis [168]. Next to the direct mitochondrial cytochrome C release, ASK1 can also activate p53, which in turn phosphorylates the pro-apoptotic Bcl-2-associated X protein (Bax), enabling it to induce cytochrome C release [168].

Activation of ASK1 can also lead to the activation of c-Jun N-terminal kinase (JNK), which leads to the decomposition of the Bax/Bcl2 complex, enabling the homo-dimerization of Bax, and the phosphorylation and downregulation of Bcl2 [152]. Similar to ASK1, JNK can be inhibited under non-stress conditions by forming a redox sensitive complex with glutathione-S-transferase- $\pi$ . Upon oxidative stress JNK is released from this complex and activated [166]. A crosstalk between NF $\kappa$ B and JNK has been suggested to be of importance for the final cell fate in response to oxidative stress [166].

In comparison to healthy tissues, ROS levels have been found to be elevated in cancer patients. Additionally to the direct measurement of elevated levels, increased lipid peroxidation serves as an indirect proof [113,158]. The increase of ROS might be caused by oncogenic stimulation, increased metabolic activity due to the higher energy demand caused by rapid proliferation, or mitochondrial malfunction. Also a decrease in the antioxidant capacity of cancer cells has been suggested as a cause. Though, documented studies comparing the levels of antioxidant enzymes in cancer patients vs. healthy subjects were not conclusive, most probably due to huge variations in patients and control populations. Also the geographical location and the time of the study (data were collected over the last three or four decades) might have caused this variation [113].

Figure 13 shows the different pathways favoring the cellular survival, tumor promotion, proliferation and progression or apoptosis in dependence of the cellular ROS levels. A higher oxidative stress level in cancer cells, might therefore provide the opportunity for a selective

targeting, since the tumor cells might be more sensitive to additionally induced oxidative stress as compared to normal (healthy) cells [113,155].

Also ABC transporter mediated multidrug resistance of cancer is partly regulated by ROS on several levels. Direct oxidation of the transport proteins might result in conformational changes that render the proteins inactive. Especially in case of MRP1, where GSH is co-transported, ROS might influence the activity of the transporter [167]. The regulation of P-gp expression on the transcriptional level has first been identified on the rat paralogues *mdr1a* and *mdr1b*, but later been confirmed for the human protein as well [167]. As indicated in Figure 13, the ROS sensitive NF $\kappa$ B and Nrf2 pathways have been suggested to not only upregulate antioxidant enzymes but also the ABC transporter P-gp [167,169]. Further effects on P-gp expression include a ROS induced gene amplification, but also regulation of expression on post-translational and epigenetic levels [167].

## 2. Objective

As indicated in the introduction, the development of multidrug resistance (MDR) is a major obstacle in cancer treatment. One strategy to overcome this obstacle is the selective targeting of MDR cells by exploiting their collateral sensitivity (CS).

As indicated in chapter 1.4, several reports can be found in the literature on diverse compounds with the potential to induce CS via different mechanisms. While some of these agents have been identified in a pharmacogenomic approach by correlating the drug activity to expression of the ABC transporter P-gp, the impact of the transporter on serendipitously found MDR selective agents seems elusive. Therefore, selected agents should be tested for their potential to induce MDR selective toxicity in a panel of cell lines. In order to exclude cell line specific effects and ensure the importance of transporter activity on the selectivity, transporter inhibition and P-gp-transfected cell lines should be investigated (addressed in chapter 3.1.1.).

New data was released in 2010, updating the database of the National Cancer Institute (NCI) – Developmental Therapeutics Program (DTP), thus enabling the re-evaluation of the reported pharmacogenomic approach. Data analysis might lead to the identification of scaffolds that can be associated with P-gp-mediated MDR selective toxicity. Furthermore, the MDR selective anticancer potential of previously identified compound classes might be verified in this new data set and a preliminary structure activity relationship analysis might be performed.

In order to confirm these (re-)identified scaffolds, and to gain more insight into the chemical features responsible for (MDR selective) toxicity of the chelators, a focused library should be designed. Isatin- $\beta$ -thiosemicarbazones, like **I-a**, have been described to be MDR selective based on the previously reported pharmacogenomic approach. Starting from this chelator, the library should be intended to cover aspects of different chelator donor-atom sets and further variations that might be applied to fine-tune toxicity. Furthermore, the scaffold should be extended to closely related compound classes like hydrazino-benzothiazoles and aryl-hydrazones (chapter 3.2.). Compounds should be investigated for their potential to overcome MDR in several cell lines. In case of compounds, identified to selectively kill MDR cell lines, the effect of P-gp should be addressed by co-administration of an inhibitor.

On the basis of the previously reported pharmacogenomic approach, also 8-hydroxyquinoline derived Mannich bases might be a promising chelator class. Closely related derivatives might provide further insight into structural motives that render these compounds MDR selective.

A set of closely related compounds with varying MDR selective activity might provide a useful tool for the elucidation of putative mechanisms of (MDR selective) action. Furthermore, the comparison to a derivative with cell line specific selective toxicity that is independent of P-gp (identified in the library, chapter 3.2.), might be interesting.

As described in the introduction, chelators might affect the intracellular redox homeostasis for example via the formation of redox active complexes, and eventually cause cellular damage through the formation of excess of reactive oxygen species (ROS). In order to address the impact of ROS on the toxicity of selected chelators toward parental and MDR cells, the ROS-scavenger *N*-acetylcysteine (NAC) should be co-administered.

Intracellular complexes might be formed with the two most physiologically relevant redox active metals iron and copper, therefore the impact of these two metals on the selective toxicity of the ligands toward MDR cell lines, should be addressed by co-administration of the metal salts.

Since a putatively differential cellular response to the metal ion co-administration to MDR selective and non-MDR selective ligands might be caused by different chemical properties of the ligands and their complexes, complex stability and redox activity of the complexes formed with iron (III) and copper (II) should be investigated.

In case of stable complex formation, pre-formed complexes should be investigated *in vitro*, in order to investigate the effect of supplemented metal ions at fixed metal to ligand ratios. The impact of redox activity of these complexes on the toxicity should be investigated by co-administration of antioxidants in the *in vitro* studies.

In order to further investigate the impact of ROS on the mechanism of (MDR selective) toxicity of ligands and metal complexes, techniques should be established for the measurement of intracellular ROS.

### 3. Results and discussion

#### 3.1. Critical evaluation of literature reports

##### 3.1.1. Serendipitous findings

Based on the increasing number of literature reports on MDR in cancer, the selective targeting of otherwise MDR cancer cell lines seems to be a promising approach. As detailed in the introduction (chapter 1.4.) very diverse agents with distinct mechanisms of action have been reported to show hypertoxicity toward MDR cell lines.

In order to elucidate the impact of P-gp on the activity of the reported compounds and to rule out cell line specific effects, several cell line models should be employed. Experimental data on the reported MDR selective agents are summarized in Table 2. The investigated cell line panel comprises pairs of MDR and parental cell lines from different origin. The ovarian carcinoma cell line A2780 and the uterine sarcoma cell line MES-SA were used in comparison to their doxorubicin-selected counterparts A2780adr and Dx5, respectively [24,170,171], while the cervix carcinoma cell line KB-3-1 was compared to the Vinblastine-selected line KB-V1 [172,173]. The NCI/ADR-res and OVCAR-8 cell lines were introduced in chapter 1.4. as parts of the NCI60 cell line panel [99]. The impact of P-gp activity on the toxicity of the compounds was furthermore addressed by co-administration of the P-gp inhibitor Tariquidar, as well as by the usage of a genetically modified Madin–Darby canine kidney (MDCK-II) cell line, which was engineered to overexpress cDNA-derived P-gp. This cell line was established by *Dr. Dóra Türk*, a brief description of the cells is given in the methods section (chapter 5.1.) [89].

While a standard method to measure cellular viability is the MTT assay, this method requires the removal of medium before the lysing of cells (for details see methods section chapter 5.6.1.), which might be a possible source of errors in case of agents, which might act via a perturbation of membrane properties. The putative loss of cells with perturbed membrane properties during the experiment might lead to artefacts in the measurement. Therefore the detergent Triton-X-100, as well as the block co-polymers pluronics P-85 and P-105 were measured with fluorescence based assays, namely with cell lines stably transfected with the fluorescent proteins eGFP or DsRed (for details, see method section chapter 5.6.3.), or by the application of Presto Blue reagent (for details, see method section chapter 5.6.2.). In comparison to the MTT reagent, this method has the advantage that a medium replacement is not necessary in cases, where an interaction of the test compound with the assay compound

**Table 2:** Evaluation of compounds reported to be MDR selective in the literature. IC<sub>50</sub> values of at least 2 independent experiments (as specified in the applied assay-column) are listed in parental and MDR cell lines. Addition of the P-gp inhibitor Tariquidar is indicated as “+ TQ”.

	IC <sub>50</sub> [μM] in parental cell	IC <sub>50</sub> [μM] in MDR cell	SR	cell line pair	Applied assay
Triton X 100	246.7 ±34.0	99.99 ±15.2	2.47	MES-SA / Dx5	Presto Blue assay
	209.2 ±5.16	109.6 ±23.6	1.95	MES-SA / Dx5 + TQ	Presto Blue assay
Pluronics					
P085	47.88 ± 1.29	51.54 ± 1.27	0.93	KB-3-1 / KB-V1	Presto Blue assay
	33.50 ± 0.563	38.48 ± 1.36	0.87	MES-SA / Dx5	Presto Blue assay
	5.692 ± 0.584	10.28 ± 1.60	0.56	OVCAR-8 / NCI	DsRed / EGfP
	30.64 ± 1.04	37.61 ± 1.36	0.81	MDCK / MDCK-B1	Presto Blue assay
P105	7051 ± 1549	1900 ± 487	3.74	KB-3-1 / KB-V1	Presto Blue assay
	438.7 ± 13.6	72.91 ± 6.68	6.04	MES-SA / Dx5	Presto Blue assay
	10.45 ± 2.41	23.45 ± 4.26	0.44	OVCAR-8 / NCI	DsRed / eGfP
	66.47 ± 9.75	90.76 ± 12.2	0.73	MDCK / MDCK-B1	Presto Blue assay
Verapamil	6.89 ± 0.037	8.96 ± 0.25	0.50	KB-3-1 / KB-V1	MTT
Isatin TSCs					
NSC73306 (I-a)	6.09 ± 0.94	3.59 ± 1.01	1.75	MES-SA / Dx5	MTT
	7.15 ± 0.66	7.42 ± 1.24	1.00	MES-SA / Dx5 + TQ	MTT
	12.1 ± 3.32	4.15 ± 0.89	2.87	MES-SA / Dx5	mCherry fluorescence
	5.79 ± 2.13	7.67 ± 1.21	0.72	MES-SA / Dx5 + TQ	mCherry fluorescence
	7.82 ± 2.06	3.78 ± 0.43	1.92	KB-3-1 / KB-V1	MTT
	7.49 ± 0.30	4.84 ± 1.21	1.60	A2780 / A2780adr	MTT
I-c	5.32 ± 1.43	3.27 ± 0.75	1.54	MES-SA / Dx5	MTT
	6.99 ± 1.37	5.73 ± 1.44	1.23	MES-SA / Dx5 + TQ	MTT
	11.3 ± 2.53	3.27 ± 0.85	3.14	MES-SA / Dx5	mCherry fluorescence
	16.0 ± 2.23	11.4 ± 3.73	1.47	MES-SA / Dx5 + TQ	mCherry fluorescence
	4.44 ± 1.47	4.00 ± 0.62	1.06	KB-3-1 / KB-V1	MTT
	9.70 ± 1.50	8.75 ± 1.93	1.07	A2780 / A2780adr	MTT
I-d	9.17 ± 3.64	4.74 ± 1.10	1.81	MES-SA / Dx5	MTT
	14.6 ± 4.54	13.0 ± 1.85	1.08	MES-SA / Dx5 + TQ	MTT
	15.8 ± 7.57	7.56 ± 6.73	1.73	MES-SA / Dx5	mCherry fluorescence
	33.6 ± 7.45	21.1 ± 14.4	1.90	MES-SA / Dx5 + TQ	mCherry fluorescence
	8.20 ± 1.52	4.58 ± 0.90	1.74	KB-3-1 / KB-V1	MTT
	25.7 ± 6.92	8.78 ± 2.35	3.63	A2780 / A2780adr	MTT



can be excluded (in case of Triton-X-100 a reaction is very unlikely by chemical means, but generally, an interaction could be excluded by using cell-free conditions).

While Triton-X-100 seemed to have a 2.47-fold increased toxicity in MES-SA/Dx5 cells as compared to the parental MES-SA cells, this difference seemed to be independent of P-gp function, as the co-administration of Tariquidar did not abolish selectivity.

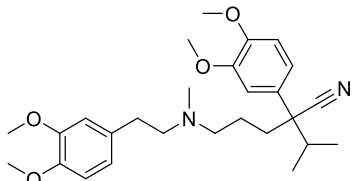
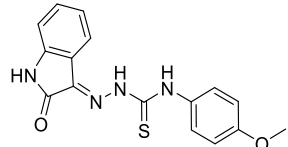
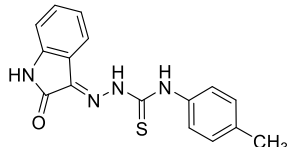
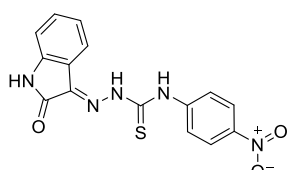
The toxicity of Pluronic P-85 was comparable throughout the investigated cell line panel. In NCI/ADR-res it even seemed less toxic as compared to the parental OVCAR-8 cell line. In contrast, the derivative P-105 showed enhanced toxicity toward MDR cells in two out of the four investigated cell line models. Experiments performed with the transfected MDCK-II-B1 cells showed, that the selectivity observed in these models was not caused by the transport protein.

Despite promising reports on up to 100-fold increased toxicity of Verapamil toward a P-gp-expressing cell line in comparison to the parental line [82], these reports seem to be based on rather cell line dependent effects, as these observations could not be confirmed in the KB-V1 vs. KB-3-1 cell line model (Table 2). Furthermore, Verapamil was found in the DTP database as NSC657799, and biodata on this compound was available on a major set of cell lines from the NCI60 panel. As summarized in Table 3, the Pearson correlation coefficient for the correlation of activity vs. P-gp expression was negative, supporting reports on the substrate properties of Verapamil, rather than those reporting about MDR selective activity. Since data for OVCAR-8 cells were not available, a selectivity ratio for the NCI/ADR-res vs. OVCAR-8 cell line pair could not be given based on the database data.

NSC73306 (**I-a**) has been identified as a putatively MDR selective agent based on the NCI60 panel data, and confirmed in several models [95,98,100]. Even though the magnitude of the effect was rather small in some cases, a selective effect could be observed in all investigated cell line pairs. Application of Tariquidar abolished the selectivity, indicating the P-gp-dependence of the selectivity. Two close derivatives have been reported to possess increased selectivity toward MDR cell lines, namely **I-c** and **I-d** [102,103]. Compound **I-d** indeed showed selective toxicity toward the investigated MDR cell lines in a P-gp-dependent manner, even though not in the reported magnitude. Compound **I-c**, in contrast, showed selective toxicity only in one test system, namely in MES-SA/Dx5 cells, measured by the mCherry assay. Since the effect could neither be verified by the MTT assay in the same cell lines, nor in other cell lines, other factors than P-gp might be responsible for the reported selectivity.

Furthermore, **I-c** and **I-d** were identified in the DTP database as NSC668502 and NSC670960, respectively. As summarized in Table 3, the available biodata and provided relatively low Pearson correlation coefficients against P-gp-expression data. Also the low SR comparing OVCAR8 and NCI/ADR-res cells, confirm (in agreement with the measured data, as summarized in Table 2) the suggestion that putatively observed selectivity of these compounds might be linked to other factors than P-gp.

**Table 3:** correlation of activity within the NCI60 panel vs. P-gp expression for isatin- $\beta$ -thiosemicarbazones in comparison to reported MDR selectivity.

NSC657799 Verapamil		Pearson correlation coefficient r: -0.25 IC <sub>50</sub> (OVCAR-8) / $\mu$ M - IC <sub>50</sub> (NCI/ADR-res) / $\mu$ M 100 SR (OVCAR8 / NCI/ADR-res) -
NSC73306 <b>I-a</b>		Pearson correlation coefficient r: 0.49 IC <sub>50</sub> (OVCAR-8) / $\mu$ M 7.56 IC <sub>50</sub> (NCI/ADR-res) / $\mu$ M 2.09 SR (OVCAR8 / NCI/ADR-res) 3.63
NSC668502 <b>I-c</b>		Pearson correlation coefficient r: 0.01 IC <sub>50</sub> (OVCAR-8) / $\mu$ M $\geq 100$ IC <sub>50</sub> (NCI/ADR-res) / $\mu$ M 51.29 SR (OVCAR8 / NCI/ADR-res) 1.95 reported SR (KB-3-1 / KB-V1) [103] 9.2
NSC670960 <b>I-d</b>		Pearson correlation coefficient r: 0.20 IC <sub>50</sub> (OVCAR-8) / $\mu$ M 1.78 IC <sub>50</sub> (NCI/ADR-res) / $\mu$ M 3.02 SR (OVCAR8 / NCI/ADR-res) 0.59 reported SR (KB-3-1 / KB-V1) [103] 8.3

Therefore, the results suggest, that the elevated toxicity of putative MDR selective compounds reported in the literature is often cell line dependent and not linked to P-gp, but rather to nonspecific factors arising during the development of the MDR phenotype. In contrast the selective toxicity of compound **I-a**, which was identified by the pharmacogenomic approach, could be confirmed in other test systems, and was found to be P-gp-mediated. Therefore, it seems to be necessary to investigate several cell lines, in order to find P-gp-mediated MDR selective agents. The approach of correlating biodata across the NCI60

cell line panel against gene expression data seems to be a reliable strategy to find general MDR selective agents.

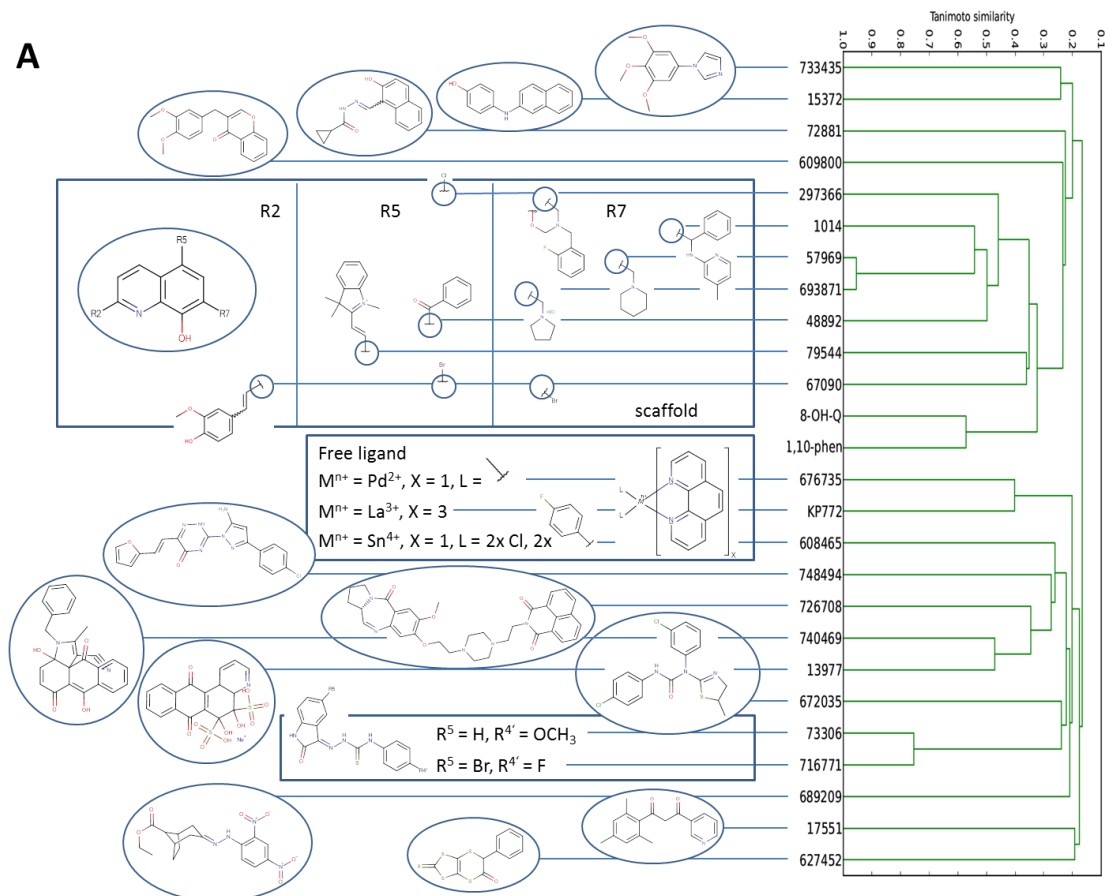
### 3.1.2. Pharmacogenomic approach

In 2010, a new updated dataset containing toxicity profiles of 49169 compounds across the NCI60 panel was released. In order to identify further MDR selective compounds, the previously described pharmacogenomic approach of correlating toxicity against P-gp expression was repeated using the new dataset. The bioinformatic analysis and biological testing of the identified compounds was performed by *Szilárd Tóth, András Füredi, and Dr. Anna Lovrics*. The analysis revealed 82 putative MDR selective compounds with Pearson correlation coefficient  $>0.4$ . Out of these, 61 compounds were already identified in the previously described set [174].

Structural motives and molecular features known to be associated with MDR selective toxicity reappear within the 21 novel compounds. Available compounds were tested in a panel of MDR (KB-V1, MES-SA/Dx5) and parental cell lines (KB-3-1, MES-SA) with the Presto Blue viability assay. To clearly delineate the effect of P-gp on the toxicity of the compounds, MDCK-II-ABCB1 cells, which were engineered to overexpress cDNA-derived P-gp and the control MDCK-II cells, were included (see chapter 3.1.1.). Additionally the effect of co-administered P-gp inhibitor Tariquidar was investigated in the MES-SA cell line pair.

In order to compare to previous findings, five reference compounds are included in the study of the newly investigated compound set (NSC693871, NSC73306, KP772, 1,10-phenanthroline, 8-hydroxyquinoline (8OHQ)). The molecular similarity of the chemical structures can be quantified by Tanimoto coefficients, which are based on molecular fingerprints, that describe molecular structures as binary vectors [175]. These coefficients were calculated with ChemAxon software and hierarchical clustered into a dendrogram [36]. Data describing structural similarity and biological activity are illustrated in Figure 14.

In agreement with prior observations based on the 2007 DTP data release, the newly identified compounds contain a significant number of structures enabling metal chelation [174].



**B**

	KB-3-1	KBV-1	KB-3-1/ KB-V1	MDCK II	MDCK II-B1	MDCK II/ MDCK II-B1	Mes-Sa	Dx5	MES-SA / Dx5	Mes-Sa (TQ)	Dx5 (TQ)	MES-SA / Dx5 (TQ)
NSC733435	NT	NT		NT	NT		NT	NT		-	-	
NSC15372	13,4	13,6	1,0	40,7	38,0	1,1	28,3	32,8	0,8	-	-	
NSC72881	16,7	10,8	1,7	18,5	13,6	1,4	34,9	12,7	2,8**	32,9	33,6	1,1
NSC609800	-	-		-	-		-	-		-	-	
NSC297366	2,1	0,1	17,6**	2,9	0,3	10,5**	2,1	0,1	19,0*	1,7	1,6	1,1
NSC1014	5,8	4,4	1,4	10,9	5,6	1,9**	18,0	10,8	1,7	17,6	11,8	1,5
NSC57969	8,6	0,6	14,6*	4,5	0,8	5,7**	4,9	0,6	8,2**	4,8	3,6	1,4
NSC693871	14,7	2,5	7,4**	15,0	3,2	5,1**	5,0	1,3	4,0**	4,9	3,5	1,4
NSC48892	3,2	1,9	1,7**	3,6	2,3	1,6*	3,7	2,0	1,9*	3,8	2,8	1,3
NSC79544	2,2	0,7	3,0**	1,3	1,1	1,2	2,6	1,8	1,5	2,2	1,9	1,1
NSC67090	4,8	2,8	1,6	3,9	1,8	2,3**	3,6	1,3	2,8**	2,4	1,4	1,7
8-OH-Q	20,1	10,0	2,2	3,3	2,8	1,2	4,8	2,8	1,7**	4,1	2,1	1,9**
1,10-phen	32,9	11,0	3,4*	5,1	2,6	2,0**	4,7	1,7	3,1**	4,6	3,7	1,3
NSC676735	7,2	3,5	2,7*	12,9	9,2	1,4**	21,8	7,1	3,2*	21,3	17,6	1,3
KP772	64,0	12,2	7,0**	6,6	4,0	1,6*	4,7	1,5	3,0**	4,9	4,3	1,2
NSC608465	2,6	1,1	2,6*	2,6	1,4	2,3*	3,6	1,2	3,0*	4,9	3,8	1,6
NSC748494	-	-		-	-		-	-		-	-	
NSC726708	-	-		-	-		-	-		-	-	
NSC740469	-	-		-	-		-	-		-	-	
NSC13977	11,3	4,6	2,6*	9,5	4,4	2,1*	8,2	3,1	2,6*	8,0	5,5	1,5
NSC672035	75,1	57,7	1,2	31,4	54,0	0,6	51,9	53,6	1,0	-	-	-
NSC73306	7,5	3,7	2,2**	6,8	2,8	2,4*	6,4	3,1	2,0**	5,3	4,0	1,3*
NSC716771	13,1	5,8	2,3	-	-		-	-		-	-	
NSC689209	-	-		-	-		-	-		-	-	
NSC17551	8,7	4,6	2,0**	14,6	4,5	3,3*	23,7	3,7	6,3**	23,6	10,9	2,2**
NSC627452	NT	NT		NT	NT		NT	NT		-	-	

Tanimoto similarity

**Figure 14:** Dendrogram and confirmatory biodata of newly identified potential MDR selective agents, including previously reported reference compounds NSC73306 and NSC693871. Furthermore, biodata of KP772, 1,10 phenanthroline and 8-hydroxyquinoline (8OHQ) were added.

NSC716771 was identified as a very close analogue of the isatin- $\beta$ -thiosemicarbazone NSC73306. While the compound was not available for testing, *Hall et al.* report the MDR selectivity of this thiosemicarbazone in the KB-V1 vs. KB-3-1 cell line pair [176].

Also the 8OHQ derived Mannich base NSC693871 has previously been identified in the pharmacogenomic approach and confirmed to possess MDR selective activity [174]. In the updated data set six further 8-hydroxyquinoline derivatives were found with putative MDR selective activity. The 7-(piperidylmethyl)-8-hydroxyquinoline NSC57969 shows the highest similarity to with the previously reported compound NSC693871, with a piperidine-ring replacing the pyrrolidine-moiety. According to their structural similarity, both compounds are comparable with respect to their preferential targeting of MDR cell lines. Interestingly, the pyrrolidino derivative is less toxic than the newly identified piperidino derivative.

NSC297366 can also be considered as a close derivative, which could be obtained by a similar Mannich reaction as the previously mentioned derivatives. The presence of an additional equivalent of formaldehyde in the synthesis process enables an additional ring-closure between the 8-OH group and the benzyl amino-nitrogen. This compound harboring a fluorobenzylamine moiety has an outstandingly high selectivity for MDR cells with  $IC_{50}$  values in the submicromolar concentration range and SR values between 10 and 19.

In contrast, introduction of an aromatic moiety at the employed aldehyde resulting in compound NSC1014 seems to have detrimental effects on toxicity and selectivity.

The cluster furthermore contains two 5-substituted 8OHQ derived derivatives (NSC79544 and NSC48892), which both show toxicity in the 1-3  $\mu$ M range with only slight selectivity toward MDR cell lines (with SR values between 1.5 and 3). A similar behavior can be observed for NSC67090, which is halogenated in positions 5 and 7 and harbors a substituted styryl-moiety in position 2. Interestingly, the unsubstituted 8OHQ scaffold does not show MDR selective properties.

The naphthol-carbaldehyde-hydrazone NSC72881 and the naphthylamine NSC15372 are relatively far analogues of the 8OHQ derived Mannich bases. They show comparable activity across the cell line panel in the range of 10 to 40  $\mu$ M, regardless of the resistance status of the cells. Two further distantly related analogues can be found in the cluster around the 8-hydroxyquinoline derived Mannich bases, namely the 1,4-benzopyrone derivative NSC609800 and the 1-(3,5-trimethoxyphenyl)-imidazole NSC733435. While the first one was not available for testing, the latter was not toxic in any of the investigated cell lines up to a concentration of 100  $\mu$ M. While chelation of metal ions might be possible for NSC72881, it is rather unlikely for the other three far derivatives (NSC15372, NSC609800 and NSC733435).

The unsubstituted 8-OHQ scaffold clusters together with 1,10-phenanthroline, which has been reported earlier to possess MDR selective activity both as the free ligand and complexed with different metals [174,177]. The [Tris(1,10-phenanthroline)lanthanum(III)] trithiocyanate complex (KP772) was included in the study as a reference compound [177]. A stock solution of the complex was prepared following the procedure described by Hart and Laming [178]. In order to be able to compare the activity of KP772 with that of the free ligand,  $IC_{50}$  are given in ligand equivalents, therefore as the  $IC_{50}$  value of  $\{1/3 [La(phen)_3](SCN)_3\}$  (accordingly, the  $IC_{50}$  value of the complex would be three times lower). The analysis of the pharmacogenomic correlation retrieved two new 1,10-phenanthroline complexes formed with either tin (NSC608465) or palladium (NSC676735). Since most programs, which calculate chemical and physicochemical properties, are mainly made for the analysis of organic compounds, and might not be able to cope with metal ions in a chemical structure, the complexes and the free ligand do not cluster together. The preferential killing effect of free ligand toward MDR cells is preserved in the presence of the metal ions lanthanum, tin and palladium.

The aryl-urea derivative NSC672035 shows some degree of similarity to the TSC structures. However, its activity was comparably low with  $IC_{50}$  values  $\geq 50 \mu M$  across the cell line panel (SR 0.6-1.2). In contrast to the 8OHQ and TSC derivatives, upon chelation this compound will form a 6-membered ring incorporating the metal ion, while the other chelators will form 5-membered rings, which is considered more stable [179]. Also the diketon NSC17551 and the naphthol-derivative NSC72881, which display moderate toxicity in the investigated cell line panel (10-35  $\mu M$ ) will form 6-membered rings, applying either the two keto-oxygen atoms or the naphthol-hydroxyl group and a hydrazone-N as donor atoms. While the selectivity of the naphthol derivative is only significant in one cell line pair (MES-SA vs. MES-SA/Dx5), the diketon NSC17551 shows selective toxicity toward several MDR lines.

One further structural connection can be seen in the newly identified compound set, namely between two structures with a quinoidic system (NSC13977 and NSC740469), the remaining molecules are quite dissimilar. Interestingly NSC13977, which is the dye Alizarin blue, shares the N,O-metal binding donors in the same distance as found in the 8OHQ-scaffold, yet the disruption of aromaticity and the presence of further substituents explain the huge distance in the dendrogram. Alizarin Blue NSC13977 showed a two-fold higher activity in MDR cells compared to the parental cells, while the derivative NSC740469 was not available for testing. NSC748494 and NSC726708 were not available, and the singleton NSC627452 was not toxic in any of the tested cell lines up to a concentration of 100  $\mu M$ .

Taken together, P-gp expressing MDR cells from different origin show enhanced sensitivity over their parental P-gp negative cell lines against the compounds identified by the correlative approach. The occurrence of this effect also in ABCB1 transfected MDCK-II cells and the ability of the P-gp inhibitor Tariquidar to abolish selectivity, point to the importance of functional transport protein in sensitizing MDR cells.

### 3.2. Development of new compounds – Design of a focused library

Having shown that the isatin- $\beta$ -thiosemicarbazones **I-a** and **I-d** show MDR selective toxicity, a focused library was designed around thiosemicarbazones and related chelator classes.

The exploration of the chemical space around thiosemicarbazones (TSCs) with anticancer activity started in 1956 with first reports about a moderate antileukemic activity of 2-formyl thiosemicarbazone [180]. The most intensively investigated TSC is Triapine, a tridentate  $\alpha$ -*N*-pyridyl thiosemicarbazone. Triapine is a potent ribonucleotide reductase (RR) inhibitor currently undergoing phase I and II clinical trials [128–130]. While the clinical efficacy of Triapine awaits confirmation, *in vitro* experiments have suggested that Triapine is subject to MDR, as it is recognized and transported by P-gp [102,181,182].

In accordance with these reports, the inhibition of P-gp by Tariquidar increases the sensitivity of MES-SA/Dx5 cells toward Triapine to that of the parental MES-SA cells, as illustrated in Figure 15.

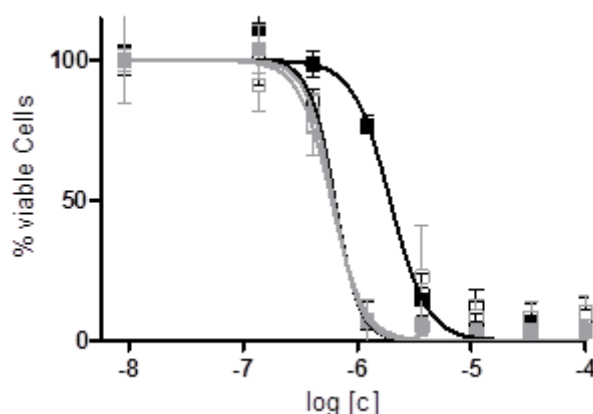


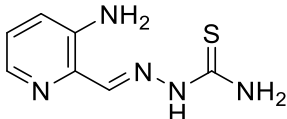
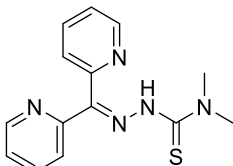
**Figure 15:** Dose-response curves for MES-SA (open squares) and MES-SA/Dx5 (filled squares) cells in the absence (black) and presence (grey) of the P-gp inhibitor Tariquidar (1  $\mu$ M). Data are mean and standard deviation from at least three independent experiments, obtained by MTT viability assay.

At the terminal nitrogen (N4) Triapine is not substituted. In contrast, substitution of the TSC moiety at this position was reported to increase the toxicity of TSC derivatives [102,183,184]. The terminally di-methylated TSC di-2-pyridylketone-4,4,-dimethyl-3-thiosemicarbazone (Dp44mT) has even been shown to exhibit a paradoxical hypertoxicity against the P-gp overexpressing cervix carcinoma cell line KB-V1 as compared to its parental cell line KB-3-1 [86,90].



Yet, as shown in Table 4, correlating the activity of both compounds against the P-gp expression within the NCI60 cell panel partially confirmed the substrate-like properties of Triapine: The selectivity ratio comparing NCI/ADR-res vs. OVCAR8 is 0.28, suggesting a putative efflux by P-gp, while the Pearson correlation coefficient of 0.15 rather suggests that there is no clear trend. Likewise, the Pearson correlation coefficient for Dp44mT (0.22) suggests only limited impact of P-gp activity on the toxicity. Since small changes in  $IC_{50}$  values can result in big changes in the selectivity ratios, these values underlie large uncertainties. With 1.74 the SR value comparing the activity of Dp44mT in NCI/ADR-res and OVCAR8 is slightly below the threshold of MDR selective activity.

**Table 4:** Correlation results of activity vs. P-gp expression in the NCI60 cell line panel

NSC663249 Triapine		Pearson correlation coefficient r:	0.15
		$IC_{50}$ (OVCAR-8) / $\mu$ M:	0.56
		$IC_{50}$ (NCI/ADR-res) / $\mu$ M:	2.04
		SR (OVCAR8 / NCI/ADR-res):	0.28
NSC744381 Dp44mT		Pearson correlation coefficient r:	0.22
		$IC_{50}$ (OVCAR-8) / $\mu$ M:	0.036
		$IC_{50}$ (NCI/ADR-res) / $\mu$ M:	0.021
		SR (OVCAR8 / NCI/ADR-res):	1.74

The introduction of an aromatic moiety at the N4 position has been reported to increase the toxicity of dipyriddyketone TSCs to a similar extent as the dimethylation (these reports are based on studies with the human leukemia cell line HL60 and the human neuroepithelioma cell line SK-N-MC) [184,185]. Furthermore, based on a pharmacophore model of isatin- $\beta$ -TSCs an aromatic moiety at N4 might be necessary for MDR-selectivity [42,102]. Selectivity toward MDR cell lines can be further increased by the introduction of a strong electron donating or withdrawing substituent to that aromatic ring in *para* position to the TSC [103].

The reported isatin- $\beta$ -TSCs are able to chelate metal ions via an ONS binding mode. In contrast, Triapine and Dp44mT are NNS chelators. A common feature of these compounds is the TSC scaffold, which enables metal binding. This scaffold is connected to pharmacological side effects, since  $H_2S$  might be released from the scaffold during the metabolism of these compounds [186,187]. To overcome this drawback, arylhydrazones and benzothiazoles have been introduced as alternative entities: Since in these compound classes the sulfur is either

replaced by a nitrogen [187], or incorporated into a ring system [186], H<sub>2</sub>S release is abolished or hindered. Nevertheless, these compound classes provide metal chelation abilities similar to the TSCs, which has been suggested to be an important feature in their mechanism of action [89,188,189].

While the set of chelators with potential MDR selective activity identified with the previously described pharmacogenomic approach includes a hydrazino-benzothiazole (NSC693630, see introduction, Table 1 for the structure) [98], also arylhydrazones have been reported in the context of multidrug resistance, yet not in the context of cancer: Several pyridinyl- or pyrimidinylhydrazones are effective even against multidrug resistant strains of leprosy and tuberculosis by inhibition of the mycobacterial RR [187,190]. Pyridylphthalazinyl- and quinolyhydrazones have been suggested to possess anticancer activity based on the inhibition of human RR [191]. Further applications of arylhydrazones can be found due to their antibacterial, antimycobacterial, analgesic and anticancer activities [190,192–194]. Derivatives with pyridinyl- or pyrimidinyl moieties chelate via an NNN binding mode.

As illustrated in Figure 16, the designed library contains ONS, NNS and NNN donor chelators. The first compound class (**I**) is built around isatin- $\beta$ -thiosemicarbazones like the reported MDR selective NSC73306 (**I-a**). In view of the reported structure-activity relationship of the DpT series [184] and the pharmacophore model of isatin- $\beta$ -TSCs [42,102] the library contains derivatives with an aromatic moiety at N4. Additionally, the current pharmacophore model suggests that either electron withdrawing or donating groups in *para* position of the aromatic ring might be beneficial for selective activity toward MDR cell lines [42,103]. Therefore compounds with either nitro, methyl, or methoxy groups in this position were included in the library.

Incorporation of these substituted aromatic moieties into the N4-position of the pyridinyl TSC scaffold resulted in compound class **II**. Additionally, the acetaniline derivative **II-p** was prepared, which is able to chelate via an NNS binding mode like the pyridinyl TSC, but has an anilinic NH<sub>2</sub> instead of the ring-incorporated pyridinyl nitrogen.

By changing the pyridinyl moiety to a hydroxyphenyl moiety, the similarity to the MDR selective isatin- $\beta$ -TSC compounds is increased, since these compounds, forming compound class **III**, again provide an ONS donor atom set for metal chelation. The previously mentioned NNN chelating arylhydrazones are embraced in compound class **IV**. Hydrazino-benzothiazole derivatives like NSC693630 can chelate via either an NNS or NNN donor atom set through rotation around a single bond. Therefore they share chemical features with the TSC as well as with the hydrazones. Benzothiazoles containing pyridine-moieties are encompassed by

compound class **V** (this class also contains the acetanilide derivative **V-d**), those with a hydroxyphenyl-moiety by compound class **VI**.

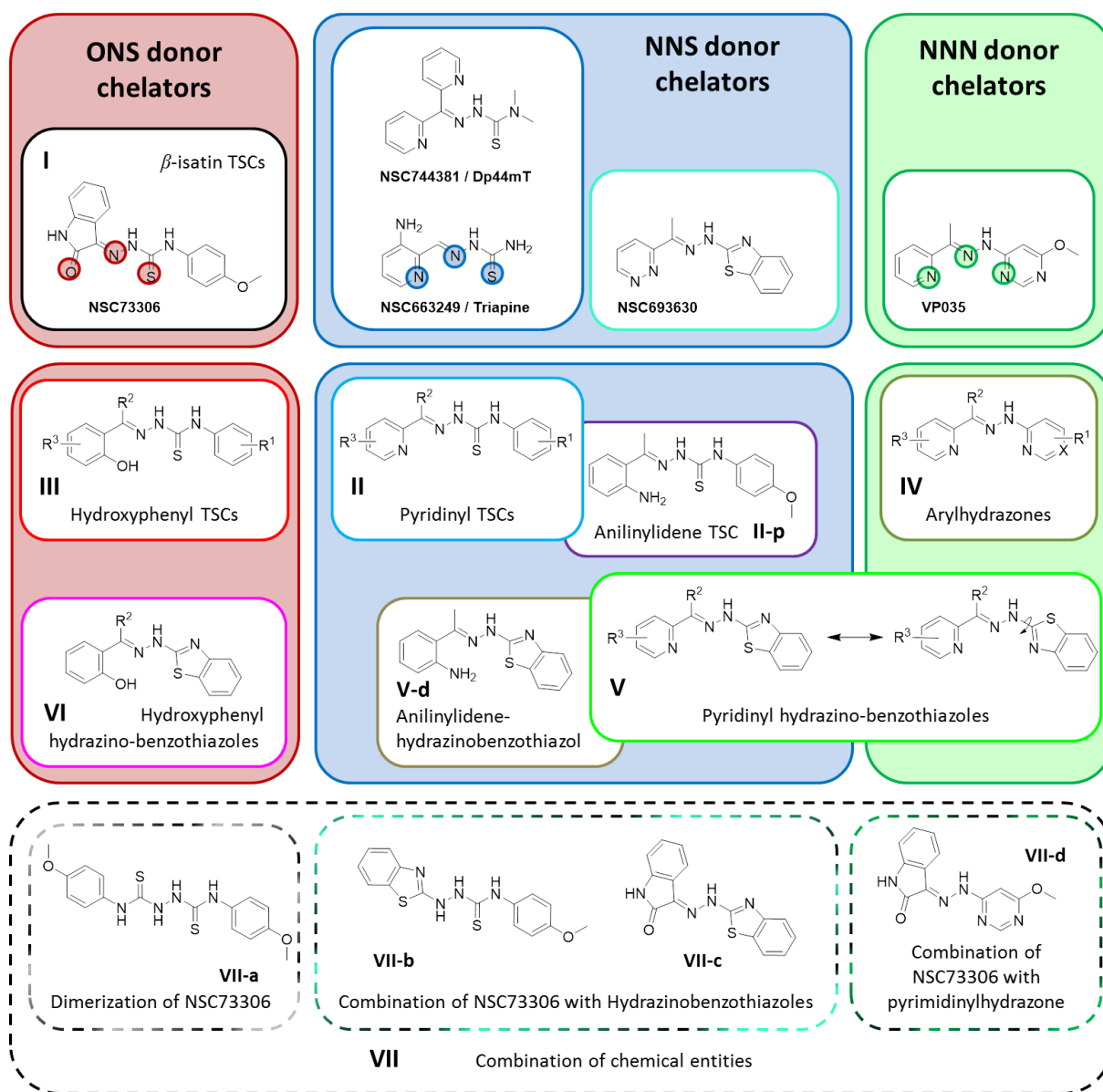


**Figure 16:** Library design. The five molecules (upper panels) possessing variable MDR selective toxicity served as starting point for the library design around isatin- $\beta$ -thiosemicarbazones (TSC, box I), pyridinyl TSCs (box II), hydroxyphenyl TSCs (box III), arylhydrazones (box IV), pyridinyl hydrazino-benzothiazoles (box V), hydroxyphenyl hydrazino-benzothiazoles (box VI), as well as molecules with combined chemical entities (box VII). Chelators with ONS, NNS and NNN donor atoms are shown in red, blue and green boxes, respectively; donor atoms of example ligands are highlighted.

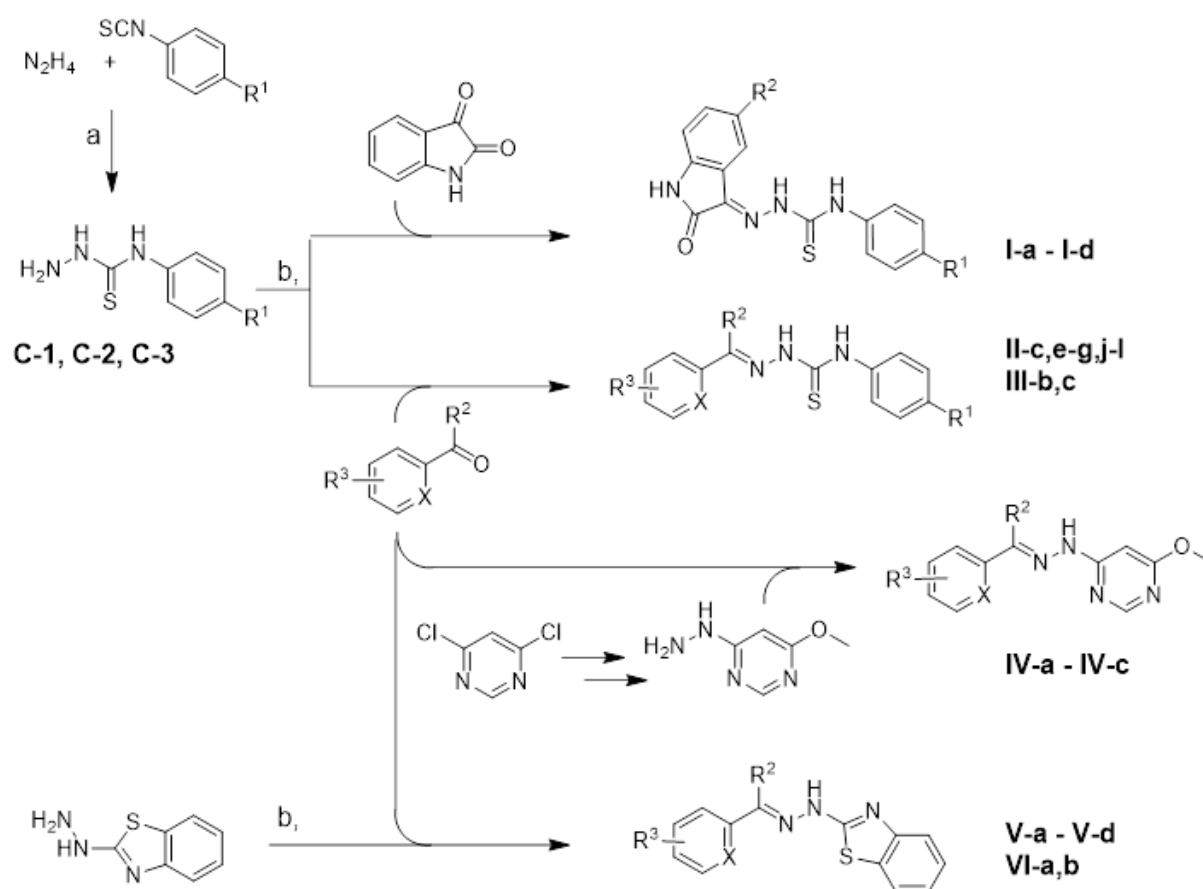
In a further step chemical entities of the previously described compound classes were combined and resulted in the four derivatives that form class **VII**: In compound **VII-a** the “non-isatin moiety” of **I-a** is dimerized. Compounds **VII-b** and **VII-c** are hydrazino-benzothiazoles that contain moieties of compound **I-a**, and compound **VII-d** is an isatin-containing arylhydrazone.

It is noteworthy, that calculations of the lowest energy confirmations of the free ligands revealed that the Schiff base double bond is in the *E*-confirmation, which rather suggests a bidentate over a tridentate binding mode [36]. Crystal structures of diverse NNS ligands like **II-b** [195] and **II-g** [196] or Triapine [197] confirm the calculated *E*-conformation. Also for hydroxyphenyl thiosemicarbazones like those related to class **III** [198,199] and for *N*-heteroarylhydrazones related to class **IV** [200] the ligands preferably crystalize in their *E*-conformations. Nevertheless, in the presence of metal ions an isomerization about the N=CH bond seems to occur, since these ligands form complexes with diverse metal ions in tridentate binding mode. Therefore, pyridinyl thiosemicarbazones like Triapine and related derivatives bind via NNS chelation motive [183,197,201–203] and hydroxyphenyl thiosemicarbazones via ONS [199,204–211]. Though some cases of hydroxyphenyl thiosemicarbazone bis-complexes of nickel and palladium, it has been reported, that the second ligand might bind either via one, two or three donor atoms [212,213]. *N*-heteroarylhydrazones without imino carbon substitution [214–216], as well as substituted derivatives [200,217] bind via an NNN donor atom set [203].

Even though for the hydroxyphenyl hydrazino-benzothiazoles related to class **VI** ONS and ONN binding modes are possible, mostly complexes with ONN binding have been crystalized [188,189,218,219]. In analogy, the acetaniline derivative **V-d** has been reported to bind via an NNN binding mode [189,220], while in case of Cu bis-complexes rather a bi-dentate (NN) binding can be found [189]. Taken together, the review of reported crystal structures shows, that the assumption of a tridentate binding mode is generally valid.

Synthesis

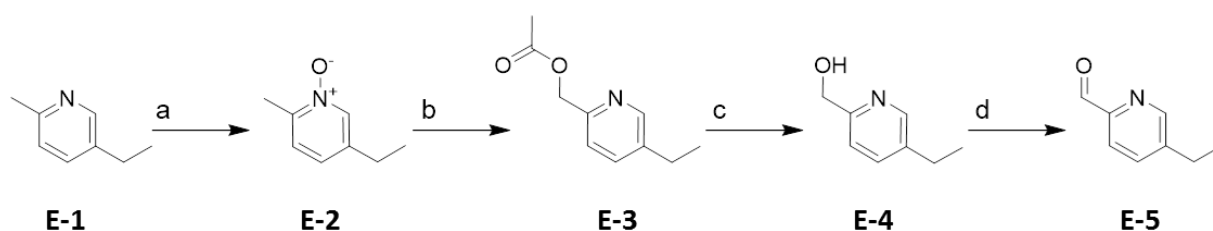
As depicted in Scheme 1, the diverse Schiff bases were obtained in an acid catalyzed condensation reaction of the particular thiosemicarbazide (**C-1**, **C-2**, or **C-3**) with the corresponding aldehyde or ketone. Products were obtained in good to moderate yields. Carbazides **C-1** to **C-3** were prepared from the particular isothiocyanates upon reaction with hydrazine in quantitative yields [103,221].



**Scheme 1:** Synthesis of different Schiff bases starting from the preparation of thiosemicarbazides **C-1** ( $R^1$ :  $OCH_3$ ), **C-2** ( $R^1$ :  $CH_3$ ), **C-3** ( $R^1$ :  $NO_2$ ), or 2-hydrazino-benzothiazole, respectively. Reaction conditions: a: MeOH, stirring at rt; b: EtOH, HCl or HOAc catalysis, refluxing. X = N for compound series **II** and **V**; X = C-OH for compound series **III** and **VI**. Substituents are  $R^1$ :  $CH_3$ ,  $OCH_3$  or  $NO_2$ ;  $R^2$ : H,  $CH_3$ ,  $R^3$ : H,  $OCF_3$ . Further compounds listed in Figure 16 were commercially available and purchased to complement the library.

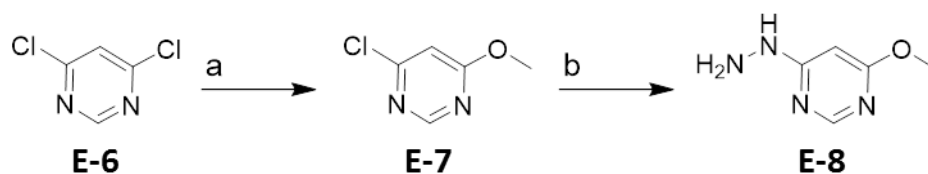
The synthesis of **II-e**, **II-k**, **IV-b** and **V-c**, in which the pyridine ring of the keto-component is substituted, required the preparation of 5-Ethylpicolinaldehyde (**E-5**). As illustrated in

Scheme 2, the product was obtained in a four step synthesis starting from 5-ethyl-2-methylpyridine following a method patented by Seydel *et al.* with minor modifications [222].



**Scheme 2:** Synthesis of 5-Ethylpicolinaldehyde. Reaction conditions: a)  $\text{H}_2\text{O}_2$ , glacial acetic acid,  $120\text{ }^\circ\text{C}$ ; b) acetic anhydride, glacial acetic acid,  $120\text{ }^\circ\text{C}$ ; c)  $\text{NaOH}$ , THF,  $70\text{ }^\circ\text{C}$ ; d) freshly prepared  $\text{MnO}_2$ ,  $\text{CHCl}_3$ , ultrasound,  $50\text{ }^\circ\text{C}$ .

The pyridine-N-oxide (**E-2**) was formed with hydrogen peroxide in glacial acetic acid, followed by alkaline reconditioning. Introduction of an acetoxy group at the methyl group of the N-oxide using acetic anhydride and glacial acetic acid provided 5-ethylpyridin-2-yl-methyl acetate (**E-3**). The cleavage of the ester to the corresponding alcohol (step c) was carried out in THF, as the suggested conditions using ethanol as a solvent provided the ethyl ether instead. The oxidation to the desired aldehyde (step d) required a long time; and reflux with freshly prepared  $\text{MnO}_2$  under ultrasound was found to be an efficient oxidizing method. Several other methods including commercially available  $\text{MnO}_2$  [222], the application of  $\text{SeO}_2$  and tert-butyl hydroperoxide [223], or the attempt to directly oxidize the 5-ethyl-2-methylpyridine [224–226] were not successful. With the help of the modifications in the first and in the last steps of the original approach, the overall yield could be increased from the reported 18% to 40%.

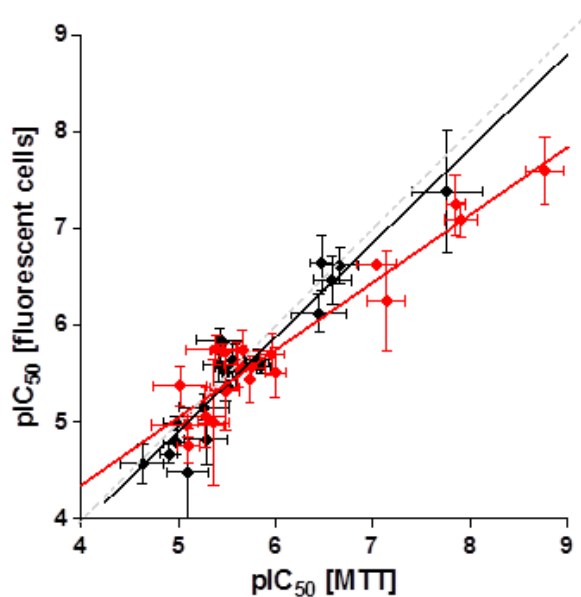


**Scheme 3:** Synthesis of 4-hydrazinyl-6-methoxypyrimidine. Reaction conditions: Reaction conditions were as follows a)  $\text{NaH}$ , methanol,  $-10\text{ }^\circ\text{C}$  to RT; b)  $\text{N}_2\text{H}_4$ , methanol,  $65\text{ }^\circ\text{C}$ .

4-hydrazinyl-6-methoxypyrimidine necessary for the synthesis of the arylhydrazones **IV-a-c** and **VII-d** was prepared in a two-step approach starting from 4,6-dichloropyrimidine as shown in Scheme 3 [89,222].

in vitro testing

As described in chapter 3.1. the cytotoxic activity of the compounds was investigated in a panel of parental (sensitive) and MDR cancer cell lines, in order to distinguish between compounds showing cell-specific and MDR selective toxicity. Cytotoxicity of the compounds was measured using the MTT viability assay. In order to avoid a putative interaction of the investigated compounds with the assay reagent, the medium containing the test compound was removed before adding the reagent. To still exclude assay dependent results, additional experiments were performed with MES-SA and MES-SA/Dx5 cells stably expressing the fluorescent protein mCherry. As shown in Figure 17, the two methods provided concordant results. Despite slight differences in the slopes obtained in the fits for both cell lines (0.97 for MES-SA and 0.70 for MES-SA/Dx5), a high intercorrelation can be found between the assays.

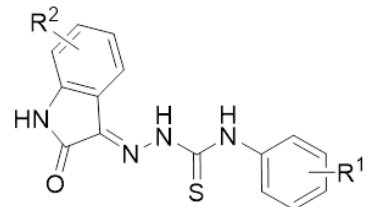


**Figure 17:** Correlation of pIC<sub>50</sub> values of 35 different compounds on MES-SA (black) and MES-SA/Dx5 (red) cell lines obtained with mCherry fluorescence assay and MTT assay. Data of at least 3 independent measurements per assay and compound are shown. The squared correlation coefficient was calculated to be  $r^2 = 0.91$  for MES-SA and 0.92 for MES-SA/Dx5 cells.

### 3.2.1. Thiosemicarbazones – Compound classes I/II/III

Several isatin- $\beta$ -thiosemicarbazones have been reported to show MDR selective toxicity [95,98,100,102,103]. According to the current SAR understanding of these compounds, derivatives were synthesized with aromatic moieties at N4 as summarized in Table 5. Compounds **I-a**, **I-c** and **I-d** were prepared for comparison with literature reports [42,102]. They are substituted in *para* position of the aromatic ring with an electron withdrawing nitro group (**I-d**) or with electron donating methoxy (**I-a**) or methyl (**I-c**) groups. Additionally **I-b** contains a trifluoromethoxy substituent at the isatin moiety. In compound **I-e** (which was commercially available) the aromatic moiety is substituted in *meta* position.

**Table 5:** Structures of investigated isatin- $\beta$ -thiosemicarbazones.

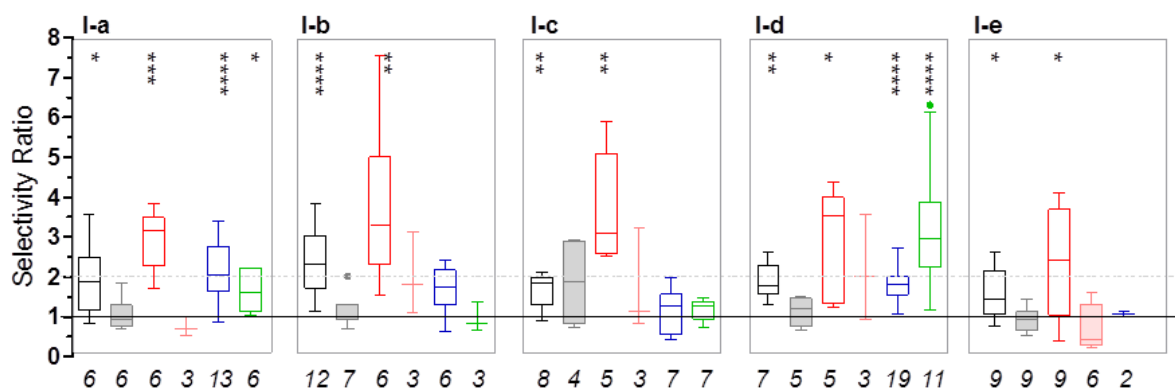
	R1	R2	
	<b>I-a</b>	4-OMe	H
	<b>I-b</b>	4-OMe	5-OCF <sub>3</sub>
	<b>I-c</b>	4-Me	H
	<b>I-d</b>	4-NO <sub>2</sub>	H
	<b>I-e</b>	3-CF <sub>3</sub>	H

The selectivity ratio, the fraction of IC<sub>50</sub> values obtained in P-gp negative vs. positive cells, serves as a quantification of the MDR selective effect. The range of SR values for the five isatin- $\beta$ -thiosemicarbazones obtained in at least three independent experiments is shown for the investigated cell lines in Figure 18. Even though the magnitude of the effect is slightly smaller than reported, the obtained results confirm literature reports on the selectivity of compound **I-a**. Also the selectivity-reverting effect of the P-gp inhibitor Tariquidar is in good agreement with the literature [95,98,100,102,103]. In contrast, the selective toxicity effect of the N4 *para* tolyl derivative **I-c** and the N4 *para* nitrophenyl derivative **I-d** is much less pronounced in our test system as compared to the reported SR values of 9.2 for **I-c** and 8.3 for **I-d** [103]. In fact, **I-c** is not selective in KB-V1 vs. KB-3-1 and A2780adr vs. A2780 cells. Together with the low Pearson correlation coefficient of activity and P-gp expression across the NCI60 cell line panel and the selectivity data for NCI/ADR-res vs. OVCAR-8 cells (see



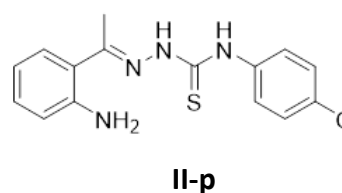
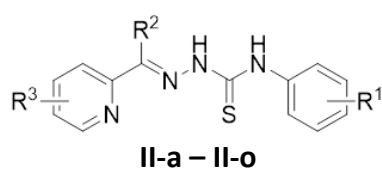
Table 3), these data suggest that in case of **I-c** the putatively observed selectivity of these compounds might be strongly influenced by other factors than P-gp

The pharmacophore model of isatin- $\beta$ -thiosemicarbazones suggests that substituents at the 5 position of the isatin moiety are tolerated, while *meta* substituents in the terminal phenyl ring might have a detrimental effect on selective toxicity [42,102]. The two novel TSC derivatives **I-b**, containing a trifluoromethoxygroup in the 5-position of the isatin moiety, and **I-e**, containing a trifluoromethyl substituent at the terminal phenyl ring support this general conclusion.



**Figure 18:** Box and whiskers plot of selectivity ratios (SR) for the isatin- $\beta$ -TSCs from Table 5 as calculated from the ratio of  $IC_{50}$  values of P-gp negative to positive cells (number of experiments indicated under the boxes). Black: Dx5 vs. MES-SA cells measured with MTT, red: Dx5 vs. MES-SA cells measured with mCherry fluorescence, blue: KB-V1 vs. KB-3-1 cells (MTT), green: A2780adr vs. A2780 (MTT); filled boxes in lighter color: Dx5 vs. MES-SA cells in presence of 1  $\mu$ M TQ: grey: measured by MTT, light red: measured by mCherry fluorescence. Significance was calculated using paired t-tests of the independent experiments and is given as \*:  $p \leq 0.05$ , \*\*:  $p \leq 0.01$ , \*\*\*:  $p \leq 0.001$ , \*\*\*\*:  $p \leq 0.0001$ .

Compound class **II** comprises the pyridinyl thiosemicarbazones and the acetaniline derivative **II-p**, as summarized in Table 6. In addition to the synthesized derivatives, compounds **II-a**, **II-b**, **II-d**, **II-h**, **II-i**, **II-l**, **II-m**, **II-n**, and **II-o** were obtained from vendors. A part of these derivatives or metal complexes thereof have been reported earlier to possess biological activity in diverse settings, including antimalarial [227], modest antibacterial [228], modest antifungal [202,229], and promising antitumor activity [195,196,202].

**Table 6:** Structures of investigated pyridinyl and acetaniline TSCs.

	R1	R2	R3		R1	R2	R3
<b>II-a</b>	H	H	H	<b>II-i</b>	2-Me	Me	H
<b>II-b</b>	H	Me	H	<b>II-j</b>	4-NO <sub>2</sub>	H	H
<b>II-c</b>	4-OMe	Me	H	<b>II-k</b>	4-NO <sub>2</sub>	H	3-Et
<b>II-d</b>	4-OMe	H	2-Me	<b>II-l</b>	3-CF <sub>3</sub>	H	H
<b>II-e</b>	4-OMe	H	3-Et	<b>II-m</b>	3-CF <sub>3</sub>	Me	H
<b>II-f</b>	4-Me	H	H	<b>II-n</b>	2-CF <sub>3</sub>	H	H
<b>II-g</b>	4-Me	Me	H	<b>II-o</b>	2-CF <sub>3</sub>	Me	H
<b>II-h</b>	3-Me	Me	H	<b>II-p</b>	H	Me	H

The selectivity ratios obtained for these compounds in the investigated cell line panel are illustrated in Figure 19. The previously described P-gp substrate Triapine was included in the Figure for comparison. Compound **II-b** lacks toxicity, and does therefore not appear in Figure 19. In most cases, the compounds show comparable toxicity throughout the cell line panel. Still, a subset of compounds shows selective toxicity toward selected cell lines.

Compound **II-c** is significantly more toxic for MES-SA/Dx5 as compared to MES-SA cells in both MTT and mCherry measurements. In the presence of Tariquidar, this selectivity seems retained, even though the effect is not significant. Selectivity of **II-f** can only be observed in MTT assays with the MES-SA cell line pair – **II-e** shows a similar trend, yet t-tests revealed that this trend lacks significance. In addition to the effect on the MES-SA cell line pair observed in MTT assays, compound **II-g** shows a small but significant preference for KB-V1 over KB-3-1 cells. Yet, since this effect is not observed in mCherry measurements and in A2780 cells, and since Tariquidar did not abolish selectivity, this effect is probably not related to the activity of P-gp.

It is striking that the compounds with a cell line dependent effect are those, in which the pyridinyl chelation motive, as also present in Triapine, is combined with an aromatic moiety

at N4, which is substituted in *para* position with an electron donating group, like the methoxy group in cases **II-c** and **II-e**, or the methyl group in cases **II-f** and **II-g**. In this compound set, changing the position of the methyl group from *para* in **II-g** to *meta* in **II-h** or *ortho* in **II-j** abrogates the cell line specific selectivity.

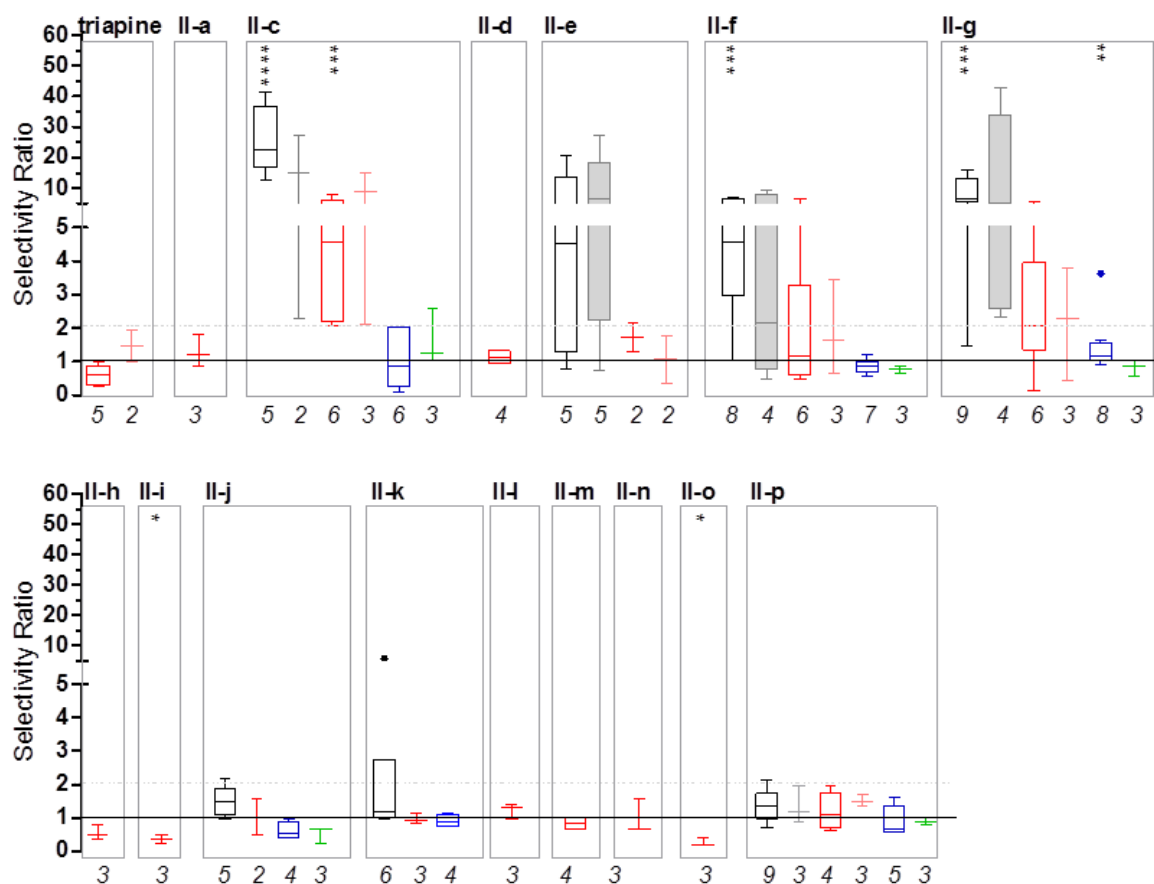


**Figure 19:** Selectivity ratios (SR) for pyridinyl TSCs and acetanilide TSC **II-p** from Table 6. Black: Dx5 vs. MES-SA (MTT), red: Dx5 vs. MES-SA (mCherry), blue: KB-V1 vs. KB-3-1 cells, green: A2780adr vs. A2780; filled boxes in lighter color: Dx5 vs. MES-SA cells in presence of 1 μM TQ measured by MTT (grey) or mCherry (light red). Significance is given as \*:  $p \leq 0.05$ , \*\*:  $p \leq 0.01$ , \*\*\*:  $p \leq 0.001$ , \*\*\*\*:  $p \leq 0.0001$ .

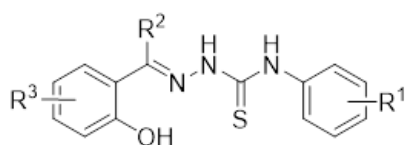
Taken together, while the terminally unsubstituted thiosemicarbazone Triapine is a substrate of P-gp, the introduction of a *para*-substituted aromatic moiety to the N4 of the pyridinyl TSC core structure (a feature associated with MDR selectivity) resulted in compounds that are not recognized and effluxed by the transporter. In some cases, the newly investigated compounds even conferred a cell line specific selective toxicity. Yet, this selectivity is linked to other factors than P-gp.

The chelation motif was changed from the NNS donor atom set present in pyridinyl TSCs to the ONS set of isatin- $\beta$ -thiosemicarbazones by replacement of the pyridinyl moiety by hydroxyphenyl. The investigated compounds are summarized in Table 7. Compound **III-c** and **III-d** were synthesized, while the other compounds were commercially available. Attempts to synthesize derivatives with nitro-substituents in position R1 did unfortunately not provide the desired products.

Similar to the previously described compound classes (**I** and **II**), also hydroxyphenyl thiosemicarbazones (class **III**) form complexes with various metal ions, like the redox active complexes with Ru(II) [204,208] and Cu(II) [205–207]. For the free ligands and the complexes formed with Ni(II) [209], Cu(II), Ru(II) and Zn(II) [206–208] an antibacterial and antifungal activity has been reported. N4-phenyl-hydroxyphenyl TSC **III-a** has also been reported to show GABA<sub>A</sub> receptor inhibition [230], a weak (500  $\mu$ M) inhibition of RR [231] and antitumor activity [198,207].

**Table 7:** Structures of investigated hydroxyphenyl thiosemicarbazones.

	R1	R2	R3
<b>III-a</b>	H	H	H
<b>III-b</b>	4-OMe	H	H
<b>III-c</b>	4-Me	H	H
<b>III-d</b>	4-Me	Me	H
<b>III-e</b>	3-CF <sub>3</sub>	H	H
<b>III-f</b>	3-CF <sub>3</sub>	H	4-NO <sub>2</sub>
<b>III-g</b>	2-CF <sub>3</sub>	H	4-NO <sub>2</sub>



As already observed for the pyridinyl TSCs, also the hydroxyphenyl TSCs show comparable toxicity across the investigated cell line panel. Two compounds show some degree of selectivity toward MES-SA/Dx5 over MES-SA cells in mCherry measurements, namely **III-a** and **III-d**. But due to the high deviation between assay results in case of **III-d**, this is rather a trend than a significant result. Even though the data in Figure 20 suggest, that Tariquidar co-administration might decrease the selectivity, a closer look at the data reveals that surprisingly the P-gp inhibitor also affects the sensitivity of the parental cells toward these two compounds. For mCherry measurements, in case of **III-a** the averaged  $IC_{50}$  value is changed upon Tariquidar co-administration from 14.1  $\mu$ M to 40.5  $\mu$ M in MES-SA, and from 6.4  $\mu$ M to 41.8  $\mu$ M in MES-SA/Dx5. Likewise for **III-d** the  $IC_{50}$  value is changed from 10.9  $\mu$ M to 13.0  $\mu$ M in MES-SA and from 3.5  $\mu$ M to 7.7  $\mu$ M in MES-SA/Dx5 (yet, even though a trend for an initial selectivity might be observable, statistical analysis suggests that the difference in response of both cell lines toward **III-d** is not significant).

In summary, these data suggest, that also in the set of hydroxyphenyl TSCs no new P-gp-mediated MDR selective compound could be identified.

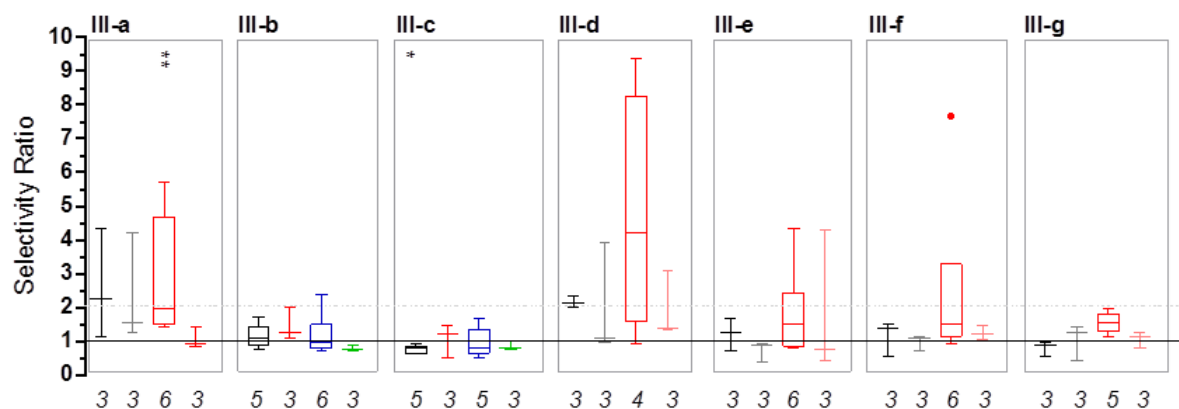


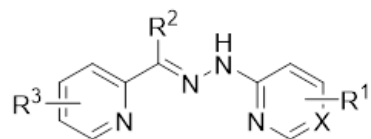
**Figure 20:** Selectivity ratios (SR) for hydroxyphenyl TSCs from Table 7. Black: Dx5 vs. MES-SA (MTT), red: Dx5 vs. MES-SA (mCherry), blue: KB-V1 vs. KB-3-1 cells, green: A2780adr vs. A2780; filled boxes in lighter color: Dx5 vs. MES-SA cells in presence of 1  $\mu$ M TQ; grey: measured by MTT, light red: measured by mCherry. Significance was calculated using paired t-tests of the independent experiments (number of experiments indicated under the boxes) and is given as \*:  $p \leq 0.05$ , \*\*:  $p \leq 0.01$ , \*\*\*:  $p \leq 0.001$ , \*\*\*\*:  $p \leq 0.0001$ .

### 3.2.2. Arylhydrazones – Compound class IV

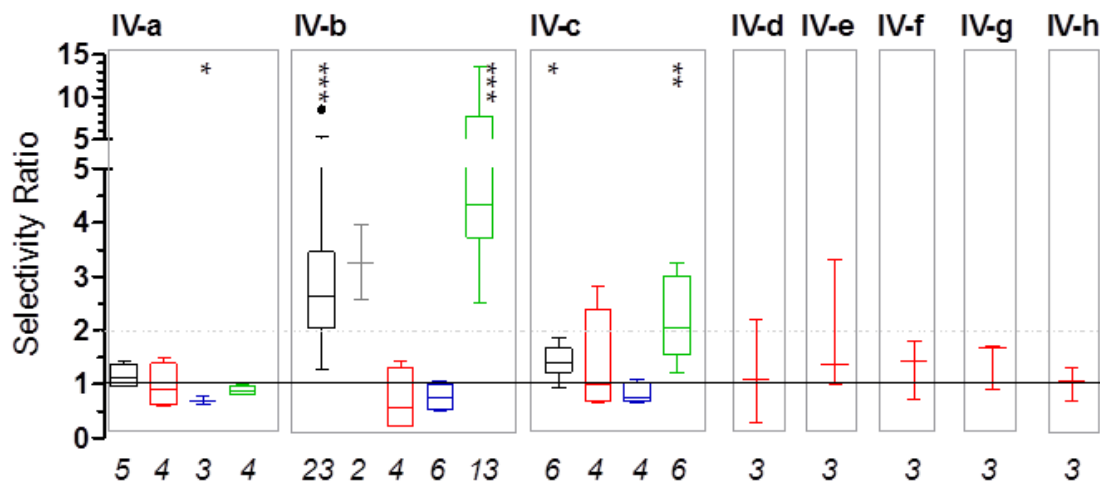
Arylhydrazones have been suggested to be superior to thiosemicarbazones, since they cannot release H<sub>2</sub>S from their structure, which might cause several side effects in clinical applications [187]. Compound **IV-c** was suggested to have a potential to overcome MDR in strains of leprosy and tuberculosis [187,190]. In order to investigate the potential of this compound class to overcome MDR in cancer, **IV-c** together with its close derivatives **IV-a** and **IV-b** were synthesized, while compounds **IV-d** to **IV-h** were purchased from vendors.

**Table 8:** Structures of investigated arylhydrazones.

	X	R1	R2	R3
<b>IV-a</b>	N	6'-OMe	H	H
<b>IV-b</b>	N	6'-OMe	Me	H
<b>IV-c</b>	N	6'-OMe	H	5-Et
<b>IV-d</b>	CH	H	Me	H
<b>IV-e</b>	CH	H	H	2,3-benzo
<b>IV-f</b>	CH	H	Me	2,3-benzo
<b>IV-g</b>	CH	H	H	2,3-benzo,4-Me
<b>IV-h</b>	CH	H	Me	2,3-benzo,4-Me



As shown in Figure 21, none of the investigated compounds is significantly less toxic in the MDR cell lines, as compared to their parental derivatives (an exception is compound **IV-a**, which seems to be significantly less toxic toward KB-V1 cells than to KB-3-1. Yet, despite being significant, the difference in toxicity toward the two cell lines is rather small), suggesting that they are not subject to P-gp-mediated efflux. Compounds **IV-b** and **IV-c** even show preferentially toxicity toward the MDR cell lines MES-SA/Dx5 and A2780adr compared to their parental counterparts MES-SA and A2780. The magnitude of the effect is much higher in case of **IV-b**. Yet, the effect observed in the MES-SA cell line pair with the MTT assay could not be verified with the mCherry fluorescence assay. Also, the P-gp inhibitor Tariquidar had no impact on the selectivity.

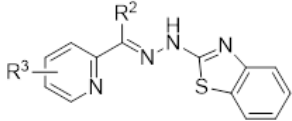
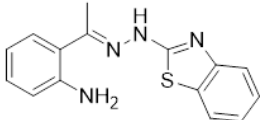


**Figure 21:** Selectivity ratios (SR) for aryldiazones from Table 8. Black: Dx5 vs. MES-SA (MTT), red: Dx5 vs. MES-SA (mCherry), blue: KB-V1 vs. KB-3-1 cells, green: A2780adr vs. A2780; filled boxes in lighter color: Dx5 vs. MES-SA cells in presence of 1µM TQ measured by MTT (grey) or mCherry (light red). Significance is given as \*:  $p \leq 0.05$ , \*\*:  $p \leq 0.01$ , \*\*\*:  $p \leq 0.001$ , \*\*\*\*:  $p \leq 0.0001$ .

### 3.2.2. Hydrazino-benzothiazoles – Compound classes V and VI

Similar to aryldiazones, also hydrazine-benzothiazoles have been suggested to be superior to thiosemicarbazones due to the incorporation of sulphur into a ring system, which hinders the release of  $H_2S$  during metabolism, while retaining the compound's activity [186]. The three pyridinyl **V-a** to **V-c** and one acetaniline derivative **V-d** summarized in Table 9 were synthesized. The biological application of benzothiazoles as well as their complexes includes – similar to that of TSCs – antibacterial and antifungal [188,189,218,220,232], as well as antitumor activity [186,188,203,219,233,234].

**Table 9:** Structures of investigated pyridinyl hydrazino-benzothiazole s, and acetaniline hydrazino-benzothiazole **V-d**.

	R2	R3
	<b>V-a</b>	H
	<b>V-b</b>	Me
	<b>V-c</b>	H      Et
	<b>V-d</b>	

As illustrated in Figure 22, in the MTT measurements all derivatives show a slightly higher toxicity toward MES-SA/Dx5 as compared to parental MES-SA cells. Yet, even though significant, this effect is rather small in most cases and could not be observed in the mCherry measurements or in other cell lines. An exception is compound **V-b**, which shows a more pronounced selectivity ratio in the before mentioned test system. Even though not significant, a clear trend can also be observed in the mCherry measurements of the MES-SA cell line pair, as well as in the MTT measurements of the A2780 cell line pair. Co-administration of Tariquidar revealed, that P-gp has no impact on the observed selectivity of compound **V-b**.

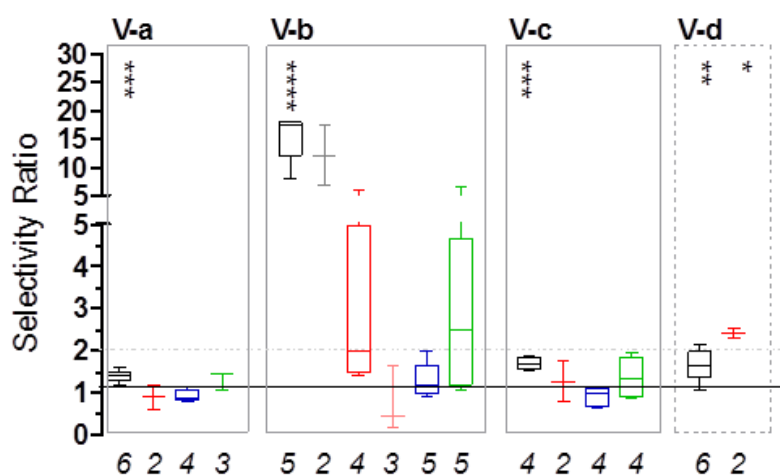


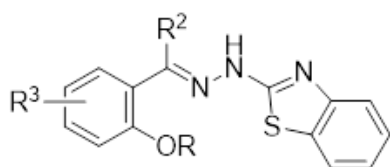
**Figure 22:** Selectivity ratios (SR) for pyridinyl hydrazino-benzothiazoles and the acetaniline hydrazino-benzothiazole **V-d** from Table 9. Black: Dx5 vs. MES-SA (MTT), red: Dx5 vs. MES-SA (mCherry), blue: KB-V1 vs. KB-3-1 cells, green: A2780adr vs. A2780; filled boxes in lighter color: Dx5 vs. MES-SA cells in presence of 1 $\mu$ M TQ measured by MTT (grey) or mCherry (light red). Significance is given as \*:  $p \leq 0.05$ , \*\*:  $p \leq 0.01$ , \*\*\*:  $p \leq 0.001$ , \*\*\*\*:  $p \leq 0.0001$ .



In order to again increase the similarity of the chelation motif to that of the MDR selective isatin- $\beta$ -thiosemicarbazones, compounds with an ONS donor atom set were investigated. Hydroxyphenyl hydrazino-benzothiazoles **VI-a** and **VI-b** were synthesized, while derivatives with substituents in *para* position of the phenolic OH **VI-c** to **VI-g** were commercially available.

**Table 10:** Structures of investigated hydroxyphenyl hydrazino-benzothiazoles.

	R	R2	R3
<b>VI-a</b>	H	H	H
<b>VI-b</b>	H	Me	H
<b>VI-c</b>	H	H	4-OMe
<b>VI-d</b>	H	Me	4-OMe
<b>VI-e</b>	H	H	4-Me
<b>VI-f</b>	H	H	4-NO <sub>2</sub>
<b>VI-g</b>	Me	H	H



Strikingly, compound **VI-g**, in which the metal binding hydroxyl group of **VI-a** is replaced by a methoxy group, lacks toxic activity. Since the methoxy group in **VI-g** hinders chelation in comparison to a free hydroxyl group, the lack of toxicity of this compound underlines the importance of chelation in the mechanism of toxicity of these compounds. Despite the deviations between the single experiments, a significant preferential toxicity toward MES-SA/Dx5 as compared to MES-SA could be observed for compounds **VI-a**, **VI-b**, **VI-d** and **VI-e**. In case of **VI-a** and **VI-b**, experiments in other cell lines could not confirm this effect (Figure 23). Although co-administration of Tariquidar seemed to abolish the selectivity, the decreased selectivity in the presence of the P-gp inhibitor is not only connected to changes in MES-SA/Dx5 sensitivity, but also to the sensitivity of the parental MES-SA cells. This is comparable to the effect seen for the investigated hydroxyphenyl thiosemicarbazones.

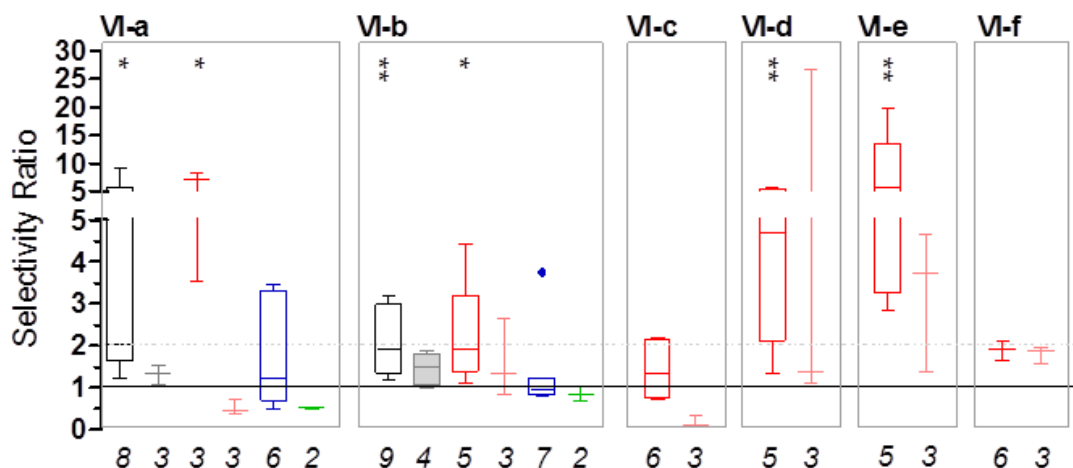


**Figure 23:** Selectivity ratios (SR) for hydroxyphenyl hydrazino-benzothiazoles from Table 10. Black: Dx5 vs. MES-SA (MTT), red: Dx5 vs. MES-SA (mCherry), blue: KB-V1 vs. KB-3-1 cells, green: A2780adr vs. A2780; filled boxes in lighter color: Dx5 vs. MES-SA cells in presence of 1 $\mu$ M TQ; grey: measured by MTT, light red: measured by mCherry. Significance was calculated using paired t-tests of the independent experiments (number of experiments indicated under the boxes) and is given as \*:  $p \leq 0.05$ , \*\*:  $p \leq 0.01$ , \*\*\*:  $p \leq 0.001$ , \*\*\*\*:  $p \leq 0.0001$ .

### 3.2.4. Combination of chemical entities – Compound class VII

As shown in Figure 16, chemical entities from different classes were combined in order to increase the similarity of newly designed compounds to **I-a**. Four compounds were prepared under similar conditions as for the other Schiff-bases. For the dimer of the non-isatin moiety of **I-a**, namely **VII-a**, 4-methoxyphenylisothiocyanat was reacted with a half equimolar amount of hydrazine. Compounds **VII-b** and **VII-c** are combinations of **I-a** with hydrazino-benzothiazole s, they were prepared by the reaction of hydrazino-benzothiazole with either 4-methoxyphenylisothiocyanat or isatin. The arylhydrazone **VII-d** was obtained in an acid catalyzed condensation of isatin and 4-hydrazinyl-6-methoxypyrimidine.

Compounds with combined entities of the parent compounds had only modest cytotoxicity with  $IC_{50}$  values above 50  $\mu$ M.

### 3.2.5. Structure activity relationships in the focused library and beyond

Even though most of the scrutinized compounds do not show enhanced toxicity toward P-gp expressing MDR cell lines over their parental P-gp negative cells, the test results of the library disclose trends in toxicity, which are independent of the resistance status of the investigated cell lines. For illustration, results are summarized in the structure activity relationship matrix (SARM) shown in Figure 24 [235]. Numbers represent averaged  $pIC_{50}$  values of at least three independent experiments and are colored according to the color code given in the inset next to the matrix.

As already mentioned in chapter 3.2.4., the combination of chemical entities resulted in nontoxic compounds **VII-a**, **VII-b**, **VII-c** and **VII-d**.

Hydrazino-benzothiazoles have been described in the literature as metabolically more stable derivatives of thiosemicarbazones with retained pharmacological activity [186]. Indeed, comparison of the respective columns in the SARM confirms the retained (anticancer-) activity of the two scaffolds: the pyridinyl hydrazino-benzothiazole **V-a** shows similar toxicity compared to the corresponding TSC **II-a**. Likewise the hydroxyphenyl hydrazino-benzothiazole **VI-a** is comparable to the corresponding TSC **III-a**. Furthermore comparing the columns of differently substituted N4-aromatic moieties in the investigated thiosemicarbazones it appears that N4-*para*-nitrophenyl derivatives have a lower toxicity compared to *para*-tolyl and *para*-methoxyphenyl substituted counterparts (**I-d** vs. **I-a**, **I-c**; **II-j** vs. **II-f**; **II-k** vs. **II-e**).

Comparing the rows of the SARM, further trends can be identified with respect to the impact of different donor atom sets and imino carbon substitution on toxicity of the compounds. Both will influence the metal binding properties of the chelators, which might be crucial in the mechanism of toxicity of these compounds.

**R1**

**R2**  $R1=N-NH-R2$

<b>ONS / ONN</b>			<b>I-a</b>	<b>I-c</b>	<b>I-d</b>	<b>VII-d</b>	<b>VII-c</b>	
			5,13 5,33	5,02 5,05	4,61 5,05	n.tox. n.tox.		
			5,12 5,40	5,38 5,40	5,11 5,35	4,26 4,17		
			5,22 5,46	5,29 5,48	5,07 5,33	4,04 3,89	n.tox. n.tox.	
			<b>I-b</b>					
			5,49 5,45					
			5,21 5,41					
			5,24 5,59					
			<b>VII-a</b>				<b>VII-b</b>	
			n.tox. n.tox.				n.tox. n.tox.	
		<b>III-a *</b>	<b>III-b</b>	<b>III-c</b>		<b>VI-a</b>		
			5,27 5,16	5,30 5,22		5,51 5,23		
			5,30 5,30	5,48 5,46		4,80 4,93		
		4,94 5,32	5,42 5,46	5,43 5,39		4,63 5,02		
				<b>3d *</b>		<b>VI-b</b>		
				5,01 5,36		5,08 5,01		
						4,86 4,94		
						4,91 5,28		
<b>NNS / NNN</b>			<b>2q</b>				<b>V-d</b>	
			5,37 5,31					
			4,69 4,65					
			4,98 5,10				4,35 4,56	
			<b>II-a *</b>		<b>II-f</b>	<b>II-j</b>	<b>IV-a</b>	<b>V-a</b>
					7,32 7,20	6,21 5,87	5,76 5,71	6,24 6,35
					6,14 6,05	5,99 5,75	5,72 5,55	6,19 6,09
			6,16 6,25		6,44 7,14	5,59 5,75	5,56 5,61	5,85 6,00
			<b>II-b *</b>	<b>II-c</b>	<b>II-g</b>		<b>IV-b</b>	<b>V-b</b>
				7,34 7,55	7,79 7,69		6,88 7,59	7,05 7,52
			6,16 5,98	7,43 7,48		6,45 6,31	6,43 6,53	
		n.tox. n.tox.	6,47 7,85	7,77 8,77		6,58 7,04	6,66 7,91	
			<b>II-e</b>		<b>II-k</b>	<b>IV-c</b>	<b>5c</b>	
					5,10 5,05	5,89 6,21	6,09 6,23	
					4,97 5,09	5,91 5,81	6,03 5,94	
						5,82 5,96	5,50 5,73	
			<b>II-d *</b>					
			5,33 5,38					

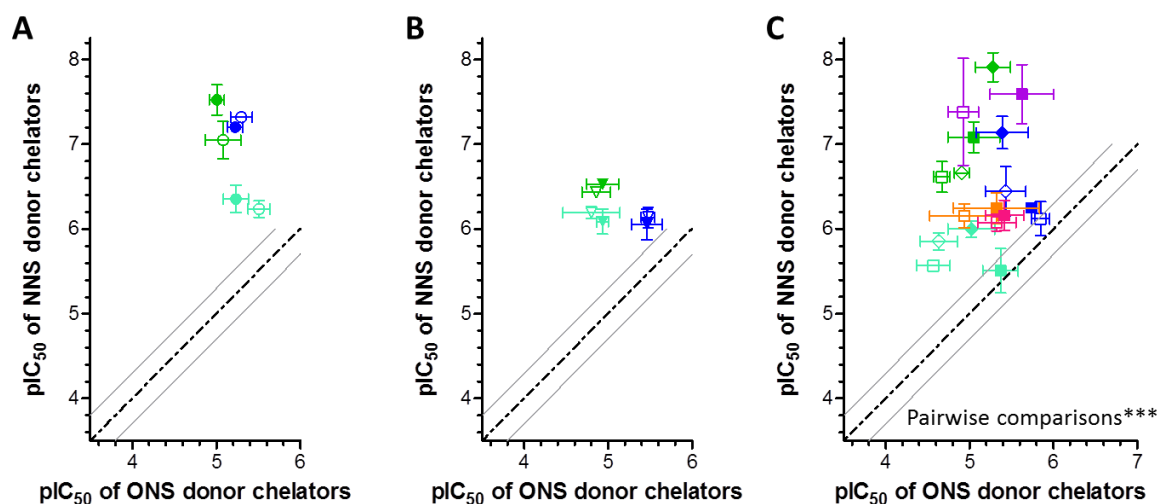
cell lines	
A2780	A2780adr
KB-3-1	KB-v1
mesa	dx5

pIC <sub>50</sub>	IC <sub>50</sub>
n.tox.	not toxic
4,00	100.0 μM
4,50	31.6 μM
5,00	10 μM
5,50	3.2 μM
6,00	1.0 μM
6,50	316.2 nM
7,00	100.0 nM
7,50	31.6 nM
8,00	10 nM
8,50	3.2 nM

**Figure 24:** SAR matrix of synthesized and purchased compounds. The average pIC<sub>50</sub> values of at least three independent experiments are given for the A2780, KB and MES-SA cell line pairs. Cell lines are arranged according to the inset. In general, data were obtained by MTT assays, while compounds marked with an asterisk were measured in mCherry fluorescence assay only.

Strikingly, the investigated hydroxyphenyl TSCs and benzothiazoles proved to be less toxic than their corresponding pyridinyl counterparts. Plotting the  $pIC_{50}$  values of matched molecular pairs (MMP) of ONS and NNS donor chelators as shown in Figure 25, a significant difference in toxicity is visible across all investigated cell lines. Including also those compounds into the analysis which do not have an MMP, the same effect can be observed: In Figure 26 A the  $pIC_{50}$  values were averaged for P-gp positive and P-gp negative cell lines for all investigated compounds and plotted for comparison. In agreement with the earlier chapters (3.2.1 – 3.2.3), no overall effect of P-gp on the toxicity could be observed, explaining the arrangement of data points close to the bisecting line of the diagram. In contrast, the differently colored data-points, representing ONS (red), NNS (blue) and NNN (green) chelators seem to cluster. The significance of this clustering is illustrated in the boxplot in Figure 26 B.



**Figure 25:** Pairwise comparison of the toxic effect ( $pIC_{50}$ ) of matched molecular pairs (MMP) of chelators with ONS and NNS donor sets. Different colors indicate the respective compound pairs: Cyan: **VI-a** vs. **V-a**, green: **VI-b** vs. **V-b**, blue: **III-c** vs. **II-f**, purple: **III-d** vs. **II-g**, orange: **III-a** vs. **II-a**, pink: **III-e** vs. **II-m**. Data are shown in panel A for A2780wt (open circles) and A2780adr (filled circles), in panel B for KB-3-1 (open triangles) and KB-V1 (filled triangles), and in panel C for MES-SA (open symbols) and MES-SA/Dx5 (filled symbols). Data were in general obtained by MTT assay, except for the diamonds in panel C, which were obtained by mCherry fluorescence assay. The indicated significance ( $***p \leq 0.001$ ) was calculated by unpaired t-test. A list of  $IC_{50}$  values is provided in the appendix.

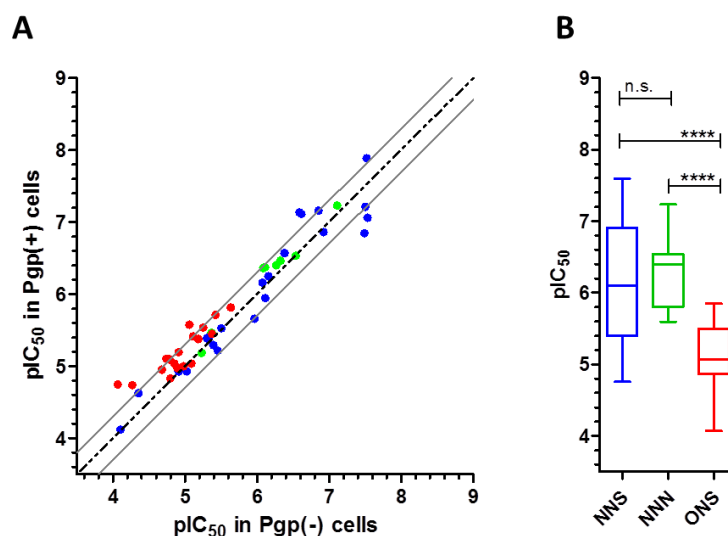


**Figure 26:** (A): Comparison of overall toxic activity of ONS (red), NNS (blue) and NNN (green) chelators with and without MMPs in P-gp (+) and P-gp (-) cells. Data for each compound was averaged over the investigated cell lines. (B): Box and Whiskers plot of toxicity data from mCherry fluorescence measurements using MES-SA and MES-SA/Dx5 cells comparing NNS, NNN and ONS chelators. Significance was calculated from unpaired t-tests (\*\*\*\*:  $p \leq 0.0000001$ ).

In the investigated set of compounds NNS chelators seemed to be have a higher toxic potential against the investigated cancer cell lines, as compared to ONS chelators. In order to test this hypothesis on a larger compound set, the DTP drug database, which contains the activity patterns of standard anticancer drugs and tens of thousands of candidate anticancer agents [96,97], appeared to be a useful tool. Substructure searches for NNS and ONS chelators were performed within the database as illustrated in Figure 27 A and 27 B. Altogether 1335 analogues were identified. Some of the identified compounds (221 NNS and 74 ONS compounds) contained metal ions in their structure and were segregated following visual inspection. Further visual inspection revealed, that despite the presence of the putative donor atoms in the right distance to each other, some of the derivatives (namely 120 NNS and 119 ONS compounds), will not be able to chelate metal ions, since the heteroatoms are occupied by substituents or incorporated into ring systems (an example for such a structure is given in Figure 27 E). Also these compounds were treated separately. Biodata was extracted from the database in case it was available (for this I am grateful to *Dr. Anna Lovrics*).

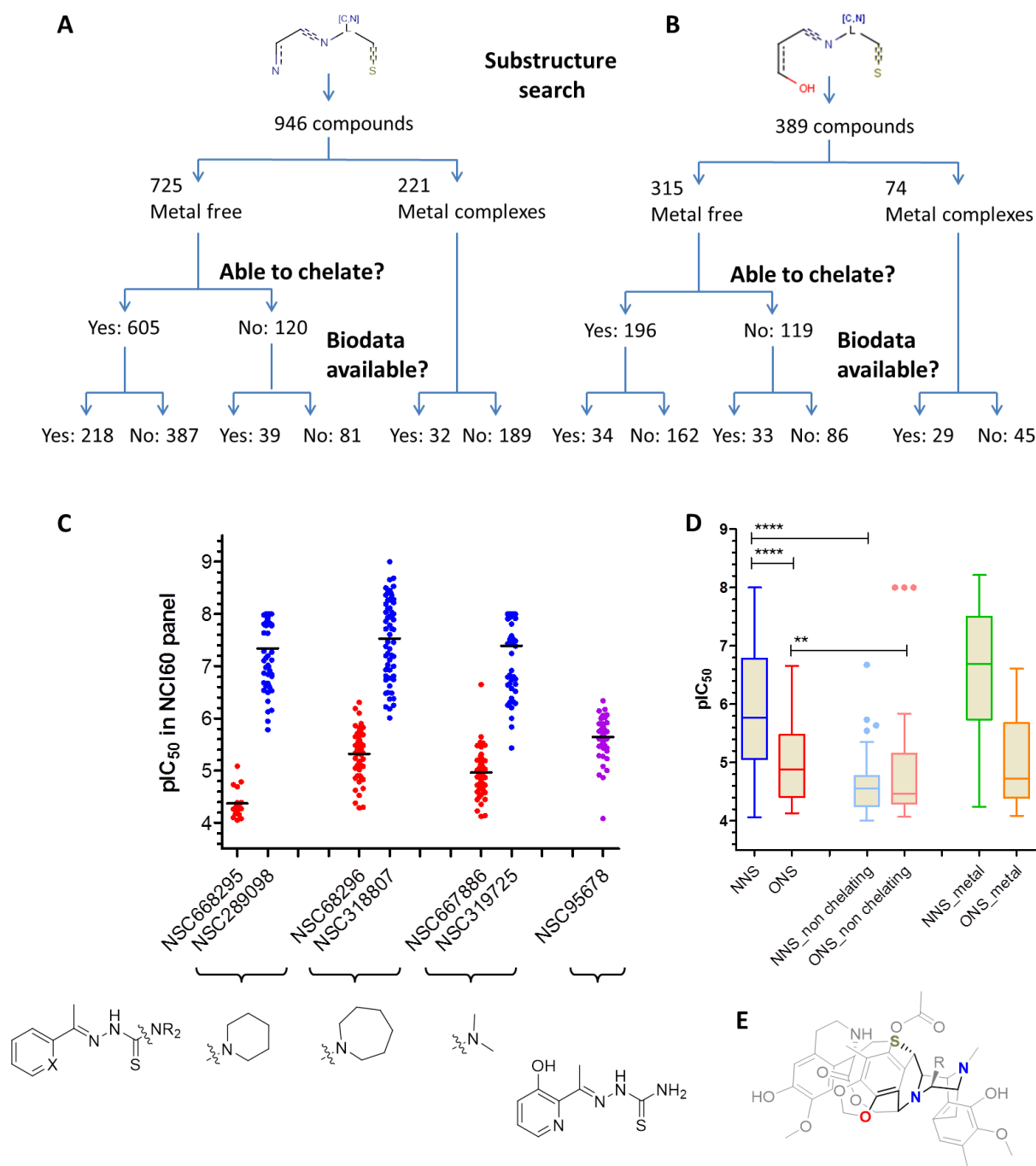


**Figure 27:** Flowchart of the identification of NNS (A) and ONS (B) donor chelators in the DTP database. (C): Pairwise comparison of cytotoxic activity of matched molecular pairs of ONS (data for X = C-OH shown in red) and NNS (data for X = N shown in blue) donor chelators across the NCI60 cell panel. Structures of the compounds are shown below the graph. NSC95678 contains both binding options (purple). (D): Average toxicity of the compounds identified by the substructure search (pIC<sub>50</sub> values averaged over the 60 cell lines). (E): outstandingly toxic non chelating ONS molecules, derivatives of Trabectedin / ecteinascidin-743 (NSC648766, NSC648767, NSC648768, NSC648769).

Within the set of compounds with available biodata, three matched molecular pairs (MMPs) could be identified with ONS and NNS donor atom sets. Figure 27 C shows the available biodata of these compounds across the NCI60 panel. The structures of these pairs are displayed below the data with X representing C-OH for the ONS donor chelators (data in red), or N for the NNS donor chelators (data in blue). The three additional MMPs confirm a higher toxicity of NNS chelators over their ONS counterparts irrespective of the investigated cell line. Interestingly, NSC95678, which is able to chelate in either NNS or ONS binding mode, has a moderate toxicity between that of the other NNS and ONS chelators.

In order to compare the activity of the 385 compounds for which biodata were available, the average  $pIC_{50}$  value over the NCI60 panel was determined for each compound. The boxplot in Figure 27 D shows that the superior activity of NNS over ONS chelators found in the DTP database is significant. This is especially interesting, since the identified compounds display a high diversity that is presumably associated with different mechanisms of toxicity.

A similar trend could also be observed for the diverse metal complexes. Though, it has to be noted, that the identified complexes contain different metal ions, which might lead to misleading conclusions, since not only the properties of the ligand, but also the nature of the metal ions that are incorporated into the complex, will affect its biological activity.

The lack of activity of the non-chelating derivative **VI-g** within the designed library suggested a huge impact of chelation on the toxicity of the investigated compounds. Indeed, non-chelating derivatives identified in the DTP, despite their structural diversity, show a significantly decreased toxicity. Within the non-chelating derivatives there is no difference in toxicity between NNS and ONS containing structures. In comparison to the chelating derivatives these compounds are generally less potent. Nevertheless, within this non-chelating subset, four compounds show an outstandingly high toxicity. The structural scaffold of these compounds is shown in Figure 27 E (within the four derivatives R is differing). It is apparent, that despite the putative metal-binding substructure motive, by which they were identified, their structure is very different from the other compounds: they are derivatives of the marine natural product Trabectedin (ecteinascidin-743, Figure 27 E), which is currently undergoing clinical trials (phase III) in the USA, while it is approved for cancer treatment in Europe [236–238].

Since chelation seems to be crucial for the activity of the investigated compounds, the superior activity of NNS (and NNN) donor atom chelators over ONS donors might be related to different metal binding preferences. Chelators with distinct donor atoms show a binding



preference for certain metal ions, and stabilize different oxidation states of these ions, according to the principle of hard and soft acids and bases (HSAB) [239,240].

The common donor atoms in the thiosemicarbazone and hydrazino-benzothiazole compound classes are a sulfur atom as a soft electron donor and a hydrazinic nitrogen as a hard donor. The third Lewis base is either a borderline pyridine nitrogen donor in case of the pyridinyl derivatives, or a hard oxygen donor in case of the hydroxyphenyl derivatives [239–241]. Therefore the hydroxyphenyl compounds prefer harder metal ions than the pyridinyl derivatives [241]. A study comparing the stability of several metal complexes formed by the N4 unsubstituted hydroxyphenyl- and pyridylcarbaldehyde TSCs supports this general trend [242]. The different chelating properties of the ligands might not only influence the stability of complexes formed with diverse metal ions, but also their redox properties. For example, ONS donors prefer higher oxidation states of iron and copper as compared to NNS donors [241]. Therefore the mechanism of action of hard donor atom containing chelators might be dominated by the depletion of metal ions (as it is exploited in the case of iron overload disease), while soft donor atom chelators are more capable of enhancing the production of ROS upon complexation with metal ions like iron [123,243].

Next to the nature of the donor atoms alone, also steric factors will affect the ligands' ability to chelate a metal ion. The impact of steric effects on the biological activity is evident from the comparison of the two investigated acetaniline compounds **II-p** and **V-d** to their respective pyridinyl counterparts **II-c** and **V-b** (see SARM, Figure 24). The latter show a greater toxic potential. This might be explained by a combination of steric and electronic reasons that have an impact on the complexation of metal ions.

Another observation that can be made upon comparison of rows within the SARM (Figure 24) is, that compounds methylated at the imino carbon of the Schiff base might be more toxic than those which are derived from the corresponding aldehyde and do not possess a methylgroup in this position. Examples for this observation are the MMPs **II-f** vs. **II-g**, **IV-a** vs. **IV-b**, and **V-a** vs. **V-b**. Together with further MMPs that are not included in the SARM, the toxicity of compounds with and without methyl group at the imino-carbon is compared in Figure 28 in dedicated panels for NNS (panel A), NNN (panel B) and ONS (panel C) chelators. Literature data suggest, that the imino carbon of thiosemicarbazones [227], aroylhydrazones [244], arylhydrazones [89] and benzothiazoles [203,233] might be a sensitive position for the fine-tuning of the biological activity of these Schiff bases. Variations in this position might influence the chelation behavior.

As apparent from panel A, in two of the four NNS donor MMPs methylation of the imino carbon results in increased toxicity (these two are the previously mentioned pairs **II-f** vs. **II-g** and **V-a** vs. **V-b**). For the MMP consisting of N4-*ortho*-trifluoromethylphenyl TSCs, the imino-methylated derivative **II-o** showed a higher toxicity than the desmethyl counterpart **II-n** in MES-SA cells, while MES-SA/Dx5 cells reacted to both compounds with the same sensitivity. In contrast, for the N4-*meta*-trifluoromethylphenyl TSC MMP the methylated derivative **II-m** was actually less toxic than the desmethyl derivative **II-l**.

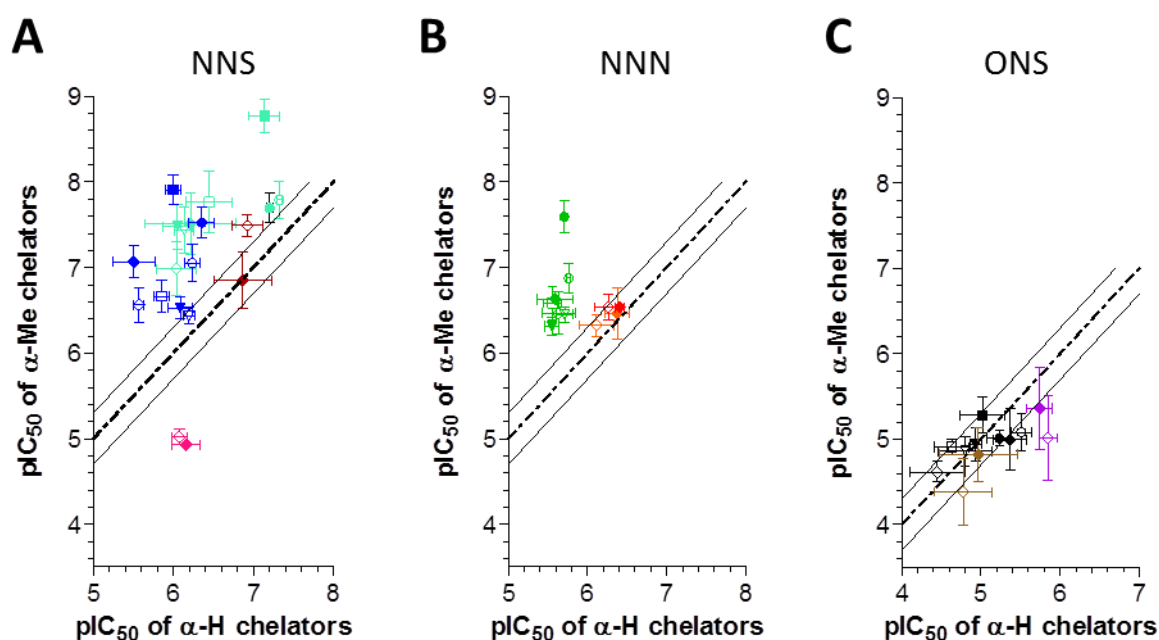


**Figure 28:** Effect of imino methylation on toxicity. Pairwise comparison of  $pIC_{50}$  values from MMPs of chelators containing NNS (A), NNN (B) and ONS (C) donor atom sets obtained in A2780wt (open circles), A2780adr (filled circles), KB-3-1 (open triangles), KB-V1 (filled triangles), MES-SA (open squares), MES-SA/Dx5 (filled). Cyan: **II-f** vs. **II-g**, green: **IV-a** vs. **IV-b**, blue: **V-a** vs. **V-b**, black: **VI-a** vs. **VI-b**, purple: **III-c** vs. **III-d**, bordeaux: **II-n** vs. **II-o**, pink: **II-l** vs. **II-m**, orange: **IV-e** vs. **IV-f**, red: **IV-g** vs. **IV-h**, brown: **VI-c** vs. **VI-d**. A list of  $IC_{50}$  values is provided in the appendix.

For the investigated NNN donor containing chelators, toxicity of the arylhydrazones **IV-e** and **IV-g** was comparable to that of their corresponding imino carbon methylated counterparts **IV-f** and **IV-h** (Figure 28 B). Here, increased toxicity upon methylation could only be observed for the pyrimidinylhydrazone **IV-b** over **IV-a**, which was already identified from the SARM. The three investigated ONS donor atom chelator MMPs showed comparable toxicity of imino carbon methylated and demethylated derivatives (Figure 28 C). Including also those compounds into the analysis, which do not have a MMP confirmed the lack of effect of imino

carbon methylation on the toxicity of hydroxyphenyl containing chelators, while the activity of the imino carbon methylated pyridinyl compounds was found to slightly but significantly surpass that of the unsubstituted derivatives (Figure 29). Together with the pairwise comparisons, these data suggest that methyl substitution of the imino carbon may influence the toxicity of NNS donor atom chelators.

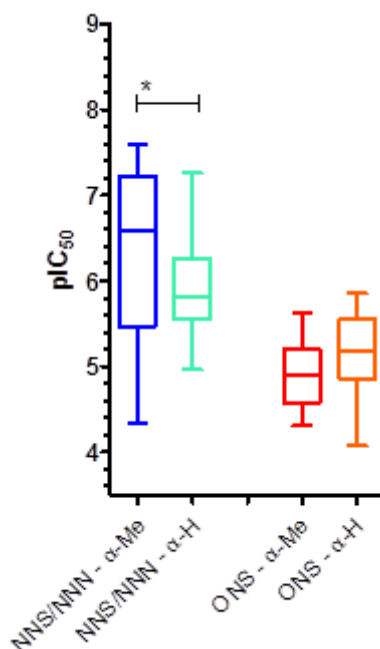
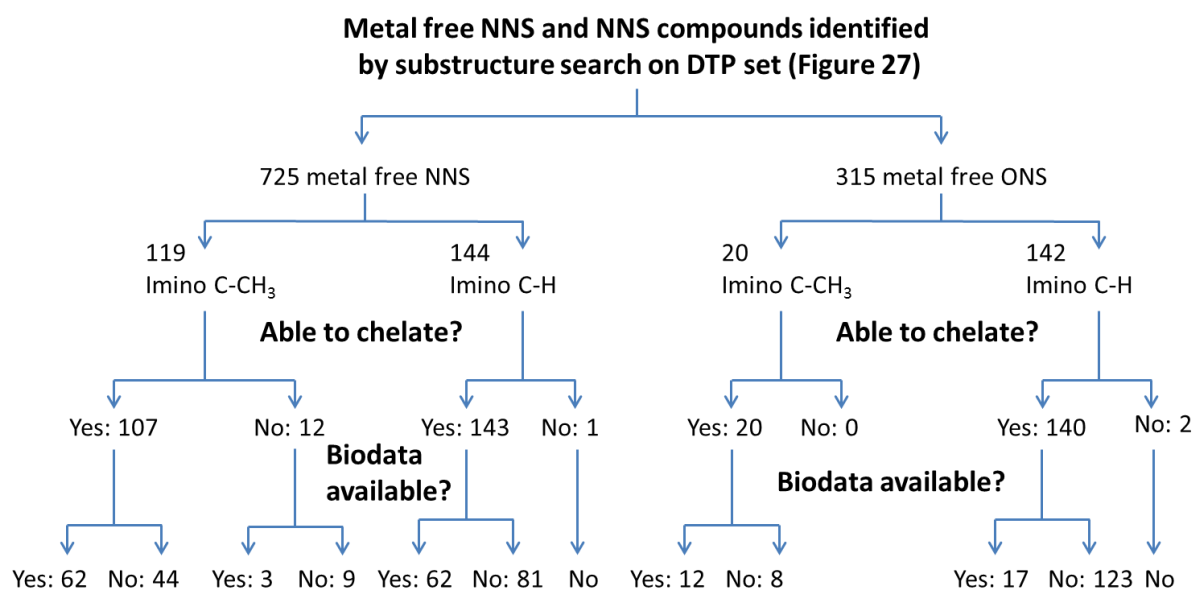


**Figure 29:** Box and Whiskers plot of toxicity data on MES-SA-mCh and MES-SA/Dx5-mCh cells comparing chelators with different donor atoms with and without methylation at the imino carbon. NNS/NNN chelators with imino methyl group are depicted in blue, without methyl group in cyan, ONS chelators with methyl group are depicted in red, without Me in orange (p=0.045).

Since the observed trend was not conclusive, the set of NNS and ONS donor atom chelators identified in the DTP database was revisited. The search results were refined, separating molecules with unsubstituted and methylated imino carbons as shown in Figure 30 A. Comparison of the available biodata of further 12 imino methylated and 17 demethylated ONS chelators confirmed our finding that a methyl substitution of the imino carbon does not significantly influence the activity of these chelators. For the NNS donor chelators biodata was available for 62 methylated and 62 demethylated derivatives. In agreement with the finding on the designed library, also in this compound set the methylated derivatives tended to be more toxic than the demethylated derivatives (Figure 30 B).

A



B

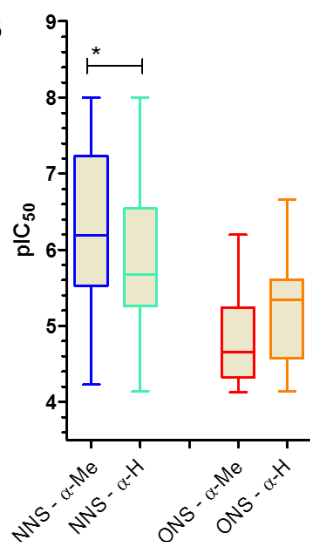


**Figure 30:** The NNS and ONS chelating compounds from Figure 27 were analyzed with respect to imino carbon substitution. (A): Flowchart of the refinement of search results from Figure 27, (B): Available biodata for 62 NNS chelators with methyl-substituted imino carbon (blue), 62 NNS chelators with unsubstituted (H) imino carbon (cyan), 12 ONS chelators with methyl-substituted (red) and 17 ONS chelators with unsubstituted (H) imino carbon (orange). pIC<sub>50</sub> values were averaged over the 60 cell lines for all compounds (p=0.039).

### 3.3. Having a closer look at the 8-hydroxyquinoline scaffold

Revisiting the set of MDR selective compounds, which were identified by the pharmacogenomic approach on the DTP data (chapter 3.1.), two compound classes seemed enriched in both, the already published (reference [98]) and the new discovery set. One cluster is formed by thiosemicarbazones, which were derivatized as presented in chapter 3.2.1. – the other cluster is formed around hydroxyquinoline derived Mannich bases. The 8-hydroxyquinoline scaffold is a privileged structure in medicinal chemistry which has various applications next to its anticancer activity, including neuroprotective, anti-HIV and antifungal, antileishmanial, antischistosomal activity, as well as inhibitory potential against 2-oxoglutarate, iron dependent enzymes and other metallo-proteins, *mycobacterium tuberculosis* and butolinum neurotoxin [245]. In the new discovery set, the piperidine Mannich base NSC57969 (**Q-3**) and the ring-closed dihydro-[1,3]-oxazine derivative NSC297366 (**Q-4b**) were identified based on their high Pearson correlation coefficients ( $\geq 0.4$ ). A structural similarity search in the database disclosed available biodata for further derivatives. Two closely related compounds are the morpholino Mannich base (NSC662298, **Q-2**) and the unsubstituted 8-hydroxyquinoline core structure (NSC2039, **Q-1**). While the Pearson correlation coefficient for **Q-1** is close to zero, for **Q-2** it is 0.37, and therefore just closely below to the set threshold of 0.4. Data in the NCI/ADR-res and OVCAR-8 cell line pair confirms the trend from the 60 cell line data, as illustrated in Figure 31.

The structural similarity of these compounds suggests a similar metal binding mode. Due to the varied spectrum of selective toxicity toward MDR cell lines that is represented by these four compounds, they seem to provide a promising tool to address questions regarding the link between metal binding properties and their biological activity. The compound set was furthermore expanded by three additional compounds in order to address the impact of chelation. **Q-4** is a close derivative of **Q-4b**, in which the dihydro-[1,3]-oxazine ring is opened. It was included to study the similarity of **Q-4b** to the 8-hydroxyquinoline metal binding motive in terms of biological and metal binding properties. In contrast, **Q-5** and **Q-6** represent analogues, which share some degree of similarity to the compound set, but are unable to chelate metal ions. While **Q-1** was commercially available, larger quantities of **Q-2** and **Q-3** were synthesized by the group of *Dr. Tibor Soós* in the framework of a collaboration with the Institute of Organic Chemistry, Hungarian Academy of Sciences, Research Centre for Natural Sciences Budapest, Hungary), **Q-4** to **Q-6** were synthesized by the group of *Prof. Ferenc Fülöp*, in the framework of a collaboration with the Institute of Pharmaceutical Chemistry, University of Szeged, Hungary.

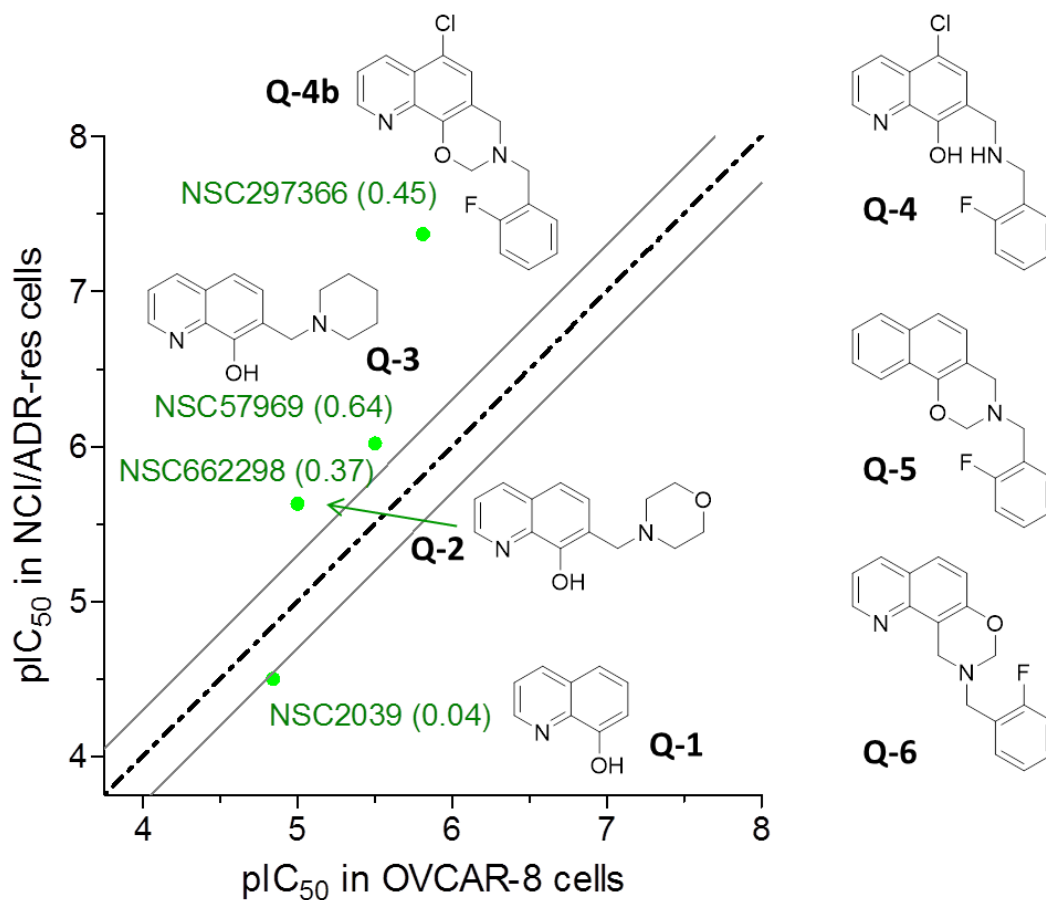


**Figure 31:** 8-hydroxyquinoline derivatives investigated on the basis of DTP screening data. Four derivatives were found in the DTP with increasing MDR selectivity: Numbers in brackets indicate the Pearson correlation coefficients obtained from the correlation of activity against the P-gp expression across the NCI60 cell line panel. The activity is shown as pIC<sub>50</sub> values in P-gp positive NCI/ADR-res and P-gp negative OVCAR-8 cells for the 8-hydroxyquinoline scaffold (NSC2038, **Q-1**), the Mannich bases NSC662298 (**Q-2**) and NSC57969 (**Q-3**) and the dihydro-[1,3]-oxazine derivative (**Q-4b**). Structures of further investigated compounds **Q-4** to **Q-6** are shown.

Having shown that the MDR selective effect of **Q-3** and **Q-4b** is not restricted to single cell line pairs, but mediated by active P-gp (chapter 3.1.), the following mechanistic studies focused on the MES-SA and MES-SA/Dx5 cell line pair. Table 11 summarizes biodata of the 8-hydroxyquinoline derivatives obtained in the absence and presence of the P-gp inhibitor Tariquidar.

**Table 11:** IC<sub>50</sub> values in  $\mu\text{M}$  as determined by MTT assays. The left part of the table summarizes results in the absence, the right part in the presence of 1  $\mu\text{M}$  of the P-gp inhibitor Tariquidar (TQ). The median SR value (quotient of parental vs. MDR cell IC<sub>50</sub>) is determined from Boxplots of the SR values from the indicated number of independent experiments. Significance was calculated using paired t-tests and results are given as \*:  $p \leq 0.05$ , \*\*:  $p \leq 0.01$ , \*\*\*:  $p \leq 0.001$ , \*\*\*\*:  $p \leq 0.0001$ .

	MES-SA	MES-SA/Dx5	median SR	MES-SA + TQ	MES-SA/Dx5 + TQ	median SR + TQ
<b>Q-1</b>	4.13 $\pm$ 1.11	2.37 $\pm$ 1.03	1.78 (10) **	5.06 $\pm$ 0.72	2.87 $\pm$ 0.99	1.59 (3) *
<b>Q-2</b>	6.76 $\pm$ 2.62	3.24 $\pm$ 0.59	1.81 (8) ***	4.56 $\pm$ 1.38	5.40 $\pm$ 1.54	0.87 (3) *
<b>Q-3</b>	3.95 $\pm$ 1.78	0.83 $\pm$ 0.39	4.86 (18) ****	2.86 $\pm$ 1.35	3.02 $\pm$ 1.38	0.96 (4)
<b>Q-4b</b>	2.58 $\pm$ 1.58	0.24 $\pm$ 0.14	11.78 (18) ****			
<b>Q-4</b>	2.71 $\pm$ 0.70	0.19 $\pm$ 0.08	13.76 (11) ****	2.20 $\pm$ 0.54	3.24 $\pm$ 0.77	0.54 (3)
<b>Q-5</b>	> 50	> 50				
<b>Q-6</b>	> 50	> 50				

As apparent from Table 11, the non-chelating compounds **Q-5** and **Q-6** lose their toxicity in comparison to their chelating counterparts **Q-4** and **Q-4b**. The selectivity obtained with the 8-hydroxyquinoline derivatives increases in the following order: **Q-1** < **Q-2** < **Q-3** < **Q-4b** = **Q-4**. The application of the P-gp inhibitor Tariquidar (TQ) shows the influence of the functional transporter on the toxicity of the selective compounds (**Q-2**), **Q-3**, **Q-4b** and **Q-4**. Considering the precision of the assay, a selectivity threshold could be set at around 2. Applying this threshold, **Q-1** and **Q-2** would not count as MDR selective agents. Additionally, the P-gp-inhibitor TQ does not significantly affect the toxicity of **Q-1**, while it increases the toxicity of **Q-2** in MES-SA/Dx5 cells. Taking this into account, **Q-2** might be considered as a weak MDR selective compound with borderline selectivity.

**Q-4** was included in the study, in order to enable comparison of the dihydro-[1,3]-oxazine derivative **Q-4b** to the 8-hydroxyquinoline based Mannich bases. Indeed, the *in vitro* activity of **Q-4** and **Q-4b** shows a remarkable similarity with regard to toxicity and selectivity toward the MDR cell line counterpart.

Since the physico-chemical properties, like the pK<sub>a</sub> values of potential chemotherapeutic agents, have a basic influence on the compounds pharmacokinetics and metal binding abilities, a detailed study on the proton dissociation processes of the promising compound set was performed in collaboration with Prof. Éva A. Enyedy from the Institute of Inorganic and Analytical Chemistry, University of Szeged, Hungary. I am grateful for the opportunity to perform the experiments in her laboratory and for her work on the data analysis using the

program PSEQUAD (as detailed in chapter 6.2.). For this purpose UV–Vis spectrophotometric titrations were applied at a concentration of 50  $\mu\text{M}$  (in the presence of 0.5% (v/v) DMSO).

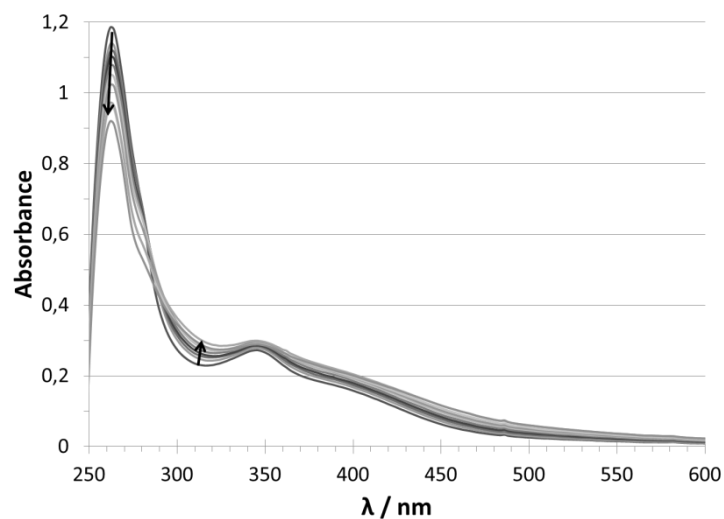


**Figure 32:** Time-dependent UV–Vis spectra of 50  $\mu\text{M}$  solution of **Q-4b** at a pH of 10.63 (measured at  $T = 25.0\text{ }^\circ\text{C}$ ;  $I = 0.20\text{ M KCl}$ ,  $l = 1\text{ cm}$ ).

The studies performed with the aim to characterize the proton dissociation processes of the ligands revealed, that the *in vitro* similarity of compounds **Q-4** and **Q-4b** might be explained by the inherent instability of the latter in solution. Time-dependent UV–Vis spectra, as shown in Figure 32, show a relatively fast decomposition process at alkaline pH. Even though at lower pH values the observed spectral changes were slower, after 24 h of incubation ESI-MS spectra of **Q-4b** solutions at different pH values (2.5, 7.4 and 10.6) suggest a decomposition of **Q-4b** to compound **Q-4** via the opening of the dihydro-[1,3]-oxazine ring. Similar reactions were observed in the literature for other compounds containing the dihydro-[1,3]-oxazine moiety [246].

Therefore, data obtained with **Q-4b** concerning ligand properties and interaction with metal ions might not be reliable due to this decomposition reaction. Opposed to that, spectra recorded with ligands **Q-2**, **Q-3** and **Q-4** at diverse pH values did not show time dependent changes. The deprotonation processes on the contrary, resulted in characteristic spectral



changes, that could be observed in the pH-dependent UV–Vis spectra recorded between pH 2 and 11.5 (representative spectra are shown exemplarily for ligands **Q-2** and **Q-3** in Figure 33).

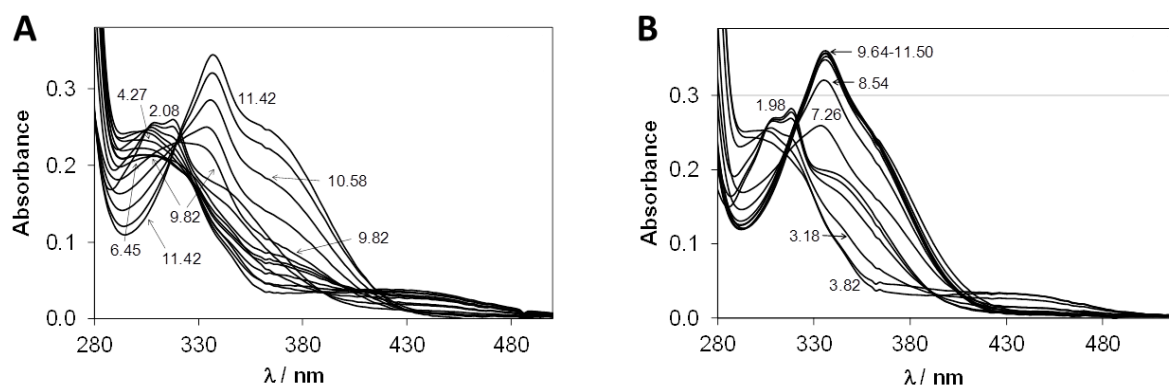


**Figure 33:** UV-Vis absorption spectra of ligands **Q-2** (A) and **Q-3** (B) recorded at different pH values of solutions containing 50  $\mu\text{M}$  of ligand ( $T = 25.0\text{ }^\circ\text{C}$ ;  $I = 0.20\text{ M KCl}$ ;  $l = 2\text{ cm}$ ).

Deconvolution of the measured spectra revealed the molar absorbance spectra of the individual ligand species in the different protonation forms, as shown in Figure 34. On the basis of these data the concentration of the ligand species in the different protonation states could be calculated as a function of pH as shown in Figure 35. The  $\text{p}K_{\text{a}}$  values were assigned to the deprotonation processes as shown in Scheme 4. The newly investigated ligands were compared to the reference compound **Q-1**, for which literature data was available [247]. Based on the obtained and published data the ligand species present at physiological pH could be calculated. While **Q-1** is present as HL only, this is also the predominant species for **Q-2** with 93%. The second species present is the deprotonated  $\text{H}_2\text{L}^+$  (7%). The predominant species for **Q-3** is L (70%), accompanied by  $\text{HL}^+$  (30%). **Q-4** is mainly present as HL (92%), with 8% of  $\text{L}^-$ .

Spectral changes and deprotonation behavior of the newly investigated ligands were compared to those of the reference compound **Q-1** [247]. The process resulting in the most pronounced spectral changes is the deprotonation of the hydroxyl functional group of the 8-hydroxyquinoline moiety. The observed development of new strong bands with higher  $\lambda_{\text{max}}$  values due to the more extended conjugated  $\pi$ -electron system in the deprotonated form is characteristic for this process and has been described for **Q-1** in the literature [247]. Similar changes could be observed also for the 7-substituted 8-hydroxyquinoline derivatives **Q-2**, **Q-3** and **Q-4**. The deprotonation of the other moieties of the studied ligands results in smaller alterations in the spectra.

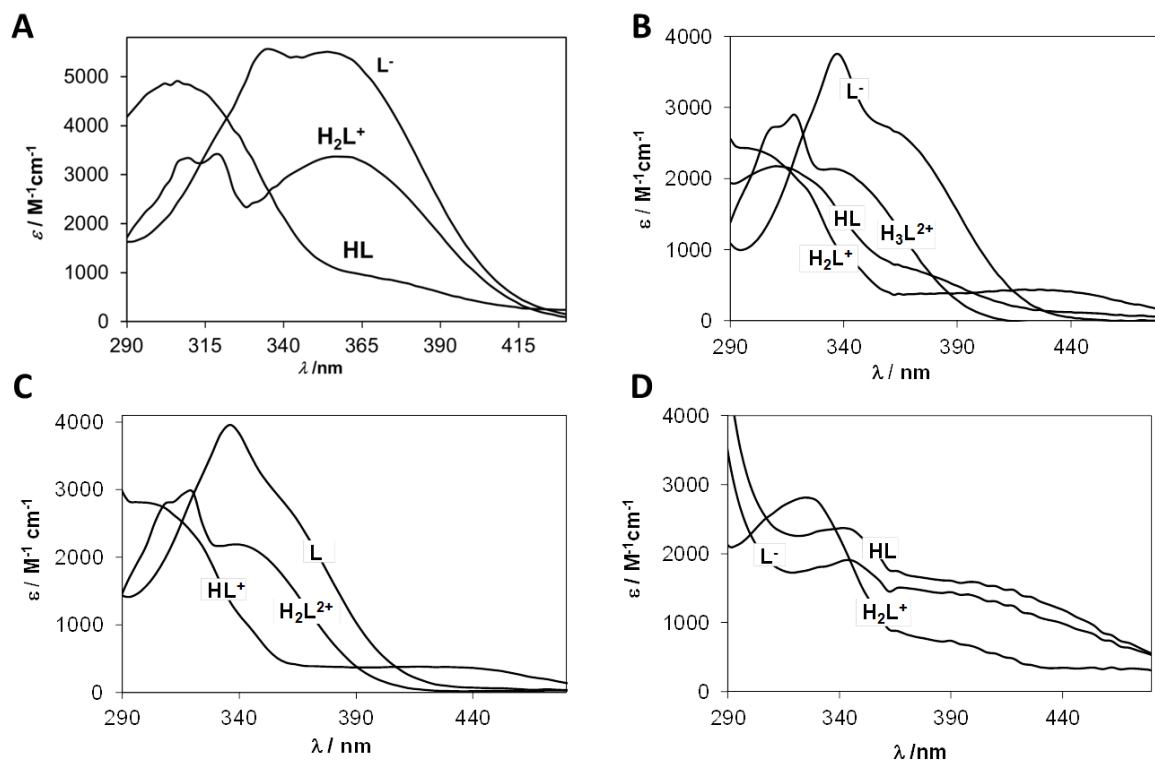


**Figure 34:** Calculated UV-Vis molar absorption spectra of the individual ligand species of ligands **Q-1** (A), **Q-2** (B), **Q-3** (C), **Q-4** (D). Measurements for **Q-2** and **Q-3** were performed with 50  $\mu\text{M}$  solutions, those for **Q-4** were performed with 10  $\mu\text{M}$  solutions, data of **Q-1** (A) are taken for the calculations from reference [247].

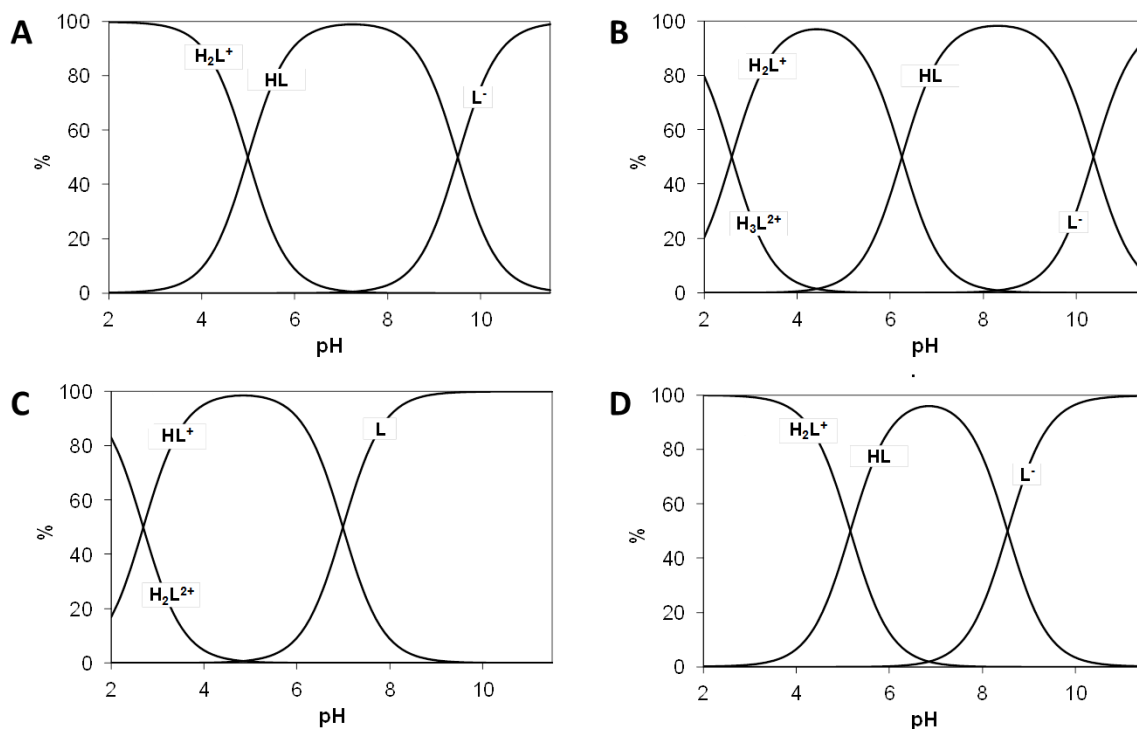
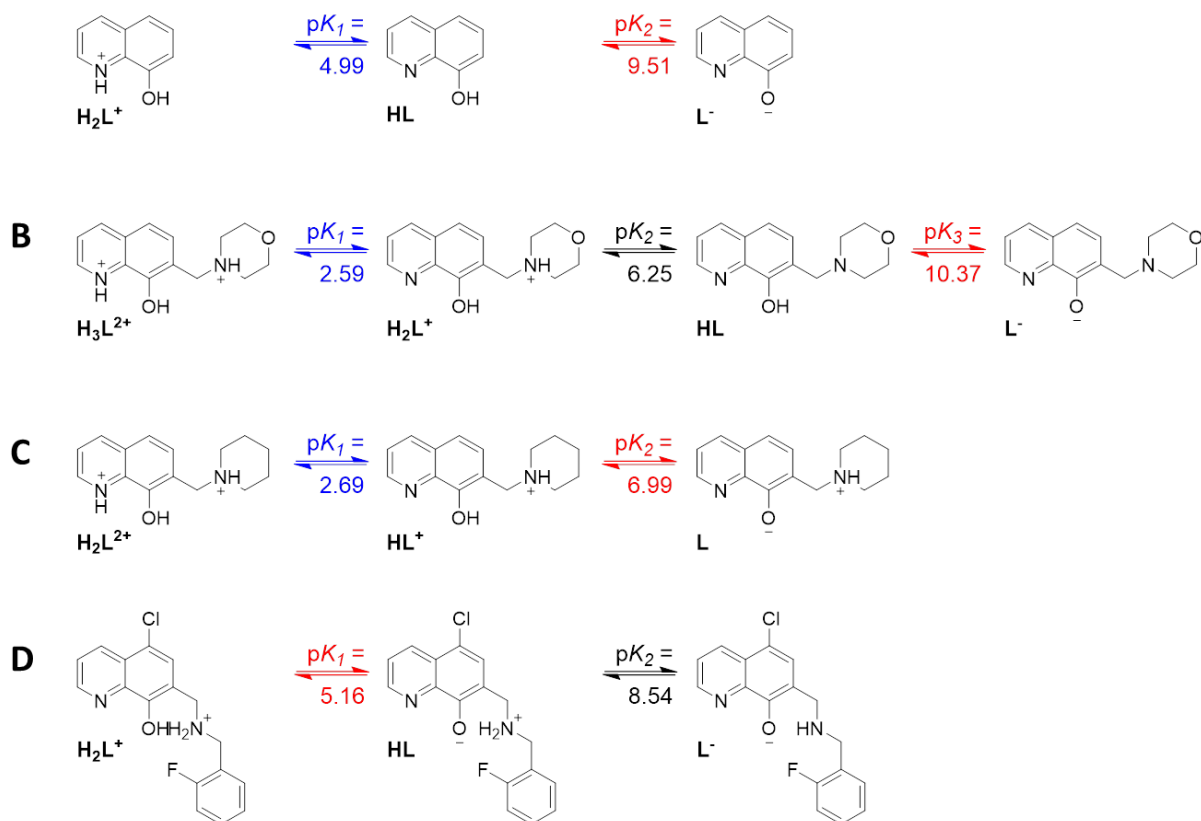


**Figure 35:** Calculated concentration distribution curves of the ligands **Q-1** (A), **Q-2** (B), **Q-3** (C) and **Q-4** (D). Data of **Q-1** are taken for the calculations from reference [247].

As highlighted in red in Scheme 4, the corresponding  $pK_a$  values attributed to the deprotonation of the phenolic OH are  $pK_2$  for **Q-1** [247],  $pK_3$  for **Q-2**,  $pK_2$  for **Q-3** and  $pK_1$  for **Q-4**. In comparison to **Q-1**, the morpholino-substituent in 7-position of **Q-2** increases the  $pK_a$  value of the phenolic-OH functional group by almost one order of magnitude possibly due to the formation of a hydrogen bond between the OH and the morpholine-N in the HL form of the ligand that hinders the deprotonation. In contrast, the protonated (thus positively charged) amine moiety of the piperidine of **Q-3** decreases the proton dissociation constant of the OH group by 2.5 orders of magnitude compared to that of **Q-1**. Lower  $pK_a$  values were also reported for numerous hydroxamic and carboxylic acids due to the electron withdrawing effect of the protonated piperidinium moiety [248]. A hydrogen bond which might form between the phenolate and the piperidinium  $NH^+$  in the L form of **Q-3** can additionally contribute to the diminished  $pK_2$  value due to the stabilization of the conjugated base (L). In **Q-4** the  $pK_a$  value of the phenolic OH is by 4.4 orders of magnitude smaller than in **Q-1**. The two factors contributing to that are the protonated benzylamine moiety, together with the electron withdrawing effect of the chlorine substituent.

As indicated in blue in Scheme 4, the  $pK_1$  values of ligands **Q-1** (reference [247]), **Q-2** and **Q-3** were assigned to the deprotonation of the quinolinium- $NH^+$  moieties of these ligands. Compared to the 8-hydroxyquinoline scaffold **Q-1**, the substitutions in R7 significantly decrease the  $pK_a$  values of the quinoline- $NH^+$  by more than 2 orders of magnitude. This might be explained by the electron withdrawing effect of the methylene linked protonated amine moieties of the Mannich bases. In case of ligand **Q-4** the deprotonation of the quinolinium- $NH^+$  moiety could not be observed in the applied experimental conditions, since it most probably takes place at lower pH values (accordingly, the predicted  $pK_a$  value for the quinolinium- $NH^+$  in **Q-4** using ChemAxon software is 0.98 [36]). Additionally to the protonated benzylamine in R7, the Chloro substituent in *para* position to the hydroxyl group causes this significant decrease in the  $pK_a$  value due to the negative inductive effect of the halogen atom. Consequently,  $pK_1$  of ligand **Q-4** was attributed to the deprotonation of the OH group, while  $pK_2$  to the secondary amine.



**Scheme 4:** Proton dissociation constants ( $pK_a$ ) of the studied ligands in comparison to published data for **Q-1** (panel A, reference [247]).  $pK_a$  values describing the deprotonation of the quinoline nitrogen are highlighted in blue, those of the hydroxyl group in red. Values for **Q-2** (panel B), **Q-3** (panel C) and **Q-4** (panel D) were obtained from the data of the UV–Vis spectrophotometric titrations.

As apparent from the structures of ligands **Q-2**, **Q-3** and **Q-4**, the different substituents on the 8-hydroxyquinoline scaffold do not only affect the  $pK_a$  values of the phenolic-OH and quinolinium-NH<sup>+</sup> moieties, but also result in additional proton dissociation processes (Scheme 4 B-D). These additional processes could be observed in case of **Q-2** ( $pK_2$ ) and **Q-4** ( $pK_2$ ). In contrast, the deprotonation of the piperidinium-NH<sup>+</sup> of **Q-3** could not be detected in the studied pH range, as its  $pK_a$  value is probably higher than 11.5.

As summarized in Table 12, the experimental results are (more or less) in agreement with calculations performed with ChemAxon software [36]. The calculated values confirm the order of deprotonation processes concluded from the measurements.

**Table 12:** Comparison of experimentally determined and calculated values. Calculations were done with ChemAxon software [36]. <sup>a</sup> experimental data for compound **Q-1** was taken from reference [247], the pK value indicated with <sup>b</sup> characterizes the deprotonation process of Mannich base related nitrogen. Values indicated with <sup>c</sup> could not be measured within the applied experimental setup.

	pK <sub>1</sub>	pK <sub>2</sub>	pK <sub>3</sub>	pK <sub>1</sub>	pK <sub>2</sub>	pK <sub>3</sub>
	-	-	-	-	-	-
	measured	measured	measured	calculated	calculated	calculated
<b>Q-1</b>	4.99 <sup>a</sup>	9.51 <sup>a</sup>		3.93	9.36	
<b>Q-2</b>	2.59	6.25 <sup>b</sup>	10.37	2.29	7.21 <sup>b</sup>	8.25
<b>Q-3</b>	2.69	6.99	> 11 <sup>b,c</sup>	2.28	7.45	10.20 <sup>b</sup>
<b>Q-4</b>	< 2 <sup>c</sup>	5.16	8.54 <sup>b</sup>	0.91	7.14	9.22 <sup>b</sup>

In order to investigate whether the pK<sub>a</sub> values might affect the (MDR selective) cytotoxicity, correlation diagrams are shown in Figure 36. In the investigated compound set, compounds with a lower pK<sub>a</sub> value of the phenolic OH tend to show an increased toxicity in P-gp expressing MES-SA/Dx5 cells, while the effect on the parental MES-SA cell line is minor. This suggests, that there might be a tendency in affecting the selective toxicity of the 8-hydroxyquinoline derived ligands. Yet, the size of the investigated data set does not allow a general conclusion about the multifactorial correlation between chemical properties and the biological effect. Between the biodata and pK<sub>a</sub> values of the quinolinium NH<sup>+</sup> moieties of these ligands no clear relationship was found.

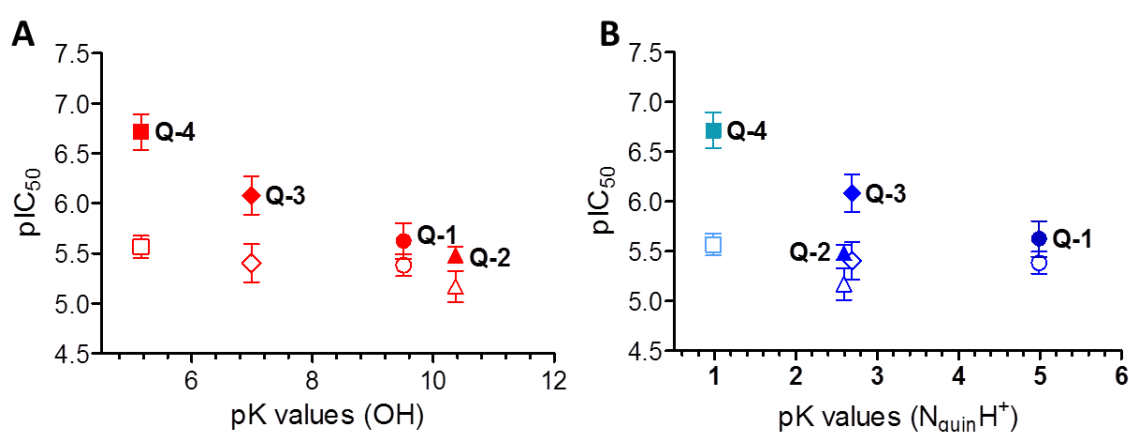


**Figure 36:** pIC<sub>50</sub> values obtained in MES-SA (open symbols) and MES-SA/Dx5 cells (filled symbols) as a function of experimentally determined phenolic-pK<sub>a</sub> (A), or quinolinium-pK<sub>a</sub> (B). Circles: **Q-1**, triangles: **Q-2**, diamonds: **Q-3**, squares: **Q-4**. Since the quinolinium-pK<sub>a</sub> for **Q-4** could not be determined in the applied measurement conditions, the calculated value (Table 12) was plotted instead.

### 3.4. Elucidation of putative mechanism(s) of action

#### 3.4.1. Impact of ROS

Since the ligands might form redox active metal complexes inside the cells, the involvement of reactive oxygen species (ROS) resulting from redox cycling of these complexes (see chapters 1.5 and 1.6), might be involved in the toxicity mechanism of the 8-hydroxyquinoline derivatives. In order to test this hypothesis, the cytotoxicity experiments were repeated in presence of the ROS-scavenger and potent antioxidant *N*-acetylcysteine (NAC). As shown in Figure 37, a different behavior could be observed for the non-MDR selective **Q-1**, the “weakly MDR selective” agent **Q-2**, and the MDR selective compounds **Q-3** and **Q-4**.

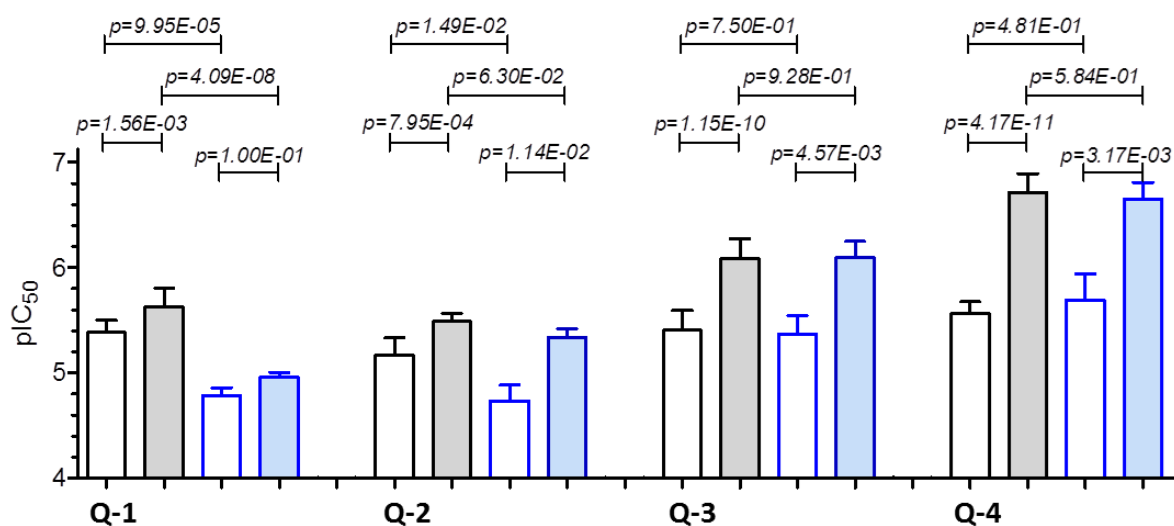


**Figure 37:** Effect of the ROS scavenger NAC on the toxicity of the 8-hydroxyquinoline derived ligands. pIC<sub>50</sub> values obtained in MES-SA (open columns) and MES-SA/Dx5 (filled columns) cells are shown in absence (black) and presence (blue) of 5 mM NAC. Significance was calculated using paired t-tests in the comparison of MES-SA and MES-SA/Dx5 cells treated in the same experiment and unpaired t-tests for the comparison of co-incubation experiments that have partly been performed in independent experiments.

In case of the non-MDR selective **Q-1** core structure, NAC protects both, the P-gp negative cell line MES-SA and the P-gp positive MES-SA/Dx5 cell line from the toxic effect of the ligand. In case of the “borderline MDR selective” agent **Q-2**, a protective effect of NAC could only be observed for the P-gp negative MES-SA cells, while there was no significant effect on MES-SA/Dx5 cells. On the contrary, the toxicity of the MDR selective compounds **Q-3** and **Q-4** is not significantly influenced by NAC in either of the investigated cell lines.

These results indicate that the production of ROS by the ligands or by putatively formed metal complexes might play a role in the toxicity of **Q-1** and **Q-2**. The lack of protective effect of NAC on the toxicity of the MDR selective agents, as compared to their structurally closely related derivatives, might be suggestive of a different mechanism of action, which might be connected to the complex interplay with the intracellular redox homeostasis.

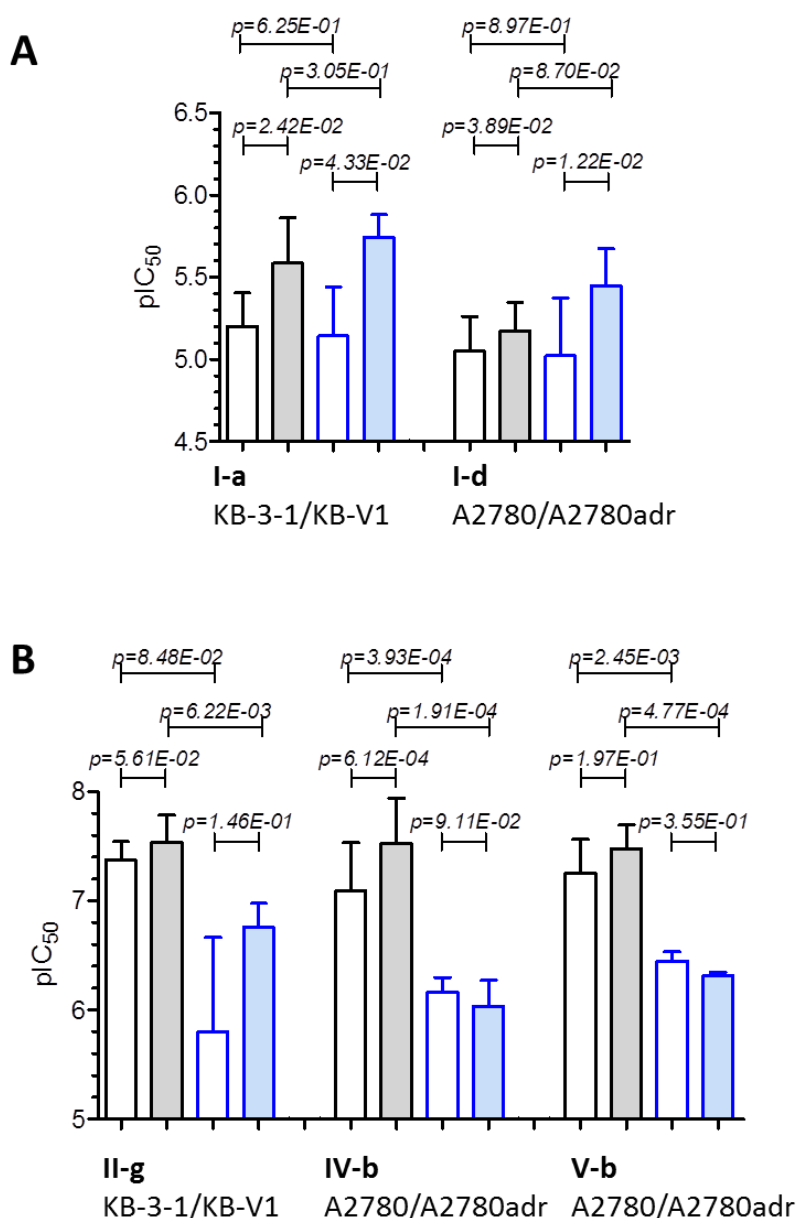


**Figure 38:** Effect of the ROS scavenger NAC on the toxicity of selected MDR selective thiosemicarbazones **I-a** and **I-d** (**A**) and cell line dependently selective compounds **II-g**, **IV-b**, **V-b** (**B**).  $pIC_{50}$  values obtained in parental (open columns) and MDR (filled columns) cells are shown in absence (black) and presence (blue) of 5 mM NAC. The cellular test system is indicated below the bar diagram. Significance was calculated as in 37.

For comparison, compounds from the focused designed library (chapters 3.2.1. – 3.2.5.) were co-administered to cells with NAC. As shown in Figure 38, comparably to the effect of the MDR selective 8-hydroxyquinoline Mannich bases **Q-3** and **Q-4**, also the toxicity of the MDR selective isatin- $\beta$ -thiosemicarbazones **I-a** and **I-d** was not affected by the ROS-scavenger. In contrast, compounds that showed an increased toxicity toward single MDR cell lines in a P-gp independent manner behaved differently. The toxicity of the pyridinyl thiosemicarbazone **II-g**, the pyrimidinyl hydrazone **IV-b**, and the hydrazino benzothiazole **V-b** was attenuated in the presence of NAC. Despite the parallel that can be drawn to the non-MDR selective **Q-1**, in contrast to the effect on the 8-hydroxyquinoline scaffold, the (relative) protective effect of the antioxidant against **IV-b** is more pronounced in the drug resistant cells as compared to their sensitive counterparts.

### **3.4.2. Impact of metals – co-incubation with $FeCl_3$ and $CuCl_2$**

Since the formation of redox active metal complexes might be a source of ROS, the biological activity of metal binding compounds is often modified upon complex formation with metal ions [87,129]. Therefore in the next step the toxicity of the ligands was compared in the absence and in the presence of increasing iron (III) and copper (II) concentrations (0.5  $\mu$ M, 5.0  $\mu$ M, 50  $\mu$ M). The metal salts alone did not influence the cell viability within the timeframe of the assay, indicating that the observed effects are not additive.

Iron (III) co-incubation did not influence the toxicity of the 8-hydroxyquinoline core structure **Q-1** (Figure 39 A). In contrast, for the weakly MDR selective agent **Q-2** in the presence of 50  $\mu$ M  $FeCl_3$  a significant protective effect could be observed for the MDR cell line MES-SA/Dx5, while the P-gp negative parental cell line MES-SA was not affected (Figure 39 B). In sharp contrast, both cell lines were significantly protected from the toxic effect of the two MDR selective derivatives **Q-3** and **Q-4** in the presence of 5 and 50  $\mu$ M  $FeCl_3$  (Figure 39 C,D). Though, the magnitude of this effect is much higher in the P-gp positive MES-SA/Dx5 cell line, resulting in a decrease of selective toxicity of the ligands in the presence of  $FeCl_3$ .

Contrary to these results, the rescuing effect of  $FeCl_3$  was more pronounced in MES-SA as compared to MES-SA/Dx5 cells in case of the P-gp independently MDR selective pyrimidinylhydrazone **IV-b**, resulting in an enhanced selectivity in the presence of iron (Figure 39 E).



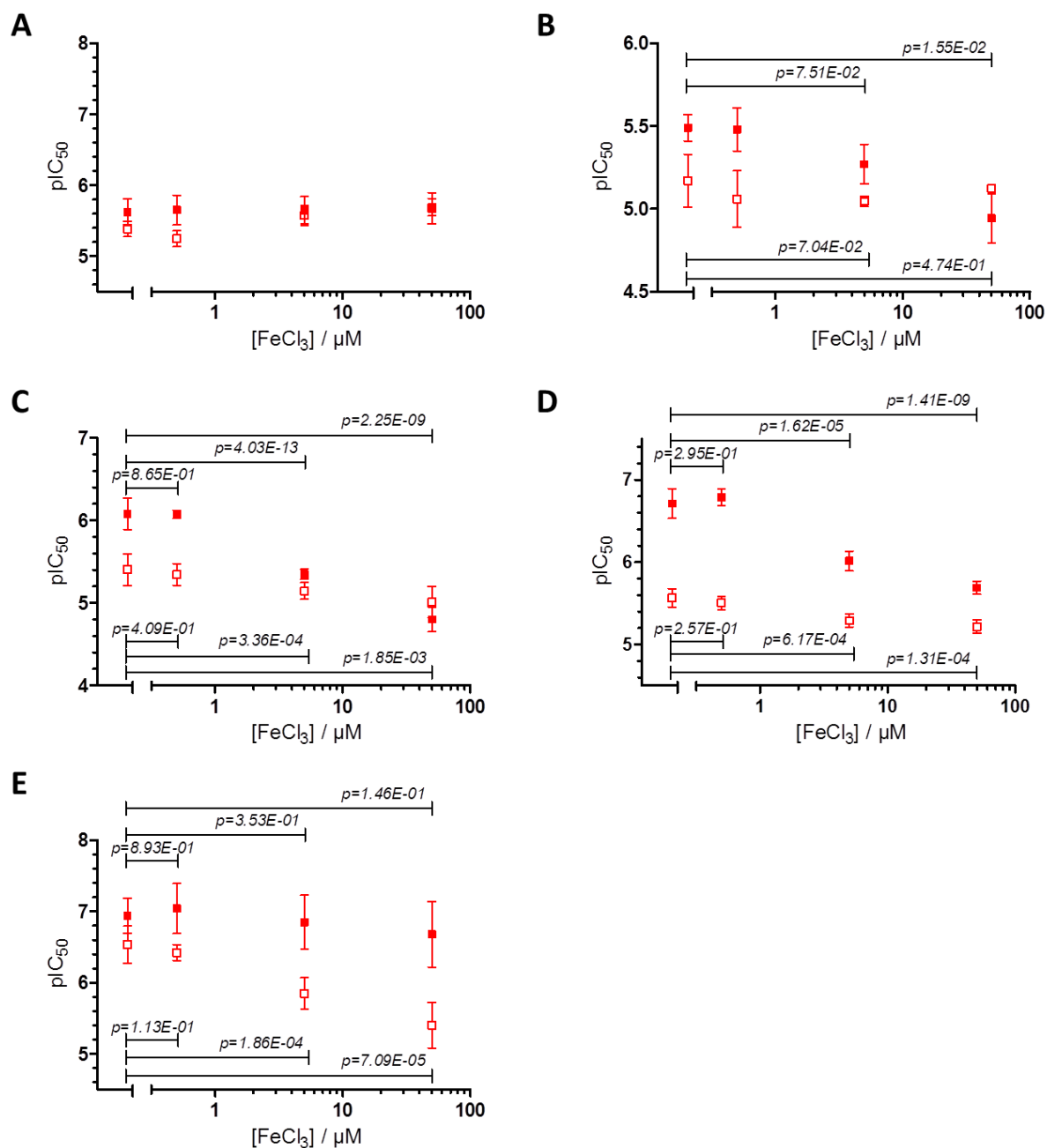


**Figure 39:** Effect of increasing concentrations of FeCl<sub>3</sub> on toxicity of the 8-hydroxyquinoline derivatives **Q-1** (A), **Q-2** (B), **Q-3** (C) and **Q-4** (D) in comparison to the arylhydrazone **IV-b** (E). pIC<sub>50</sub> values of the ligands were obtained by the MTT assay after 72 h incubation of MES-SA (open squares) and MES-SA/Dx5 (filled squares) cells with the compounds in absence or presence of constant metal ion concentrations. Data represent mean and standard deviation obtained in at least three independent experiments. Significant differences between results in presence and absence of metal ion were calculated with unpaired t-test.

A rescuing effect of iron co-administration might imply an influence of iron depletion in the toxicity mechanism of the applied chelators. Another conceivable explanation might be that the added excess of iron (III) prevents the binding of the chelators to either the target or to

other metal ions (like copper) and therefore leads to protection of the cells. The different response of P-gp positive and negative cells to this effect, as observed for the MDR selective ligands **Q-3** and **Q-4**, supports the hypothesis of an altered metal homeostasis in MDR vs. sensitive cancer cells [42,89].

The presence of copper (II) increased the toxicity of ligands **Q-1** and **Q-2** in a dose dependent manner (Figure 40 A,B). A similar effect could be observed for the pyrimidinyldiazone **IV-b** (Figure 40 E). In contrast, P-gp positive MES-SA/Dx5 cells seem unresponsive to copper (II) co-administration to the MDR selective ligands **Q-3** and **Q-4**. Yet, in the parental MES-SA cell line an increase in toxicity could be observed upon copper (II) co-administration (Figure 40 C,D). It is worth mentioning, that the sensitizing effect starts at higher metal ion concentrations as compared to the non-MDR selective ligands **Q-1**, **Q-2** and **IV-b**, and that it is more pronounced for the ligand with the higher selectivity ratio (**Q-4**). Due to the difference in the response of MES-SA and MES-SA/Dx5 cells toward the co-administration of copper, the selectivity in the toxic effect toward P-gp expressing cells vanishes upon metal co-administration in case of the MDR selective ligands **Q-3** and **Q-4**.

The increase in toxicity caused by copper, as observed in both cell lines for **Q-1**, **Q-2** (and **IV-b**), as well as in MES-SA cells for **Q-3** and **Q-4** might be explained by the formation of redox active copper complexes. In an “activation by reduction” mechanism, following Fenton-like chemistry, these complexes can produce harmful reactive oxygen species (ROS) – in particular the hydroxyl-radical – which might lead to cell death [86,89,116,135].

The lack of response on copper co-administration in the P-gp positive MES-SA/Dx5 cells might be explained by several factors. Similar to the different response of the investigated P-gp positive and negative cells to the co-administration of iron (III), also the effect induced by copper (II), might point to an altered metal homeostasis in MDR vs. sensitive cancer cells [4,8]. Since the metal homeostasis is tightly connected to intracellular redox homeostasis, also an altered redox state of the cells might possibly be involved in the mechanism of (MDR selective) toxicity [88,89,116].

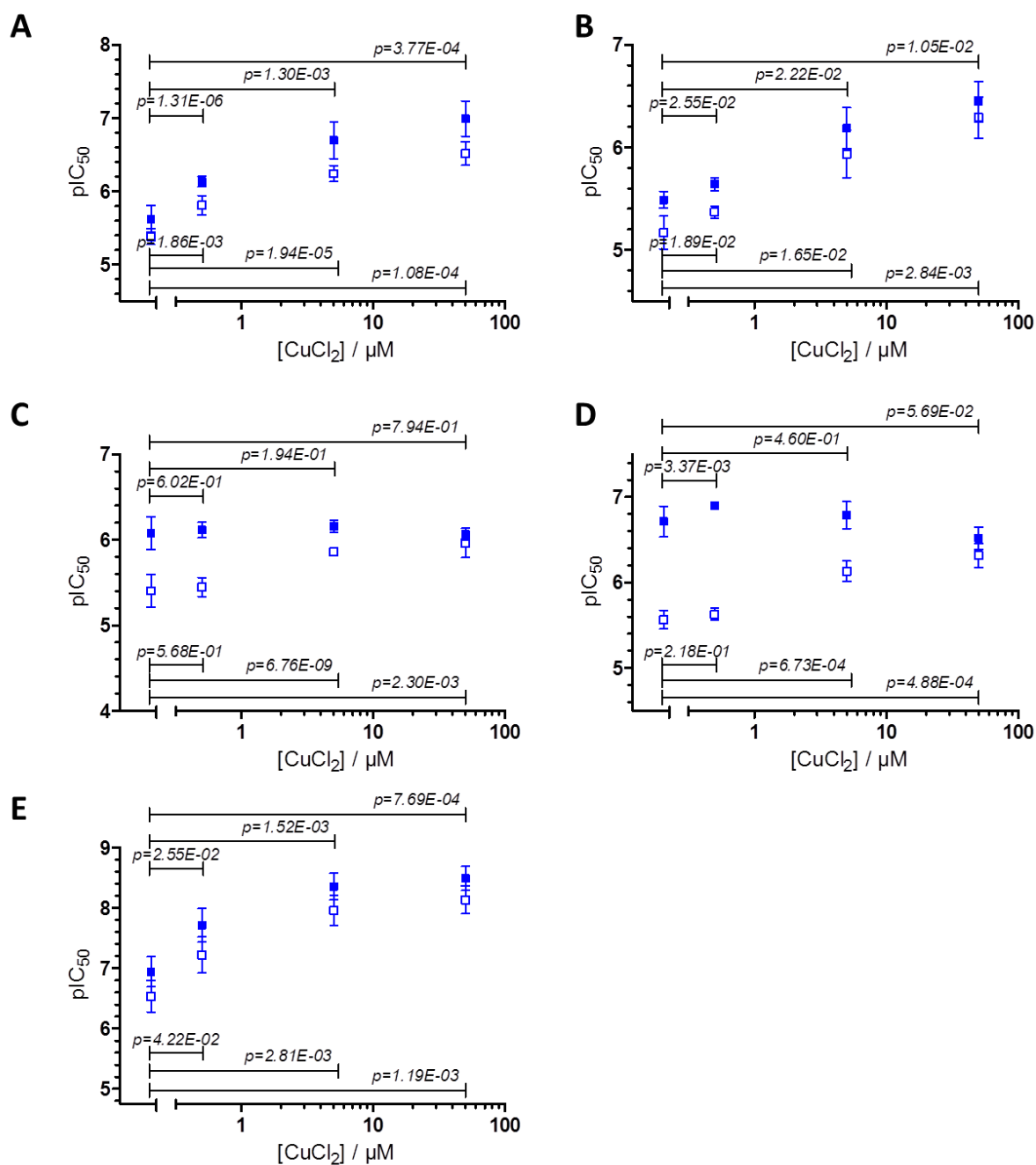


**Figure 40:** Effect of increasing concentrations of  $\text{CuCl}_2$  on toxicity of the 8-hydroxyquinoline derivatives **Q-1** (A), **Q-2** (B), **Q-3** (C) and **Q-4** (D) in comparison to the arylhydrazone **IV-b** (E).  $\text{pIC}_{50}$  values of the ligands were measured by the MTT assay after 72 h incubation of MES-SA (open squares) and MES-SA/Dx5 (filled squares) cells with the compounds in absence or presence of constant metal ion concentrations. Data represent mean and standard deviation obtained in at least three independent experiments. Significant differences between results in presence and absence of metal ion were calculated with unpaired t-test.

### 3.4.3. Investigation of Fe(III) and Cu(II) complexes – stabilities and stoichiometries

Characterization of the ligands' metal binding ability, and the most plausible chemical species formed in aqueous solution in the biologically relevant pH range might give further insight into the mechanism of action of metal binding compounds [89]. Therefore the stoichiometry and stability constants of the complexes of the ligands **Q-2**, **Q-3** and **Q-4** in the presence of iron (III) and copper (II) were determined by means of UV–Vis spectrophotometry. These studies were performed in collaboration with *Prof. Éva A. Enyedy* from the Institute of Inorganic and Analytical Chemistry, University of Szeged, Hungary. The solution speciation data were furthermore compared to those of the reference compound **Q-1** [249,250]. The complex formation processes could be followed by the characteristic changes of charge transfer (CT) bands, which are partially overlapping with the ligands' bands. In case of iron (III), additional changes of the d-d bands could be monitored. In case of copper (II) the d-d bands could not be detected under the applied conditions due to their fairly low molar absorptivities.

In the spectra obtained during titrations with both metal ions the absorbance values tend to decrease at  $\text{pH} > \sim 8$ . In case of the iron (III) complexes the hydrolysis of the metal ion, which might occur at alkaline pH values, might suppress the complex formation. Compared to the titrations in the presence of iron (III), the decrease in absorbance seems to be even more pronounced in the case of the copper (II) complexes. This might be explained by a precipitation of the formed neutral complexes, which also becomes visible in form of yellow precipitates at  $\text{pH} > \sim 9$ . Thus, only data collected at  $\text{pH} < 8$  were evaluated in all cases.

In the case of the iron (III) complexes the spectral changes upon complexation detected in the 350-750 nm wavelength range were most useful for the calculations since bands located in this range are relatively well-separated from the ligands' bands. Representative spectra are shown for the ligands **Q-2** (Figure 41 A) and **Q-3** (Figure 41 B) in the presence of 0.33 equivalents of iron (III). The arrow indicates the shift of the peak maxima  $\lambda_{\text{max}}$  upon alkalization of the solution. Molar absorbance spectra were computed by the deconvolution of UV-Vis spectra recorded at different pH values and revealed that the shift in absorbance maxima is indicative for the consecutive coordination of the ligands to the metal ion. The coordination sphere of iron (III) is octahedral, therefore with the ( $\text{N}_{\text{quinoline}}, \text{O}$ ) bidentate 8-hydroxyquinoline derivatives the formation of mono-, bis- and tris-ligand complexes is expected [251]. A shift in  $\lambda_{\text{max}}$  values upon filling of the metal coordination-sphere, as indicated by the arrows in Figure 41, has also been reported for the complexes of **Q-1** [250].

The stability data resulting from the deconvolution of the spectra are summarized in comparison to the previously reported data on the **Q-1** core structure in Table 13 [250].

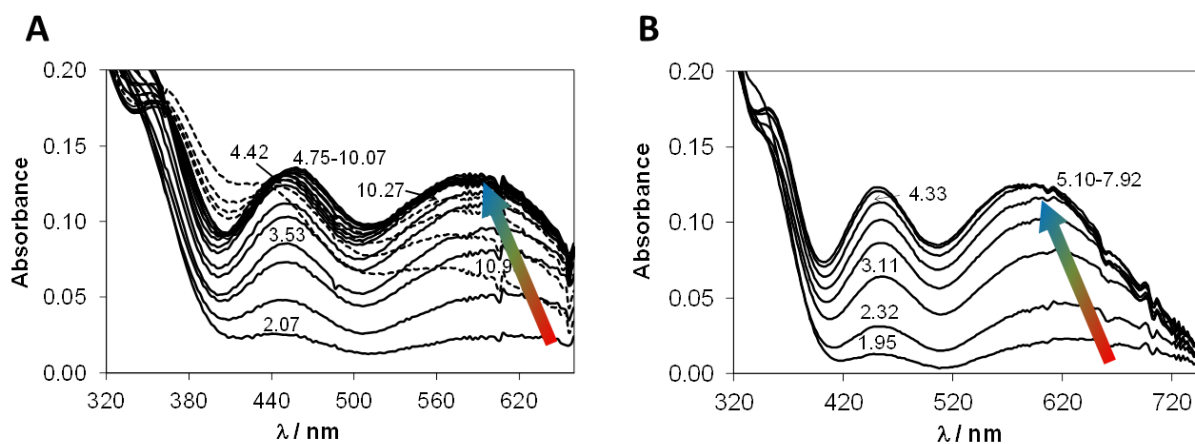


**Figure 41:** Recorded spectra at different pH values for samples in iron (III) to ligand ratio 1:3 for **Q-2** (A) and **Q-3** (B). The arrow indicates a shift in the absorbance maxima upon alkalinization of the solution. Dotted spectra at high pH values were excluded from calculations (see text for details).

Based on the determined stability constants (Table 13), concentration distribution curves of the species formed with the ligands **Q-1** to **Q-4** in the presence of given concentrations of metal ions could be calculated as functions of pH or ligand concentration. These calculations disclosed the species that are likely present at physiological pH (7.4) at the respective  $IC_{50}$  values obtained in the experiments presented in chapter 3.4.2. (Figures 39, 42).

While at low metal ion concentrations (0.5  $\mu$ M), the major fraction of the investigated ligands is not bound to metal ions, at higher metal concentrations, the ligands are incorporated to metal complexes. Similarly to **Q-1**, the predominant species of **Q-2** is the tris-ligand complex  $[FeL_3]$ . While **Q-1** also forms small fractions of bis complex  $[FeL_2]$ , in case of **Q-2** the protonated tris complex  $[FeL_3H]$  is present in small fractions. Presumably, the proton can be attributed to the non-coordinating tertiary amine of the morpholinium moiety. In contrast, the presence of the bis complex is more pronounced in the case of **Q-3** (accompanied by a small fraction of tris complex). Complexation of iron by **Q-4** results mainly in mono complex  $[FeL]$ , accompanied by the protonated bis complex  $[FeL_2H]$ . Similar to the protonated complex of **Q-2**, the protonation is most likely to be found at the secondary amine, which is not taking part in the coordination of the metal ion. The predominance of the mono complex might be explained by the sterical hindrance caused by the aromatic moiety.

Predominant species are comparable at the  $IC_{50}$  values measured against MES-SA and MES-SA/Dx5 cells in general. Though, a difference can be observed in case of the complexes formed by ligand **Q-4** at the respective  $IC_{50}$  values in the presence of  $0.5 \mu\text{M}$  iron (III). While at the  $IC_{50}$  value in MES-SA cells, around 70 % of the ligand is free, at the  $IC_{50}$  value in MES-SA/Dx5, 90 % of the ligand is incorporated into metal complexes (mainly  $[\text{FeL}]$ ).

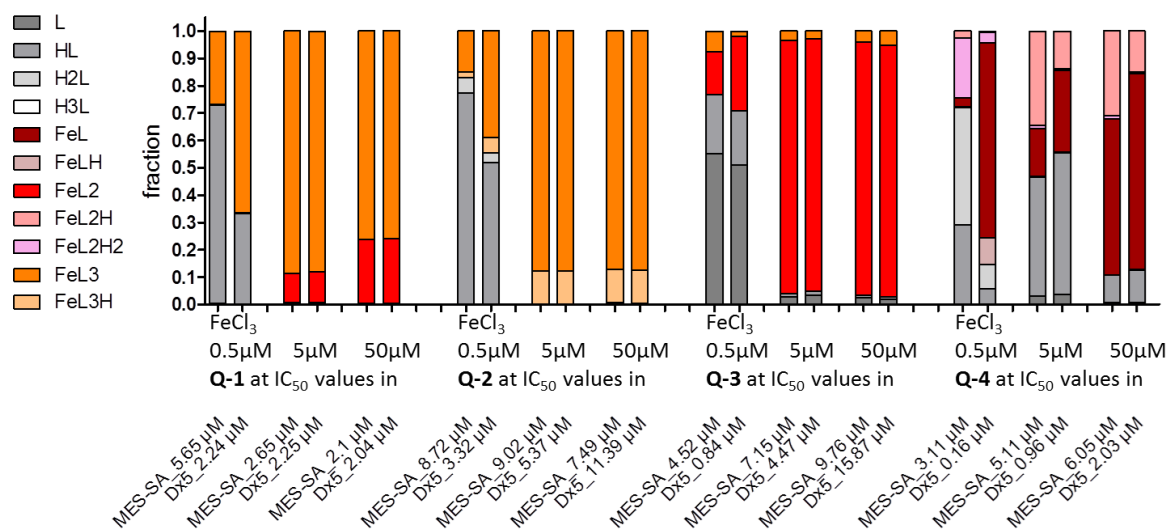


**Figure 42:** Calculated distribution of ligand fractions in the species formed at pH 7.4 at the ligand- $IC_{50}$  values in MES-SA and MES-SA/Dx5 upon co-incubation with 0.5, 5, or 50  $\mu\text{M}$   $\text{FeCl}_3$  (experiments from Figure 39). The color code of the single species is given on the left side, charges are omitted for clarity.

In order to compare the metal binding ability of the four investigated chelators, the  $pM$  values, representing the negative decadic logarithm of the free metal ion concentration found at physiological pH (at  $c_M = 1 \mu\text{M}$ ;  $c_L/c_M = 10$ ), were computed using the experimentally determined stability constants. Higher  $pM$  values indicate a more favored complex formation. Since iron(III) tends to hydrolyze at physiological pH, its hydroxido species were also taken into account ( $pM^* = -\log ([\text{Fe}] + \Sigma[\text{Fe}_i(\text{OH})_i])$ ), providing data that are comparable to those of other metal ions. As summarized in Table 13, according to both  $pM$  and  $pM^*$  values, the iron binding effectivity of the investigated ligands at pH 7.4 follows the order **Q-1**  $\approx$  **Q-2** > **Q-3** > **Q-4**. This reflects the inverse order of selectivity in the toxicity of the ligands toward MES-SA/Dx5 vs. MES-SA cells. Figure 43 shows the cytotoxicity of the ligands toward both

cell lines and the selectivity ratios as a function the  $p(\text{Fe})^*$  values reflecting complex stabilities at pH 7.4.

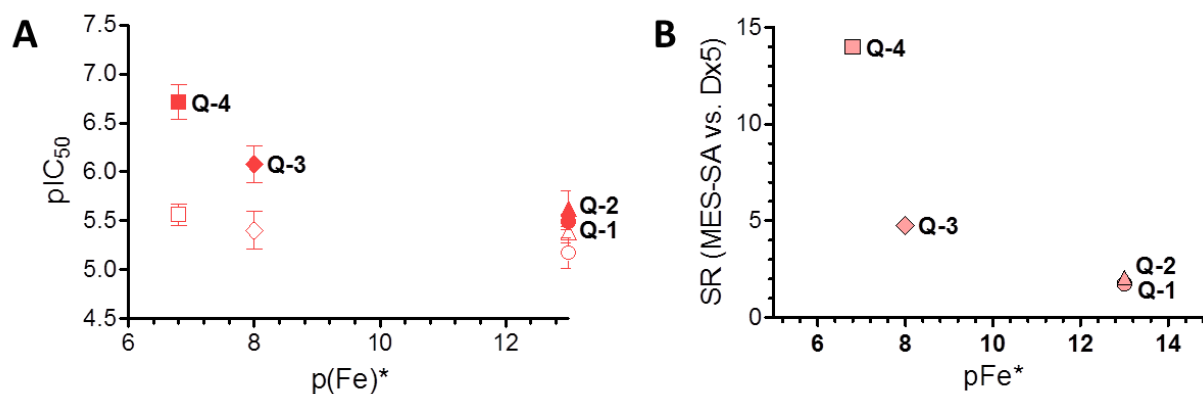


**Figure 43:** Impact of iron (III) binding capacity of the ligands (expressed as  $p(\text{Fe})^*$ ) on their cytotoxicity (expressed as  $pIC_{50}$ ) in MES-SA (open symbols) and MES-SA/Dx5 (filled symbols) cells (A) and on the selectivity ratio (SR) between the investigated cell lines (B). Results of the different ligands are depicted as circles for Q-1, triangles for Q-2, diamonds for Q-3 and squares for Q-4.

In the investigated compound set, toxicity toward MES-SA/Dx5 cells and accordingly also MDR-selectivity seem to increase with decreasing iron (III) complex stability.

The complex stabilities and stoichiometries were also investigated for complexes formed with copper (II). Novel (CT) bands with higher wavelength maxima relative to the spectra of the ligands also appeared in the UV-Vis spectra recorded in the presence of the metal ion (Figure 44). While the consecutive coordination of iron (III) resulted in a decrease in  $\lambda_{\text{max}}$  values (Figure 41), the bis-ligand copper (II) complexes, which form upon alkalization of the sample, possess somewhat higher  $\lambda_{\text{max}}$  values compared to those of the mono species, as indicated by the arrow in Figure 44.

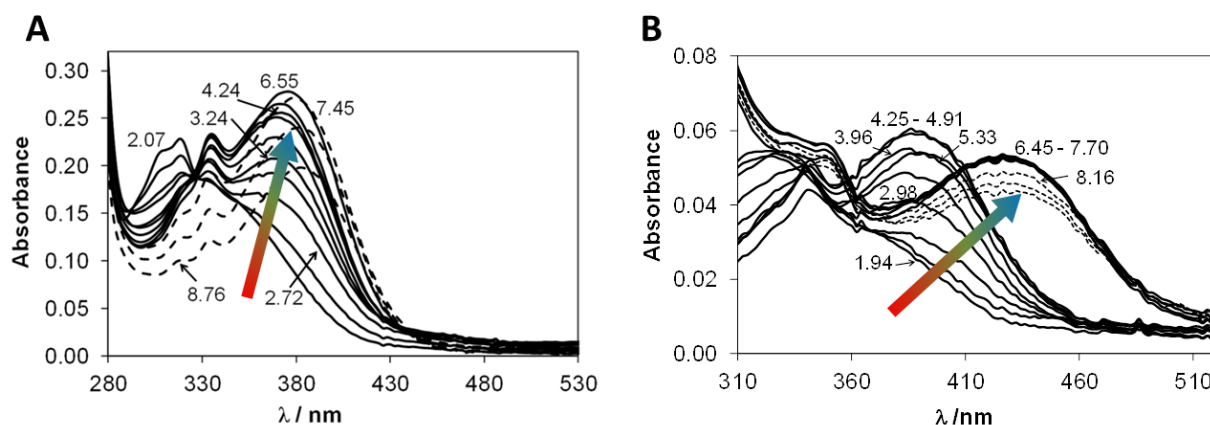


**Figure 44:** Recorded spectra at different pH values for samples in the copper to ligand ratio 1:2 for **Q-2** (A) and **Q-4** (B). The arrow indicates a shift in the absorbance maxima upon alkalization of the solution.

For **Q-1** the formation of square planar bis complexes via a ( $N_{\text{quinoline}}, O^-$ ) bidentate coordination mode has been reported [252]. In agreement with this report, distribution curves, calculated on the basis of the determined stability data, suggest a favored formation of bis complexes (and protonated) bis complexes for the ligands **Q-1** to **Q-4** under conditions of ligand excess in solution (predominant species at physiological pH are  $[CuL_2]$  for **Q-1**,  $[CuL_2]$  and  $[CuL_2H]^+$  for **Q-2**,  $[CuL_2]^{2+}$  for **Q-3** and  $[CuL_2H]^{2+}$  for **Q-4**). In the protonated complexes, the protons can presumably be attributed to the non-coordinating amine. On the contrary, calculations performed to disclose the species, present at the  $IC_{50}$  values obtained in the co-incubation experiments presented in chapter 3.4.2. (Figure 40) are shown in Figure 45. These data reveal that in the presence of 5 and 50  $\mu M$   $CuCl_2$ , where toxicity was significantly increased in a cell line dependent manner, the only species present at the concentration of the  $IC_{50}$  values is  $[CuL]$  (for all ligands - regardless of the cell line).



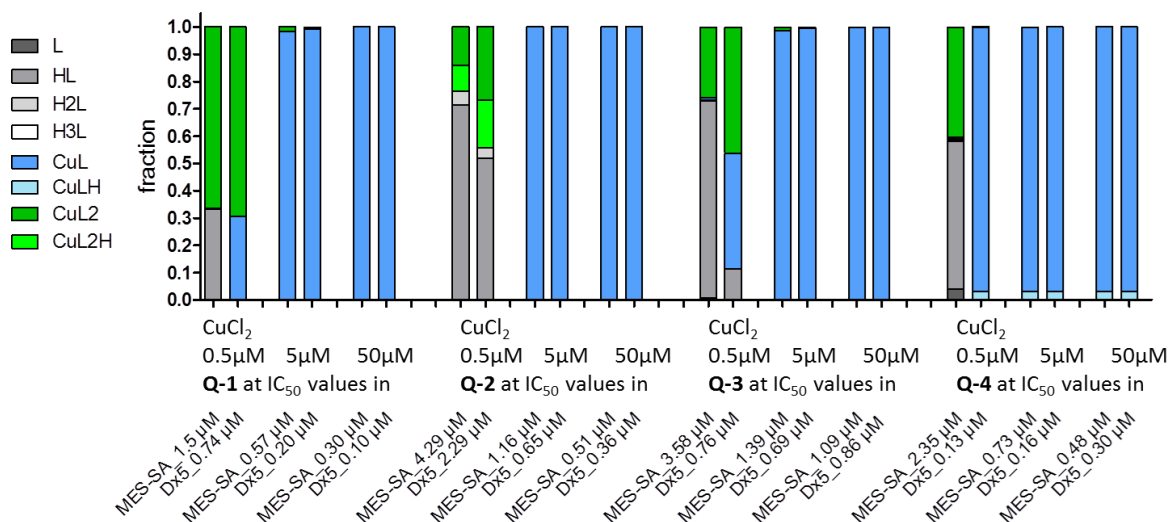


**Figure 45:** Calculated distribution of ligand fractions in the species formed at pH 7.4 at the ligand- $IC_{50}$  values in MES-SA and MES-SA/Dx5 upon co-incubation with  $CuCl_2$  (experiments from Figure 40). The color code of the single species is given on the left side, charges are omitted for clarity.

Comparably to the calculations done for iron (III), also for copper (II) co-incubation with a concentration of  $0.5 \mu M$  a clear difference can be seen for the predominant species formed at the  $IC_{50}$  values of **Q-4** in the different cell lines. While at the  $IC_{50}$  value in the MDR MES-SA/Dx5 cells the predominant species is still the  $[CuL]$  complex, at the  $IC_{50}$  value of the parental cell line most of the ligand is unbound, while approximately 40% are incorporated in the  $[CuL_2]$  complex. Also in case of **Q-3** a difference in species formed at the respective  $IC_{50}$  could be observed: Similar to **Q-4** also here  $[CuL]$  is present at the  $IC_{50}$  value in the resistant cell line, but not at the  $IC_{50}$  value of the parental counterpart. Even though in a smaller fraction, this can also be observed in case of the non MDR selective ligand **Q-1**.

In order to compare the copper (II) binding ability between the investigated ligands and to the previously described iron (III) binding ability, pM values were also computed for the copper (II) systems based on the experimentally determined stability constants. The relative copper (II) chelating ability of the ligands at physiological pH follows the order **Q-2** > **Q-1** > **Q-3** > **Q-4** (Table 13). Compared to the iron binding abilities, the order is similar, with the exception, that for iron (III) binding **Q-2** and **Q-1** were equally potent. Like in case of iron (III), the biological data can be correlated with the p(Cu) values, revealing a higher toxicity and selectivity for ligands with lower p(Cu) values (Figure 46).

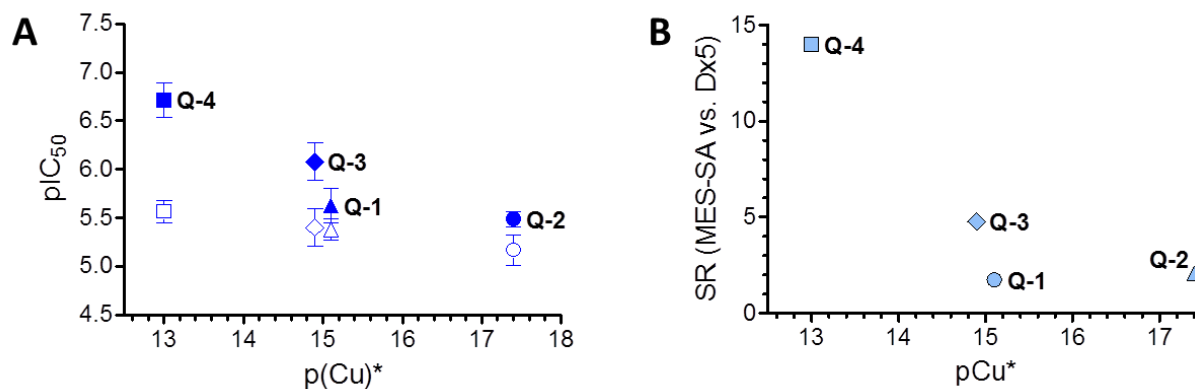


**Figure 46:** Impact of copper (II) binding capacity of the ligands (expressed as  $p(\text{Cu})^*$ ) on their cytotoxicity (expressed as  $p\text{IC}_{50}$ ) in MES-SA (open symbols) and MES-SA/Dx5 (filled symbols) cells (A) and on the selectivity ratio (SR) between the investigated cell lines (B). Results of the different ligands are depicted as circles for Q-1, triangles for Q-2, diamonds for Q-3 and squares for Q-4.

Comparing the binding abilities of the ligands toward the two investigated metal ions, the higher  $p(\text{Cu})$  values over the  $p(\text{Fe})^*$  values indicate a preference of the ligands for copper(II) binding over the complexation with iron(III) at pH 7.4. Interestingly, this preference is much more pronounced in case of the MDR selective ligands Q-3 and Q-4 as compared to the non-MDR selective derivatives Q-1 and Q-2 (Figure 47).

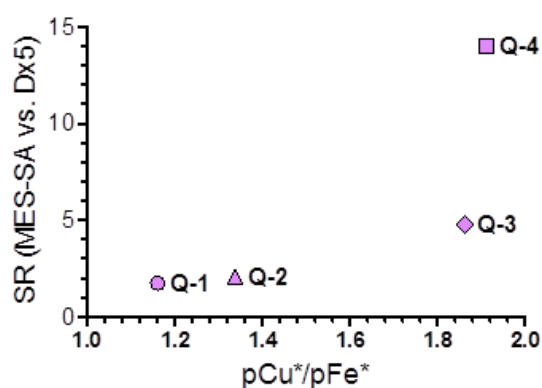


**Figure 47:** Selectivity ratio (SR) between MES-SA and MES-SA/Dx5 cells as a function of preferential binding toward copper over iron (expressed as the fraction of  $p\text{M}^*$  values). Results of the different ligands are depicted as circles for Q-1, triangles for Q-2, diamonds for Q-3 and squares for Q-4.

The pyrimidinylhydrazone **IV-b** showed MDR selective toxicity in a cell line dependent manner. Similar to **Q-1** and further cell line dependently selective agents, namely the pyridinyl TSC **II-g** and the pyridinyl hydrazino-benzothiazole **V-b**, its toxicity was attenuated in the presence of NAC (see chapter 3.4.1.). Since metal complexes might be involved in this process, the metal binding properties of **IV-b** were investigated in similar experiments, in order to compare its metal binding properties to that of the presented 8-hydroxyquinoline derivatives. pK values were determined and are given in the Scheme in Figure 48. In contrast to the 8-hydroxyquinoline compound set, which binds to metal ions via an ( $N_{\text{quinoline}}, O^-$ ) bidentate coordination mode [252], ligand **IV-b** binds to metal ions via an NNN coordination mode (see chapter 3.2.).

Upon metal binding, well-defined charge transfer bands appear in the visible wavelength range of the pH-dependent UV-Vis spectra shown in Figure 48 D and E. While the CT bands considerably overlap with the ligand bands, the d-d bands are too weak to be detected in the applied concentration of 50  $\mu\text{M}$ . Deconvolution of the spectra suggests the formation of mono and bis complexes with iron (III), with a predominance for the bis-complex  $[\text{FeL}_2]^{3+}$  in the physiologic pH range, although the hydrolysis of the metal ion suppresses the complex formation at alkaline pH values. Surprisingly, at alkaline pH values ( $\text{pH} > \sim 8.5$ ), the development of CT bands in the 510–610 nm wavelength range could be detected. These bands are characteristic for the formation of Fe (II) complexes formed with ligands consisting of aromatic nitrogen donor atoms. Also at lower pH values, the formation of minor amounts of iron (II) complexes might be possible, but the redox process of the complex seems to be pH-dependent and much faster in the basic pH range. Thus data collected at  $\text{pH} > 7.5$  were not used for the complex stability calculations. The pM value of the ligand allows the comparison of its iron (III) binding ability to that of other ligands. With a pM of 17.6, the iron (III) binding ability of **IV-b** can be settled between that of the borderline MDR selective ligand **Q-2** and the MDR selective agent **Q-3**.

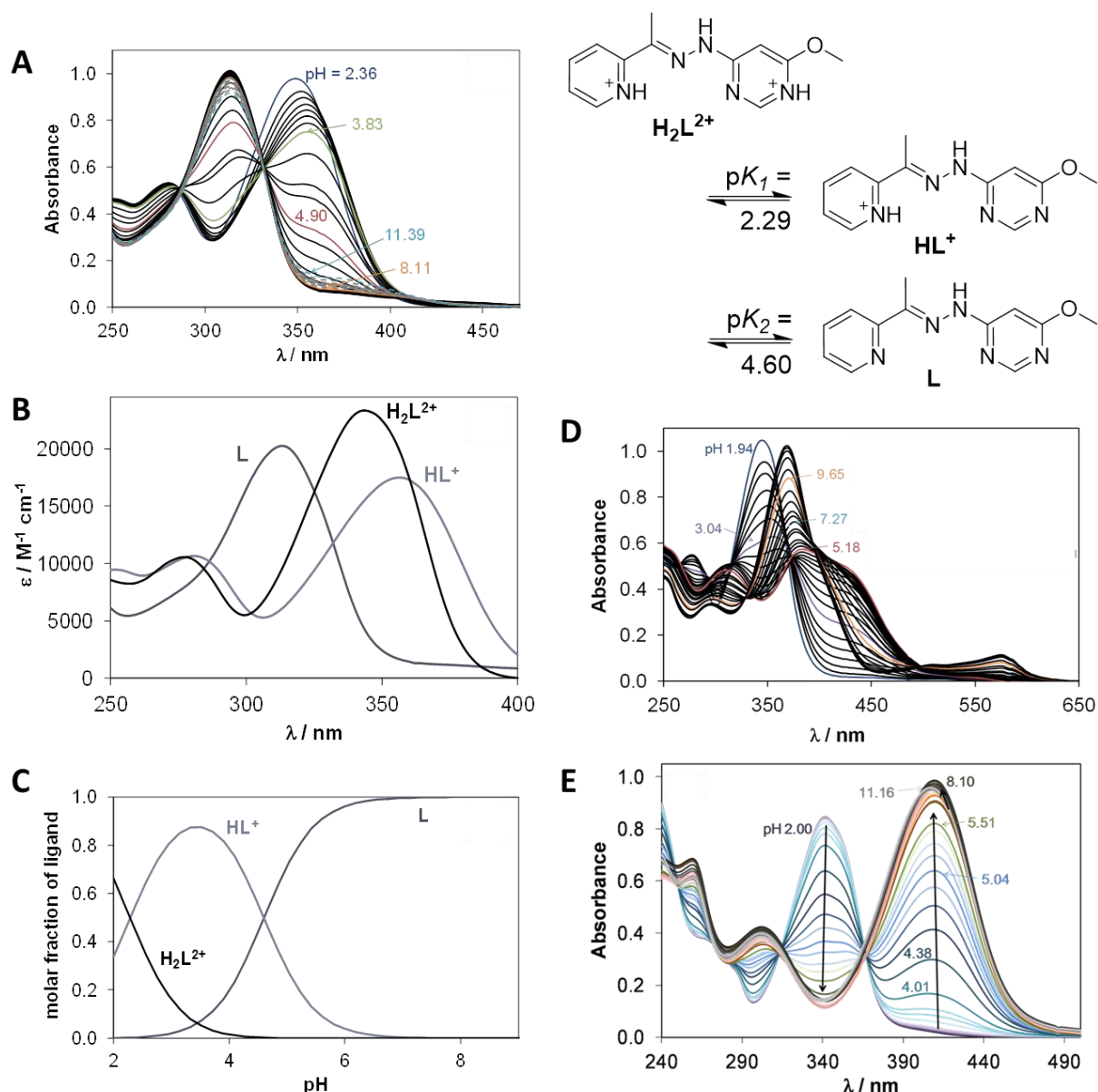


**Figure 48:** UV-Vis absorption spectra recorded at different pH values for 50  $\mu\text{M}$  ligand **IV-b** (A) alone or in the presence of 20  $\mu\text{M}$   $\text{FeCl}_3$  (D), or 50  $\mu\text{M}$   $\text{CuCl}_2$  (E). The molar absorption spectra for the ligand species (B) and pH dependent species distribution of the ligand (C) were calculated from the spectral data, and pK values were assigned as indicated in the Scheme. Data of **IV-b** were published in reference [89].

Also in case of copper complexation, the formation of mono-, protonated mono- and bis-complexes could be observed, although the formation of the  $[\text{CuL}_2]^{2+}$  complex seems less pronounced as in the case of iron (III). With a pM value of 8.6 calculated for the copper binding ability, **IV-b** is a much weaker copper chelator compared to the 8-hydroxyquinoline set of chelators **Q-1** to **Q-4**. A further difference to the 8-hydroxyquinolines can be seen in the metal binding preference: While in case of the MDR selective ligands **Q-3** and **Q-4** a clear

preference for copper (II) binding over iron (III) was concluded, ligand **IV-b**, which shows cell line specific selective effects, seems to preferentially bind iron (III) over copper (II).

**Table 13:** Overall stability constants ( $\log\beta$ ) of the copper (II) and iron (III) complexes of ligands **Q-1** to **Q-4** and **VI-b** determined by UV-vis spectrophotometric titrations and pM values calculated at pH 7.4. Charges of the complexes are omitted for clarity. **L** is singly negatively charged in case of **Q-1**, **Q-2** and **Q-4** and neutral in case of **Q-3** and **IV-b**. Data of **IV-b** were published in reference [89].

	Q-1	Q-2	Q-3	Q-4	IV-b
$\log\beta$ [FeLH]		19.80 $\pm$ 0.04		18.46 $\pm$ 0.04	
$\log\beta$ [FeL]	13.7 <sup>a</sup>	16.90 $\pm$ 0.04	11.11 $\pm$ 0.02	14.31 $\pm$ 0.05	15.69 $\pm$ 0.07
$\log\beta$ [FeL <sub>2</sub> H <sub>2</sub> ]				34.44 $\pm$ 0.04	
$\log\beta$ [FeL <sub>2</sub> H]		35.18 $\pm$ 0.04		28.50 $\pm$ 0.06	
$\log\beta$ [FeL <sub>2</sub> ]	26.3 <sup>a</sup>		20.32 $\pm$ 0.03		21.71 $\pm$ 0.06
$\log\beta$ [FeL <sub>3</sub> H]		49.03 $\pm$ 0.03			
$\log\beta$ [FeL <sub>3</sub> ]	36.9 <sup>a</sup>	42.49 $\pm$ 0.03	25.42 $\pm$ 0.07		
pM <sup>b</sup>	21.1	21.1	16.0	14.8	17.6
pM* <sup>f</sup>	13.0	13.0	8.0	6.8	9.5
$\log\beta$ [CuLH]				16.87 $\pm$ 0.03	12.16 $\pm$ 0.09
$\log\beta$ [CuL]	12.1 <sup>d</sup>	16.54 $\pm$ 0.04	10.60 $\pm$ 0.1	10.96 $\pm$ 0.07	7.39 $\pm$ 0.01
$\log\beta$ [CuL <sub>2</sub> H <sub>2</sub> ]				32.54 $\pm$ 0.06	
$\log\beta$ [CuL <sub>2</sub> H]		34.67 $\pm$ 0.04		26.94 $\pm$ 0.06	
$\log\beta$ [CuL <sub>2</sub> ]	23.0 <sup>d</sup>	27.50 $\pm$ 0.10	19.40 $\pm$ 0.1		12.35 $\pm$ 0.03
pM <sup>b</sup>	15.1	17.4	14.9	13.0	8.6

<sup>a</sup> Data taken from reference [250].

<sup>b</sup> pM =  $-\log [M]$  calculated at pH = 7.4,  $c_M = 1 \mu\text{M}$ ;  $c_L = 10 \mu\text{M}$ .

<sup>c</sup> pM\* =  $-\log ([\text{Fe}] + \sum [\text{Fe}_i(\text{OH})_j])$  calculated at pH = 7.4,  $c_M = 1 \mu\text{M}$ ;  $c_L = 10 \mu\text{M}$ .

<sup>d</sup> Data taken from reference [253].

### 3.4.4. *In vitro* testing of preformed complexes – and the impact of P-gp on their toxicity

Following the characterization of the iron (III) and copper (II) binding ability of the selected ligands, complexes were prepared in solution in order to test their antitumor potential *in vitro*. Since metal complexes of these ligand types are reported to be poorly soluble in water [254], for the biological tests, 10 mM stock solutions of ligands were prepared in DMSO in presence of 1, 0.5 and 0.33 equivalents of the respective metal ion. In contrast to the co-incubation experiments (presented in 3.4.2.), a constant metal-to-ligand ratio is ensured over the investigated concentration range by the application of preformed complexes. In order to avoid misinterpretation due to different amount of ligand present in the respective complexes, concentrations are expressed as ligand equivalents. Therefore in the 1:3 metal-to-ligand ratio, the IC<sub>50</sub> values were in general viewed as 1/3 [ML<sub>3</sub>]. In order to compare the activity of the free and complexed ligands, fold changes upon metal binding were calculated as the fraction of the average IC<sub>50</sub> values of free vs. complexed ligands with negative values representing a decrease in toxicity, while positive values are indicating an increase in toxicity upon metal ion complexation. The results are summarized and illustrated in Figure 49 A-D for the 8-hydroxyquinoline compound set. In agreement with the co-incubation data (chapter 3.4.2.), the iron (III) complexes of **Q-1** behaved very similar to the free ligand – the only significant difference is a slight increase in toxicity in MES-SA cells at 1:1 ratio. Comparably, the toxicity of **Q-2** upon iron (III) complexation was slightly increased in MES-SA cells in the metal-to-ligand ratios 1:3 and 1:2, and significantly decreased in MES-SA/Dx5 cells at the 1:1 ratio. While the tris complex [FeL<sub>3</sub>] of the MDR selective ligand **Q-3** was more toxic in MES-SA cells, the bis and mono complexes ([FeL<sub>2</sub>]<sup>+</sup> and [FeL]<sup>2+</sup>) were less toxic than the free ligands in MES-SA/Dx5 cells. This is in agreement with the protection of MES-SA/Dx5 cells against the toxicity of **Q-3** by co-incubated FeCl<sub>3</sub>. Also the bis- and mono-complexes of ligand **Q-4** were found to be less toxic than the free ligand.

On the contrary, complexation with copper generally seemed to increase the toxicity of the ligands. While for **Q-1** a significant effect could only be observed for the mono complex in both cell lines, for **Q-2** complexation in the metal to ligand ratios 1:3 to 1:1 resulted in increased toxicity in both cell lines, with a higher magnitude in MES-SA as compared to the MDR MES-SA/Dx5 cells. For the MDR selective ligands **Q-3** and **Q-4** a significant increase could be observed upon complexation with copper (II) in all investigated metal-to-ligand ratios in MES-SA cells, but not in P-gp-expressing MES-SA/Dx5 cells.

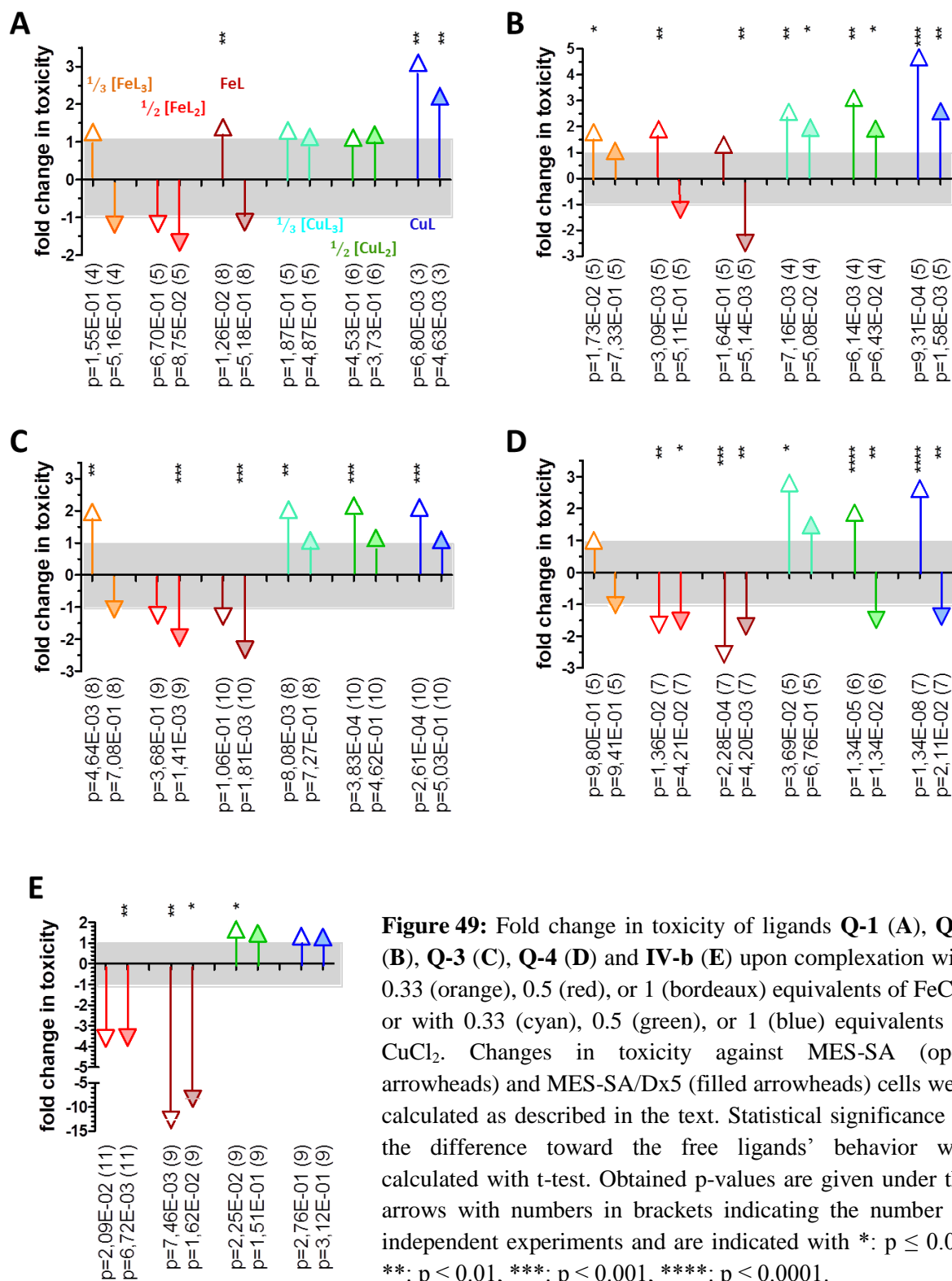


**Figure 49:** Fold change in toxicity of ligands **Q-1** (A), **Q-2** (B), **Q-3** (C), **Q-4** (D) and **IV-b** (E) upon complexation with 0.33 (orange), 0.5 (red), or 1 (bordeaux) equivalents of FeCl<sub>3</sub>, or with 0.33 (cyan), 0.5 (green), or 1 (blue) equivalents of CuCl<sub>2</sub>. Changes in toxicity against MES-SA (open arrowheads) and MES-SA/Dx5 (filled arrowheads) cells were calculated as described in the text. Statistical significance of the difference toward the free ligands' behavior was calculated with t-test. Obtained p-values are given under the arrows with numbers in brackets indicating the number of independent experiments and are indicated with \*:  $p \leq 0.05$ , \*\*:  $p \leq 0.01$ , \*\*\*:  $p \leq 0.001$ , \*\*\*\*:  $p \leq 0.0001$ .

Similar to the 8-hydroxyquinoline set, the compound **IV-b**, which showed enhanced toxicity only toward a subset of investigated MDR cells, also showed decreased toxicity upon complexation with iron (III), yet, the magnitude of the change was remarkably big. Copper (II) complexation at the 1:2 metal-to-ligand ratio slightly increased toxicity in MES-SA cells only (Figure 49 E).

The comparison of the toxicity data of the complexes obtained in P-gp positive MES-SA/Dx5 and P-gp negative MES-SA cells reveals that the complexes of ligands without MDR selective activity (**Q-1**, circles in Figure 50 A) or with a very low selectivity (**Q-2**, triangles in Figure 50 B) do not show a preferential toxic effect in P-gp expressing cells, either. In contrast, iron (III) and copper (II) complexes formed with the MDR selective ligands **Q-3** (diamonds in Figure 50 C) and **Q-4** (squares in Figure 50 D), show enhanced toxicity toward the P-gp expressing MES-SA/Dx5 cells as compared to the P-gp negative parental cell line MES-SA.

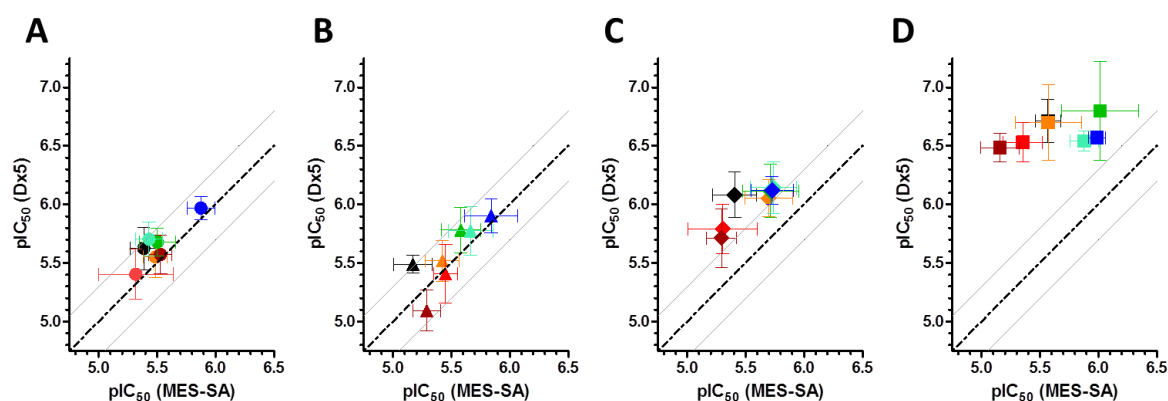


**Figure 50:** Comparison of the toxic activity of ligands (black) and complexes in P-gp negative (MES-SA, x-Axis) and P-gp positive (Dx5, y-Axis) cells. Non-MDR selective ligands: **Q-1** (circles, panel A), **Q-2** (triangles, panel B) and their metal complexes. MDR selective ligands: **Q-3** (diamonds, panel C), **Q-4** (squares, panel D) and their metal complexes. The  $pIC_{50}$  values of the ligand at different metal to ligand ratios are shown in different colors: 1/3  $[FeL_3]$  (orange), 1/2  $[FeL_2]$  (light red),  $[FeL]$  (bordeaux), 1/3  $[CuL_3]$  (green), 1/2  $[CuL_2]$  (cyan) and  $[CuL]$  (blue).

The impact of P-gp on the toxicity of the complexes was furthermore followed up by co-incubation experiments with the P-gp inhibitor Tariquidar. The results of these experiments suggest that the described behavior is dependent on the function of the transporter (Figure 51). As expected, the presence of TQ had no impact on the toxicity of any ligands or complexes



toward the P-gp negative MES-SA cells, which were included as a control (Figure 51 E-H). In MES-SA/Dx5 cells also the toxicity of **Q-1** and its iron (III) and copper (II) complexes remained unaffected in the presence of the P-gp inhibitor (Figure 51 A). In case of ligand **Q-2** results look similar, with one exception of the iron (III) complex at 1:1 ratio (bordeaux triangle, Figure 51 B). Here the presence of the inhibitor significantly increased the toxicity by a factor of 2.4, suggesting that the  $[\text{Fe}(\mathbf{Q-2})]$  complex might be a weak substrate for the transporter. In contrast, the complexes formed by the MDR selective ligands **Q-3** (Figure 51 C) and **Q-4** (Figure 51 D) show a significantly decreased toxicity in the presence of the P-gp inhibitor. The magnitude of the selective toxic effect of the complexes is bigger for **Q-4** compared to **Q-3**, reflecting the MDR selective properties of the ligands. These results suggest that the iron (III) and copper (II) complexes of the MDR selective ligands show a MDR selective toxicity pattern similar to their free ligands and are not transported by P-gp.

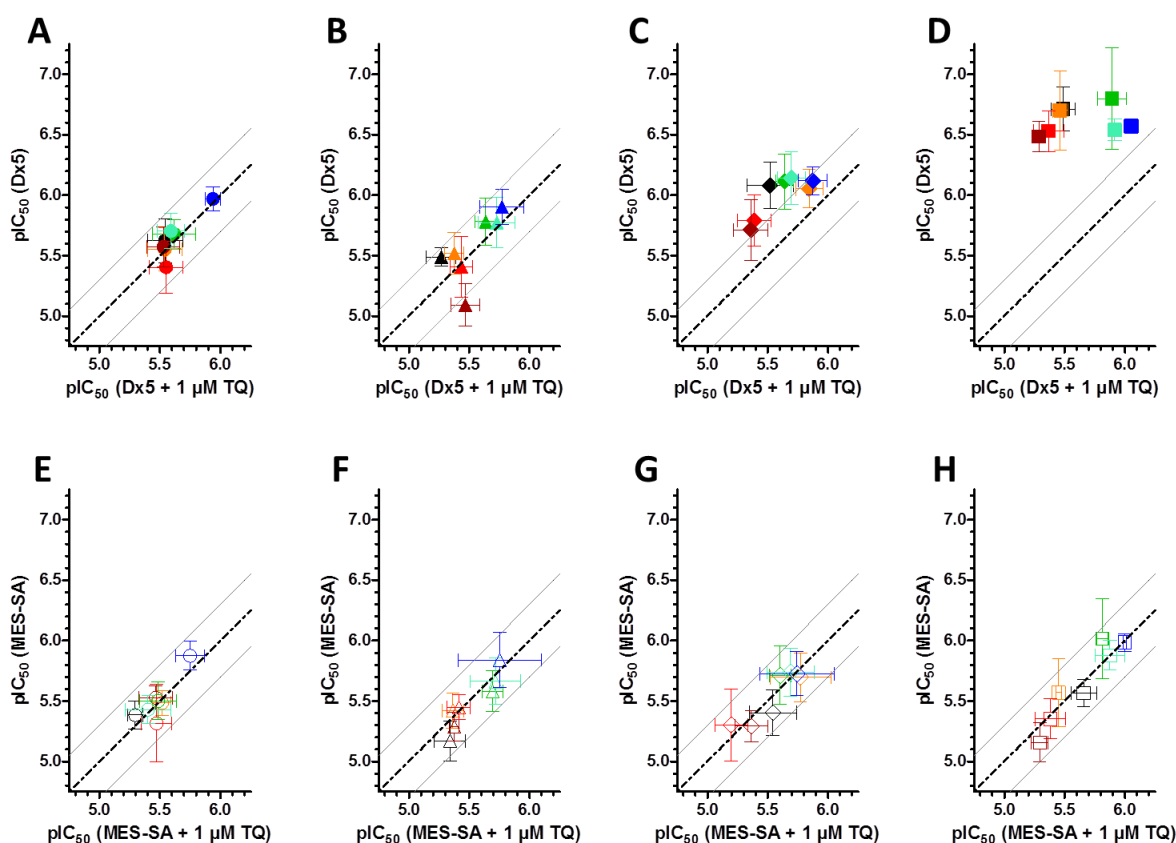


**Figure 51:** Comparison of the toxic activity of ligands (black) and complexes in the absence and presence of the P-gp-inhibitor Tariquidar (TQ) in MES-SA/Dx5 cells (A-D) and MES-SA cells (E-H). The  $pIC_{50}$  values of the ligand at different metal-to-ligand ratios illustrated by different colors: 1/3  $[\text{FeL}_3]$  (orange), 1/2  $[\text{FeL}_2]$  (light red),  $[\text{FeL}]$  (bordeaux), 1/3  $[\text{CuL}_3]$  (green), 1/2  $[\text{CuL}_2]$  (cyan),  $[\text{CuL}]$  (blue) and L (black). Data shown for **Q-1** (A, E), **Q-2** (B, F), **Q-3** (C, G) and **Q-4** (D, H).

### 3.4.5. Redox activity of complexes

#### 3.4.5.1. Cyclic voltammetry

Having shown that the formed complexes are stable and active in the *in vitro* setting with a similar selective toxicity profile against the investigated drug sensitive and MDR cancer cell lines as the free ligands, the putative influence of reactive oxygen species in their (selective) mechanism of toxicity should be addressed in the next step. Since ROS might evolve as a result of Fenton like reactions, which involve redox active metal complexes, the redox properties of iron and copper complexes were investigated using cyclic voltammetry. Since the low water solubility of the complexes did not allow a sufficiently concentrated aqueous solution, studies were performed in a 90% (v/v) DMSO-water mixture. The electrochemical data obtained for ligands **Q-1** to **Q-4** as well as **IV-b** in the presence of  $\text{FeCl}_3$  and  $\text{CuCl}_2$  are summarized in Table 14.

In most cases, the cyclic voltammograms recorded for the metal salts or in the presence of ligand at different metal-to-ligand ratios appear to be significantly different due to the formation of various complex species, as shown in representative voltammograms for complexes of **Q-3** and the cell line specific agent **IV-b** (Figure 52). However, for the ligand **Q-4** the voltammograms of the metal ions in the absence of the ligand were quite similar to those in the presence of **Q-4** in the case of both metal ions. This might be a result of the relatively low stability of the complexes; thus cathodic and anodic peaks could only be identified for the aqua metal ions formed from the metal chlorides in solution. In contrast, the addition of ligands **Q-1**, **Q-2** and **Q-3** to iron (III) results in the appearance of a new set of peaks at lower potentials compared to the aqua ion peaks. The detected redox process due to the iron complex formation were found to be quasi-reversible under the applied conditions and the formal reduction potential values ( $E^\circ$ , Table 14) might be assigned to the tris-complexes, in which the coordination sphere of the metal ion is saturated. The highest shift in the  $E^\circ$  value in comparison to the free metal ion is obtained for **Q-1**, followed by **Q-3** and **Q-2**. Thus, the formal potential of the iron complexes does not seem to follow the trend in selective toxicity of these three ligands. All determined  $E^\circ$  values are higher than that of the biological reductant GSH, which is reported to have the formal potential of the GSSG/GSH couple at -0.26 V at pH 7.4 [255]. Compared to dehydro-L-ascorbic acid, another important antioxidant, the iron complex formed with **Q-3** has a similar potential (+0.05 V at pH 7.4 [256]), while the redox potential of the iron complexes of **Q-2** is more positive.

The complexation of iron by ligand **IV-b** in contrast results in the appearance of a new set of peaks with a more positive potential as compared to the aqua complex. This positive shift of the formal potential indicates a preference of the complex for the Fe (II) oxidation state, which has already been suggested in the UV-Vis spectrophotometric titrations (chapter 3.4.4.).

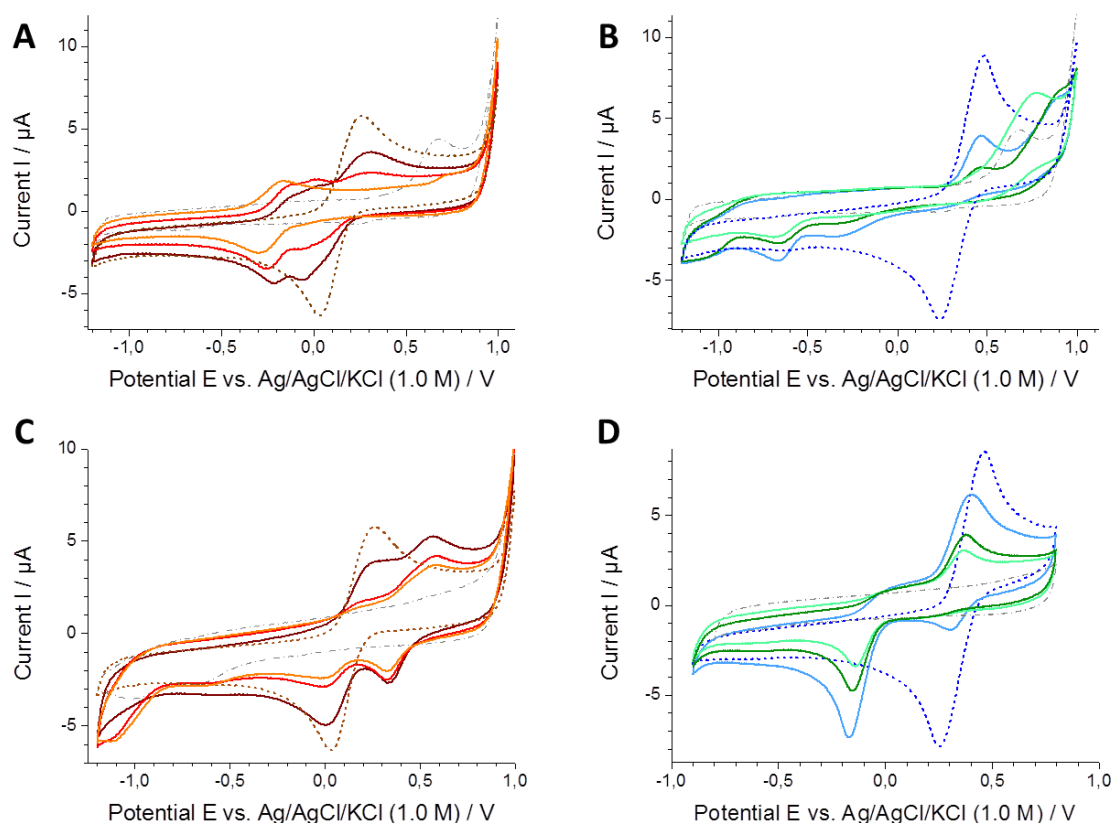


**Figure 52:** Cyclic voltammograms of iron (A, C) and copper (B, D) complexes of ligands **Q-3** (A,B) and **IV-b** (C,D) vs. Ag/AgCl/KCl (1.0 M) for ligand concentrations of  $c_L = 1.0$  mM. Solutions were prepared in 90% (v/v) DMSO/H<sub>2</sub>O with an ionic strength of  $I = 0.01\text{M}$  (TBACl). Measurements were performed with a glassy carbon working electrode at a temperature of  $T = 25$  °C with a scan rate of 100 mV/s. Data are shown for the ligand alone (dashed grey), for FeCl<sub>3</sub> (dotted brown), iron complexes at the M:L ratios 1:1 (solid bordeaux), 1:2 (solid red) and 1:3 (solid orange), as well as for CuCl<sub>2</sub> (dotted dark blue), and copper complexes at the M:L ratios 1:1 (solid blue), 1:2 (solid green) and 1:3 (solid cyan).

While the voltammograms recorded for the copper aqua complexes, formed in the solution of CuCl<sub>2</sub>, display a reversible redox process, for its complexes formed with the 8-hydroxyquinoline derivatives **Q-1** to **Q-3** only irreversible redox processes could be observed under the applied conditions, in which only the reduction peaks could be seen (cathodic peak

potentials in Table 14). Upon complexation of the copper ion, two reduction peaks appeared at much lower potentials compared to the copper aqua complexes. Based on the changes of their intensity ratio with increasing ligand excess they can be assigned to the mono- and bis-ligand complexes. It is noteworthy that the consecutive coordination of the ligands to the metal ion results in progressive shifts in the reduction potential as compared to the aqua complex. In the case of the copper-**Q-3** system a further oxidation peak appears at the 1:3 metal to ligand ratio, which can be assigned to the presence of unbound ligand. Since the formal reduction potential values could not be calculated for the copper complexes due to the irreversible electrode reactions, to this state, an estimation of behavior of the copper species in the presence of intracellular antioxidants is not possible; however it should be noted that their cathodic peak potentials are significantly lower than those obtained for the aqua copper ion and for the iron complexes.

**Table 14:** Electrochemical data for the iron and copper complexes formed with ligands **Q-1** to **Q-3**, as well as **IV-b**, in comparison to the metal chlorides. Cyclic voltammograms were recorded for 90% (v/v) DMSO/H<sub>2</sub>O solutions of the ligands in concentrations of  $c_L = 1.0$  mM with an ionic strength of  $I = 0.01$  M (TBACl). Measurements were performed with a glassy carbon working electrode against an Ag/AgCl/KCl (1.0 M) reference electrode at a temperature of  $T = 25$  °C with a scan rate of  $\nu = 100$  mV/s scan rate. Data of **IV-b** were published in reference [89].

	$MCl_x$	<b>Q-1</b>	<b>Q-2</b>	<b>Q-3</b>	<b>Q-4</b>	<b>IV-b</b>
ligand						
$E_{ox}$ vs. NHE / V				0.916		
$E_{red}$ vs. NHE / V		-0.412 (0.687)	-1.004		< - 1 <sup>a</sup>	-0.774
[FeL <sub>3</sub> ]						[FeL <sub>2</sub> ]
$E_{ox}$ vs. NHE / V	0.466	0.049	0.262	0.068	free FeCl <sub>3</sub>	0.823
$E_{red}$ vs. NHE / V	0.241	-0.484	0.007	-0.058	"	0.558
$E^\circ$ vs. NHE / V	0.354	-0.218	0.134	0.005	"	0.691
$\Delta E$ ( $E^\circ ML_3 - E^\circ M$ )		-0.572	-0.220	-0.349		+0.337
[CuL]						
$E_{ox}$ vs. NHE / V	0.709	-	-	-	free CuCl <sub>2</sub>	
$E_{red}$ vs. NHE / V	0.481	0.101 <sup>b</sup>	-0.355	-0.076	"	
[CuL <sub>2</sub> ]						
$E_{ox}$ vs. NHE / V	0.709	-	-	-	free CuCl <sub>2</sub>	0.244 <sup>a</sup>
$E_{red}$ vs. NHE / V	0.481	-0.440	-0.491	-0.076	"	0.070
$E^\circ$ vs. NHE / V						0.157
$\Delta E$ ( $E^\circ ML_3 - E^\circ M$ )						-0.438

<sup>a</sup> broad peak, not complete in measurement, <sup>b</sup> very low peak intensity

On the contrary copper complexes formed with the arylhydrazone **IV-b** display a quasi-reversible redox process as shown in Figure 52 and Table 14. The formal potential of the new set of peaks is shifted by 0.44 V to the negative potential range. With 0.16 V against the normal hydrogen electrode, the potential is still more positive than that of the biological reductants glutathione and ascorbate, therefore the reduction by these agents is thermodynamically possible [116,255].

#### 3.4.5.2. Reactivity with antioxidants

The formal potentials that were derived from cyclic voltammetry experiments provide information about the thermodynamic possibility of interactions with intracellular components. The potential of the formed metal complexes to undergo intracellular redox reactions can furthermore be investigated by monitoring the reactions with biologically relevant antioxidants. Glutathione (GSH) is the predominant intracellular reducing agent with a lower formal potential compared to that of dehydro-L-ascorbic acid (ASC). The formal potential of the GSSG/GSH and the dehydro-L-ascorbic acid/ASC redox pairs at pH 7.4 are -0.26 V and +0.05 V, respectively [255,256]. Oxidation of ASC or GSH are often monitored by measuring the changes in absorbance at their  $\lambda_{\text{max}}$  values (265 and 262 nm, respectively) over a given time period [185,257–262]. Since many compounds – free ligands as well as metal complexes – show absorbance at the required wavelengths themselves, an alternative strategy is, to follow the changes in the characteristic regions of the compounds' spectra upon reaction with the antioxidants under strictly anaerobic conditions [89,263]. Monitoring the interaction of the investigated compounds with biologically relevant antioxidants addresses one half of the redox cycling. The other half, namely the oxidation reaction, is often monitored by the benzoate hydroxylation assay [185,257,259–261]. The emission of the fluorescent products that occur in that assay can be measured at 410 nm upon excitation at 308 nm [185,257,259–261]. Also this assay may be hampered by the spectral properties of the investigated compounds, since they might show intrinsic fluorescence. In order to still be able to address the whole redox cycle, and to investigate, if observed reductions were reversible, hydrogen peroxide was added at the end of the reaction with the antioxidant [89].

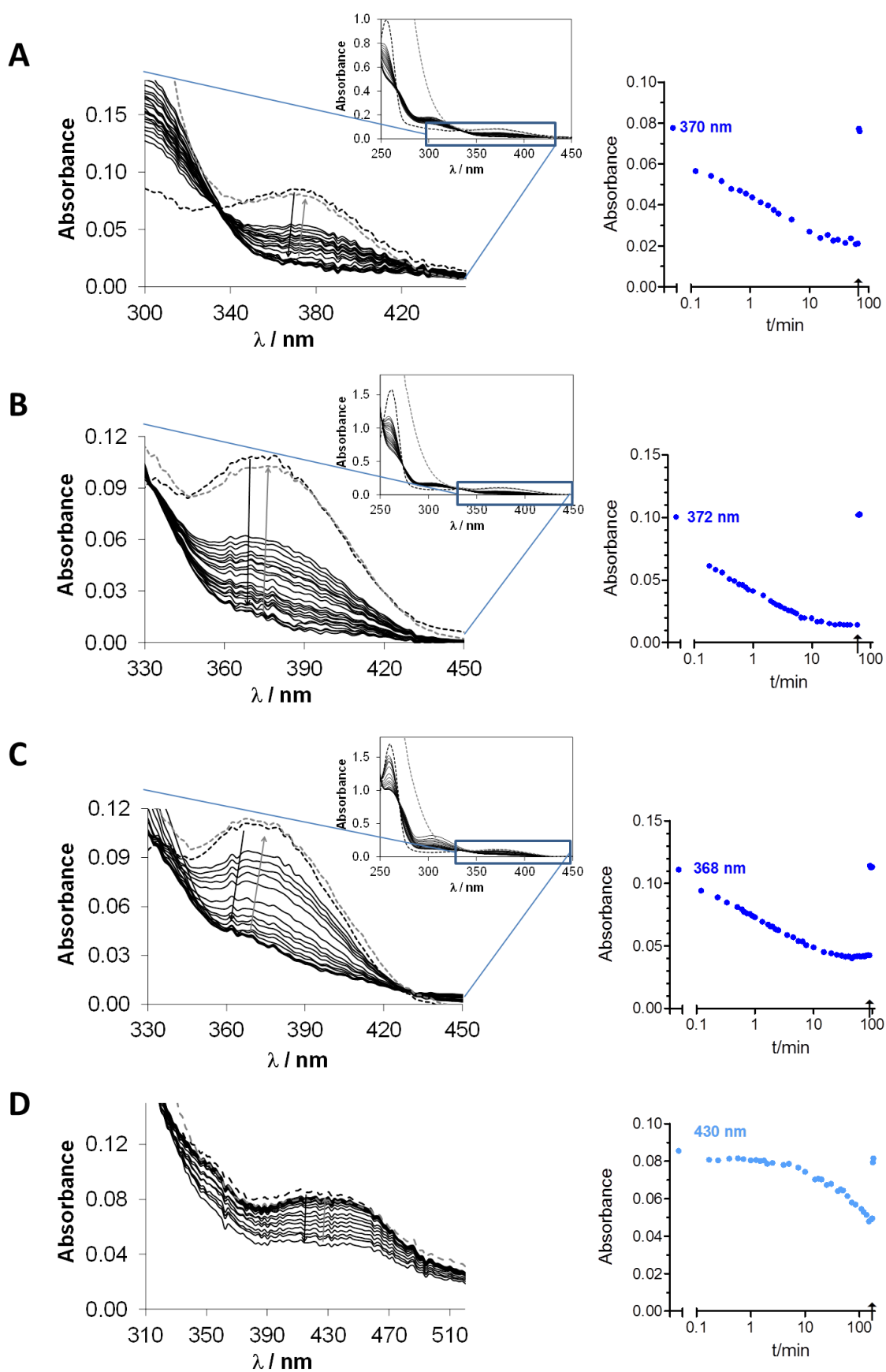


**Figure 53:** Time-dependent UV-Vis spectra of the [CuL] complexes of **Q-1** (A), **Q-2** (B), **Q-3** (C) and **Q-4** (D) upon addition of 5 equivalents of GSH. Black dashed line denotes the initial spectrum before addition of GSH, grey dashed line the spectrum upon addition of H<sub>2</sub>O<sub>2</sub>.

Even though the formal redox potentials obtained from cyclic voltammetric studies of the 8-hydroxyquinoline set suggested a putative reduction by GSH, spectral changes were not observed in any of the investigated iron complexes upon addition of GSH ( $t_{\max} = 90$  min). This suggests that under the applied conditions the formed iron complexes of ligands **Q-1** to **Q-4** seem to be redox inert.

In contrast, moderately fast redox reactions were observed in case of the copper (II) complexes when GSH was added. As illustrated in Figure 53, the recorded time-dependent spectra revealed a significant decrease of the absorbance values at the respective  $\lambda_{\max}$  of the copper (II) complexes of ligands **Q-1** to **Q-4** during the reaction with GSH. Additionally, the absorbance at the  $\lambda_{\max}$  values of the free ligands ( $\sim 304$  nm) seemed to increase with progressing time, indicating a possible ligand release of ligand upon re-organization of the coordination sphere in the reduced copper (I) complexes. In order to investigate the reversibility of the observed reaction,  $\text{H}_2\text{O}_2$  was added to the samples. The oxidant restored the spectra obtained with the original copper (II) complexes, showing the reversibility of the redox process.

Comparing the rates of the reduction reactions (as on the right side on the Figure 53), it seems, that the reduction of the  $[\text{Cu}(\mathbf{Q-4})]$  complex, which possessed the highest MDR selectivity among the studied systems, shows the slowest reaction. Yet, the investigation of two further compounds with high MDR selectivity did not follow that trend (data not shown), suggesting that this observation might not be an explanation for the selectivity.

As for the 8-hydroxyquinoline ligand set, also the kinetic runs of the  $[\text{CuL}]^{2+}$  complex formed with ligand **IV-b** were performed at pH 7.40, while in case of the  $[\text{FeL}]^{3+}$  complex the pH was lowered to 5.45 in order to avoid metal ion hydrolysis and the possible formation of the Fe (II) species in the Fe (III) - ligand system in the basic pH range (see chapters 3.4.3. and 3.4.5.1.). In line with the high redox potential observed for  $[\text{Fe}(\mathbf{IV-b})]^{3+}$  (chapter 3.4.5.1.), this complex was reduced by ascorbate, as shown in Figure 54 B. Addition of hydrogen peroxide at the end of the kinetic run resulted in only negligible changes in the spectra, even after 30 min, suggesting that the observed reduction is not reversible, and that the complex is therefore unlikely to undergo intracellular redox cycling. Surprisingly, a ten-fold excess of the stronger reducing agent GSH did not provoke spectral changes in the  $[\text{Fe}(\mathbf{IV-b})]^{3+}$  system within 90 min. This suggests that this reaction might be kinetically hindered. A similar trend in the reduction kinetics of the two reducing agents has been reported for the reactions of vanadium complexes [262,263].

Furthermore, the formal potentials of both reducing agents are pH-dependent, which might also explain the lack of GSH-induced reduction of the iron complex at pH 5.45. Based on studies on the pH dependence of the redox potentials, it can be estimated that in comparison to the potentials at a pH of 7.4, at the lower pH (5.45) the redox potential of GSH is shifted by 116 mV, while that of ASC is shifted by 52 mV only [255,256,264]. Together these reasons might explain why ASC was able to reduce the complex, while GSH was not.

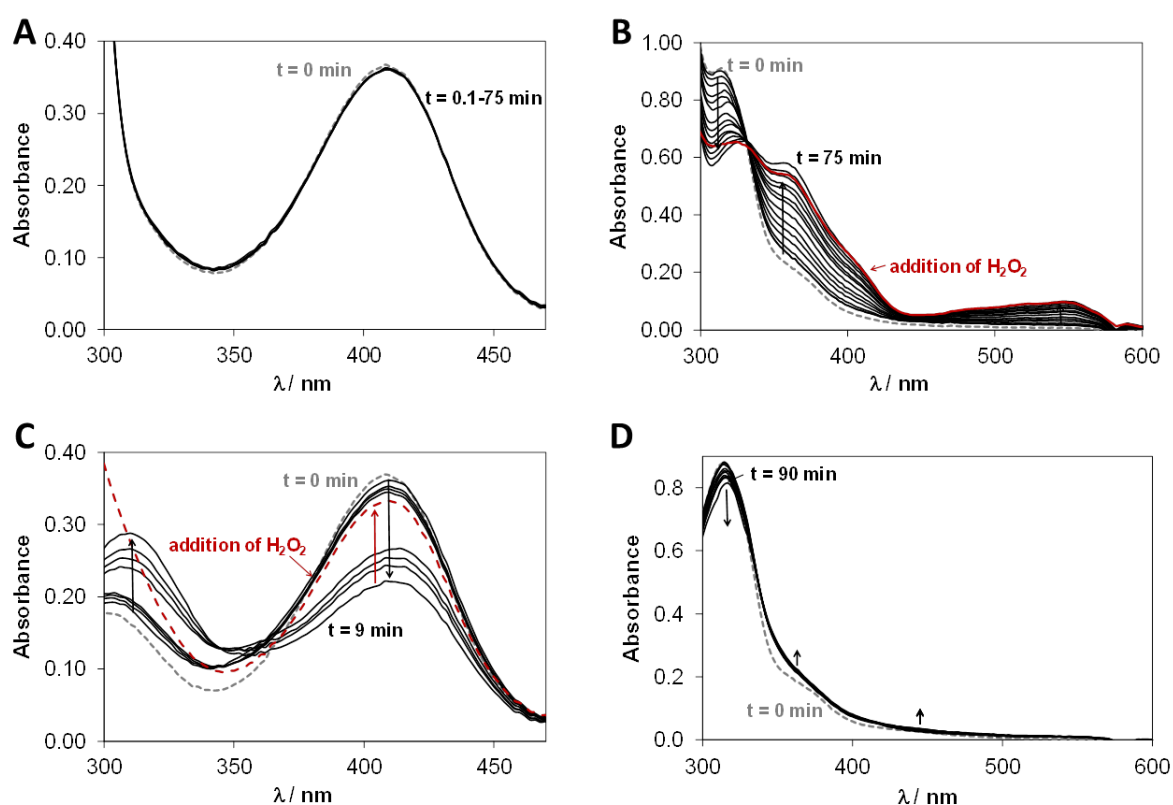


**Figure 54:** Time-dependent UV-Vis spectra of  $[\text{Cu}(\text{IV-b})]^{2+}$  (A, C – pH 7.40) and  $[\text{Fe}(\text{IV-b})]^{3+}$  (B, D – pH 5.45) in the presence of 10 equivalents of ASC (A, B) and GSH (C, D). Red lines denote spectra obtained upon addition of  $\text{H}_2\text{O}_2$ . These data of **IV-b** were published in reference [89].

In contrast, the addition of ascorbate did not provoke changes in the spectra of the  $[\text{Cu}(\text{IV-b})]^{2+}$  complex at a (pH of 7.4) within 75 min, suggesting that the complex is not reduced under the applied conditions (Figure 54 D). The reaction of the complex with glutathione on the contrary seemed to happen relatively fast, as the decrease in the  $\lambda_{\text{max}}$  value of the Cu (II) complex (408 nm) during the redox reaction suggests. In parallel, an increase in absorbance at the  $\lambda_{\text{max}}$  of the free ligand (~310 nm) could be observed, which is most



probably the result of the decomposition of the generated instable Cu (I) complex (Figure 54 C). Furthermore, addition of hydrogen peroxide at the end of the kinetic run restored the original spectrum, suggesting that the complex can undergo a reversible redox process, which might contribute to the toxicity of the compound.

#### 3.4.6. Relevance of redox activity of the complexes for toxicity

The differential behavior of P-gp positive and negative cell lines in response to co-treatment with the 8-hydroxyquinoline derivatives **Q-1** to **Q-4** and the antioxidant *N*-acetylcysteine (NAC) suggested a putative influence of ROS on the (selective) toxicity mechanism of the compounds. Having shown that the ligands form stable and redox active complexes with iron (III) and copper (II), experiments were designed to evaluate the impact of the metal complexes on this behavior. Therefore cells were co-incubated with the preformed metal complexes and three antioxidants with varying reduction power. NAC is considered to be an intracellular precursor for GSH, since the availability of cysteine is rate-limiting for glutathione re-synthesis [265], but NAC also has reducing activity itself based on its thiol group. The redox potential of NAC is by 68 mV more positive than that of the GSH/GSSG redox pair, therefore at pH 7.4 it is at  $-192$  mV [255,266]. At this pH, the reduction of pyruvate to lactate is characterized by a potential of  $-200$  mV [267], while dithiothreitol (DTT) has a reduction potential at  $-345.6$  mV [268,269].

Results that showed significant changes upon co-incubation with one of the antioxidants are summarized in Figure 55. The protective effect of NAC for MES-SA and MES-SA/Dx5 cells toward the toxicity of **Q-1** was also found in case of mixtures of the ligand with one equivalent of iron (III) or 0.33 equivalents of copper (II), though the relative observed protection was smaller than in case of the free ligand. In case of the ligand **Q-2**, NAC protected MES-SA and MES-SA/Dx5 from the iron (III) complexes formed in all metal to ligand ratios. The magnitude of this protective effect is much more pronounced in the P-gp expressing MES-SA/Dx5 cells than in MES-SA cells. In case of the MDR selective ligands **Q-3** and **Q-4**, significant protection could only be observed for the P-gp expressing MES-SA/Dx5 cells against the iron (III) complexes formed at the metal-to-ligand ratio of 1:1. Pyruvate and DTT did not affect the toxicity of any investigated compound toward the parental MES-SA cells. Yet, a protective effect could be observed in MES-SA/Dx5 cells for the iron complexes of **Q-2** ( $[\text{FeL}]$  and  $[\text{FeL}_2]$  for pyruvate;  $[\text{FeL}]$ ,  $[\text{FeL}_2]$  and  $[\text{FeL}_3]$  for DTT).

DTT additionally protected MES-SA/Dx5 cells from the free ligand **Q-1** and the iron (III) complex formed with **Q-3** at 1:1 ratio.

These results seem to be contradictory to the lack of observed interaction with GSH in the monitored reactions (chapter 3.4.5.2.). Though, this ostensible contradiction might show a weakness of the model, since it has to be kept in mind that the (intracellular) redox reactions depend on actual concentrations and are also not independent of pH. Furthermore, it has been reported that the reduction by GSH in the model might be kinetically hindered in some cases. Accordingly, for some metal complexes that did not show reactions with GSH, a reduction by the weaker antioxidant ascorbate has been reported [262,263].

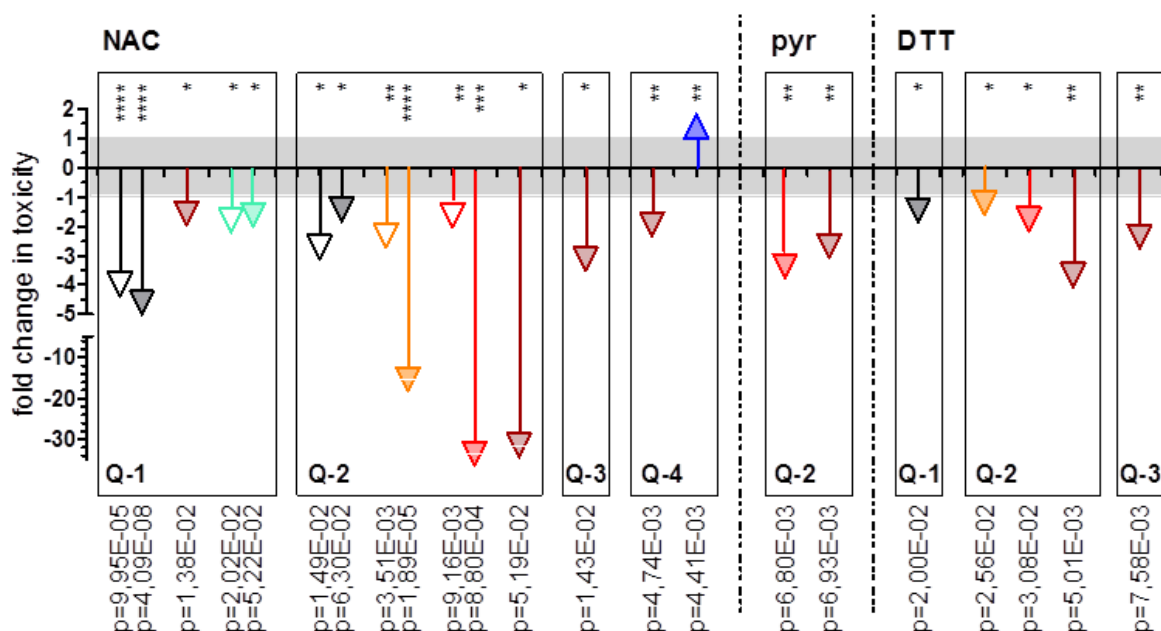


**Figure 55:** Significant fold changes in toxicity upon co-incubation with the indicated antioxidants (concentrations were 5 mM for NAC, 5 mM for pyruvate (pyr) and 100  $\mu$ M for DTT). Ligands are indicated in the boxes. Changes in toxicity against MES-SA (open arrowheads) and MES-SA/Dx5 (filled arrowheads) cells were calculated as the fraction of  $IC_{50}$  values in the presence vs. the absence of the antioxidant. Thereby positive values indicate an increase in toxicity, while negative values indicate a decrease in toxicity. Results obtained with free ligands are shown in black, that of  $[FeL_3]$  in orange,  $[FeL_2]$  in red,  $[FeL]$  in bordeaux,  $[CuL_3]$  in cyan, and  $[CuL]$  in blue. Statistical significance was calculated with t-test, three independent experiments were performed. Obtained p-values are given under the arrows and are indicated with \*:  $p \leq 0.05$ , \*\*:  $p \leq 0.01$ , \*\*\*:  $p \leq 0.001$ , \*\*\*\*:  $p \leq 0.0001$ .

In contrast, for the copper (II) complexes, the only significant change upon co-incubation was observed for  $[Cu(Q-4)]^{2+}$ . Even though this observation could not be found with the other

antioxidants pyruvate and DTT, the toxicity toward MES-SA/Dx5 cells was found to be slightly increased in the presence of NAC.

Taken together, these observations underline the “Janus-face” like character of the antioxidant: while on one hand it can scavenge reactive oxygen species, on the other hand, it might induce a mechanism of “activation by reduction” [86,116,135], and increase the oxidative stress leading to increased cellular damage. The lack of effect of antioxidants on the toxicity of most copper complexes might therefore either mean a real lack of effect, or be caused by parallel processes that counteract each other.

The different reactivity of MES-SA and MES-SA/Dx5 cells toward the combination of 8-hydroxyquinoline derivatives of different MDR selectivity, or metal complexes thereof, with antioxidants might again imply a different redox homeostasis of the parental and drug resistant cells.

## 4. Establishing techniques to measure ROS

### 4.1. DCFDA

The inherent instability and reactivity of most ROS and their very low steady state levels render the precise determination of their intracellular levels challenging [270]. The most frequently used method to measure intracellular ROS is based on the membrane permeable reagent 2',7'-Dichlorofluoresceindiacetate (DCFDA). As detailed in the methods section (Chapter 5.8.1.), upon cleavage of the ester bonds by intracellular esterases, the membrane impermeable, but still non-fluorescent Dichlorofluorescin (DCF-H) is formed, which is oxidized by ROS to the fluorescent Dichlorofluorescein (DCF) [271,272]. Even though being membrane impermeable in principle, studies revealed, that it is a substrate for the ABC-transporters MRP1 and BCRP. In contrast it is not recognized and exported by P-gp, allowing the application in the test setup of MDR selective compounds [273].

As summarized in Table 15, different protocols can be found for the application of the DCF-DA dye in the literature. The dye can be used for measurements of ROS levels within tumor spheroids [274], primary cells [275], as well as in suspension [135,276,277] and adherent cell lines [278–282]. Applicable methods for the measurement of intracellular fluorescence of the dye include flow cytometry, microscopy and spectrofluorimetric measurements. Often, the effect of test compounds on the cellular redox homeostasis is investigated. In these cases, three different experimental setups can be found with respect to the incubation protocols. The treatment of the cells can occur in parallel (Table 15, entry 2, [278]), prior to (Table 15, entries 3-6, [276,279–281,283]) or after loading of the cells with the DCFDA-reagent (Table 15, entries 7-10, [135,271,275,277,282]).

In order to establish a measurement system, the assay protocol was optimized using hydrogen peroxide ( $\text{H}_2\text{O}_2$ ) and *tert*-butyl hydroperoxide (<sup>t</sup>BHP) as positive controls. Furthermore, cell free controls were used, to detect interactions of the dye with the oxidants as well as background reactions that might occur in solution (in the absence of the oxidants) due to hydrolysis and subsequent oxidation by atmospheric oxygen. Changes in fluorescence were investigated over a time period of one to four hours. A simultaneous incubation of cells with the test compounds and the DCFDA dye did not seem to be a preferential method, as high background signals were observed, which caused an unsatisfactory signal-to-noise ratio.

In a next step, cells were seeded to plates, attached overnight and treated with the oxidants.

**Table 15:** Different protocols used for the measurement of reactive oxygen species with the DCFDA-dye in the literature.

	loading with DCFDA	treatment with compound	measurement method	medium	Ref.
1	multicellular tumor spheroids	no compound treatment	confocal laser scanning microscopy	HEPES-containing buffer	[274]
2	simultaneous incubation with DCFDA and test compound; trypsinization of adherent cells after incubation		flow cytometry	not specified	[278]
3	after treatment, test-compound not removed during loading, trypsinization after loading	cells attached, compound treatment prior to DCFDA loading	flow cytometry after washing with cold buffer	culture medium	[279] [280]
4	after treatment, test-compound not removed during loading	suspension cells, treatment prior to DCFDA-loading	flow cytometry	not specified	[276]
5	after treatment, putatively in the presence of test compound (not specified)	prior to DCFDA loading	measurement of cell-lysates at spectrofluorimeter; cell free controls added	not specified	[283]
6	a) after treatment, test-compound not removed, trypsinization after loading b) attached cells, simultaneously with treatment	a) cells attached, treatment prior to DCFDA loading. b) attached cells, simultaneously with DCFDA-loading	a) flow cytometry after washing with buffer b) laser cytometry on attached cells	a) buffer b) serum-free culture medium	[281]
7	cells attached on a chip, DCFDA-loading prior to treatment	treatment after loading, DCFDA not removed	fluorescence microscopy	culture medium	[282]
8	suspension cells, labeling prior to treatment	treatment after loading	flow cytometry	not specified ([277]) / HBSS buffer ([135])	[277] [135]
9	freshly isolated glomeruli, loading prior to treatment	treatment after DCFDA-loading and removal of loading medium	plate reader (note: cell free control missing)	culture medium	[275]
10	loading of suspended cells in buffer prior to treatment, removal of loading buffer for treatment	treatment after loading, following a recovery time for esterases	not specified	(amine-free) buffer	[271]

Before incubation with the dye, the test compounds were removed. After loading with the dye, recovery times of 0 min, 30 min, 60 min, or 120 min were applied before trypsinization and subsequent measurement of the cell suspensions by flow cytometry. Differences in the fluorescence of treated and untreated cells were minor; the overall signals decreased with an elongated recovery time. Since the process of trypsinization might represent a certain stress for the cells, which might elevate the overall ROS levels, the protocol was modified for measurement with the microplate reader. However, this modification did not result in a reliable method either, since only one of four investigated cell lines showed small changes in fluorescence upon treatment with the oxidants.

Therefore the protocol was further modified, shifting the loading of the cells with the dye prior to the treatment with the oxidants in the schedule of the experiment. After staining with DCFDA for 30 min at 37°C, cells were washed and seeded to 96 well plates in a density of 20.000 C/W. Basal fluorescence levels were determined prior to the addition of test compounds and the measured data could be expressed as fold change toward the basal levels and the untreated controls (see methods part, chapter 5.8.1. for details).

Figure 56 shows results obtained with the optimized protocol using the oxidant <sup>1</sup>BHP. The induced signal was found to be dose dependent and increasing over time. MES-SA and MES-SA/Dx5 cells showed a comparable behavior in the assay.

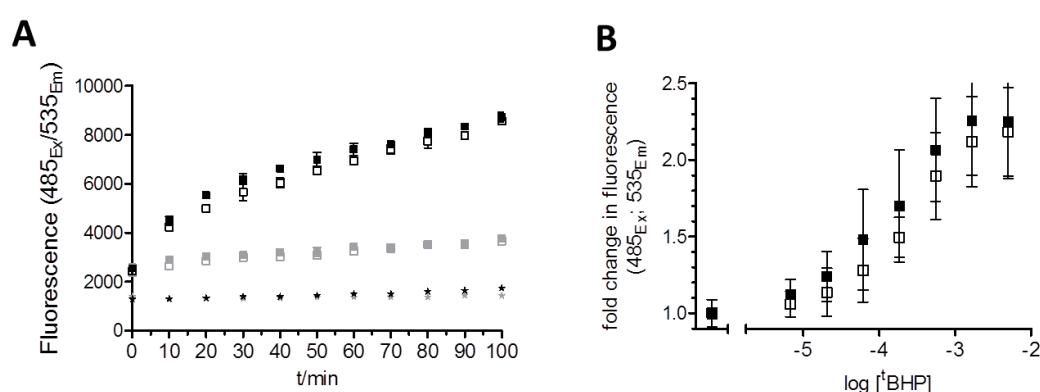


**Figure 56:** Using the DCFDA assay for the measurement of intracellular <sup>1</sup>BHP. (A): representative kinetic curve of an experiment showing the measured fluorescence signal of stained, but untreated (grey) MES-SA (open squares) and MES-SA/Dx5 (filled squares), with the cell-free control (stars) in comparison to the treatment condition with 5 mM of <sup>1</sup>BHP. (B): Dose-dependence of induced signal by <sup>1</sup>BHP after 60 min of incubation. Average and standard deviation of 6 independent experiments performed in duplicates are shown.

Being able to detect the addition of the peroxide <sup>1</sup>BHP, which can be considered as a ROS itself, the next step was, to test the established system with a compound that is able to induce reactive oxygen species as a cellular response. One example for such a compound is the natural occurring naphthoquinone Plumbagin, which is used in Traditional Chinese Medicine. It has antitumor activity, which is reported to involve the formation of ROS via its copper complexes [284–287].

Prior to the experiments, the impact of ROS in the mechanism of cytotoxicity of Plumbagin was investigated by co-incubation with N-acetylcysteine. As shown in Figure 57, the ROS-scavenger was able to protect MES-SA and MES-SA/Dx5 from the toxic effect of Plumbagin in a dose-dependent manner, confirming a role of ROS in the activity of the compound.

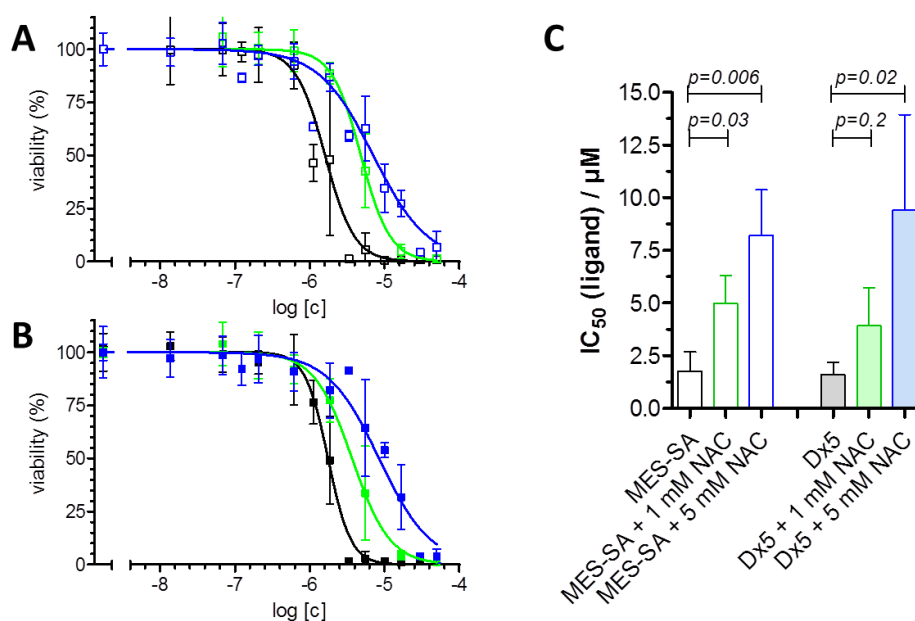


**Figure 57:** Involvement of ROS in the toxicity mechanism of Plumbagin. Dose response curves showing average and standard deviation of 5 independent experiments with MES-SA (A) and MES-SA/Dx5 (B) cells in the absence (black) and presence of 1 mM (green) and 5 mM (blue) NAC. Resulting IC<sub>50</sub> values are summarized in panel C.

As apparent from Figure 58, Plumbagin was able to induce a fluorescence signal in the DCFDA-assay in both MES-SA and MES-SA/Dx5 cells. Furthermore, co-administration of the ROS-scavenger NAC attenuated the intensity of the signal, confirming a connection between signal intensity and ROS production.

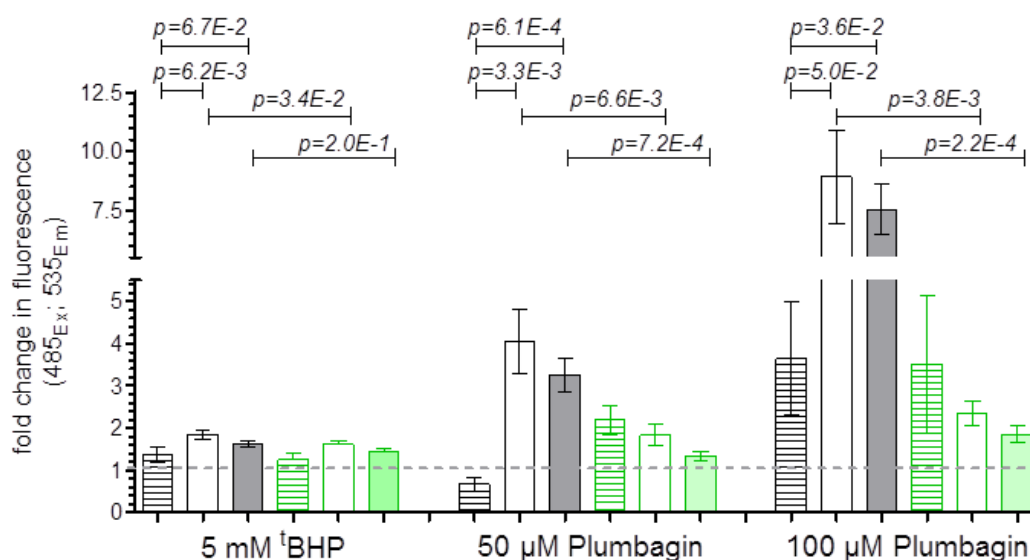


**Figure 58:** ROS induction of tBHP and Plumbagin as measured by DCFDA assay in the absence (black) or presence of 1mM (green) NAC. Data represent the mean and standard error (SEM) of compound induced change in fluorescence after 1 h obtained in 5 independent experiments performed in duplicate. Cell free controls are shown in striped columns, while open columns show the signals obtained with MES-SA and filled columns that in MES-SA/Dx5 cells.

It is noteworthy, that also in cell-free conditions, an increased fluorescence could be observed for the measurements with 100 μM of Plumbagin. Its quinoidic substructure enables the compound to redox cycle and consequently take part in chemical reactions with the dye. This indicates, that results obtained with the assay, might have to be interpreted with caution in some cases. Still, the difference between cell free and cellular samples is significant and relatively high. Therefore the established assay seems to provide a powerful tool for the measurement of ROS in cellular systems.



In a next step, a set of 8-hydroxyquinoline derivatives **Q-1**, **Q-3** and **Q-4**, as well as their iron (III) and copper (II) complexes were investigated for their potential to induce reactive oxygen species in a cellular context. As shown in Figure 59, the pronounced signal induction in cell free conditions does unfortunately not allow a reliable conclusion in the cases of the MDR selective compounds **Q-3** and **Q-4**.

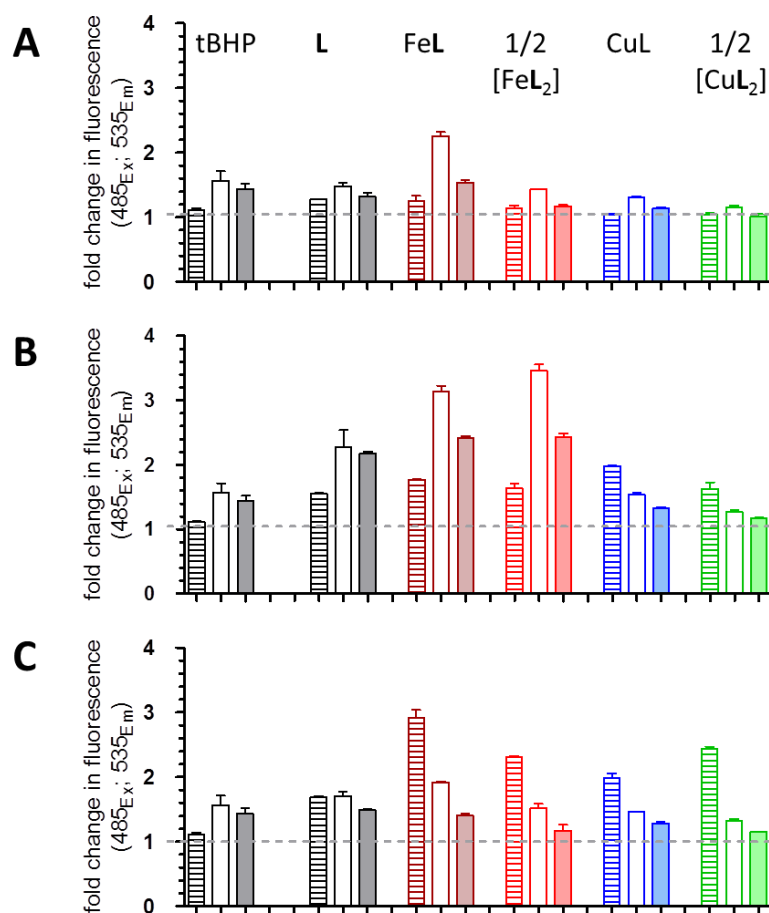


**Figure 59:** ROS induction of 8-hydroxyquinoline derivatives **Q-1** (A), **Q-3** (B) and **Q-4** (C) and their metal complexes in comparison to tBHP as measured by the DCFDA assay. Changes in fluorescence after 1h of treatment with 100  $\mu$ M of the indicated compounds are shown. Cell free controls are shown in striped columns, while open columns show the signals obtained with MES-SA and filled columns that in MES-SA/Dx5 cells. Free ligands are shown in black, iron complexes FeL in bordeaux and 1/2 [FeL<sub>2</sub>] in bright red, copper complexes CuL in blue and 1/2 [CuL<sub>2</sub>] in green.

In chapter 3.4. the set of 8-hydroxyquinoline derivatives with varying MDR selective activity was compared to the arylhydrazone **IV-b**, which showed enhanced toxicity toward a subset of MDR cell lines, yet in a P-gp independent manner. It has been shown, that – similar to the 8-hydroxyquinolines **Q-1** to **Q-4** – compound **IV-b** is able to form stable and redox active complexes. Cellular antioxidants could interact with the formed complexes of iron (III) and copper (II). Furthermore protection of cells against the toxic effect of **IV-b** and its metal complexes by the ROS-scavenger NAC indicates an involvement of ROS in the toxicity mechanism of the ligand and its complexes.

In order to characterize the extent of ROS formation, the newly established assay was applied. Figure 60 summarizes the fold changes in fluorescence obtained after 80 min of incubation with either 50 or 100  $\mu\text{M}$  of the ligand or the indicated complexes. In contrast to the 8-hydroxyquinoline derivatives, **IV-b** and its complexes showed only minor interaction with the DCFDA dye in cell free conditions, rendering the obtained results more reliable. The ligand alone did not provoke a ROS-related increase in fluorescence, suggesting that the presence of metal ions is necessary for the induction of ROS. In contrast, complexation with iron (III) in both metal-to-ligand ratios ( $[\text{FeL}]^{3+}$  and  $[\text{FeL}_2]^{3+}$ ) resulted in a dose dependent ROS induction in equal measure in MES-SA and in MES-SA/Dx5 cells. The presence of NAC prevented the signal induction (Figure 60 A). In case of the copper complexes, ROS induction could be observed in the 1:1 metal-to-ligand ratio in both investigated cell lines, but not in case of the 1:2 ratio, in which the Cu-coordination sphere of the formed complexes is saturated (Figure 60 B). Interestingly, the effect of NAC on the observed ROS-induction of  $[\text{CuL}]^{2+}$  depended on the concentration of the complex. While at 50  $\mu\text{M}$  concentration NAC reduced the fluorescent signal, an increase in fluorescence could be observed at 100  $\mu\text{M}$ . The diminishing effect of NAC on the signal, induced by 50  $\mu\text{M}$  of the complex is in agreement with a scavenging activity of the antioxidant. In contrast, the augmenting effect of NAC at the higher concentration could also be observed in the cell free condition, suggesting that a direct oxidation of the DCF-H is possible under this condition [288,289]. Still, it is possible that NAC initiates redox cycling of the formed complex within the cellular context, which – following Fenton-like chemistry (see Chapter 1.6.) – will increase the formation of reactive oxygen species by a mechanism of “activation by reduction” [89,135].

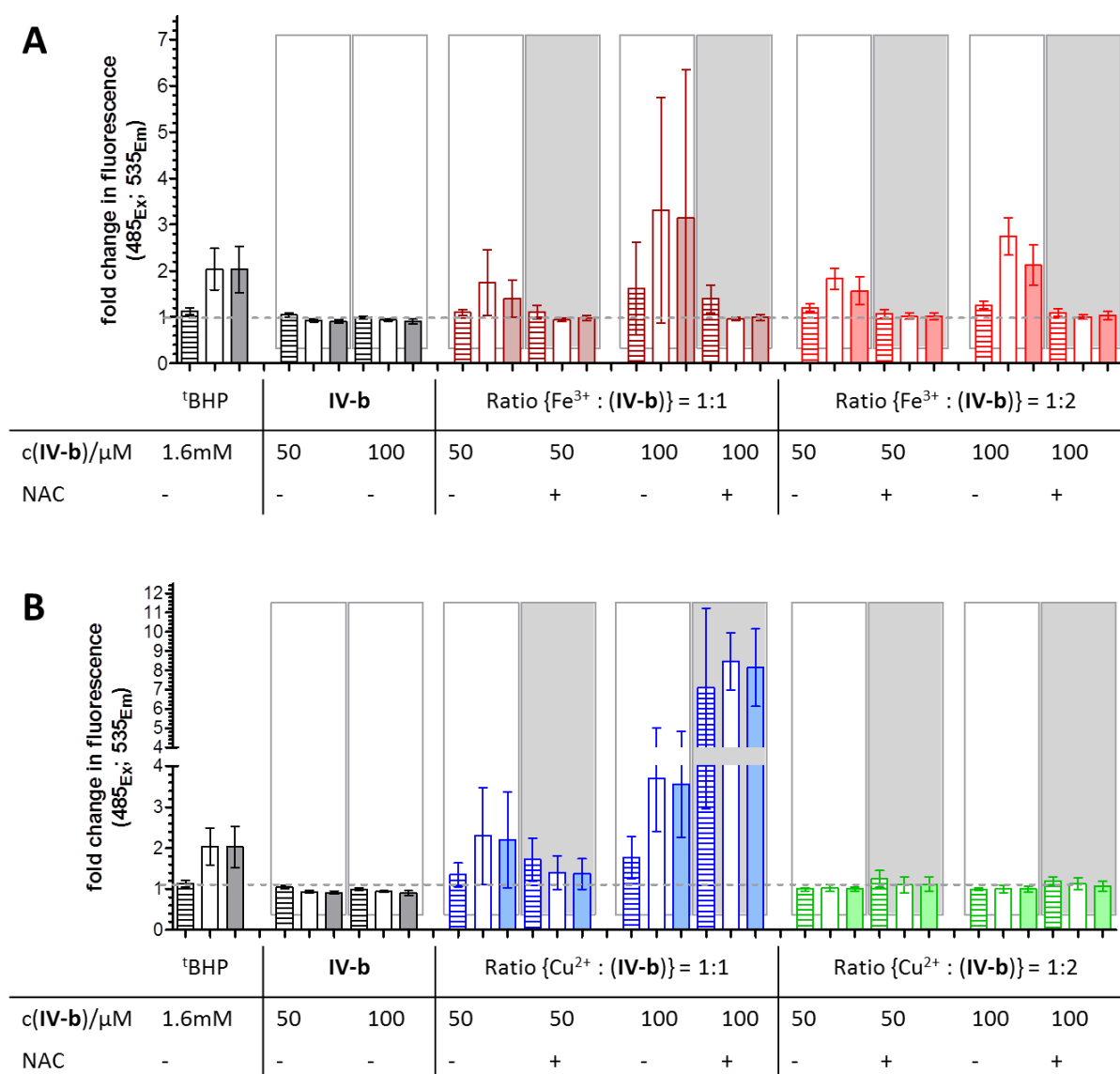


**Figure 60:** ROS induction of arylhydrazone **IV-b** and its iron (III) (**A**) and Cu (II) (**B**) in comparison to <sup>t</sup>BHP, as measured by the DCFDA assay. Changes in fluorescence after 80 min of treatment with indicated concentrations are shown. Co-incubation with 1 mM NAC is indicated in the table and highlighted with a grey background. Cell free controls are shown in striped columns, while open columns show the signals obtained with MES-SA and filled columns that in MES-SA/Dx5 cells. Free ligands are shown in black, iron complexes FeL in bordeaux and 1/2 [FeL<sub>2</sub>] in bright red, copper complexes CuL in blue and 1/2 [CuL<sub>2</sub>] in green.

The application of DCFDA for the measurement of reactive oxygen species is frequently used, since it is based on an easy principle; it is cheap and enables the detection of a broad range of ROS [288,289]. Despite these advantages, the method has certain limitations, which have to be kept in mind analyzing the data obtained with this system: several intracellular enzymes have been reported to interact with the ROS mediated oxidation of DCFH to DCF, such as diverse oxidases [288,290], peroxidases [288,290], catalase [288] and superoxide dismutase [288], but also non-enzymatic interaction partners can be found like hematin, hemoglobin, myoglobin [283] and cytochrome c [283,288,289,291]. Furthermore an artifactual increase in fluorescence can also be the result of photochemistry (followed by oxidation of the semiquinone radical) [288,289,292,293]. The DCFDA reagent (or derived intermediates) can also directly interact with the investigated compounds, metal ions and metal complexes [289,293]. This could be observed in the cases of the 8-hydroxyquinoline derivatives **Q-1**, **Q-3** and **Q-4** as well as for Plumbagin and the copper (II) complex of compound **IV-a**, underlining the importance of cell free controls in the application of the method. A rational use of the DCFDA probe requires an increased awareness for the possible pitfalls of the assay, which are related to possible mechanistic interactions and pathways [293]. The number of compounds which might theoretically interfere with DCFDA emphasizes the importance of proper controls and a careful interpretation of the results. It has been suggested to use the assay rather as a marker of the cellular oxidative stress, than as quantitative indicator for the formation of certain reactive oxygen species [270,271,288].

#### 4.2. HyPer - A genetically encoded sensor for H<sub>2</sub>O<sub>2</sub>

In order to overcome the drawbacks of artifactual side reactions observed with redox-sensitive probes [159], a recently developed method allows the selective quantification of transient fluxes of intracellular H<sub>2</sub>O<sub>2</sub> utilizing the genetically encoded fluorescent sensor protein HyPer [294]. HyPer is a fusion protein consisting of the circularly permuted yellow fluorescent protein cpYFP and an OxyR-RD domain. The latter is a well-known regulatory domain of a physiological sensor in *Escherichia coli*, which undergoes conformational changes upon oxidation by H<sub>2</sub>O<sub>2</sub> [294–296]. Its selectivity toward H<sub>2</sub>O<sub>2</sub> results from the localization of the oxidation site, which is situated in a hydrophobic pocket of the protein and is therefore inaccessible for charged oxidants such as superoxide anion [297]. Insertion of cpYFP to OxyR-RD with a short three amino acid linker resulted in the ratiometric probe HyPer [295]. As shown in Figure 61, the excitation spectrum of the protein has two maxima, one at 420 nm and one at around 500 nm. Upon oxidation by H<sub>2</sub>O<sub>2</sub>, the intensity of the peak at 420 nm decreases, while that of the peak at the higher wavelength increases, enabling a ratiometric readout of the probe [295,297]. Applying this method, artefacts associated with cell movement or differences in the sensor expression level between cells can be avoided [297].

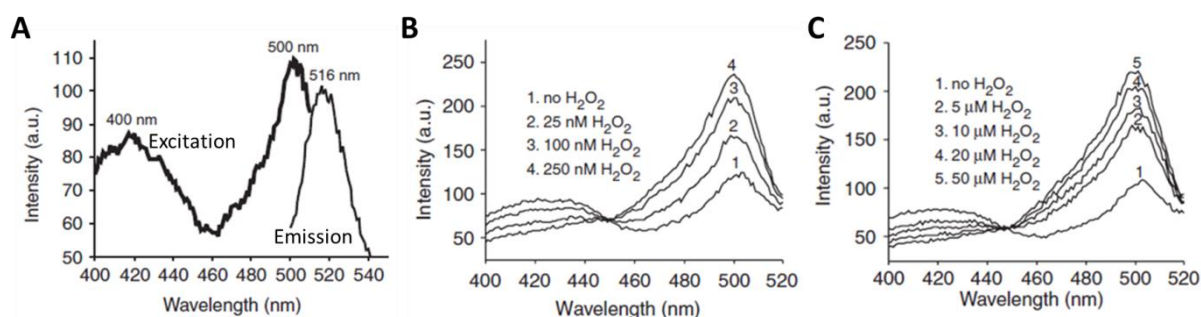


**Figure 61:** Spectral properties of the ratiometric probe HyPer, modified from [295]. (A): excitation and emission spectra; spectral changes upon H<sub>2</sub>O<sub>2</sub> addition, enabling the ratiometric measurement are shown for the pure protein (B) and for HyPer expressing *E. coli* cells in suspension (C).

A further advantage of HyPer over fluorescent redox sensitive dyes is the reversibility of the protein oxidation, which enables the visualization of dynamic changes in intracellular H<sub>2</sub>O<sub>2</sub> levels [298,299]. Furthermore, HyPer is not prone to autoxidation, more photo-stable and retained very well within the cells [298]. Unspecific signals might be possible for compounds which interfere with the spectral properties of the sensor, or with compounds that significantly change the pH of the sample, since HyPer is pH sensitive [295,298,300]. In order to exclude

those unspecific signals, the mutant HyPerC121s, in which a single amino acid exchange disables the signal induction upon H<sub>2</sub>O<sub>2</sub> stress, serves as a valuable control [156].

For the investigation of the effect of ROS in short and long term experiments, cell lines stably expressing the sensor protein would be beneficial, as transiently transfected cells should usually be assayed within 24 to 48 h after transfection [301]. The plasmids for HyPerC and HyPerC121s were kind gifts of *Dr. Miklós Geiszt* (Semmelweis University, Budapest, Hungary). The attempt to create stably HyPer expressing cells, by selection of transiently transfected cells with the antibiotic G418 (see chapter 5.8.2.1.4. for details) failed to provide stably expressing clones. Therefore a lentiviral transfection protocol was applied. I am grateful for the work of *Nóra Kucsma* and *Áron Szepesi* on creating the following stably transfected cell lines: MES-SA-259.75, MES-SA-259.200, MES-SA/Dx5-259.75, MES-SA/Dx5-259.200 (with 259 encoding the viral supernatant of HyPerC, and the number behind the applied volume in  $\mu$ L), MES-SA-260.75, MES-SA-260.200, MES-SA/Dx5-260.75, MES-SA/Dx5-260.200 (with 260 encoding the viral supernatant of HyPerC121s, and the number behind the applied volume in  $\mu$ L).

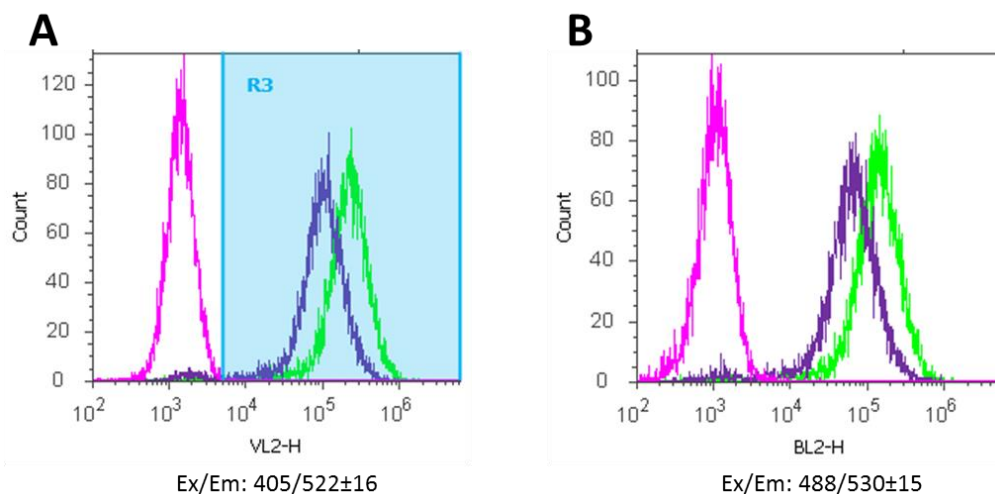


**Figure 62:** Histograms of transfected MES-SA-HyPerC cells after sorting detected using two filters to address the two excitation maxima (**A**: 405 nm, **B**: 488 nm). The auto-fluorescence of non-transfected MES-SA cells is shown in magenta, cells transfected with 75  $\mu$ L viral supernatant (MES-SA-HyPerC-75 / messa.259.75) are shown in violet, cells transfected with 200  $\mu$ L (MES-SA-HyPerC.200 / messa.259.200) are shown in green.

Due to their basal fluorescence, the transfected cells could be sorted by flow cytometry. Exemplarily, Figure 62 shows histograms of sorted MES-SA cells transfected with two different volumes of HyPerC viral supernatant in comparison to the non-transfected cells. Transfection with the mutant HyPerC121s and of MES-SA/Dx5 cells resulted in comparable histograms, as shown in the methods part (Chapter 5.8.2.1.5).

Due to the ratiometric use of the sensor, the results should not depend on the transfection efficiency [297]. Since initial trials incorporating all eight cell lines were in agreement with this, in the following studies only those cells transfected with 200  $\mu$ L supernatant were used. As MES-SA and MES-SA/Dx5 are adherent cell lines, the signal induction of H<sub>2</sub>O<sub>2</sub> on the transfected cells was initially investigated on cells that were allowed to attach to 96 well plates overnight. In order to optimize fluorescence intensity, the cell number was adjusted to reach confluency for the time of the measurement (40.000C/W were used). In order to avoid putative disturbance through the components of the medium, measurements were performed in PBS buffer. Upon baseline measurement, H<sub>2</sub>O<sub>2</sub> was added, and changes in emission at 525 nm upon excitation at 420 and 490 nm were followed. Figure 63 A shows the fold change of the ratio between both measurements compared to the baseline over time for a representative experiment upon treatment with 200  $\mu$ M H<sub>2</sub>O<sub>2</sub>. While a signal is induced in cell lines transfected with HyPerC, cell lines transfected with the mutant HyPerC121s served as the negative control and did not show signal induction. The induced oxidative stress is compensated for by the antioxidant system of the cells, provoking a decrease of intracellular H<sub>2</sub>O<sub>2</sub> levels and concordantly in signal intensity over time.

In Figure 63 B the dose-dependent signal inductions in MES-SA and MES-SA/Dx5 cells are compared at the time point of 5 min. Based on the three independent experiments (performed in duplicate) presented in this figure, no significant difference can be observed between the cell lines. Even though the measurements performed with the plate reader appeared promising, a drawback of this method is the time shift between the measurements of each sample with the different excitation wavelength, that provide data for one ratiometric data point. This time-shift is not negligible and might cause an uncertainty in kinetic measurements when fast changes occur.

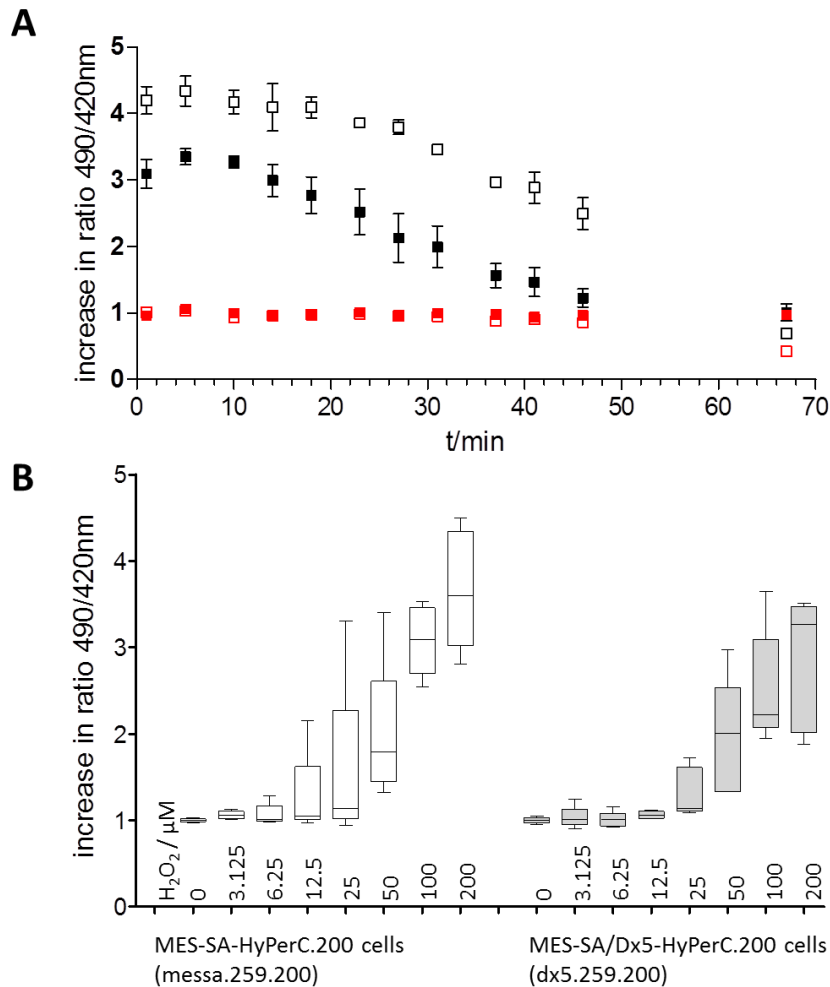


**Figure 63:** (A): kinetic of a representative experiment using MES-SA and MES-SA/Dx5 cells transfected with 200  $\mu\text{L}$  of HyPer containing virus. Cells were seeded to a 96 well plate (40.000 cells/well), and allowed to attach overnight. Before addition of the compound, culture medium was replaced by PBS buffer. Fluorescence was followed at 525 nm upon excitation at 420 and 490 nm prior to and after addition of H<sub>2</sub>O<sub>2</sub> (200  $\mu\text{M}$  are shown in the figure). MES-SA cells are depicted with open symbols, MES-SA/Dx5 with filled symbols. Results of HyPerC transfected cells are shown in black, results of the mutant HyPerC121s transfected cells in red. (B): Increases in fluorescence ratio values are shown for the time point of 5 min incubation with the indicated concentration of H<sub>2</sub>O<sub>2</sub>. Data of 3 independent experiments performed in duplicates are shown.

A more reliable measurement can be achieved with a spectrofluorimeter, with which two wavelengths can be measured almost simultaneously. While the microplate reader allowed the measurement of attached cells, in this method, cells are measured in suspension. The cell density was optimized to 1.5 Mio cells per milliliter. In order to allow a more physiologic condition, HPMI buffer was applied (containing Ca<sup>2+</sup>, Mg<sup>2+</sup> and glucose, see chapter 5.1.). Representative measurement curves with this system are shown in Figure 64 for the single



wavelengths (panel A) and the ratiometric evaluation (panel B) of transfected MES-SA cells. As in the previous setup, cells transfected with the mutant HyPerC121s served as a negative control, and did not show any change in signal upon addition of  $\text{H}_2\text{O}_2$ . Furthermore it can be seen in panel B, that the ROS scavenger NAC is able to attenuate the signal induced in MES-SA-HyPerC cells.

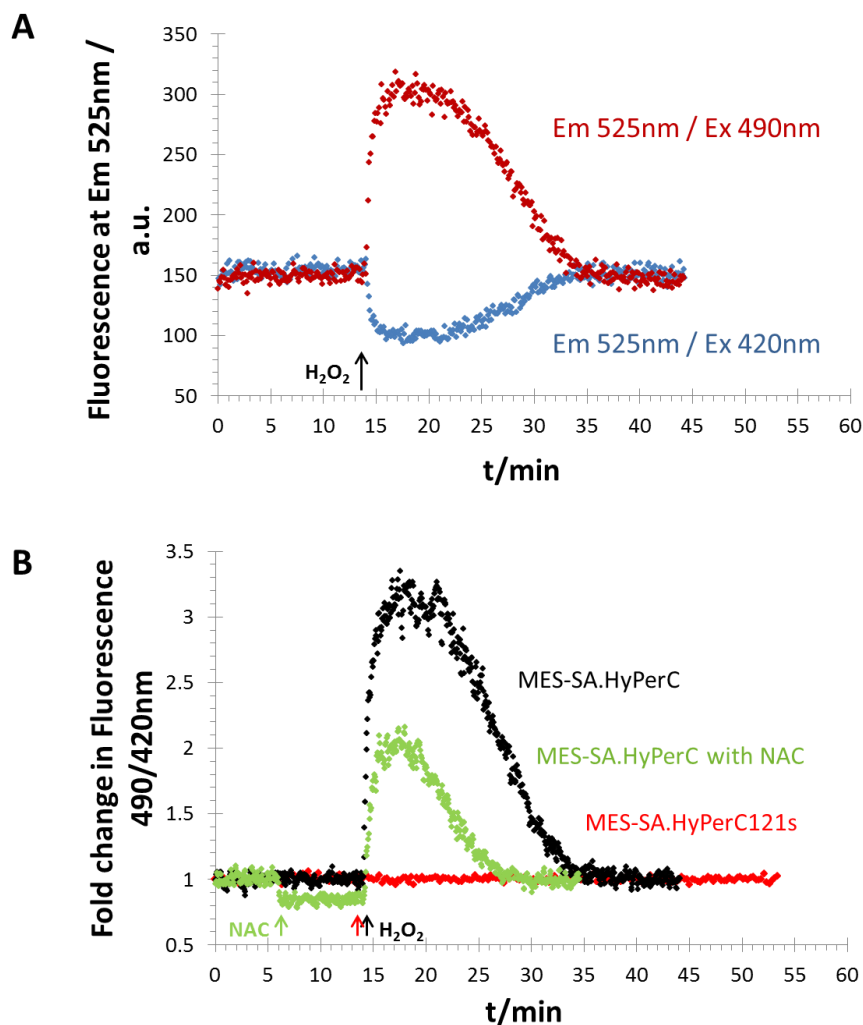


**Figure 64:** Representative curves showing the kinetic of the response of transfected MES-SA cells to  $50 \mu\text{M}$   $\text{H}_2\text{O}_2$ . Panel A shows the changes in fluorescence at  $525 \text{ nm}$  upon excitation with the single wavelengths ( $490 \text{ nm}$  is shown in red,  $420 \text{ nm}$  is shown in blue), panel B shows the changes in the ratiometric evaluation for the same measurement of MES-SA. HyPerC cells (black) in comparison to the mutant MES-SA.HyPerC121s (red). Furthermore the effect of NAC on the signal induced in MES-SA.HyPerC is shown (green).

The real time monitoring measurement technique using the spectrofluorimeter opens up new readout possibilities for the investigation of the kinetics of the intracellularly induced  $\text{H}_2\text{O}_2$  levels in different cell lines. To quantify observed differences in curve kinetics, the Hill equation was applied as a mathematical model to describe the decay of the induced signal. Curve parameters were defined as indicated in Figure 65. Due to the fast response to the addition of  $\text{H}_2\text{O}_2$ , for the increase in signal no reliable fit could be found.

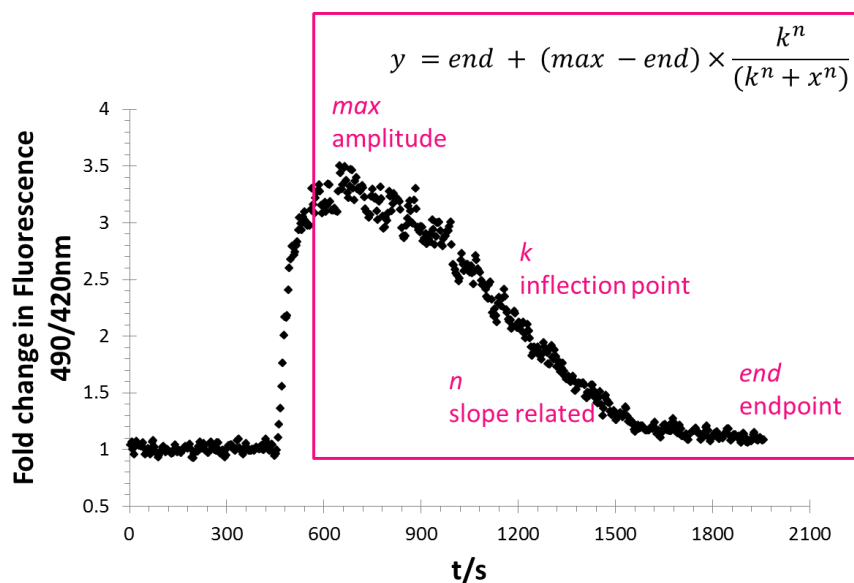


**Figure 65:** The *Hill equation* was used to describe the time dependent decay of the signal. Definition of curve parameters for a representative response to treatment with  $50 \mu\text{M H}_2\text{O}_2$ : The amplitude is described by the value *max*, the inflection point of the curve, which is showing the time dependence in seconds is described by *k*. Further variables in the equation are the endpoint *end* and a slope related factor *n*.

As stated above, the ratiometric measuring mode makes the signal independent of HyPer-protein expression levels. Different cell densities were applied in order to investigate the effect of cell numbers on signal reproducibility. While the curve parameters describing the amplitude (*max*), the endpoint (*end*) and the slope (*n*) of the curve were not markedly influenced, the inflection point *k* seemed to depend on the cell number, as shown in Figure 66. The high values of *k* in the figure result from the plot of time in the SI unit seconds.

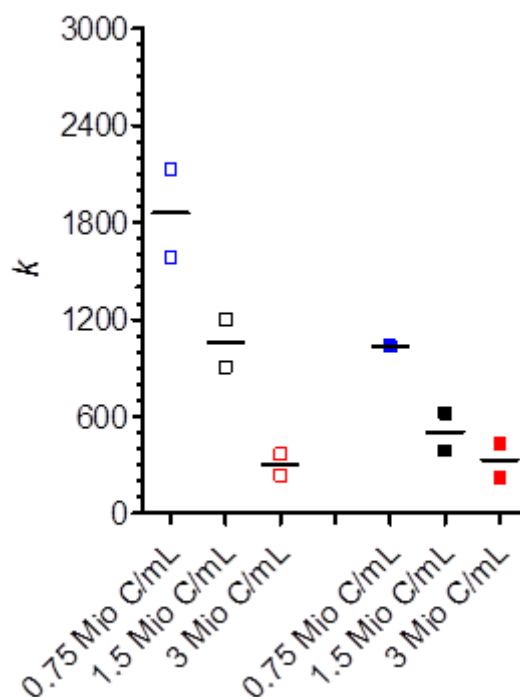


**Figure 66:** Impact of the applied cell number on the inflection point  $k$  in the response of HyPerC transfected MES-SA (open symbols) and MES-SA/Dx5 cells (filled symbols) toward 50  $\mu\text{M}$   $\text{H}_2\text{O}_2$ .

The dependence of  $k$  on the cell density can be explained by the ability of a higher number of cells to metabolize externally added  $\text{H}_2\text{O}_2$  in a shorter time. Therefore, in the following measurements the cell number was kept constant at 1.5 Mio cells per milliliter. MES-SA and MES-SA/Dx5 cells transfected with HyPerC can be compared with regard to their response toward  $\text{H}_2\text{O}_2$  analyzing the introduced curve parameters. Figure 67 provides an overview over the characteristics of the response of the two cell lines toward 50  $\mu\text{M}$   $\text{H}_2\text{O}_2$ . As Figure 66 already suggests, there is a significant difference in  $k$  values between the sensitive and MDR cell line. The inflection point  $k$  represents the time, that the cells need, to cope with half of the induced stress. Comparing a number of independent experiments performed with MES-SA.HyPerC (33) and the MDR MES-SA/Dx5.HyPerC cells (45), the MDR cell line seems to be able to cope with the induced stress in a shorter time window compared to the sensitive counterpart (Figure 67 A). Co-administration of the antioxidant NAC, added some minutes prior to  $\text{H}_2\text{O}_2$ , accelerates the  $\text{H}_2\text{O}_2$  metabolism in MES-SA cells, but seems to have no significant effect on the speed of metabolism in MES-SA/Dx5 cells. In contrast, the amplitude of the induced signal ( $max$ , Figure 67 B) is attenuated by NAC in both cell lines. Similar to the differences observed in the inflection point, also the slope related factor  $n$  and the

endpoint of the measurement (*end*) seem to be different between MES-SA and MES-SA/Dx5 cells, yet, these differences are rather small (Figure 67 C,D). These differences, especially in the time, needed to cope with induced stress (*k*) and in the degree of induced signal (*max*) that could be observed between the cell lines and upon co-incubation with NAC, suggest a different redox homeostasis of the sensitive and MDR counterpart. In agreement with this, Wartenberg *et al.* reported a negative correlation between intracellular ROS levels and P-gp expression [22,274,302,303].

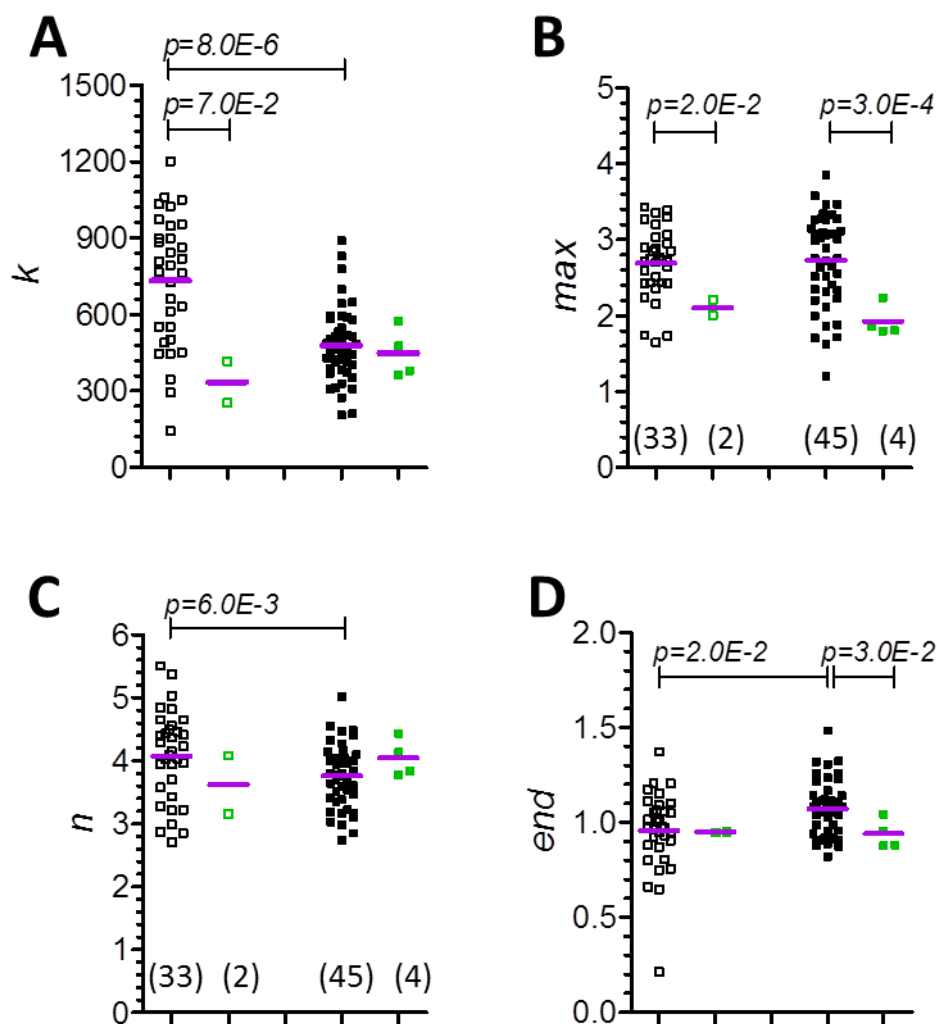


**Figure 67:** Curve parameters comparing HyPerC transfected MES-SA (open symbols) and MES-SA/Dx5 cells (filled symbols) in their response to 50  $\mu\text{M}$   $\text{H}_2\text{O}_2$ . Additionally, the effect of 1 mM NAC added prior to  $\text{H}_2\text{O}_2$  is shown (green symbols). Significance was calculated from unpaired t-tests. The number of the independent experiments is indicated in brackets.

In order to test, whether the observed differences in the cellular response to  $\text{H}_2\text{O}_2$  between MES-SA and MES-SA/Dx5 cells was dependent on the function of P-gp, the effect of Tariquidar was investigated. The inhibitor was administered either directly before the measurement (Figure 68 A,B) or cells were incubated with TQ for 72 h (Figure 68 C,D). As seen from the curve parameters  $k$  and  $max$  of these experiments, the currently available data do not allow a conclusion. Surprisingly, the curve parameters also changed in case of MES-SA cells. Further experiments would be needed to draw conclusions.

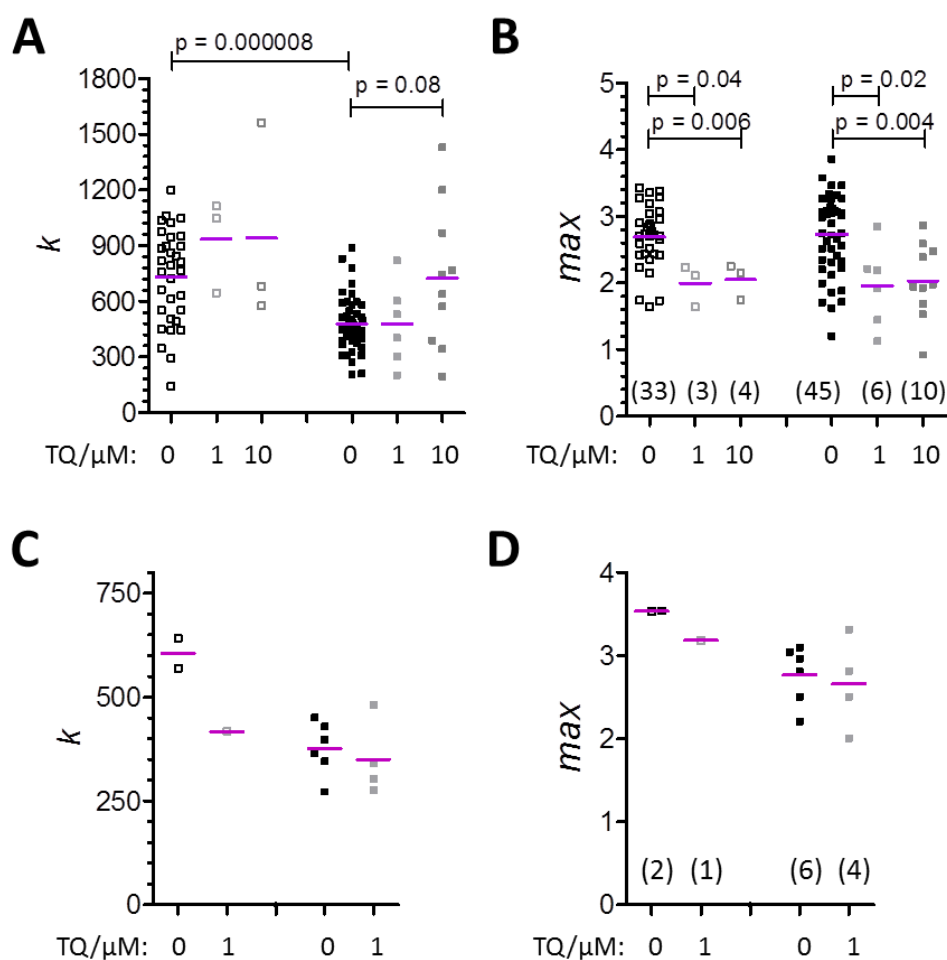


**Figure 68:** Curve parameters  $k$  and  $max$  comparing HyPerC transfected MES-SA (open symbols) and MES-SA/Dx5 cells (filled symbols) in their response to 50  $\mu\text{M}$   $\text{H}_2\text{O}_2$ . The effect of 1 or 10  $\mu\text{M}$  TQ, added 5 min (A, B) or 72 h (C, D) prior to  $\text{H}_2\text{O}_2$  is shown (grey symbols). The 72 h treatment was performed on 6 well plates, the untreated samples in this experiment are given as control values in these panels (in case of MES-SA cells in the presence of TQ over 72 h, a reliable curve fitting was only possible for one prepared sample). Significance was calculated from unpaired t-tests. The number of the independent experiments is indicated in brackets.

While the addition of extracellular  $\text{H}_2\text{O}_2$  was able to provoke a signal in the experimental setup, the 8-hydroxyquinoline derivatives **Q-1** to **Q-4** as well as some of their investigated iron and copper complexes did not induce signals of comparable patterns. In some cases, slight changes in signal intensity could be observed over a longer measurement time, yet these effects were not reliably reproducible.

Plumbagin (PG) proved to be a good control reagent for intracellular ROS induction in the DCFDA assay (Chapter 4.1.). Though, the species responsible for the induced oxidative stress is not specified in the literature. As shown in Figure 69, cells react to Plumbagin in a similar pattern as to the extracellularly added  $\text{H}_2\text{O}_2$ . The concentration that was needed to induce a curve of similar shape to the  $\text{H}_2\text{O}_2$  positive control was as low as  $2.5 \mu\text{M}$ , suggesting that the naphthoquinone is a very potent inducer of oxidative stress. This for the first time identifies the reactive oxygen species induced by Plumbagin to be  $\text{H}_2\text{O}_2$ . Unspecific effects could be excluded by the application of cells transfected with the mutant HyPerC121s. Furthermore, the presence of NAC attenuates the signal.

Even though the MDR selective ligands and their metal complexes did not result in an increase in intracellular  $\text{H}_2\text{O}_2$  levels, the application of Plumbagin shows, that the system is able to detect intracellularly induced changes in  $\text{H}_2\text{O}_2$  levels.

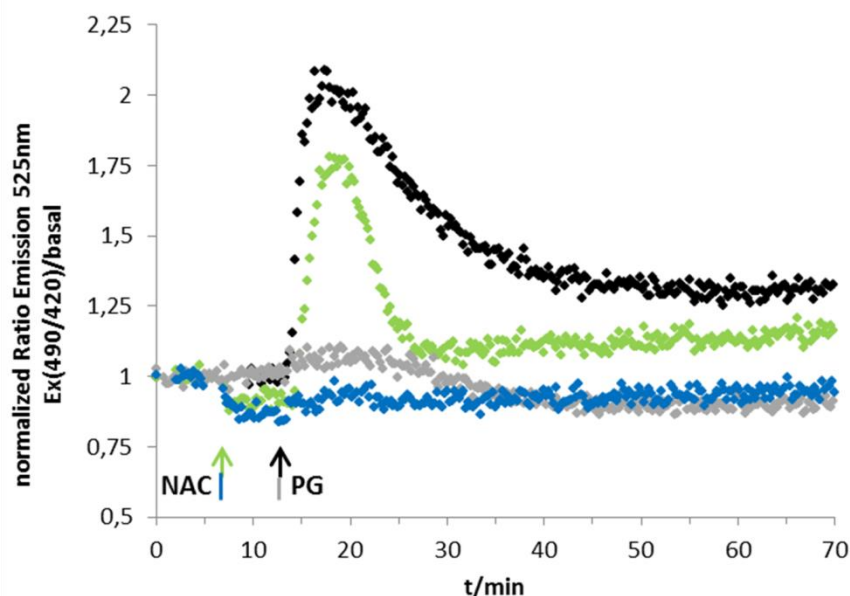


**Figure 69:** Intracellular  $\text{H}_2\text{O}_2$  levels measured with HyPer system upon addition of  $2.5 \mu\text{M}$  PG: MES-SA.HyPerC cells (black), in presence of NAC (green), MES-SA.HyPerC121s cells (grey), in presence of NAC (blue).

#### 4. Summary

The development of the multidrug resistant phenotype is a multi-factorial process [3]. The multiple changes that endow MDR cells with benefits in survival might also create vulnerabilities that can be exploited to selectively target resistant cancer cells [42]. Therefore, the application of such MDR selective agents appears to be a promising approach to overcome multidrug resistance in cancer.

In order to find P-gp mediated MDR selective agents, a panel of several cell lines and the application of a P-gp inhibitor should be considered:

Analysis of reported compounds, that were serendipitously found to have higher toxicity toward MDR as compared to sensitive cell lines, revealed that the reported selectivity seems to be related to cell-line specific alterations other than the expression and function of P-gp (chapter 3.1.1.). In contrast, compounds that were identified as a result of data analysis from several cell lines of different P-gp expression levels proved to be more potent in MDR cell lines as compared to their sensitive counterparts (chapter 3.1.2. – common project with *Szilárd Tóth, András Füredi, and Dr. Anna Lovrics*). Furthermore, the selectivity of those compounds could be abrogated in the presence of the P-gp inhibitor Tariquidar, confirming that the activity of the transport protein is indeed responsible for the increased toxicity.

Chelation is necessary for MDR selective anticancer activity – but not sufficient:

Despite some degree of chemical diversity, a commonality between the identified MDR selective agents is their ability to chelate metal ions. Especially thiosemicarbazones (like **I-a**) and 8-hydroxyquinoline derived Mannich bases (like **Q-3**) are prevalently found scaffolds. Modification of the compounds' scaffold in a way that disables the binding of metal ions leads to inactive compounds, with a lack of anticancer toxicity regardless of the resistance status of investigated cells. Nevertheless, by far not every chelator shows an enhanced activity toward MDR cell lines.

A focused library around the chemical space of the chelator **I-a** was designed and tested for the potential to overcome MDR (chapter 3.2.). While most of the scrutinized compounds from the focused library show a comparable toxicity throughout the investigated cell line panel, single compounds show an enhanced toxicity toward certain P-gp expressing cell lines. Though, this effect appears to be restricted to single cell line pairs and not reversible in the presence of the P-gp inhibitor Tariquidar.

Despite the lack of new generally MDR selective compounds in this library, structure-activity relationships can be observed with respect to the toxicity of the investigated compounds. In a comparison of chelators with different metal binding motives – namely pyridinyl TSCs (NNS), hydroxyphenyl TSCs (ONS), arylhydrazones (NNN), pyridinyl hydrazino-benzothiazoles (NNS) and hydroxyphenyl hydrazino-benzothiazoles (ONS) – NNS and NNN donor atom chelators show a superior activity over ONS chelators. Analysis of larger compound sets in the DTP database could confirm this trend. A putative explanation might be the preferential binding of these different chelators to certain metal ions, and the stabilization of different oxidation states of these ions according to the principle of hard and soft acids and bases (HSAB) [239,240]. Furthermore, a tendency could be observed for higher toxicity among NNS donors with imino carbon methylation. Though, a pairwise comparison of matched molecular pairs did not always follow this trend. For the ONS donor chelators, methylation of the imino carbon did not significantly influence the toxicity of the investigated compounds.

#### Differences between MDR selective and non-MDR selective chelators from a bioinorganic chemical viewpoint:

Experiments were designed and performed in order to find characteristics, which discriminate those chelators that show a preferential toxicity toward P-gp expressing cells from other non-MDR selective chelators.

In particular, a set of four structurally related compounds with a range of P-gp mediated MDR selectivity (**Q-1** < **Q-2** < **Q-3** < **Q-4**) was investigated in detail and compared to a compound with cell-line specific selectivity, identified in the library (**IV-b**). Despite the limited size of this compound set, that does not allow general conclusions, differences and trends could be observed, that are promising starting points for follow up studies on larger compound sets.

As implied in the introduction, chelators can have a wide range of various targets within biological setups including the inhibition of metallo-proteins, interfering with gene regulation and cell cycle progression [115,116]. By binding to intracellular metal ions chelators can deplete the labile ion pools, but also form biologically active complexes with a broad range of possible activities [124]. Since these complexes might be redox-active, also a disturbance of redox homeostasis and an interaction with the cellular antioxidant network is possible.

In order to investigate a putative involvement of reactive oxygen species (ROS) in the mechanism of (selective) toxicity of the compounds, the ability of the ROS-scavenger and potent antioxidant *N*-acetylcysteine (NAC), to protect cells from the toxic effect of the



compounds was investigated. Remarkably, NAC had different effects on the cellular response toward MDR selective and non-MDR selective compounds (chapter 3.4.1.). While the toxicity of the not MDR selective core structure **Q-1** was attenuated in the presence of NAC in both, MES-SA and MES-SA/Dx5 cells, NAC had no effect on the toxicity of the MDR selective agents **Q-3** and **Q-4**. The same trend could be observed in a subset of structurally unrelated chelators. The toxicity of the two MDR selective isatin- $\beta$ -thiosemicarbazones **I-a** and **I-d** was not influenced by co-administration of NAC. In contrast, cells were significantly protected against the toxic effect of the pyridinyl TSC **II-g**, the arylhydrazone **IV-b** and the pyridinyl hydrazino-benzothiazole **V-b**, which showed a cell-line specific selective toxicity.

These results might suggest a different interaction of MDR selective and non-MDR selective chelators with the intracellular redox homeostasis, which could be a consequential characteristic involved in the selective targeting of MDR cells.

In those cases, where NAC offered protection, redox active metal complexes might cause oxidative stress, which is antagonized by the ROS-scavenger. On the other hand, antioxidants might not only protect, but also sensitize cells to the toxic effect of metal complexes via an “activation by reduction” mechanism, following Fenton-like chemistry, that will increase the ROS levels and therefore cause cellular damage [86,116,135]. Since these two processes might occur in parallel, they might counteract each other, which might be a hypothetical explanation for the lack of detectable effect of NAC on the toxicity of MDR selective ligands.

The differential response of MDR selective and non-MDR selective ligands to the co-administration of NAC might be caused by different properties of the putatively formed metal complexes. In order to investigate this theory, complexes formed with iron (III) and copper (II) were characterized with regards to stability and redox activity.

The spider-net diagrams in Figure 70 summarize some characteristics that describe the metal binding and biological activity of the 8-hydroxyquinoline derivatives **Q-1** to **Q-4** and the pyrimidinylhydrazone **IV-b** (chapters 3.3. / 3.4.3.). A correlation of chemical properties like the  $pK_a$  values and metal binding abilities (expressed as  $pM^*$  values) with toxicity and selectivity can be found in the set of 8-hydroxyquinolines. While MDR selectivity seems to increase with decreasing  $pK_a$  and  $pM^*$  values, a clear tendency can be seen that derivatives with higher MDR selectivity show a higher preference for copper (II) over Fe (III) binding. The trend in copper binding preference seems to follow the trend of MDR selectivity. Though the size of the investigated compound set does not allow a general conclusion, these results might indicate an impact of copper chelation on the mechanism of (selective) toxicity.

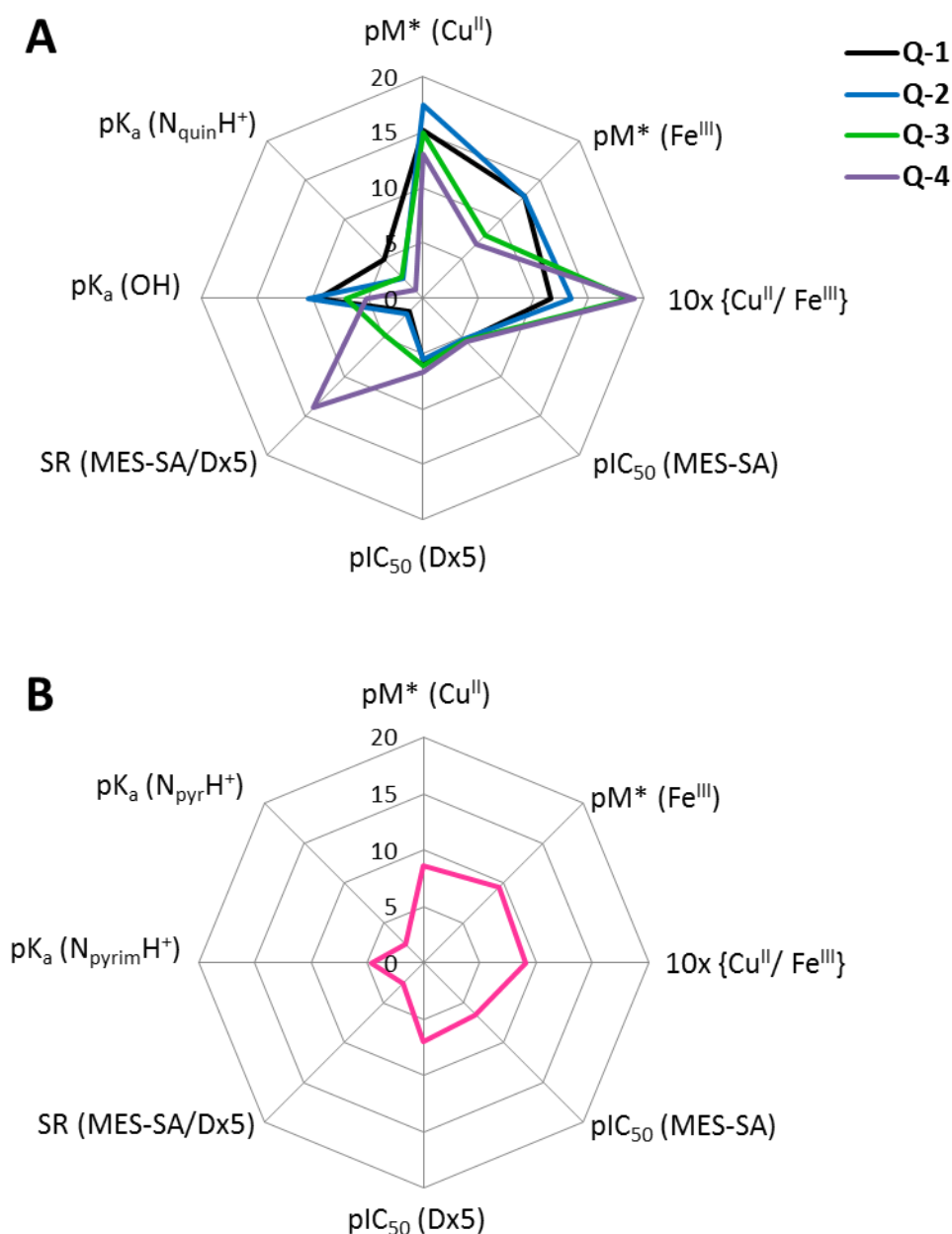


**Figure 70:** Bioinorganic chemistry in a spider diagram – comparison of biological and metal binding activity of the 8-hydroxyquinolines **Q-1** to **Q-4** (A) and the pyrimidinyl-hydrazone **IV-b** (B). The illustrated  $pK_a$  values were determined experimentally, except for the  $pK_a(N_{\text{quin}}H^+)$  of ligand **Q-4**, which was calculated using ChemAxon software [36].  $pM^*$  values represent the free metal ion concentration at physiological pH, which is present in a solution of  $1 \mu\text{M}$  metal salt in a ten-fold excess of ligand. As detailed in the text and methods part data characterizing the bioinorganic chemistry of compounds was obtained in collaboration with *Prof. Éva A. Enyedy* (Institute of Inorganic and Analytical Chemistry, University of Szeged, Hungary).

Since **IV-b** does not share the same scaffold, its  $pK_a$  values, on which the ligands' ability to bind to metal ions highly depends, belong to different chemical entities. Therefore this compound is shown separately in panel B of Figure 70. Remarkably, for this cell line dependently selective pyrimidinylhydrazone **IV-b**, a clear difference in the metal chelating properties could be observed in comparison to the 8-hydroxyquinoline set, since **IV-b** shows a slight preference for iron (III) over copper (II) binding. Thus, these observed trends in metal binding preferences (chapter 3.4.3.) provide a promising starting point for further investigations on larger compound sets.

In order to address the impact of iron and copper on the toxicity of the compounds, the toxicity of the ligands was investigated in the presence of non-toxic, fixed concentrations of  $FeCl_3$  or  $CuCl_2$  (chapter 3.4.2.). Depending on the investigated ligand, MDR and parental cell lines responded differently toward the co-administration of the metal ions.

Upon iron co-administration, the MDR cell line MES-SA/Dx5 was protected from the toxic effect of the MDR selective ligands Q-2, Q-3 and Q-4 in a dose dependent manner. The fold protection appeared to follow the trend of MDR selectivity, since in the presence of the highest applied  $FeCl_3$ -concentration (50  $\mu M$ ) MDR and parental cell lines were comparably sensitive to the toxic effect of the investigated ligands. In contrast, iron co-administration had no significant effect on the toxicity of the non-MDR selective core structure **Q-1**. Furthermore the sensitivity of parental MES-SA cells to the investigated 8-hydroxyquinoline set was comparable in the presence and in the absence of  $FeCl_3$ .

In contrast,  $FeCl_3$  offered protection to MES-SA cells against the pyrimidinylhydrazone **IV-b**, while it did not affect the sensitivity of the MDR cell line MES-SA/Dx5 against **IV-b**.

The rescuing effect of iron that could be observed in MDR cell lines in case of MDR selective ligands might indicate an involvement of iron-depletion in the mechanism of toxicity, which might be more pronounced in the MDR cell line as compared to the parental counterpart. On the other hand, an excess of iron (III) might also prevent the binding of the chelators to its target or to other metal ions (like copper) and therefore result in protection of the cells.

Also in the case of copper co-administration, differences could be observed in a cell line and compound specific manner. Both, parental and MDR cells, became more sensitive to the ligand in the presence of copper for the non-MDR selective quinoline **Q-1**, the "borderline" derivative **Q-2**, and the cell line dependently selective pyrimidinylhydrazone **IV-b**. In contrast, copper co-administration only sensitized the parental MES-SA cells toward the

MDR selective ligands Q-3 and Q-4, while the MDR cell line MES-SA/Dx5 did not show an increase in sensitivity.

Similar to the rescuing effect of FeCl<sub>3</sub>, also the differential response of the two cell lines toward the sensitizing by CuCl<sub>2</sub> causes a loss in selectivity in the presence of the highest applied the metal ion concentration (50 μM). In contrast to the protection by iron, a sensitizing effect of copper co-administration might be explained by an involvement of redox active complexes. The redox cycling of the complexes in Fenton-like reactions can harm the cells by the production of reactive oxygen species (ROS) – in particular the hydroxyl-radical [86,116,135].

The application of preformed complexes in fixed metal-to-ligand ratios confirmed the observations made on the co-incubation with a fixed metal concentration (chapter 3.4.4.): While iron complexes show a lower toxicity as compared to the free ligand (partially more pronounced in the parental cell line), copper complexes have an increased toxicity (especially in the MDR cell line). Furthermore, the inhibition of P-gp had similar effects on the toxicity of the complexes, as it had to the free ligands. While metal complexes formed with Q-1 were comparably toxic in the presence and in the absence of the inhibitor Tariquidar, the enhanced activity of both iron (III) and copper (II) complexes formed with the MDR selective ligands Q-3 and Q-4 seemed to require the activity of the transporter.

Taken together these results might point to an altered metal homeostasis in MDR vs. sensitive cancer cells [42]. Since the metal homeostasis is tightly linked to intracellular redox homeostasis, also an altered redox state of the cells might be a possible explanation for the differential response of the cells toward MDR selective ligands [88,116].

The redox properties of the iron (III) and copper (II) complexes formed with the respective ligands might result in a different ability to induce ROS, and therefore cause the differential cellular response toward the complexes in the presence of the ROS scavenger. Therefore the redox behavior of the complexes was investigated by cyclic voltammetry (chapter 3.4.5.1.) and by monitoring reactions with intracellular antioxidants (chapter 3.4.5.2.).

All formed complexes occurred to be redox active. In case of the iron complexes formed with the 8-hydroxyquinoline derivatives Q-1 to Q-4, the redox potential was shifted to the negative direction in comparison to the iron-aqua complex, indicating a preferential stabilization of the ferric (III) oxidation state. In contrast, the redox potential of iron complexes formed with the

NNN-donating pyrimidinylhydrazone **IV-b** was more positive than the aqua complex, indicating a stabilization of the ferrous (II) oxidation state.

The reactions of the copper complexes were irreversible (**Q-1** to **Q-4**) or quasi-reversible (**IV-b**) under the applied conditions. Yet, reduction potentials were found to be (much) more negative than that of the copper aqua complex.

Monitoring of reactions with intracellular antioxidants in a buffered solution serves as a model of intracellular conditions. While under the applied conditions, GSH was not able to reduce the investigated iron (III) complexes, it underwent redox reactions with the copper complexes formed with the investigated ligands. The observed re-oxidation upon addition of H<sub>2</sub>O<sub>2</sub> suggests the reversibility of the reaction, enabling intracellular redox cycling of the investigated copper (II) complexes and Fenton-like chemistry.

In order to investigate the relevance of the redox activity of the complexes *in vitro*, co-incubation experiments were performed with NAC, pyruvate and DTT. The toxicity of some iron complexes (mostly of **Q-2**) was markedly reduced in the presence of the antioxidants (chapter 3.4.6.). This ostensible contradiction to the lack of observed interaction with GSH in the monitored reactions might show a weakness of the model, since many factors will influence the intracellular redox reactions (e.g. actual concentrations and pH).

In case of the copper-complexes, the cellular response to most complexes was not affected by the addition of antioxidants. An exception is the [Cu(**Q-4**)] complex, which exhibits a slightly increased toxicity toward MES-SA/Dx5 cells in the presence of NAC.

These observations might underline the “Janus-face” like character of the antioxidant: while on one hand it can scavenge reactive oxygen species, on the other hand, it might induce a mechanism of “activation by reduction”, and increase the oxidative stress leading to increased cellular damage. While the lack of effect of antioxidants on the toxicity of most copper complexes might of course mean a real lack of effect, it might also be caused by parallel processes that counteract each other.

It is noteworthy, that both effects of the antioxidants (protection against iron-complexes and sensitization against the copper-complex of **Q-4**) seem more pronounced in MES-SA/Dx5 cells as compared to the parental MES-SA cells.

#### Techniques for the measurement of ROS were established:

In order to further investigate the hypotheses about the involvement of reactive oxygen species (ROS) on the toxicity of the investigated ligands and complexes, and the differential

response of parental and MDR cell lines, the detection and monitoring of ROS on a cellular level would be eligible.

Therefore, two complementary measurement techniques were established (chapter 3.5.). While the application of the redox-sensitive dye DCFDA can detect a broad range of ROS, it is also prone to artefacts (as discussed in chapter 3.5.1.). Due to an interaction of compounds with the assay reagent, the ROS induction by the free ligands as well as the complexes formed with ligands Q-1 to Q-4 could not reliably be investigated. In contrast, **IV-b** and its complexes did not show unspecific interactions with the reagent. For this ligand and its complexes an involvement of ROS in the mechanism of toxicity of the complexes formed with the pyrimidinylhydrazone could be concluded from the measurements. The two-faced character of NAC becomes apparent from its effect on the induced fluorescent signal upon treatment with different concentrations of the  $[\text{Cu}(\text{IV-b})]^{2+}$  complex. While NAC reduces the signal intensity up to concentrations of 50  $\mu\text{M}$  of the complex, at higher complex concentrations, the co-administration of NAC increases the signal. This indicates a higher ROS production, which might putatively be the result of the “activation by reduction” mechanism.

The application of the fluorescent sensor protein HyPer provides a more specific measurement method [156,295,300]. Upon selective oxidation by hydrogen peroxide the spectral properties of the sensor change in a way that the fluorescence intensity in one maximum (emission 525 nm / excitation 500 nm) increases while it decreases in the other (emission 525 nm / excitation 420 nm). This property enables a ratiometric measurement of intracellular  $\text{H}_2\text{O}_2$  levels in real-time. As detailed in the methods part (chapter 5.8.2.), cell lines stably expressing HyPerC and the mutant HyPerC121s, which can serve as a control to exclude unspecific effects [156], were created with the help of *Nóra Kucsma*, *Áron Szepesi* and *Zsuzsana Nagy* (plasmids were kind gifts of *Miklós Geiszt*, Semmelweis University, Budapest, Hungary). Stably transfected MES-SA and MES-SA/Dx5 cell lines were characterized and their differential response to  $\text{H}_2\text{O}_2$  was investigated using a plate reader and a spectro-fluorimeter measurement setup. The “half-live” of the induced signal ( $k$ ) and its amplitude ( $max$ ) were defined as important characteristics describing the cellular response toward intracellular  $\text{H}_2\text{O}_2$  (-induced stress). Comparison of multidrug resistant MES-SA/Dx5 to parental MES-SA cells revealed, that the antioxidant system of both cell lines might be different, enabling the resistant counterpart to cope with induced stress faster than their sensitive counterpart.

These results show the previously suggested difference in redox homeostasis of the two investigated cell lines. In comparison to MES-SA cells, the higher capability of MES-SA/Dx5 cells to cope with oxidative stress might be indicative of a stronger antioxidant system.

Following a mechanism of “activation by reduction” of formed copper complexes [86,116,135], the potentially stronger antioxidant system of MES-SA/Dx5 (in comparison to the parental MES-SA cells) cells might therefore result in a more pronounced production of ROS following the Fenton-like chemistry of formed metal complexes with the MDR selective ligands.

The toxicity increasing effect of copper co-administration only in MES-SA cells, but not in the MDR MES-SA/Dx5 cells, might be in agreement with this. Also the metal binding preference of MDR selective ligands for copper over iron and the observed ability of the copper complexes to redox cycle in biologically relevant conditions are in line with this theory.

The respective preferences in metal binding and the redox properties of the formed complexes might be relevant descriptors of the MDR selective ligands. In order to find out, if these descriptors are putative discrimination factors of MDR vs. non-MDR ligands, a higher number of compounds should be investigated.

While experiments investigating the effect of P-gp activity and MDR selective compounds on the intracellular H<sub>2</sub>O<sub>2</sub> levels with the HyPer measurement system did not provide conclusive results so far, the naphthoquinone Plumbagin, which was reported to have anticancer activity via ROS formation, induced a signal that was comparable to that of H<sub>2</sub>O<sub>2</sub> already in the low micro-molar concentration range. This shows that an intracellular response in H<sub>2</sub>O<sub>2</sub> levels can be provoked by the addition of compounds. Therefore the established measurement system provides a useful tool for further investigation of the impact of MDR selective compounds on the H<sub>2</sub>O<sub>2</sub> levels and on the intracellular antioxidant network. This tool also enables the cellular monitoring over longer incubation time periods.

## 5. Tumor models and biological methods

### 5.1. Cell lines, media and buffer

The human ovarian carcinoma cell lines *A2780* and the Doxorubicin selected multidrug resistant counterpart *A2780adr* were obtained from ECACC, UK, (*A2780*: No. 93112519, *A2780adr*: No. 93112520) [304], and cultivated in RPMI (Sigma Aldrich, Germany) supplemented with 10% fetal bovine serum and 50 unit/mL penicillin and streptomycin, respectively (Sigma Aldrich, Germany).

The human uterine sarcoma cell lines *MES-SA* and the Doxorubicin selected *MES-SA/Dx5* were obtained from ATCC (*MES-SA*: No. CRL-1976™, *MES-SA/Dx5*: No. CRL-1977™) and cultivated in Dulbecco's Modified Eagle Medium (DMEM, Sigma Aldrich, Hungary) [24,171].

The Madin–Darby canine kidney (*MDCK-II*) cell line was genetically modified by *Dr. Dóra Türk*, to overexpress cDNA-derived P-gp. by the Sleeping Beauty (SB) transposon-based gene delivery system, using the 100x hyperactive SB transposase [305]. Cells were co-transfected with the SB transposon vector containing the wild type human MDR1 cDNA [306] and the SB transposase vector construct, using the Lipofectamine 2000 reagent (Life Technologies) in accordance with the manufacturer's instructions. Transfected cells were sorted by flow cytometry (FACS Aria High Speed Cell Sorter, Beckton-Dickinson) based on the cell surface expression of MDR1/ABCB1. Protein expression was measured by antibody labeling using the human MDR1/ABCB1 specific monoclonal antibody MRK16 (Abnova). In order to obtain homogenous transgene positive cell population, sorting procedure was repeated 4 times in 2-week intervals [89]. *MDCK-II* and *MDCK-II-ABCB1* cells were cultured in DMEM medium.

The human cervix carcinoma cell line *KB-3-1* and the Vinblastine selected *KB-V1* as well as the human ovarian carcinoma cell line *OVCAR-8* and the Doxorubicin selected counterpart *NCI/ADR-RES* stably expressing fluorescent label proteins (see chapter 5.6.3.) were kind gifts of *Dr. Michael M. Gottesman*, National Institutes of Health [172,307]. *KB-3-1* and *KB-V1* cells were cultivated in DMEM. *OVCAR-8* and *NCI/ADR-RES* cells were maintained in RPMI medium (Life Technologies, Hungary) supplemented with 10% fetal bovine serum, 5 mmol/L glutamine, and 50 unit/mL penicillin and streptomycin, respectively (Life Technologies, Hungary).



DMEM media (Sigma Aldrich, Hungary) were supplemented with 10% fetal bovine serum, 5 mmol/L glutamine, and 50 unit/mL penicillin and streptomycin, respectively (Life Technologies).

The most frequently applied buffers in the biological testing were phosphate-buffered saline (PBS) and HPMI. Buffers were prepared in 10x concentrated stock solutions and diluted for usage. The pH was adjusted to 7.4 using NaOH and HCl. The ingredients are given in Table 16 [308].

**Table 16:** Composition of PBS and HPMI buffers [308].

	PBS		HPMI	
	conc mmol/L	g/L for 10x stock	conc mmol/L	g/L for 10x stock
NaCl	136.89	80.00	119.77	70.00
KCl	2.68	2.00	5.00	3.73
Na <sub>2</sub> HPO <sub>4</sub>	9.86	14.00	5.00	7.10
KH <sub>2</sub> PO <sub>4</sub>	1.41	2.00		
MgCl <sub>2</sub>			0.85	0.81
CaCl <sub>2</sub> ·2H <sub>2</sub> O			0.04	0.06
HEPES			10.00	23.83
NaHCO <sub>3</sub>			10.00	8.40
Glucose			10.00	18.00

## 5.2. Cell culturing

All cell lines were cultivated under aseptic conditions using a laminar air flow cabinet and sterilized equipment (serological pipets and pipet tips), work surfaces were chemically disinfected prior to and following work using 70% ethanol and (in Budapest additionally) exposed to UV-light at the end of each working day [309–311]. Cells were kept in the indicated media at 37 °C, 5% CO<sub>2</sub> with a relative humidity of 96%. All used cell lines display adherent growth properties. Therefore, the described general cultivation protocol is valid for all cell lines used in this study. Dependent on the required cell numbers, cells were grown in T-25, T-75, or T-175 culture flasks. The used volumes for the respective culture flask sizes are given in the table below (Table 17). Cells were sub-cultivated after reaching a confluency level of 80-90%. Briefly, after removal of the culture medium, the cell layer was rinsed with PBS buffer, in order to remove traces of serum which contains trypsin inhibitor. The buffer was removed and the indicated volume of Trypsin (0.25% (w/v))-EDTA (0.53 mM) (Sigma,

Germany / Hungary) solution was added and allowed to incubate until the cell layer started to disperse. Cells were aspirated by gently pipetting with fresh growth medium. Cells were transferred to falcon tubes and sub-cultivated in a 1:4 to 1:12 ratio or used for assays after washing with PBS buffer.

The general washing procedure consisted of a centrifugation of cell suspension with 281 x g for four minutes, following by resuspension of the cell pellet in PBS buffer, a repeated centrifugation step, and the resuspension of the pellet in the desired medium (buffer or culture medium). Further mentioning of washing steps will refer to this general procedure if not stated otherwise.

**Table 17:** Volumes of Media, Trypsin and buffer used for the different cell culture flasks

Flask	Surface area / mm <sup>2</sup>	Total Volume of medium / mL	Initial cell number / Mio Cells	Harvested cell number / Mio Cells	Volume of PBS for washing	Volume of Trypsin-EDTA / mL	Volume of Medium for Resusp. / mL
T-25	2.500	5-6	0.5-1	3-5	3 mL	0.75	4
T-75	7.500	15-18	1.5-3	5-10	5 mL	2.0	5
T-175	17.500	23-26	3-5	15-20	8 mL	3.0	7

### 5.3. Determination of cell numbers

To determine the cell numbers in the suspension after harvesting, two instruments were used. For cell counting with the *CASY@1 TT* (Schärfe, Germany) instrument, 20 µL of the cell suspension were transferred to 10 mL of the sterile filtered isosmotic electrolyte solution *CASY@ton* and counted with the indicated instrument. The *CASY* technology is an electric field multi-channel cell counting system that combines the measurements of particle size and resistance based on the interaction of the cells with the applied low voltage field in the capillary. Based on the number and extent of changes in resistance upon flow of cell suspension through the capillary the instrument creates a histogram of cellular size distribution.

For determination of the cell numbers using the *BioRad TC10™* instrument (Biorad, Hungary), samples were prepared by mixing the cell suspension with Trypan Blue 0.4% stock solution (Sigma Aldrich, Hungary) in a 1:1 ratio, in order to and exclude stain dead cells.

Ten  $\mu\text{L}$  of the mixture were transferred to respective counting slides (*Biorad TC10 dual-chamber counting slides* (Biorad, Hungary)) and measured. The instrument uses an autofocus technology and a digital image analysis algorithm to provide the number of cells and the percentage of viability (which is based on the Trypan blue staining).

#### **5.4. *Cryo-conservation and revitalization of cells***

For the long term storage of cellular samples, aliquots of 2-4 Mio Cells were frozen in the respective culture medium supplemented with 40% FBS containing 10% DMSO. Aliquots of 1 mL of the suspensions were filled into screw cap cryo vials (Greiner bio-one, Germany / Corning, New York) and cooled down to  $-80^{\circ}\text{C}$ , using a *Cryo Freezing Container* (Nalgene, Sigma, Hungary) filled with isopropanol, which allows a constant cooling rate of  $1^{\circ}\text{C}/\text{min}$ . After that, vials were transferred to a tank of liquid nitrogen.

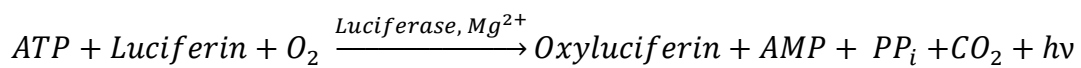
To revitalize the cells, vials were thawed in a  $37^{\circ}\text{C}$  water bath, transferred into falcon tubes containing 5 mL of culture medium and centrifuged to remove the DMSO. After resuspension of the cell pellet in fresh medium, cells were transferred to culture flasks and cultured as described above. In order to ensure the resistant phenotype of drug selected cell lines, at the second passage after thawing, cells were selected for two passages in medium supplemented with 500 nM Doxorubicin for A2780adr and Dx5 cells, or 300 nM Vinblastine for KB-V1 cells. Before using the cells for experiments, cells were grown without selection agents for at least one passage.

#### **5.5. *Testing for Mycoplasma***

Mycoplasma are the smallest known Gram-negative bacteria and represent a common kind of contamination in cell culture [312]. Firstly noted in the 1950s, until today mycoplasma became probably the most prevalent and serious microbial contaminant of cell culture systems used in research and industry today [309]. They can pass through pores of more than 0.1  $\mu\text{m}$  in diameter and often stay unnoticed due to the lack of visible signs of the infection [309,313]. Still they alter many host cell functions including growth, morphology, metabolism, the genome and antigenicity, leading to unreliable experimental results [309,310,313,314]. In order to ensure that cell lines are free of contamination good tissue culture practice and frequent

testing is required [309]. A specific method to test for mycoplasma is the MycoAlert kit [309,313].

It exploits the activity of certain mycoplasmal enzymes, which are set free upon lysis with the assay reagent. The enzymes react with the assay substrate, catalyzing the conversion of ADP to ATP:



Comparing the ATP levels of a sample before and after the addition of the mycoplasma specific MycoAlert™ substrate, a ratio can be obtained which is indicative of the presence or absence of mycoplasma [313]. Cells were tested for mycoplasma infections one or two passages after thawing using the MycoAlert™ mycoplasma detection kit (Lonza, Hungary) [313]. From a confluent culture flask 1 mL medium was transferred to an Eppendorf tube and centrifuged for 5 minutes at 129 x g. 35 µL of the upper layer were transferred to an OptiPlate (white 96 well plate, Perkin Elmer, Hungary) and 35 µL of MycoAlert reagent was added to each well. After 5 minutes of incubation the first luminescence measurement was performed (measurement 1). 35 µL of MycoAlert substrate were added to each well and incubated for 10 minutes. Luminescence was measured (measurement 2) and the ratio of both measurement values was calculated:

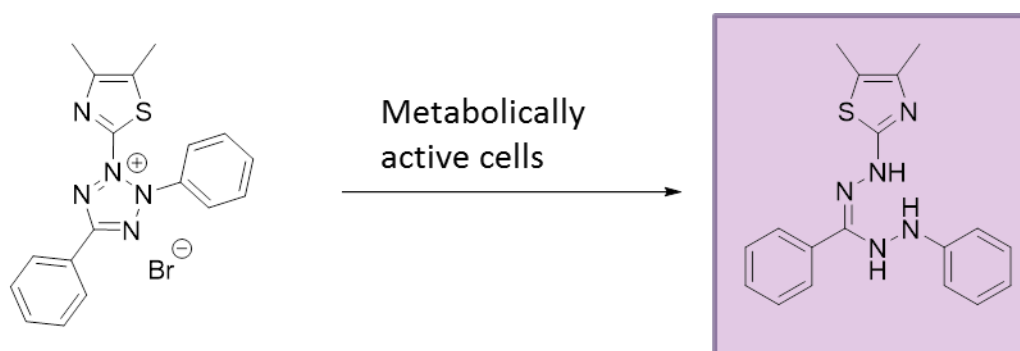
$$X = \frac{\text{measurement 2}}{\text{measurement 1}}$$

If the ratio X was smaller than 1, the sample was negative for mycoplasma. If it was between 1 and 1.3, the determination should be repeated at the next passage, a ratio higher than 1.3 indicates an infection of the investigated cell line. Only non-infected cell lines were used.

## 5.6. Measurement of cell viability

### 5.6.1. MTT viability assay

The MTT viability assay was developed by Mosmann *et al.* in 1983 as a quantitative colorimetric assay for the measurement of survival and proliferation of mammalian cells [315]. Within living cells the pale yellow tetrazolium salt MTT (3-(4,5-dimethylthiazol-2-yl)-2,5-diphenyl tetrazolium bromide) is reduced to a dark blue formazan as depicted in Scheme 5, which can be detected spectrometrically. The amount of formed formazan correlates with the number of metabolically active cells over a wide range. The cellular reduction has been suggested to involve mitochondrial mechanisms like mitochondrial NADPH and succinate [316,317] and mitochondrial enzymes like succinate dehydrogenase [318]. Yet, MTT reduction was also detected in other cellular compartments [319] and connected to (microsomal) NADH and NADPH [316,320,321].



**Scheme 5:** Reduction of MTT reagent in living cells

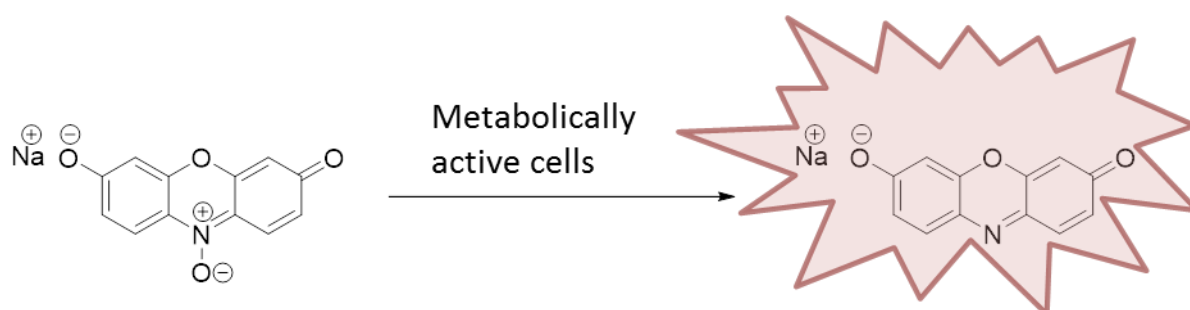
MTT viability assays were performed as described earlier with minor modifications [55,322]. Briefly, cells were seeded into 96 well tissue culture plates (CytoOne Starlab, Hamburg, Germany/ Sarstedt, Newton, USA / Orange, Braine-l'Alleud, Belgium) in the appropriate density which was optimized to reach 90% confluence in the untreated wells by the end of the incubation time and allowed to attach for 6-12 h. For the different cell lines these cell numbers 5000 cells per well for MES-SA and Dx5, as well as for KB-3-1 and KB-V1 cells, 10000 cells per well for A2780 and A2780adr cells. After attachment of the cells, test compounds were added to achieve the required final concentration in a final volume of 200  $\mu$ L per well. After an incubation period of 72 h, the supernatant was removed and fresh medium supplemented with the MTT reagent (0.83 mg/mL) was added. Incubation with MTT

at 37 °C was terminated after 1 h by removing the supernatants and lysing the cells with 100  $\mu$ L DMSO per well. Viability of the cells was measured spectrophotometrically by absorbance at 540 nm using either a *Perkin Elmer Victor X3*, *Perkin Elmer EnSpire* or a *BMG POLARstar* microplate reader. Data was background corrected by subtraction of the signal obtained from unstained cell lysates and normalized to untreated cells.

### 5.6.2. Presto Blue viability assay

An alternative to the measurement of cell viability by MTT assay is the utilization of a resazurin based assay [323–325]. Even though resazurin powder is commercially available, several assay kits are on the market containing the dye in performance verified quality together with additional agents, that stabilize the signal and reduce the background [317]. The used assay kit had the brand name PrestoBlue (A-13262, Life technologies, Budapest, Hungary).

Similar to the MTT assay, the PrestoBlue assay is based on an intracellular redox reaction. Here, the blue, non-fluorescent 7-hydroxy-10-oxidophenoxazin-10-ium-3-one (resazurin) is reduced to the pink, fluorescent 7-hydroxyphenoxazin-3-one (resorufin) as depicted in Scheme 6 [326,327]. The product can be detected both by absorbance or fluorescence measurements, with the latter method showing a higher sensitivity [317,327–330]. An advantage of the PrestoBlue over the MTT assay is, that the cells do not have to be lysed, The reduction of resazurin can be mediated by mitochondrial reductases, cytochromes, several cytosolic enzymes, as well as by the intracellular reductants NADH, NADPH, FADH, FMNH [330].



**Scheme 6:** Reduction of PrestoBlue reagent in living cells

Cells are seeded in plates and treated with test compounds as described for the MTT assay (chapter 5.6.1.). After 72 h of incubation with the test compounds, supernatants were either removed, and a diluted solution of the PrestoBlue reagent (10%) was added to each well, or in the case, where an interaction of the test compound with the resazurin dye could be excluded, the reagent was directly added to yield a final concentration of 10% (as in case of Triton-X-100 viability assays). After incubation with the reagent for one hour at 37 °C emission was measured at 579 nm upon excitation at 540 nm using either a *Perkin Elmer Victor X3* or *Perkin Elmer EnSpire* microplate reader.

### 5.6.3. *mCherry, eGFP, DsRed fluorescence assays*

An alternative method which avoids the addition of exogenous assay substrate compounds to indicate viability relies on the expression and retention of an intracellular fluorescent protein, produced by a transfected cell [331]. Besides of avoiding putative side reactions, another advantage of the fluorescent protein labeling is, that cells can be monitored in real time without altering the system in any way, other than illuminating with light of the proper excitation wavelength [307,331]. Damages in the cell membrane of dying or dead cells will cause a leak-out of the soluble fluorescent proteins [332]. The basis of this technique was established by Shimomura *et al.*, who isolated the green fluorescent protein (GFP) from the jellyfish *Aequorea victoria* in 1962, characterized its optical properties, and, in 1979, identified the chemical nature of the fluorophore [333]. Following the recombinant expression of GFP in *E. coli* Chalfie *et al.* envisioned that GFP could be used as a vital marker for the in situ monitoring of cell growth [334]. Tsien *et al.* further characterized the fluorophore and could engineer further fluorescent proteins with different colors based on GFP and DsRed [333,335–337]. The latter protein was isolated from a coral *Discosoma* species [338,339]. In 2008, the Nobel Prize in Chemistry was awarded to those three researchers for the discovery and development of the green fluorescent protein, GFP [333].

The fluorescent label proteins used in this study were eGFP, DsRed-II and mCherry. Stable transfectants of *OVCAR-8-DsRed-II* and *NCI/ADR-RES-eGFP* (kind gifts Dr. Michael M. Gottesman, National Institutes of Health, Bethesda) were obtained by lipofectamine transfection upon by selection in presence of G418 [307]. MES-SA-mCherry and Dx5-mCherry cells were created in the laboratory of *Katalin Németh* (Hungarian Academy of Sciences, Budapest) by a lentiviral method. Briefly, they inserted the sequence of the

fluorescent protein mCherry (kind gift of Erwin Welker, Hungarian Academy of Sciences, Budapest) into the pRRL lentiviral plasmid vector containing the EF-1 $\alpha$  (human elongation factor-1 $\alpha$ ) promoter (obtained from Didier Trono, Lausanne, Switzerland) using XbaI-SalI restriction sites, replacing the originally present GFP sequence. Cells were treated with the virus containing supernatant with a multiplicity of infection of four (4 virus particles per cell). Stable transfectants were sorted twice with a *BD FACS Aria* cell sorter (BD, Budapest, Hungary), keeping only the cells with high fluorescence intensity. Thus, no antibiotic selection was needed to eliminate non transfected cells.

For the viability assays, the stably transfected cells are seeded in plates and treated with test compounds as described for the MTT assay (chapter 5.6.1.). After 72 h of incubation the fluorescence of the respective protein was measured with a *Perkin Elmer Victor X3* or *Perkin Elmer EnSpire* microplate reader.

For eGFP transfected cells the emission was measured at 535 nm upon excitation at 490 nm, for DsRed-II transfected cells the emission was measured at 579 nm upon excitation at 540 nm and the fluorescence of mCherry transfected cells was measured at 610 nm upon excitation at 585 nm.

#### **5.6.4. Evaluation of dose response curves**

In order to compare the effectiveness of the investigated compounds, half maximal growth inhibitory concentrations (IC<sub>50</sub>) were determined with the help of *Prism* software [340]. The raw data was normalized to measured controls representing 100% cell viability for untreated and 0% viability for dead controls (10% DMSO, or high concentration of toxic compounds, respectively). The normalized data was analyzed with a sigmoidal dose-response model using the four parameter logistic equation:

$$y = Bottom + \frac{(Top - Bottom)}{1 + 10^{(LogIC_{50} - X) \cdot Hillslope}}$$

The Top represents the Y-value at the top plateau, which is reached at 100% cell viability; the bottom plateau is reached at 0% viability. The Hillslope describes the steepness of the curve.



### 5.7. Verification of MDR phenotype

The phenotype of the resistant cells was verified in two ways. In each cytotoxicity assay additionally to the test compounds, a P-gp substrate was used as described in 5.7.1.

Furthermore the MDR phenotype and the P-gp expressing cell population were ascertained by the functional Calcein AM assay as detailed in 5.7.2.

#### 5.7.1. Using P-gp substrates as control in viability assays

The phenotype of the resistant cells was verified in each cytotoxicity assay by using at least one of the P-gp substrates Doxorubicin, Rhodamine-123 or Vinblastine. Figure 71 shows representative dose response curves for the three cell line pairs MES-SA vs. MES-SA/Dx5 (Figure 71 A), A2780 vs. A2780adr (Figure 71 B) and KB-3-1 vs. KB-V1 (Figure 71 C) obtained by MTT assays (see Chapter 5.6.1.).

It is apparent from the figure, that the dose response curves of the resistant cell lines (filled symbols) are shifted to higher concentrations as compared to the curves of the parental cells (open symbols).

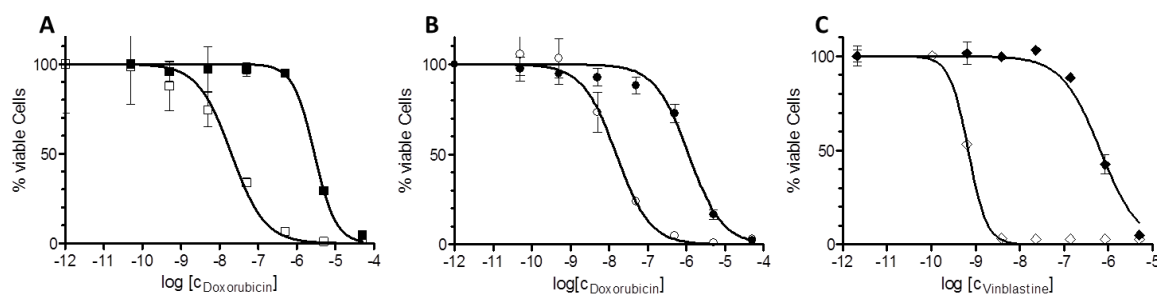
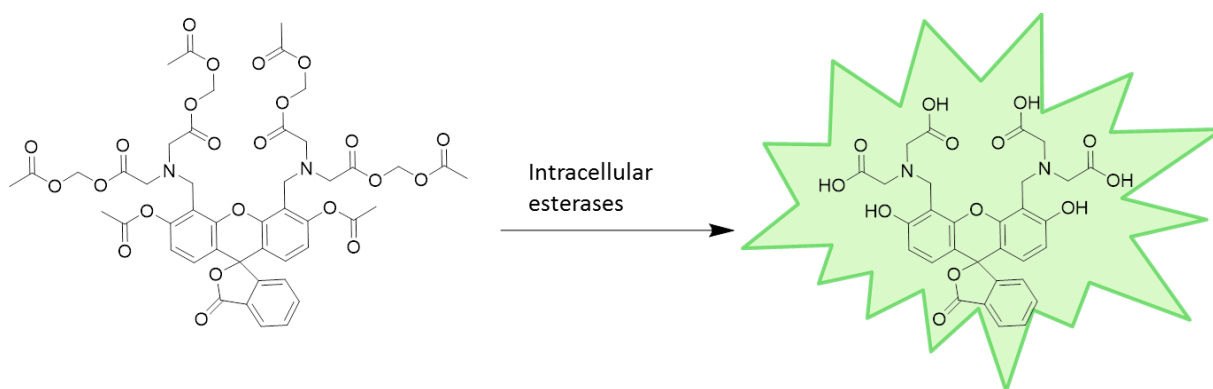


**Figure 71:** MDR cells show decreased sensitivity toward P-gp substrates Doxorubicin and Vinblastine as compared to parental counterparts. Dose-response curves obtained by MTT assay (Chapter 5.6.1.) are shown for **A:** MES-SA (open squares) and MES-SA/Dx5 (filled squares), **B:** A2780 (open circles) and A2780adr (filled circles), **C:** KB-3-1 (open diamonds) and KB-V1 (filled diamond).

### 5.7.2. Calcein AM accumulation assay

An alternative diagnostic method to study the function of P-gp is to measure the accumulation of the fluorescent cell viability marker, Calcein. Calcein acetoxymethyl ester (AM) is a non-fluorescent substrate of P-gp. As shown in Scheme 7, upon cleavage of the ester bonds by intracellular esterases, the free Calcein has a high fluorescence intensity in the visible range and is not transported by P-gp. Thus changes in Calcein uptake can be easily visualized by fluorescence measurements using microplate readers or conventional flow cytometry [341,342].



**Scheme 7:** Cleavage of Calcein AM ester bonds by intracellular esterases delivers the fluorescent Calcein, which can be detected by plate readers and flow cytometers to study the function of P-gp.

After counting, a cell suspension was prepared for each cell line, containing 7.5 Mio cells in serum free medium, and transferred to a FACS tube. The FACS tubes were centrifuged at 250 x g for 3 minutes and the supernatant was discarded. Due to the shape of the tube, in this procedure 50  $\mu$ L of supernatant remained, therefore 250  $\mu$ L of serum free medium were added to obtain a total volume of 300  $\mu$ L of cell suspension. This volume was distributed to three FACS tubes, each containing 2.5 Mio cells in 100  $\mu$ L per FACS tube. Out of the three, one sample served as an unstained control for auto-fluorescence of the cells and did not receive further treatment. One sample was treated with the P-gp inhibitor Verapamil, while the other one served as a vehicle control and obtained the same amount of DMSO as the Verapamil sample: Treatment solutions were prepared freshly from 50  $\mu$ L serum free medium per sample supplemented with 1  $\mu$ L of either a 20 mM Verapamil stock solution in DMSO or DMSO alone for the vehicle control. In order to ensure a sufficient amount of treatment solution, the amount for one additional sample was prepared in each case. Since the uptake and accumulation of Calcein AM are time sensitive processes, a strict time schedule was

followed: Upon addition of the 50  $\mu$ L treatment solution, the sample was vortexed and set into a water bath shaker, thermostated to 37 °C. The time that passed between two sample treatments was exactly 20 seconds. After the 5 minutes incubation time, the first sample was treated with 50  $\mu$ L of a Calcein AM treatment solution (100  $\mu$ M in serum free medium), vortexed and put back to the water bath shaker. The order and the time shifts between the treated samples were kept as in the first treatment. After 10 minutes of incubation, the cellular reaction was stopped by addition of 1 mL ice cold PBS per sample (again keeping the 20 seconds time shifts). Samples were centrifuged at 250 x g and 4 °C for 3 minutes, and after one washing step, the supernatant was discarded and the cell pellet was resuspended in 250  $\mu$ L of ice cold PBS. Samples were kept on ice until measured by flow cytometry on a *FACS Calibur* instrument (BD Biosciences, USA) or an *attune* flow cytometer [343].

The data was visualized with the help of the program *Cell-Quest Pro* (BD Biosciences, USA). Figure 72 shows an example experiment using MES-SA and MES-SA/Dx5 cells. In the so called dot plots cellular detection is aligned with respect to cellular size (Forward scatter, FSC: low angle light scatter, the light that strikes the cell) and granularity or structural complexity inside the cell (Side scatter, SSC: scattered at larger angles). A “gate” was set, selecting only viable cells according in the auto-fluorescence sample. Dead cells generally have a lower size and intracellular complexity, and in a simple Calcein AM staining experiment they should be low in quantity, but where necessary, they could be detected and excluded by staining with the *TO-PRO®-3* DNA dye (Life Technologies, USA).

Histograms, as shown in Figure 72, visualize the frequency distribution of fluorescently labelled cells. It can be seen that P-gp expressing MES-SA/Dx5 (Figure 72 F) and KB-V1 (Figure 72 I) cells accumulate less amount of fluorescent Calcein as compared to their P-gp negative MES-SA (Figure 72 E) and KB-3-1 (Figure 72 G) counterparts. The histogram of P-gp positive cells is shifted to the right. The impact of P-gp on this accumulation is proven by the impact of the P-gp inhibitor Verapamil, which shifts the histogram to the direction of P-gp negative cells. The described panels show homogenous cell populations, while panel H shows the histograms of KB-V1 cells, which partially lost the P-gp upon long term cell culture, resulting in a heterogenous cell population.

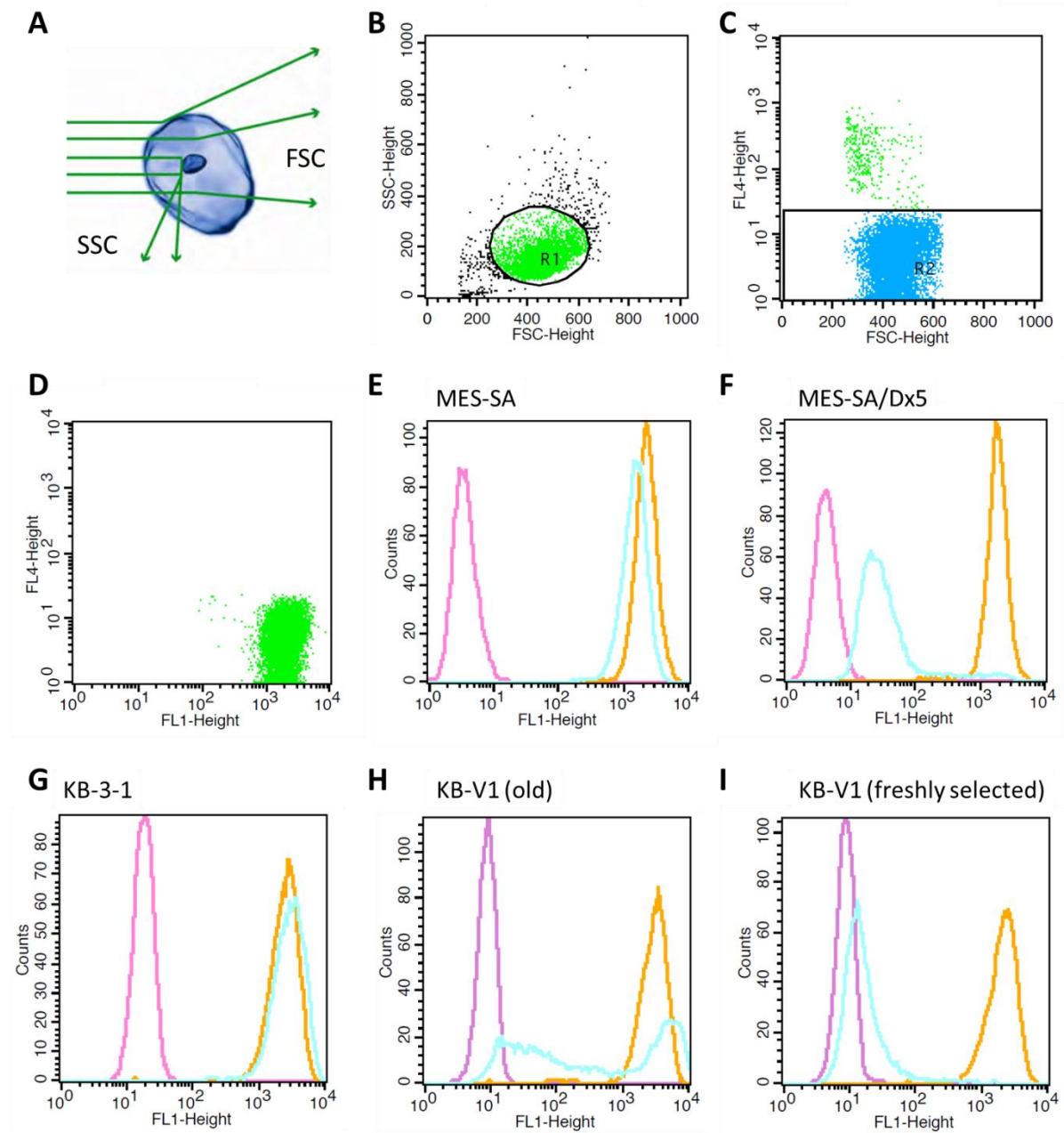


**Figure 72:** Calcein AM accumulation measurement used as a rapid and sensitive flow cytometric assay for studying the function of P-glycoprotein on MES-SA and MES-SA/Dx5 cells. A: Visualization of Forward (FSC) and Side Scatter (SSC), modified from [343], B: Dot plot of MES-SA cells after staining with Calcein-AM and *TO-PRO*<sup>®</sup>-3 DNA dye, C: Gating out dead cells with *TO-PRO*<sup>®</sup>-3 (fluorescence channel FL4) staining, D: Calcein-AM stained cells (fluorescence detection in FL1), only living cells (no fluorescence in FL4); Histograms of P-gp negative MES-SA (E) and KB-3-1 (G) as well as of P-gp positive MES-SA/Dx5 (F) and KB-V1 (H,I) cells. Magenta curves show the autofluorescence of unstained cells, cyan curves show histograms of Calcein-AM stained cells, orange curves show cells that had been pre-incubated with Verapamil.

## 5.8. ROS determination

### 5.8.1. DCFDA assay

The use of DCFDA is the most frequently applied method for the measurement of reactive oxygen species. As illustrated in Figure 73, the principle of this assay is based on the fluorescence detection of the oxidation product of the non-fluorescent Dichlorofluorescein (DCF-H). It is applied in an esterified form as the Diacetate (DCFDA), which is non-fluorescent and readily taken up by cells. Intracellularly, the reagent is cleaved by esterases to DCF-H. Upon oxidation by ROS the fluorescent Dichlorofluorescein (DCF) is formed [271,272].

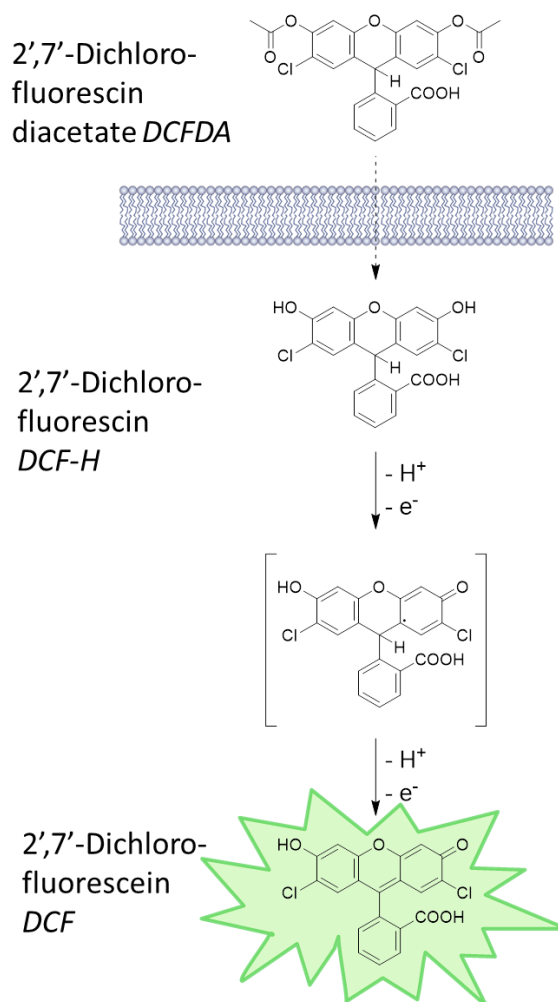


**Figure 73:** Assay principle of ROS detection. The non-fluorescent Dichlorofluorescein diacetate (DCFDA) ester is taken up by the cells and cleaved by intracellular esterases to Dichlorofluorescein (DCF-H). Upon oxidation by ROS the fluorescent Dichlorofluorescein (DCF) is formed, which can be measured with the microplate reader [271,272].

As detailed in the results section, the protocol for the measurement of reactive oxygen species (ROS) using DCFDA was thoroughly optimized on the basis of literature reports [135,275,283]. After harvesting and washing with PBS buffer, cells were re-suspended in PBS in a density of approximately 3 Mio cells per mL and incubated with 10  $\mu$ M DCFDA (a 10 mM stock solution was used, preferably prepared freshly or stored at -20 °C, keeping freeze-re-thawing cycles at a minimum) in a water bath shaker at 37 °C for 30 min. After washing with PBS, cells were plated to 96 well plates in a density of 20,000 cells/well in PBS. In each experiment a control reagent was applied, namely hydrogen peroxide or *tert*-butyl hydroperoxide. Additionally, for each tested compound, cell free controls were included using DCFDA solution in buffer to test for interaction of the test compounds with DCFDA (on the exemplary plate map in Figure 74: columns 1 and 2). Also untreated cells and DCFDA solutions were used, in order to distinguish the compound induced signal from unspecific signals as detailed in the results section (row A in Figure 74).

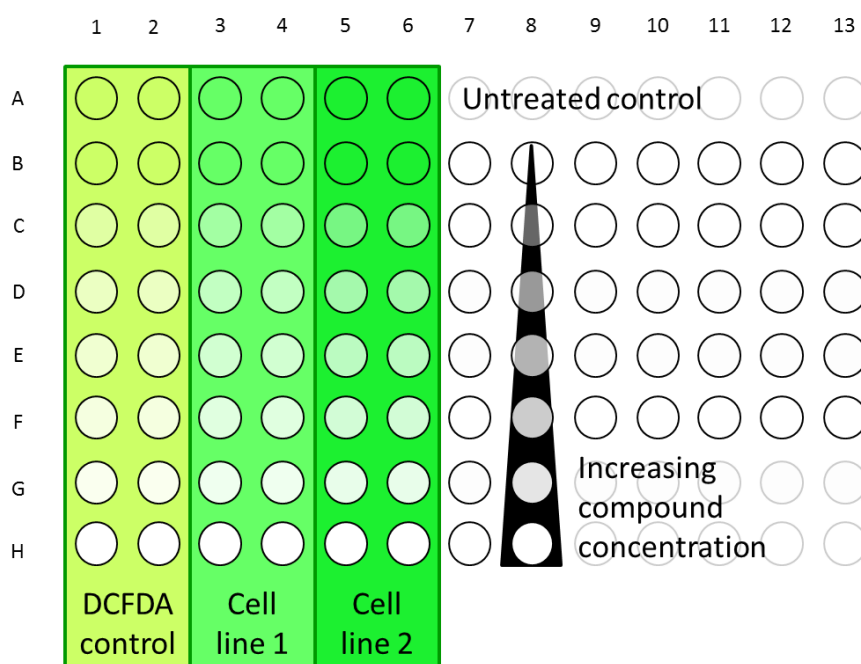


**Figure 74:** exemplary plate layout for a typical DCFDA measurement.

The fluorescence of DCF was detected at an emission wavelength of 535 nm upon excitation at 485 nm. Basal fluorescence was measured at  $t_0$  and upon addition of the test compounds in different concentrations, the changes in fluorescence were monitored in time intervals of 10 or 20 min after addition of the test compound. Measurements were performed at 14 time points

$t_x$  where  $x = 1$  referred to the measurement after 10 min or 20 min, and  $x = 14$  to that after 140 min or 280 min, respectively. Data was expressed as fold change of fluorescence compared to the basal levels (measurement of Sample at  $t_0$ ) and to the untreated cell control at the respective time-point (measurement of untreated control at  $t_x$ ) by the following normalization:

$$y = \frac{\text{Sample data}(t_x)}{\text{Sample data}(t_0) \cdot \text{Control data}(t_x)}$$

### 5.8.2. HyPer fluorescent protein

Changes in intracellular  $\text{H}_2\text{O}_2$  levels can be tracked in real time using HyPer, a ratiometric genetically encoded fluorescent probe [297]. The fluorescence properties of circular permuted (cp) fluorescent proteins are sensitive to protein conformation. The fusion of cpYFP (yellow fluorescent protein) with the OxyR-RD regulatory domain of *E. coli* OxyR provides a sensor protein, which will show increased fluorescence upon selective oxidation by hydrogen peroxide [295]. The spectral properties of the reduced and oxidized sensor enable a ratiometric measurement. Stably transfected cell lines would be beneficial for the investigation of the effect of compounds on intracellular ROS – or  $\text{H}_2\text{O}_2$  – levels, since transiently transfected cells have to be assayed within 24 to 48 h after transfection [301].

#### 5.8.2.1. Preparation of stably HyPer-expressing cells

Several people participated in the preparation of stably transfected cell lines, and I would like to acknowledge their work. The plasmids encoding the  $\text{H}_2\text{O}_2$  sensitive fluorescent proteins HyPerC and the mutant HyPerC121s were kind gifts of *Dr. Miklós Geiszt* (Semmelweis University, Budapest, Hungary). I want to thank *Zsuzsanna Nagy* (working group of *Dr. Gergely Szakács*) for supervising me in performing the gene amplification and purification of the plasmids, and *Nóra Kucsma* (working group of *Dr. Gergely Szakács*) and *Áron Szepesi* (working group of *Dr. Katalin Német*) for performing the subsequent steps from the cloning of DNA into a lentiviral vector to the transduction and sorting of MES-SA and MES-SA/Dx5 cells.

### 5.8.2.1.1. Transformation into Top10 competent E.coli cells

In order to have sufficient DNA material, the first step of the protocol was the amplification of the received plasmids. For this purpose the DNA was transformed into *Top10* competent *E. coli* cells (Life Technologies, Hungary) [344]. Two vials with each 100  $\mu\text{L}$  cell suspension were taken from  $-80\text{ }^{\circ}\text{C}$  and allowed to thaw on ice. 1  $\mu\text{L}$  of the respective plasmid solution (with a DNA content of 1.4  $\mu\text{g}/\mu\text{L}$  in case of HyPerC, and 0.55  $\mu\text{g}/\mu\text{L}$  in case of HyPerC121s plasmids) was added to either of the vials and incubated on ice for 30 minutes. A  $42\text{ }^{\circ}\text{C}$  heat-shock was applied to the vials for exactly 2 minutes, following the immediate placement on ice for 2 minutes [344,345]. After addition of 900  $\mu\text{L}$  of lysogeny broth (LB) medium [346], the vials were incubated in a water bath shaker at  $37\text{ }^{\circ}\text{C}$  for 1 hour. 100  $\mu\text{L}$  of the respective suspensions were plated out each on a 10 cm diameter kanamycin containing LB agar plate and incubated at  $37\text{ }^{\circ}\text{C}$  overnight with the agar side up and the lid side down. The remaining suspension was stored at  $4\text{ }^{\circ}\text{C}$  until the end of the procedure.

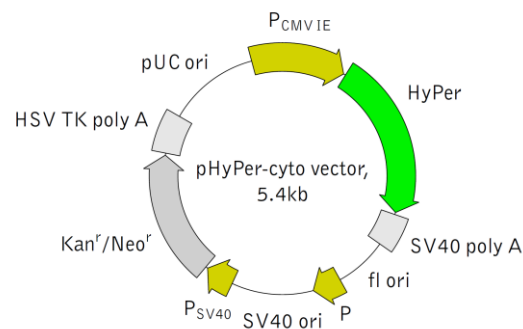


**Figure 75:** HyPerC-vector sequence as provided by Evrogen [347].

As depicted in Figure 75, the original plasmids contain a sequence for kanamycin resistance [347]. Therefore, only transformed bacteria will be able to grow on the kanamycin containing plates.

On the next day, one colony was picked per plate using a 200  $\mu\text{L}$  pipet tip. The tip was transferred into a 50 mL falcon tube containing 10 mL of LB medium. In this (not to tightly closed) tube bacteria were allowed to grow at  $37\text{ }^{\circ}\text{C}$  for an additional 24 hours. The agar plates were stored at  $4\text{ }^{\circ}\text{C}$  until the end of the procedure.



#### 5.8.2.1.2. Isolation and Purification of amplified plasmid DNA

Plasmid DNA was isolated and purified from the bacteria using the *QIAprep Spin Miniprep Kit* (QIAGEN, Hungary) [348]. The process is based on the selective alkaline denaturation of high molecular weight DNA over closed circular double-stranded DNA. Upon re-neutralization the chromosomal DNA renaturates to precipitate as a clot, while the plasmid DNA stays in the supernatant [349].

Underlined buffers and solutions were components of the *QIAprep Spin Miniprep Kit* (QIAGEN, Hungary) [348]. Prior to the procedure, buffers were controlled for precipitations. If precipitations were observed, buffers were heated to 37 °C to re-dissolve the components. The bacteria (as described in 5.8.2.1.1.) were centrifuged at 4500 x g at 25 °C for 3 min and the pellet was resuspended in 500 µL of buffer P1, which was prior supplemented with RNase A solution. 500 µL of buffer P2 was added and the vials were mixed thoroughly by inverting the tubes 4-6 times. After addition of 700 µL of buffer N3 the vials were mixed immediately and thoroughly by inverting the tubes 4-6 times, and centrifuged for 10 min at 17949 x g and 25 °C. The supernatants were pipetted to *QIAprep spin columns*, and centrifuged (17949 x g, 25 °C) for 1 min. The filtrate was discarded and the columns washed with 500 µL buffer PB, following centrifugation for 1 min. After discarding the filtrate, columns were washed with 750 µL buffer PE (prior supplemented with ethanol), centrifuged for 1 min, and after discarding of the filtrate again centrifuged for 1 min in order to remove residual washing buffer. The columns were eluted into a 1.5 mL Eppendorf tube by twice adding 50 µL of water and centrifuging for 1 min after a 1 min exposure time.

#### 5.8.2.1.3. Quantification of DNA

The amount of DNA in the samples was quantified using a NanoDrop™ 2000 (Thermo Scientific, Hungary). This device is a spectrophotometer capable of measuring small sample volumes [350]. From the absorbance spectra of a DNA sample, the quantity and purity of DNA can be estimated [351].

After cleaning of the optical pedestals of the instrument with 3 µL of MilliQ (MQ) water and a laboratory wipe, a background spectrum was recorded of 1 µL of the buffer used for the DNA-elution (MQ water). Following cleaning, the spectra of the DNA samples were measured. The instrument calculates the ratios of absorbance values recorded at 260/280 nm,

which is indicative for protein contaminations, and at 260/230 nm, which indicates other contaminations [350,351]. Results are given in Table 18.

**Table 18:** Volumes of Media, Trypsin and buffer used for the different cell culture flasks

plasmid	quantity / [ $\mu\text{g}/\mu\text{L}$ ]	Absorbance at $\lambda= 260\text{nm}$	Absorbance at $\lambda= 280\text{nm}$	Ratio 260/280 nm	Ratio 260/230 nm	purity
HyPerC	227.5	5.450	2.907	1.87	2.13	ok
HyPerC121s	276.6	5.531	2.960	1.87	2.12	ok

#### 5.8.2.1.4. Transient expression and selection in neomycin G418

A transient transfection with the plasmid was attempted in MES-SA, MES-SA/Dx5 and KB-3-1 cells following selection in presence of G418 [347]. *FuGENE®HD* (Promega, Hungary) was used as a transfection reagent [301].

Cells were seeded into 6 well plates with a density of 0.2 Mio cells/well in 2 mL of culture medium. After an overnight incubation, the medium was removed and replaced by 1.5 mL of serum free DMEM.

Per well an solution of 30 ng DNA (7.3  $\mu\text{L}$  of HyPerC DNA and 7.2  $\mu\text{L}$  of HyPerC121s DNA) in 100  $\mu\text{L}$  serum free IMDM (Life technology, Hungary) medium was prepared and mixed gently with 6  $\mu\text{L}$  of the room temperature thermostated *FuGENE®HD* reagent. Following a 30 minutes incubation time at room temperature the mixtures were added to the wells drop by drop and the cells were incubated at 37 °C overnight. At the next day 1.5 mL of complete DMEM medium was added per well. After yet another 24 hours incubation time the cells were spaced out in two wells in each 1.5 mL of DMEM. To one of them G418 was added in a concentration of 1 mg/mL, the other well served as an untreated control.

At confluence, cells were investigated for fluorescence behavior; the untreated control was frozen, while the cells under selection were seeded into a T-25 flask and kept under G418 selection for the next 10 days.

#### 5.8.2.1.5. Lentiviral transfection

As mentioned previously, the steps in this chapter were performed by *Nóra Kucsma* (working group of *Dr. Gergely Szakács*) and *Áron Szepesi* (working group of *Dr. Katalin Német*).

The DNA was cloned into a lentiviral vector, and lentiviral particles were produced in HEK293T cells transfected by the calcium phosphate co-precipitation method 2nd generation lentiviral system. Viral titers were estimated from HEK cells infected with a dilution series of HyPerC (259) and HyPerC121s (260) virus supernatants. For the transduction of MES-SA and MES-SA/Dx5 cells, cells were seeded into 6 well plates at a density of 250.000 cells per well and allowed to attach overnight. At the next day, cells were transduced in 1.5 ml fresh DMEM with 75 or 200  $\mu$ l virus supernatants and 15  $\mu$ l (0.6 mg/ml) polybrene. At the following day, cells were supplied with an additional 1.5 ml of fresh DMEM. The next day (day 4), cells were passaged into T-25 (day 8) and subsequently to T-75 (day 10) culture flasks. Upon confluency the cells were sorted FACS Aria for fluorescence at 488/530 ( $\pm$ 15) nm and seeded into T-25 flasks. Upon confluency cells were transferred to T-75 cells. Propagated sorted cells were frozen and measured at the *attune* flow cytometer [343]. The histograms characterizing the cells are shown in Figure 76.

#### 5.8.2.2. Real time measurement of intracellular $H_2O_2$ -levels

Additional to the microplate reader experiments (*PerkinElmer EnSpire*), real time measurements were performed with either a *PerkinElmer Luminescence Spectrometer LS50B* or a *Varian Cary Eclipse Fluorescence Spectrophotometer* in dual wavelengths kinetic mode. 4x optical acryl cuvettes were used (67.655, Sarstedt, Hungary). A homogenous distribution of cells in the suspension was ensured with a mini magnetic stir bar (length: 5 mm, diameter: 2 mm; 442-0361, VWR, Hungary). Fluorescence was detected simultaneously at the emission wavelength of 525 nm upon excitation at 490 and 420 nm and was followed over time. Times of compound addition were noted, in order to follow the kinetics of induced effects.

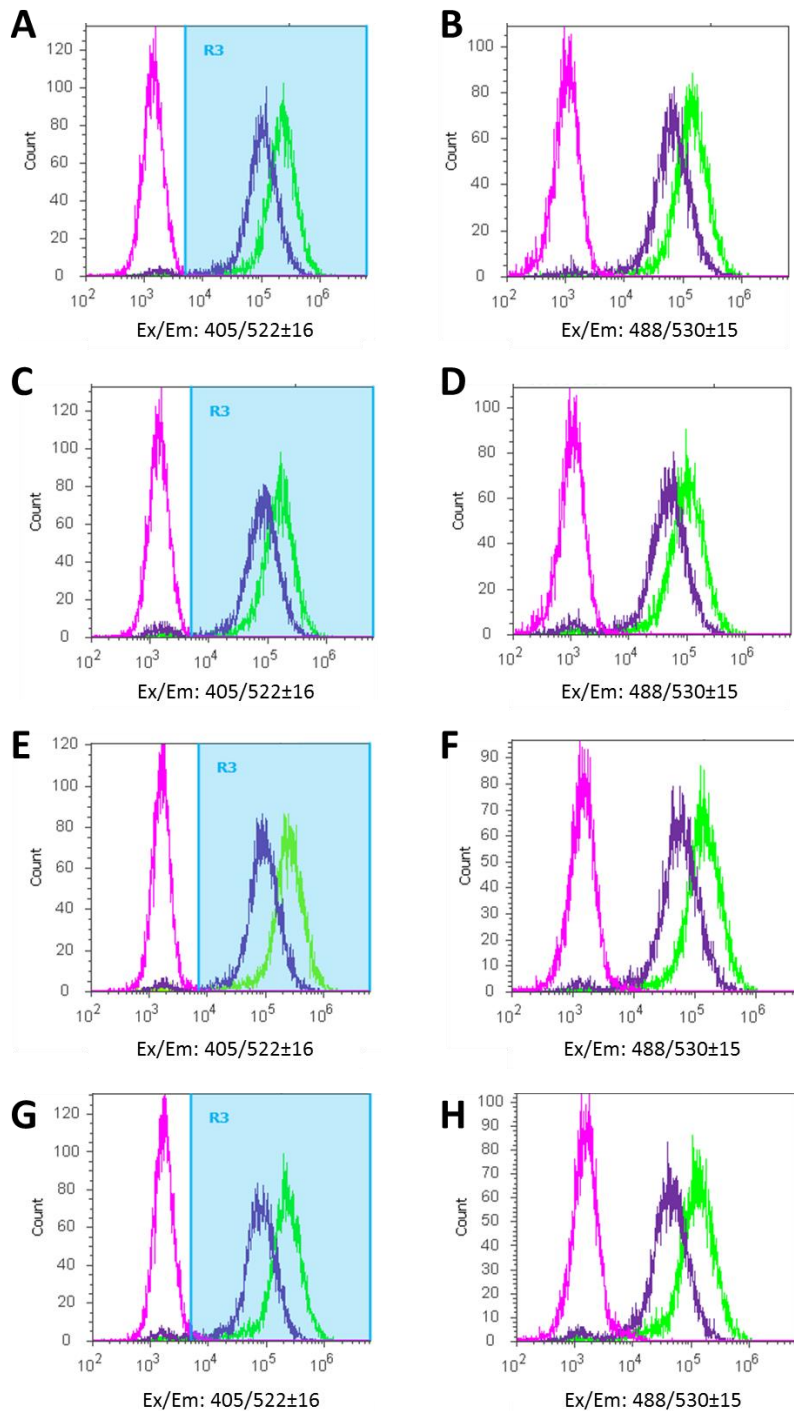


**Figure 76:** Histograms of transfected cells after sorting, detected using two filters to address the two excitation maxima (A, C, E, G: 405 nm, B, D, F, H: 488 nm). The auto-fluorescence of non-transfected cells is shown in magenta, cells transfected with 75 µL viral supernatant are shown in violet, and cells transfected with 200 µL are shown in green. A,B show MES-SA cells transfected with HyPerC; C,D show MES-SA cells transfected with HyPerC121s; E,F show MES-SA/Dx5 cells transfected with HyPerC; G,H show MES-SA/Dx5 cells transfected with HyPerC121s.

## 6. Synthesis and analytical chemical methods

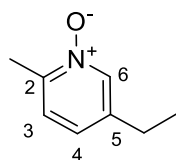
### 6.1. Synthesis of a focused library

General method: The Schiff bases were obtained by adding an ethanolic solution of the hydrazinyl component to the solution of the keto component in equimolar amounts, refluxing the mixture in the presence of catalytic amounts of acid. If not indicated otherwise, purification was carried out by recrystallization.

Carbazides were prepared by adding an equimolar amount of hydrazine to the methanolic solution of the respective isothiocyanate [221]. Where necessary, purification was carried out by recrystallization.

For the pyridinyl derivatives with ethyl group substitution in 5-position of the pyridine moiety (**II-e**, **II-l**, **IV-c**), 5-Ethylpicolinaldehyde (**E-5**) was prepared from 5-ethyl-2-methyl-pyridine as reported [89,222].

#### 5-ethyl-2-methyl-pyridine-*N*-oxid (**E-2**)

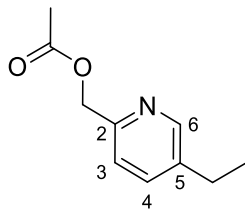


35 mL of hydrogenperoxid (35% solution, 0.41 mol) was added to a solution of 5-ethyl-2-methyl-pyridine (**E-1**, 21.76 mL, 0.17 mol) in glacial acetic acid (200 mL) and refluxed for 16 hours. After concentration, the reaction mixture was neutralized with sodium hydroxide and carbonate and the starting material was retrieved by

extraction with petroleum ether. 5-Ethyl-2-methyl-pyridine-*N*-oxid was extracted from the aqueous phase with chloroform, dried over sodium sulphate and after removal of the solvent obtained as a bright yellow liquid in 99% yield.

$^1\text{H-NMR}$  (500 MHz,  $\text{CDCl}_3$ ):  $\delta$  = 8.14 – 8.09 (m,  $1\text{H}_{\text{ar}}$ , *H*-6), 7.12 (d,  $^3J(\text{H,H}) = 7.9$  Hz,  $1\text{H}_{\text{ar}}$ , *H*-3), 7.00 (dd,  $^4J(\text{H,H}) = 1.3$  Hz,  $^3J(\text{H,H}) = 7.9$  Hz,  $1\text{H}_{\text{ar}}$ , *H*-4), 2.55 (q,  $^3J(\text{H,H}) = 7.7$  Hz, 2H,  $\text{CH}_2\text{CH}_3$ ), 2.48 (s, 3H,  $\text{CH}_3$ ), 1.20 (t,  $^3J(\text{H,H}) = 7.7$  Hz, 3H,  $\text{CH}_2\text{CH}_3$ ).

### 5-ethylpyridin-2-yl-methyl acetate (E-3)

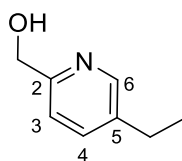


A solution of 5-ethyl-2-methyl-pyridine-*N*-oxid (**E-2**, 22.28 g, 0.16 mol) and acetic anhydride (28 mL, 0.23 mol) in glacial acetic acid (7 mL) was refluxed for 3 hours, put on ice, neutralized, and extracted with methylene chloride. After removal of the solvent, the extract was dissolved in diethyl ether, washed with a saturated solution of sodium carbonate and dried over sodium sulphate to give the product in 85% yield.

$^1\text{H-NMR}$  (500 MHz,  $\text{CDCl}_3$ ):  $\delta = 8.42$  (d,  $^4J(\text{H,H}) = 2.1$  Hz,  $1\text{H}_{\text{ar}}$ , *H*-6),  $7.50$  (dd,  $^4J(\text{H,H}) = 2.2$  Hz,  $^3J(\text{H,H}) = 7.9$  Hz,  $1\text{H}_{\text{ar}}$ , *H*-4),  $7.24$  (d,  $^3J(\text{H,H}) = 7.9$  Hz,  $1\text{H}_{\text{ar}}$ , *H*-3),  $5.16$  (s, 2H,  $\text{CH}_2\text{OAc}$ ),  $2.63$  (q,  $^3J(\text{H,H}) = 7.6$  Hz, 2H,  $\text{CH}_2\text{CH}_3$ ),  $2.11$  (s, 3H,  $\text{OOCCH}_3$ ),  $1.22$  (t,  $^3J(\text{H,H}) = 7.6$  Hz, 3H,  $\text{CH}_2\text{CH}_3$ ).

$^{13}\text{C-NMR}$  (126 MHz,  $\text{CDCl}_3$ ):  $\delta = 170.79$  ( $\text{C}_{\text{q}}$ ,  $\text{C}=\text{O}$ ),  $153.04$  ( $\text{C}_{\text{q,ar}}$ , *C*-2),  $149.35$  ( $\text{C-H}_{\text{ar}}$ , *C*-6),  $138.70$  ( $\text{C}_{\text{q,ar}}$ , *C*-5),  $136.11$  ( $\text{C-H}_{\text{ar}}$ , *C*-4),  $121.89$  ( $\text{C-H}_{\text{ar}}$ , *C*-3),  $66.98$  ( $\text{CH}_2\text{OAc}$ ),  $25.89$  ( $\text{CH}_2\text{CH}_3$ ),  $21.01$  ( $\text{OOCCH}_3$ ),  $15.36$  ( $\text{CH}_2\text{CH}_3$ ).

### 5-ethylpyridin-2-yl-methanol (E-4)

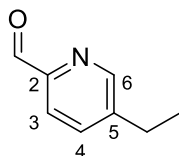


5-ethylpyridin-2-yl-methyl acetate (**E-3**, 24.29 g, 0.14 mol) was dissolved in tetrahydrofuran and refluxed with an aqueous solution of sodium hydroxide (8.1 g, 0.20 mol) for 5 hours. After reboiling the reaction mixture was reboiled with activated charcoal, it was neutralized with glacial acetic acid, filtered. After concentration of the

crude product under reduced pressure, it was dissolved in a saturated solution of sodium hydrogen carbonate, extracted with diethyl ether and dried over sodium sulphate to give the product as a brown oil in 80% yield.

$^1\text{H-NMR}$  (500 MHz,  $\text{CDCl}_3$ ):  $\delta = 8.32$  (d,  $^4J(\text{H,H}) = 1.9$  Hz,  $1\text{H}_{\text{ar}}$ , *H*-6),  $7.48$  (dd,  $^4J(\text{H,H}) = 2.2$  Hz,  $^3J(\text{H,H}) = 7.9$  Hz,  $1\text{H}_{\text{ar}}$ , *H*-4),  $7.20$  (d,  $^3J(\text{H,H}) = 7.9$  Hz,  $1\text{H}_{\text{ar}}$ , *H*-3),  $4.70$  (s, 2H,  $\text{CH}_2\text{OH}$ ),  $2.60$  (q,  $^3J(\text{H,H}) = 7.6$  Hz, 2H,  $\text{CH}_2\text{CH}_3$ ),  $1.20$  (t,  $^3J(\text{H,H}) = 7.6$  Hz, 3H,  $\text{CH}_2\text{CH}_3$ ).

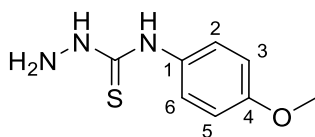
$^{13}\text{C-NMR}$  (500 MHz,  $\text{CDCl}_3$ ):  $\delta = 157.10$  ( $\text{C}_{\text{q,ar}}$ , *C*-5),  $148.12$  ( $\text{C-H}_{\text{ar}}$ , *C*-6),  $137.99$  ( $\text{C}_{\text{q,ar}}$ , *C*-2),  $136.34$  ( $\text{C-H}_{\text{ar}}$ , *C*-4),  $120.55$  ( $\text{C-H}_{\text{ar}}$ , *C*-3),  $64.29$  ( $\text{CH}_2\text{OH}$ ),  $25.81$  ( $\text{CH}_2\text{CH}_3$ ),  $15.40$  ( $\text{CH}_2\text{CH}_3$ ).

**5-ethylpicolinaldehyde (E-5)**

Manganese dioxide was prepared freshly by simultaneously adding a solution of Manganese(II)sulphate hydrate (14.5 g, 0.09 mol in 25 mL water) and sodium hydroxide (7.6 g, 0.19 mol in 20 mL water) to a warm solution of potassium permanganate  $\text{KMnO}_4$  (15.5 g, 0.10 mol in 100 mL water), refluxing the mixture for 6 hours, filtered and dried under reduced pressure. 5-ethylpyridin-2-yl-methanol (**E-4**, 12.82 g, 93.4 mmol) was dissolved in chloroform and given to the dried  $\text{MnO}_2$  (16.24 g, 186.8 mmol). The mixture was refluxed in an ultrasonic bath for 5 days, filtered and purified with column chromatography using a mixture petroleum ether and ethyl acetate (4:1) on silica gel to give the product as a bright yellow liquid in 61% yield.

$^1\text{H-NMR}$  (500 MHz,  $\text{CDCl}_3$ ):  $\delta$  = 10.03 (s, 1H, CHO), 8.60 (d,  $^4J(\text{H,H}) = 1.9$  Hz, 1H<sub>ar</sub>, H-6), 7.87 (d,  $^3J(\text{H,H}) = 8.0$  Hz, 1H<sub>ar</sub>, H-3), 7.70 – 7.63 (m, 1H<sub>ar</sub>, H-4), 2.73 (q,  $^3J(\text{H,H}) = 7.6$  Hz, 2H,  $\text{CH}_2\text{CH}_3$ ), 1.28 (t,  $^3J(\text{H,H}) = 7.6$  Hz, 3H,  $\text{CH}_2\text{CH}_3$ ).

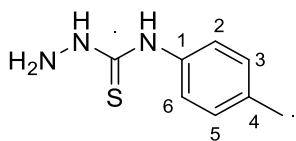
$^{13}\text{C-NMR}$  (500 MHz,  $\text{CDCl}_3$ ):  $\delta$  = 193.30 (CHO), 151.06 ( $\text{C}_{\text{q,ar}}$ , C-2), 150.18 (C-H<sub>ar</sub>, C-6), 144.67 ( $\text{C}_{\text{q,ar}}$ , C-5), 136.28 (C-H<sub>ar</sub>, C-4), 121.72 (C-H<sub>ar</sub>, C-3), 26.43 ( $\text{CH}_2\text{CH}_3$ ), 15.02 ( $\text{CH}_2\text{CH}_3$ ).

Preparation of Carbazides:**N-(4-methoxyphenyl)hydrazinecarbothioamide (C-1)**

The reaction of 4-methoxyphenylisothiocyanate (1.000 g, 6.052 mmol) with hydrazine (0.37 mL 80% aqueous, 6.052 mmol) resulted in white crystals of the product in 97% yield (1.163 g, 5.90 mmol).

$^1\text{H-NMR}$  (500 MHz,  $\text{DMSO-}d_6$ ):  $\delta$  = 9.51 (s, 1H, NH), 8.94 (s, 1H, NH), 7.44 (d,  $^3J(\text{H,H}) = 8.2$  Hz, 2H<sub>ar</sub>, H-3, H-5), 6.88 – 6.83 (m, 2H<sub>ar</sub>, H-2, H-6), 4.70 (s, 2H,  $\text{NH}_2$ ), 3.74 (s, 3H,  $\text{OCH}_3$ ).

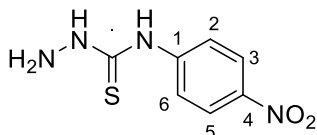
$^{13}\text{C-NMR}$  (126 MHz,  $\text{DMSO-}d_6$ ):  $\delta$  = 179.82 ( $\text{C}_{\text{q}}$ , C=S), 156.13 ( $\text{C}_{\text{q,ar}}$ , C-4), 132.17 ( $\text{C}_{\text{q,ar}}$ , C-1), 125.51 (2C-H<sub>ar</sub>, C-2, C-6), 113.20 (2C-H<sub>ar</sub>, C-3, C-5), 55.16 ( $\text{OCH}_3$ ).

***N*-(4-tolyl)hydrazinecarbothioamide (C-2)**

The reaction of 4-tolylisothiocyanate (500 mg, 3.35 mmol) with hydrazine (0.20 mL 80% aqueous, 3.35 mmol) resulted in white needles of the product in 98% yield (594 mg, 3.27 mmol).

$^1\text{H-NMR}$  (500 MHz,  $\text{DMSO-}d_6$ ):  $\delta$  = 9.55 (s, 1H, N-*H*), 9.00 (s, 1H, N-*H*), 7.49 (d,  $^3J(\text{H,H}) = 7.2$  Hz, 2 $\text{H}_{\text{ar}}$ , *H*-3, *H*-5), 7.10 (d,  $^3J(\text{H,H}) = 8.2$  Hz, 2 $\text{H}_{\text{ar}}$ , *H*-2, *H*-6), 4.74 (s, 2H,  $\text{NH}_2$ ), 2.27 (s, 3H,  $\text{CH}_3$ ).

$^{13}\text{C-NMR}$  (126 MHz,  $\text{DMSO-}d_6$ ):  $\delta$  = 179.49 ( $\text{C}_q$ , C=S), 136.64 ( $\text{C}_{q,\text{ar}}$ , C-4), 133.14 ( $\text{C}_{q,\text{ar}}$ , C-1), 128.45 (2 $\text{C-H}_{\text{ar}}$ , C-2, C6), 123.51 (2 $\text{C-H}_{\text{ar}}$ , C-3, C5), 20.43 ( $\text{CH}_3$ ).

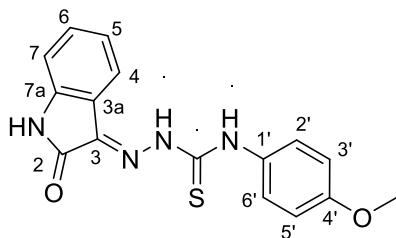
***N*-(4-nitrophenyl)hydrazinecarbothioamide (C-3)**

The reaction of 4-nitrophenylisothiocyanate (1.000 g, 5.56 mmol) with hydrazine (0.34 mL 80% aqueous, 5.56 mmol), was carried out in a mixture of toluene and methanol, due to the low solubility of the starting material and resulted in ochre product crystals in 93% yield (1.095 g, 5.16 mmol).

$^1\text{H-NMR}$  (500 MHz,  $\text{DMSO-}d_6$ ):  $\delta$  = 9.55 (s, 1H, N-*H*), 8.14 (s, 4 $\text{H}_{\text{ar}}$ ), 7.83 (s, 1H, N-*H*), 6.55 (bs, 2H,  $\text{NH}_2$ ).

$^{13}\text{C-NMR}$  (126 MHz,  $\text{DMSO-}d_6$ ):  $\delta$  = 178.77 ( $\text{C}_q$ , C=S), 145.73 ( $\text{C}_{q,\text{ar}}$ , C-4), 142.49 ( $\text{C}_{q,\text{ar}}$ , C-1), 123.80 (2 $\text{C-H}_{\text{ar}}$ , C-3, C5), 122.05 (2 $\text{C-H}_{\text{ar}}$ , C-2, C6).



Preparation of  $\beta$ -isatin thiosemicarbazones (Figure 16, box I):***N*-(4'-methoxyphenyl)-2-(2-oxoindoline-3-ylidene)hydrazinecarbothioamide (I-a) [102]**

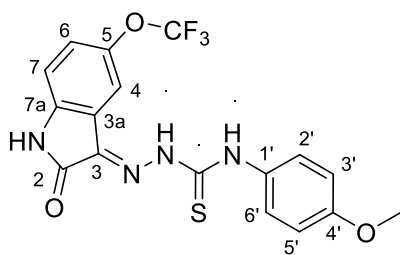
The reaction of isatin (147.13 mg, 1.0 mmol) with *N*-(4-methoxyphenyl)hydrazinecarbothioamide **C-1** (197.26 mg, 1.0 mmol) in ethanolic solution under HCl-catalysis resulted in a yellow fluffy precipitate, which was identified as the product in 89% yield (291 mg, 0.89 mmol).

$^1\text{H-NMR}$  (500 MHz,  $\text{DMSO-}d_6$ ):  $\delta$  = 12.75 (s, 1H, N-*H*), 11.22 (s, 1H, N-*H*), 10.70 (s, 1H, N-*H*), 7.76 (d,  $^3J(\text{H,H}) = 7.6$  Hz, 1H<sub>ar</sub>, *H*-4), 7.50 – 7.44 (m, 2H<sub>ar</sub>, *H*-2', *H*-6'), 7.36 (td,  $^3J(\text{H,H}) = 7.7$  Hz,  $^4J(\text{H,H}) = 1.3$  Hz, 1H<sub>ar</sub>, *H*-6), 7.13 – 7.08 (m, 1H<sub>ar</sub>, *H*-5), 6.99 – 6.95 (m, 2H<sub>ar</sub>, *H*-3', *H*-5'), 6.94 (d,  $^3J(\text{H,H}) = 7.9$  Hz, 1H<sub>ar</sub>, *H*-7), 3.78 (s, 3H,  $\text{OCH}_3$ ).

$^{13}\text{C-NMR}$  (126 MHz,  $\text{DMSO-}d_6$ ):  $\delta$  = 176.51 ( $\text{C}_q$ , C=S), 162.64 ( $\text{C}_q$ , C=O, C-2), 157.35 ( $\text{C}_{q,\text{ar}}$ , C-OCH<sub>3</sub>, C-4'), 142.37 ( $\text{C}_{q,\text{ar}}$ , bridge, C-7a), 132.01 ( $\text{C}_{q,\text{ar}}$ , C-1'), 131.28 (C-H<sub>ar</sub>, C-6), 131.25 ( $\text{C}_q$ , C=N, C-3), 127.14 (C-H<sub>ar</sub>, C-5), 122.30 (C-H<sub>ar</sub>, C-4), 121.26 (2C-H<sub>ar</sub>, C-2', C-6'), 119.92 ( $\text{C}_{q,\text{ar}}$ , bridge, C-3a), 113.54 (2C-H<sub>ar</sub>, C-3', C-5'), 111.02 (C-H<sub>ar</sub>, C-7), 55.25 ( $\text{OCH}_3$ ).

Anal. Calcd. for  $\text{C}_{16}\text{H}_{14}\text{N}_4\text{SO}_2$ : C: 58.88; H: 4.32; N: 17.17. Found: C: 58.58; H: 4.349; N: 16.95.

***N*-(4'-methoxyphenyl)-2-(2-oxo-5-(trifluoromethoxy)indoline-3-ylidene)hydrazinecarbothioamide (I-b)**



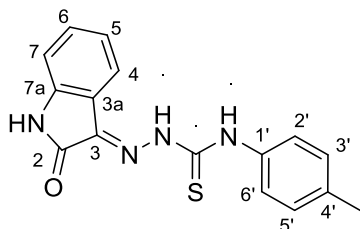
The reaction of 5-trifluoromethoxyisatin (50 mg, 0.22 mmol) with *N*-(4-methoxyphenyl)hydrazinecarbothioamide **C-1** (43 mg, 0.22 mmol) in ethanolic solution under HCl-catalysis resulted in a yellow fluffy precipitate, which was identified as the product in 70% yield (65.7 mg, 0.16 mmol).

$^1\text{H-NMR}$  (500 MHz,  $\text{DMSO-}d_6$ ):  $\delta$  = 12.60 (s, 1H, N-H), 11.36 (s, 1H, N-H), 10.78 (s, 1H, N-H), 7.78 (s, 1H<sub>ar</sub>, H-4), 7.49 – 7.41 (m, 2H<sub>ar</sub>, H-2', H-6'), 7.41 – 7.31 (m, 1H<sub>ar</sub>, H-6), 7.02 (d,  $^3J(\text{H,H}) = 5.0$  Hz, 1H<sub>ar</sub>, H-7), 7.01 – 6.95 (m, 2H<sub>ar</sub>, H-3', H-5'), 3.78 (s, 3H, OCH<sub>3</sub>).

$^{13}\text{C-NMR}$  (126 MHz,  $\text{DMSO-}d_6$ ):  $\delta$  = 176.56 (C<sub>q</sub>, C=S), 162.70 (C<sub>q</sub>, C=O, C-2), 157.50 (C<sub>q,ar</sub>, C-OCH<sub>3</sub>, C-4'), 143.53 (C<sub>q,ar</sub>, C-OCF<sub>3</sub>, C-5), 141.23 (C<sub>q,ar</sub>, C-1'), 131.06 (C<sub>q,ar</sub>, bridge, C-7a), 130.92 (C<sub>q</sub>, C=N, C-3), 127.31 (2C-H<sub>ar</sub>, C-2', C-6'), 124.03 (C-H<sub>ar</sub>, C-6), 121.45 (C<sub>q,ar</sub>, bridge, C-3a), 120.66 (C<sub>q</sub>, d {121.19, 119.15},  $^1J(\text{C,F}) = 255.7$  Hz, OCF<sub>3</sub>), 114.35 (2C-H<sub>ar</sub>, C-3', C-5'), 113.62 (C-H<sub>ar</sub>, C-4), 112.10 (C-H<sub>ar</sub>, C-7), 55.27 (OCH<sub>3</sub>).

Anal. Calcd. for C<sub>17</sub>H<sub>13</sub>N<sub>4</sub>SO<sub>3</sub>F<sub>3</sub>: C: 49.76; H: 3.19; N: 13.65. Found: C: 49.61; H: 3.477; N: 13.53.

***N*-(4'-tolyl)-2-(2-oxoindoline-3-ylidene)hydrazinecarbothioamide (I-c) [103]**

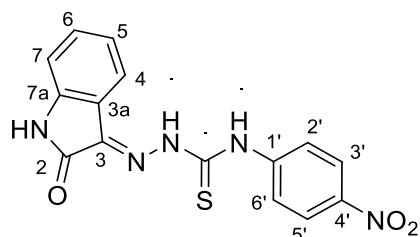


The reaction of isatin (147.13 mg, 1.0 mmol) with *N*-(4-tolyl)hydrazinecarbothioamide **C-2** (181.26 mg, 1.0 mmol) in ethanolic solution under acetic acid catalysis resulted in a yellow fluffy precipitate, which was identified as the product in 53% yield (162.8 mg, 0.53 mmol).

$^1\text{H-NMR}$  (500 MHz,  $\text{DMSO-}d_6$ ):  $\delta$  = 12.78 (s, 1H, NH), 11.22 (s, 1H, NH), 10.71 (s, 1H, NH), 7.78 (d,  $^3J(\text{H,H}) = 7.5$  Hz, 1H, H-4), 7.49 (d,  $^3J(\text{H,H}) = 8.3$  Hz, 2H<sub>ar</sub>, H-3', H-5'), 7.36 (td,  $^4J(\text{H,H}) = 1.2$  Hz,  $^3J(\text{H,H}) = 7.7$  Hz, 1H, H-6), 7.22 (d,  $^3J(\text{H,H}) = 8.2$  Hz, 2H<sub>ar</sub>, H-2', H-6'), 7.10 (td,  $^4J(\text{H,H}) = 0.7$  Hz,  $^3J(\text{H,H}) = 7.6$  Hz, 1H, H-5), 6.94 (d,  $^3J(\text{H,H}) = 7.8$  Hz, 1H, H-7), 2.33 (s, 3H, CH<sub>3</sub>).

$^{13}\text{C-NMR}$  (126 MHz,  $\text{DMSO-}d_6$ ):  $\delta$  = 176.26 (C<sub>q</sub>, C=S), 162.63 (C<sub>q</sub>, C=O), 142.39 (C<sub>q,ar</sub>, bridge, C-7a), 135.85 (C<sub>q,ar</sub>, C-4'), 135.27 (C<sub>q,ar</sub>, C-1'), 132.06 (C<sub>q</sub>, C=N, C-3), 131.29 (C-H<sub>ar</sub>, C-6), 128.77 (2C-H<sub>ar</sub>, C-3', C5'), 125.41 (2C-H<sub>ar</sub>, C-2', C-6'), 122.27 (C-H<sub>ar</sub>, C-4), 121.30 (C-H<sub>ar</sub>, C-5), 119.89 (C-H<sub>ar</sub>, C-7), 111.01 (C<sub>q,ar</sub>, bridge, C-3a), 20.57 (CH<sub>3</sub>).

Anal. Calcd. for C<sub>16</sub>H<sub>14</sub>N<sub>4</sub>SO: C: 61.92; H: 4.55; N: 18.05. Found: C: 62.4; H: 4.402; N: 18.54.

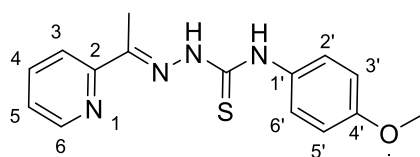
***N*-(4'-nitrophenyl)-2-(2-oxoindoline-3-ylidene)hydrazinecarbothioamide (I-d)** [103]

The reaction of isatin (147.13 mg, 1.0 mmol) with *N*-(4-tolyl)hydrazinecarbothioamide **C-3** (212.23 mg, 1.0 mmol) in ethanolic solution under acetic acid catalysis resulted in an orange-yellowish fluffy precipitate, which was identified as the product in 71% yield (242 mg, 0.71 mmol).

$^1\text{H-NMR}$  (500 MHz, DMSO- $d_6$ ):  $\delta$  = 13.01 (s, 1H, N-*H*), 11.28 (s, 1H, N-*H*), 11.10 (s, 1H, N-*H*), 8.36 – 8.24 (m, 2H<sub>ar</sub>, *H*-3', *H*-5'), 8.14 – 8.03 (m, 2H<sub>ar</sub>, *H*-2', *H*-6'), 7.78 (d,  $^3J(\text{H,H}) = 7.4$  Hz, 1H<sub>ar</sub>, *H*-4), 7.40 (td,  $^4J(\text{H,H}) = 1.2$  Hz,  $^3J(\text{H,H}) = 7.7$  Hz, 1H<sub>ar</sub>, *H*-6), 7.13 (td,  $^4J(\text{H,H}) = 0.8$  Hz,  $^3J(\text{H,H}) = 7.6$  Hz, 1H<sub>ar</sub>, *H*-5), 6.96 (d,  $^3J(\text{H,H}) = 7.8$  Hz, 1H<sub>ar</sub>, *H*-7).

$^{13}\text{C-NMR}$  (126 MHz, DMSO- $d_6$ ):  $\delta$  = 176.02 (C<sub>q</sub>, C=S), 162.66 (C<sub>q</sub>, C=O), 144.59 (C<sub>q,ar</sub>, C-1'), 144.09 (C<sub>q,ar</sub>, C-4'), 142.72 (C<sub>q,ar</sub>, bridge, C-7a), 133.24 (C<sub>q</sub>, C=N, C-3), 131.75 (C-H<sub>ar</sub>, C-6), 124.61 (2C-H<sub>ar</sub>, C-2', C6'), 123.91 (2C-H<sub>ar</sub>, C-3', C5'), 122.38 (C-H<sub>ar</sub>, C-5), 121.54 (C-H<sub>ar</sub>, C-7), 119.63 (C<sub>q,ar</sub>, bridge, C-3a), 111.16 (C-H<sub>ar</sub>, C-4).

Anal. Calcd. for C<sub>15</sub>H<sub>11</sub>N<sub>5</sub>SO<sub>3</sub>: C: 52.78; H: 3.25; N: 20.52. Found: C: 53.24; H: 3.57; N: 20.9.

Preparation of pyridinyl thiosemicarbazones (Figure 16, box II):***N*-(4'-methoxyphenyl)-2-(1-(pyridin-2-yl)ethylidene)hydrazinecarbothioamide (II-c)**

The reaction of 1-(pyridin-2-yl)ethanone (0.15 mL, 1.325 mmol) with *N*-(4-tolyl)hydrazinecarbothioamide **C-2** (250 mg, 1.325 mmol) in ethanolic solution under acetic acid catalysis resulted in a white precipitate,

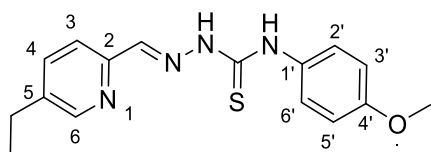
which was recrystallized to afford the product in 63% yield (250.6 mg, 0.83 mmol).

$^1\text{H-NMR}$  (500 MHz, DMSO- $d_6$ ):  $\delta$  = 10.54 (s, 1H, NH), 10.07 (s, 1H, NH), 8.60 (ddd,  $^5J(\text{H,H}) = 0.9$  Hz,  $^4J(\text{H,H}) = 1.9$  Hz,  $^3J(\text{H,H}) = 4.7$  Hz, 1H<sub>ar</sub>, *H*-6), 8.54 (d,  $^3J(\text{H,H}) = 8.2$  Hz, 1H<sub>ar</sub>, *H*-3), 7.84 – 7.75 (sm, 1H<sub>ar</sub>, *H*-4), 7.43 – 7.36 (sm, 3H<sub>ar</sub>, *H*-5, *H*-3', *H*-5'), 6.97 – 6.91 (sm, 2H<sub>ar</sub>, *H*-2', *H*-6'), 3.78 (s, 3H, OCH<sub>3</sub>), 2.46 (s, 3H, CH<sub>3</sub>).

$^{13}\text{C-NMR}$  (126 MHz, DMSO- $d_6$ ):  $\delta$  = 177.74 (C<sub>q</sub>, C=S), 157.24 (C<sub>q,ar</sub>, C-4'), 154.71 (C<sub>q,ar</sub>, C-2), 49.03 (C<sub>q</sub>, C=N), 148.57 (C-H<sub>ar</sub>, C-6), 136.45 (C-H<sub>ar</sub>, C-4), 132.17 (C<sub>q,ar</sub>, C-1'), 127.86 (2C-H<sub>ar</sub>, C-2', C-6'), 124.16 (C-H<sub>ar</sub>, C-5), 121.34 (C-H<sub>ar</sub>, C-3), 113.45 (2C-H<sub>ar</sub>, C-3', C-5'), 55.40 (OCH<sub>3</sub>), 12.50 (CH<sub>3</sub>).

Anal. Calcd. for C<sub>15</sub>H<sub>16</sub>N<sub>4</sub>SO: C: 59.98; H: 5.37; N: 18.65. Found: C: 60.0; H: 5.3; N: 18.76.

**2-((5-ethylpyridin-2-yl)methylene)-N-(4'-methoxyphenyl)hydrazinecarbothioamide (II-e)**



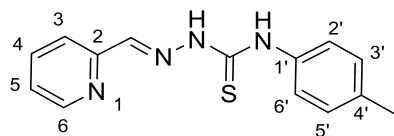
The reaction of 5-ethylpicolinaldehyde (**E-5**, 200 mg, 1.48 mmol) with *N*-(4-methoxyphenyl)hydrazinecarbothioamide **C-1** (291.9 mg, 1.48 mmol) in ethanolic solution under acetic acid catalysis resulted in white crystals, of product in 60% yield (229 mg, 0.73 mmol).

The product seemed to be thermo labile, since it decomposed upon a further recrystallization trial.

$^1\text{H-NMR}$  (500 MHz,  $\text{DMSO-}d_6$ ):  $\delta$  = 11.87 (s, 1H, NH), 10.09 (s, 1H, NH), 8.44 (dd,  $^5J(\text{H,H}) = 0.5$  Hz,  $^4J(\text{H,H}) = 1.9$  Hz,  $1\text{H}_{\text{ar}}$ , *H*-6), 8.35 (d,  $^3J(\text{H,H}) = 8.2$  Hz,  $1\text{H}_{\text{ar}}$ , *H*-3), 8.17 (s, 1H, HC=N), 7.69 (dd,  $^4J(\text{H,H}) = 2.2$  Hz,  $^3J(\text{H,H}) = 8.2$  Hz,  $1\text{H}_{\text{ar}}$ , *H*-4), 7.43 – 7.37 (sm,  $2\text{H}_{\text{ar}}$ , *H*-3', *H*-5'), 6.97 – 6.91 (sm,  $2\text{H}_{\text{ar}}$ , *H*-2', *H*-6'), 3.77 (s, 3H,  $\text{OCH}_3$ ), 2.65 (q,  $^3J(\text{H,H}) = 7.6$  Hz, 2H,  $\text{CH}_2\text{CH}_3$ ), 1.21 (t,  $^3J(\text{H,H}) = 7.6$  Hz, 3H,  $\text{CH}_2\text{CH}_3$ ).

$^{13}\text{C-NMR}$  (126 MHz,  $\text{DMSO-}d_6$ ):  $\delta$  = 176.62 ( $\text{C}_{\text{q}}$ , C=S), 157.00 ( $\text{C}_{\text{q,ar}}$ , C-4'), 150.93 ( $\text{C}_{\text{q,ar}}$ , C-2), 148.72 (C- $\text{H}_{\text{ar}}$ , C-6), 142.93 (HC=N), 139.75 ( $\text{C}_{\text{q,ar}}$ , C-5), 135.70 (C- $\text{H}_{\text{ar}}$ , C-4), 131.83 ( $\text{C}_{\text{q,ar}}$ , C-1'), 127.59 (2C- $\text{H}_{\text{ar}}$ , C-2', C-6'), 120.20 (C- $\text{H}_{\text{ar}}$ , C-3), 113.26 (2C- $\text{H}_{\text{ar}}$ , C-3', C-5'), 55.21 ( $\text{OCH}_3$ ), 25.22 ( $\text{CH}_2\text{CH}_3$ ), 15.09 ( $\text{CH}_2\text{CH}_3$ ).

Purity was determined with HPLC MS to be  $\geq 95\%$  ( $m/z$  calculated for [M]: 314.41, found 315.2 for  $[\text{M} + \text{H}]^+$ ).

**2-(pyridin-2-ylmethylene)-*N*-(4'-tolyl)hydrazinecarbothioamide (II-f)**

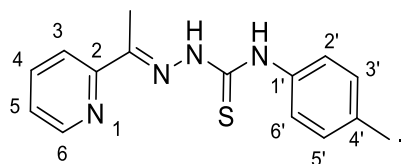
The reaction of pyridine-2-carbaldehyde (160.7 mg, 1.5 mmol) with *N*-(4-tolyl)hydrazinecarbothioamide **C-2** (271.9 mg, 1.5 mmol) in ethanolic solution under acetic acid catalysis resulted in a white fluffy precipitate, which

was identified as the product in 83% yield (334.5 mg, 1.237 mmol).

$^1\text{H-NMR}$  (500 MHz,  $\text{DMSO-}d_6$ ):  $\delta$  = 11.95 (s, 1H, N-*H*), 10.15 (s, 1H, N-*H*), 8.58 (ddd,  $^5J(\text{H,H})$  = 1.0 Hz,  $^4J(\text{H,H})$  = 1.7 Hz,  $^3J(\text{H,H})$  = 4.9 Hz, 1H<sub>ar</sub>, *H*-6), 8.43 (d,  $^3J(\text{H,H})$  = 8.0 Hz, 1H<sub>ar</sub>, *H*-4), 8.19 (s, 1H, CHN), 7.84 (ddd,  $^5J(\text{H,H})$  = 0.9 Hz,  $^4J(\text{H,H})$  = 1.8 Hz,  $^3J(\text{H,H})$  = 7.6 Hz, 1H<sub>ar</sub>, *H*-3), 7.44 – 7.40 (m, 2H<sub>ar</sub>, *H*-3', *H*-5'), 7.39 (ddd,  $^3J(\text{H,H})$  = 1.2 Hz,  $^3J(\text{H,H})$  = 4.9 Hz,  $^3J(\text{H,H})$  = 7.5 Hz, 1H<sub>ar</sub>, *H*-5), 7.18 (d,  $^3J(\text{H,H})$  = 8.0 Hz, 2H<sub>ar</sub>, *H*-2', *H*-6'), 2.32 (s, 3H, CH<sub>3</sub>).

$^{13}\text{C-NMR}$  (126 MHz,  $\text{DMSO-}d_6$ ):  $\delta$  = 176.54 (C<sub>q</sub>, C=S), 153.26 (C<sub>q,ar</sub>, C-2), 149.36 (C-H, CHN), 143.00 (C-H<sub>ar</sub>, C-6), 136.48 (C-H<sub>ar</sub>, C-4), 136.45 (C<sub>q,ar</sub>, C-CH<sub>3</sub>, C-4'), 134.74 (C<sub>q,ar</sub>, C-1'), 128.61 (2C-H<sub>ar</sub>, C-3', C5'), 125.98 (2C-H<sub>ar</sub>, C-2', C6'), 124.22 (C-H<sub>ar</sub>, C-5), 120.64 (C-H<sub>ar</sub>, C-3), 20.65 (CH<sub>3</sub>).

Anal. Calcd. for C<sub>14</sub>H<sub>14</sub>N<sub>4</sub>S: C: 62.2; H: 5.22; N: 20.72. Found: C: 62.36; H: 5.228; N: 20.93.

**2-(1-(pyridin-2-yl)ethylidene)-*N*-(4'-tolyl)hydrazinecarbothioamide (II-g)**

The reaction of 1-(pyridin-2-yl)ethanone (0.17 mL, 1.5 mmol) with *N*-(4-tolyl)hydrazinecarbothioamide **C-2** (271.9 mg, 1.5 mmol) in ethanolic solution under acetic acid catalysis resulted in white crystals, which were

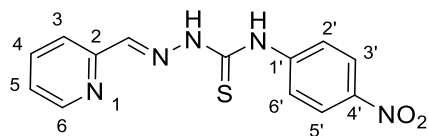
recrystallized from a CHCl<sub>3</sub>:EtOH mixture (1.5:1) to afford the product in 41% yield (174 mg, 0.61 mmol).

$^1\text{H-NMR}$  (500 MHz,  $\text{DMSO-}d_6$ ):  $\delta$  = 10.58 (s, 1H, N-*H*), 10.10 (s, 1H, N-*H*), 8.60 (ddd,  $^5J(\text{H,H})$  = 0.9 Hz,  $^4J(\text{H,H})$  = 1.7,  $^3J(\text{H,H})$  = 4.7 Hz, 1H<sub>ar</sub>, *H*-6), 8.52 (d,  $^3J(\text{H,H})$  = 8.2 Hz, 1H<sub>ar</sub>, *H*-3), 7.81 (ddd,  $^5J(\text{H,H})$  = 1.9 Hz,  $^5J(\text{H,H})$  = 7.4 Hz,  $^5J(\text{H,H})$  = 8.2 Hz, 1H<sub>ar</sub>, *H*-4), 7.45 – 7.37 (m, 3H<sub>ar</sub>, *H*-5, *H*-3', *H*-5'), 7.18 (d,  $^3J(\text{H,H})$  = 7.9 Hz, 2H<sub>ar</sub>, *H*-2', *H*-6'), 2.46 (s, 3H, C=NCH<sub>3</sub>), 2.32 (s, 3H, CH<sub>3</sub>).

$^{13}\text{C-NMR}$  (126 MHz,  $\text{DMSO-}d_6$ ):  $\delta$  = 177.25 (C<sub>q</sub>, C=S), 154.50 (C<sub>q,ar</sub>, C-2), 148.98 (C<sub>q</sub>, C=N), 148.41 (C-H<sub>ar</sub>, C-6), 136.52 (C<sub>q,ar</sub>, C-4'), 136.30 (C-H<sub>ar</sub>, C-4), 134.65 (C<sub>q,ar</sub>, C-1'), 128.50 (2C-H<sub>ar</sub>, C-3', C-5'), 125.94 (2C-H<sub>ar</sub>, C-2', C-6'), 124.01 (C-H<sub>ar</sub>, C-5), 121.16 (C-H<sub>ar</sub>, C-3), 20.56 (CH<sub>3</sub>), 12.37 (C=NCH<sub>3</sub>).

Anal. Calcd. for C<sub>15</sub>H<sub>16</sub>N<sub>4</sub>S: C: 63.35; H: 5.67; N: 19.70. Found: C: 62.92; H: 5.602; N: 19.81.

## 2-(pyridin-2-ylmethylene)-*N*-(4-nitrophenyl)hydrazinecarbothioamide (II-j)



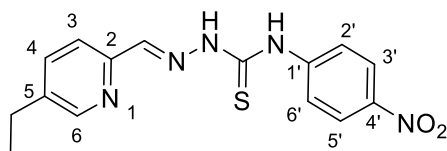
The reaction of picolinaldehyde (**E-5**, 160.7 mg, 1.5 mmol) with *N*-(4-nitrophenyl)hydrazinecarbothioamide **C-3** (318.3 mg, 1.5 mmol) in ethanolic solution under acetic acid catalysis resulted in a bright yellow fluffy precipitate, which was recrystallized to afford the product in 97% yield (437 mg, 1.45 mmol).

$^1\text{H-NMR}$  (500 MHz,  $\text{DMSO-}d_6$ ):  $\delta$  = 12.34 (s, 1H, N-H), 10.53 (s, 1H, N-H), 8.61 (ddd,  $^5J(\text{H,H})$  = 0.9 Hz,  $^4J(\text{H,H})$  = 1.6 Hz,  $^3J(\text{H,H})$  = 4.8 Hz, 1H<sub>ar</sub>, H-6), 8.41 (d,  $^3J(\text{H,H})$  = 8.0 Hz, 1H<sub>ar</sub>, H-3), 8.28 – 8.23 (m, 3H, CHN, H-7, 2H<sub>ar</sub>, H-9, H-9'), 8.08 – 8.03 (m, 2H<sub>ar</sub>, H-8, H-8'), 7.89 (td,  $^4J(\text{H,H})$  = 1.5 Hz,  $^3J(\text{H,H})$  = 7.7 Hz, 1H<sub>ar</sub>, H-4), 7.43 (ddd,  $^5J(\text{H,H})$  = 1.1 Hz,  $^4J(\text{H,H})$  = 4.9 Hz,  $^3J(\text{H,H})$  = 7.5 Hz, 1H<sub>ar</sub>, H-5).

$^{13}\text{C-NMR}$  (126 MHz,  $\text{DMSO-}d_6$ ):  $\delta$  = 175.83 (C<sub>q</sub>, C=S), 152.78 (C<sub>q,ar</sub>, C-2), 149.42 (C-H<sub>ar</sub>, C-6), 145.19 (C<sub>q,ar</sub>, C-4'), 144.23 (CHN), 143.64 (C<sub>q,ar</sub>, C-1'), 136.50 (C-H<sub>ar</sub>, C-4), 124.68 (2C-H<sub>ar</sub>, C-3', C-5'), 124.46 (C-H<sub>ar</sub>, C-5), 123.68 (2C-H<sub>ar</sub>, C-2', C-6'), 120.74 (C-H<sub>ar</sub>, C-3).

Anal. Calcd. for  $\text{C}_{13}\text{H}_{11}\text{N}_5\text{SO}_2$ : C: 51.82; H: 3.68; N: 23.24. Found: C: 52.13; H: 3.679; N: 23.51.

## 2-((5-ethylpyridin-2-yl)methylene)-*N*-(4'-nitrophenyl)hydrazinecarbothioamide (II-k)

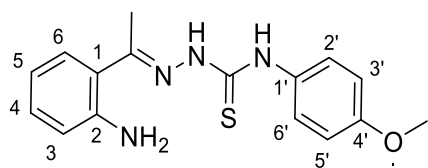


The reaction of 5-ethylpicolinaldehyde (**E-5**, 202.74 mg, 1.5 mmol) with *N*-(4-nitrophenyl)hydrazinecarbothioamide **C-3** (318.3 mg, 1.5 mmol) in ethanolic solution under acetic acid catalysis resulted in orange crystals, which provided the pure product in 49% yield (242 mg, 0.74 mmol) after column chromatography and recrystallization.

$^1\text{H-NMR}$  (500 MHz,  $\text{DMSO-}d_6$ ):  $\delta$  = 12.21 (bs, 1H, N-H), 10.52 (bs, 1H, N-H), 8.47 (d,  $^4J(\text{H,H})$  = 1.6 Hz, 1H<sub>ar</sub>, H-6), 8.32 (d,  $^3J(\text{H,H})$  = 7.9 Hz, 1H<sub>ar</sub>, H-3), 8.27 – 8.24 (sm, 2H<sub>ar</sub>, H-3', H-5'), 8.23 (s, 1H, HC=N), 8.07 – 8.03 (sm, 2H<sub>ar</sub>, H-2', H-6'), 7.74 (dd,  $^4J(\text{H,H})$  = 2.0 Hz,  $^3J(\text{H,H})$  = 8.4 Hz, 1H<sub>ar</sub>, H-4), 2.67 (q,  $^3J(\text{H,H})$  = 7.6 Hz, 2H,  $\text{CH}_2\text{CH}_3$ ), 1.22 (t,  $^3J(\text{H,H})$  = 7.6 Hz, 3H,  $\text{CH}_2\text{CH}_3$ ).

$^{13}\text{C-NMR}$  (126 MHz,  $\text{DMSO-}d_6$ ):  $\delta$  = 175.71 (C<sub>q</sub>, C=S), 150.53 (C<sub>q,ar</sub>, C-2), 148.91 (C-H<sub>ar</sub>, C-6), 145.31 (C<sub>q,ar</sub>, C-1'), 144.39 (C=NH), 143.54 (C<sub>q,ar</sub>, C-4'), 140.16 (C<sub>q,ar</sub>, C-5), 135.77 (C-H<sub>ar</sub>, C-4), 124.62 (C-H<sub>ar</sub>, C-3), 123.68 (2C-H<sub>ar</sub>, C-3', C-5'), 120.44 (2C-H<sub>ar</sub>, C-2', C-6'), 25.25 ( $\text{CH}_2\text{CH}_3$ ), 15.07 ( $\text{CH}_2\text{CH}_3$ ).

Anal. Calcd. for  $\text{C}_{15}\text{H}_{15}\text{N}_5\text{SO}_2 \times 0.5 \text{H}_2\text{O}$ : C: 53.24; H: 4.77; N: 20.70. Found: C: 53.44; H: 4.72; N: 20.75.

Preparation of the acetaniline thiosemicarbazone**(1-(1-(2-aminophenyl)ethylidene)amino)-3-(4'-methoxyphenyl)thiourea (II-p):**

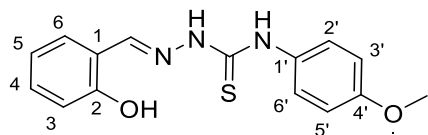
The reaction of 2-aceto-anilin (0.11 mL, 1.27 mmol) with 2-hydrazino-benzothiazole (250 mg, 1.27 mmol) in ethanolic solution under acetic acid catalysis delivered the product as a bright yellow solid in 10% yield

(38 mg, 0.121 mmol) after column chromatography (PE:EE 4:1) recrystallization.

$^1\text{H-NMR}$  (500 MHz,  $\text{DMSO-}d_6$ ):  $\delta = 10.44$  (s, 1H, N-H), 9.69 (s, 1H, N-H), 7.46 (d,  $^3J(\text{H,H}) = 9.1$  Hz, 2H<sub>ar</sub>, H-2', H-6'), 7.36 (dd,  $^4J(\text{H,H}) = 1.4$  Hz,  $^3J(\text{H,H}) = 8.0$  Hz, 1H<sub>ar</sub>, H-6), 7.06 – 7.01 (sm, 1H<sub>ar</sub>, H-4), 6.92 – 6.88 (m, 2H<sub>ar</sub>, H-3', H-5'), 6.71 (dd,  $^4J(\text{H,H}) = 1.1$  Hz,  $^3J(\text{H,H}) = 8.0$  Hz, 1H<sub>ar</sub>, H-3), 6.57 – 6.52 (sm, 1H<sub>ar</sub>, H-5), 3.75 (s, 3H, OCH<sub>3</sub>), 2.32 (s, 3H, CH<sub>3</sub>) – NH<sub>2</sub> not visible. The purity of the compound was determined with HPLC MS to be between 75% (detection at 254 nm) and 85% (detection at 280 nm) ( $m/z$  calculated for [M]: 314.41, found 315.2 for [M + H]<sup>+</sup>). This amount of impurity will lead to an uncertainty of pIC<sub>50</sub> estimations, which however lies within the standard error of the experiments. In the thesis, compound **II-p** is compared to its pyridinyl thiosemicarbazone counterpart **II-c**. The toxicities of these two compounds are significantly different: depending on the investigated cell lines, **II-c** is 1.49-2.75 log units more toxic than **II-p**. Therefore, the drawn conclusions might still be considered, despite the remarkable impurity of this compound.

Preparation of hydroxyphenyl thiosemicarbazones (Figure 16, box III):

**2-(2-hydroxybenzylidene)-*N*-(4'-methoxyphenyl)hydrazinecarbothioamide (III-b)**



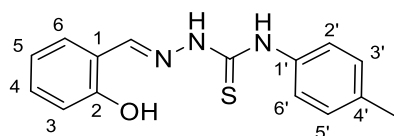
Salicylic aldehyde (0.135 mL, 1.267 mmol) was reacted with *N*-(4-methoxyphenyl)hydrazinecarbothioamide **C-1** (250 mg, 1.267 mmol) in ethanolic solution under acetic acid catalysis. The crude product was purified with column chromatography (PE:EE 4:1) and allowed to crystallize at  $-20^{\circ}\text{C}$ . The product was obtained as white crystals in a yield of 62% (236 mg, 0.78 mmol).

$^1\text{H-NMR}$  (500 MHz,  $\text{CDCl}_3$ ):  $\delta$  = 10.92 (s, 1H, N-*H*), 8.55 (s, 1H, N-*H*), 7.52 – 7.48 (sm, 2H<sub>ar</sub>, *H*-3', *H*-5'), 7.37 – 7.31 (m, 2H, CHN, 1H<sub>ar</sub>, *H*-4), 7.29 (dd,  $^4J(\text{H,H}) = 1.6$  Hz,  $^3J(\text{H,H}) = 7.6$  Hz, 1H<sub>ar</sub>, *H*-6), 7.04 (d,  $^3J(\text{H,H}) = 7.9$  Hz, 1H<sub>ar</sub>, *H*-3), 6.95 (td,  $^4J(\text{H,H}) = 1.1$  Hz,  $^3J(\text{H,H}) = 7.6$  Hz, 1H<sub>ar</sub>, *H*-5), 6.89 – 6.84 (sm, 2H<sub>ar</sub>, *H*-2', *H*-6'), 3.79 (s, 3H, OCH<sub>3</sub>) – OH not visible.

$^{13}\text{C-NMR}$  (126 MHz,  $\text{CDCl}_3$ ):  $\delta$  = 158.90 (C<sub>q</sub>, C=S), 158.83 (CHN), 156.78 (C<sub>q,ar</sub>, C-2), 150.04 (C<sub>q,ar</sub>, C-4'), 132.15 (C-H<sub>ar</sub>, C-4), 131.75 (C-H<sub>ar</sub>, C-6), 131.52 (C<sub>q,ar</sub>, C-1'), 122.35 (2C-H<sub>ar</sub>, C-2', C6'), 119.82 (C-H<sub>ar</sub>, C-5), 118.31 (C<sub>q,ar</sub>, C-1), 116.97 (C-H<sub>ar</sub>, C-3), 114.41 (2C-H<sub>ar</sub>, C-3', C-5'), 55.67 (OCH<sub>3</sub>).

Anal. Calcd. for C<sub>15</sub>H<sub>15</sub>N<sub>3</sub>SO<sub>2</sub>: C: 59.78; H: 5.02; N: 13.94. Found: C: 59.75; H: 5.047; N: 14.11.

**2-(2-hydroxybenzylidene)-*N*-(4'-tolyl)hydrazinecarbothioamide (III-c)**



The reaction of salicylic aldehyde (0.147 mL, 1.379 mmol) with *N*-(4-tolyl)hydrazinecarbothioamide **C-2** (250 mg, 1.267 mmol) in ethanolic solution under acetic acid catalysis resulted in yellowish crystals, which

delivered the pure product in 34% yield (133.8 mg, 0.47 mmol) after recrystallization.

$^1\text{H-NMR}$  (500 MHz, DMSO-*d*<sub>6</sub>):  $\delta$  = 11.67 (s, 1H, OH), 9.94 (s, 2 N-*H*), 8.48 (s, 1H, CHN), 8.04 (d,  $^3J(\text{H,H}) = 7.6$  Hz, 1H<sub>ar</sub>, *H*-6), 7.45 – 7.39 (sm, 2H<sub>ar</sub>, *H*-3', *H*-5'), 7.25 – 7.20 (sm, 1H<sub>ar</sub>, *H*-4), 7.15 (d,  $^3J(\text{H,H}) = 8.1$  Hz, 2H<sub>ar</sub>, *H*-2', *H*-6'), 6.87 (dd,  $^4J(\text{H,H}) = 0.9$  Hz,  $^3J(\text{H,H}) = 8.2$  Hz, 1H<sub>ar</sub>, *H*-5), 6.82 (t,  $^3J(\text{H,H}) = 7.5$  Hz, 1H<sub>ar</sub>, *H*-3), 2.30 (s, 3H, CH<sub>3</sub>).

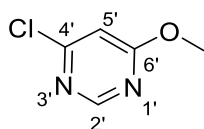
$^{13}\text{C NMR}$  (101 MHz, DMSO-*d*<sub>6</sub>):  $\delta$  = 175.77 (C<sub>q</sub>, C=S), 156.54 (CHN), 139.88 (C<sub>q,ar</sub>, C-2), 136.57 (C<sub>q,ar</sub>, C-1'), 134.30 (C-H<sub>ar</sub>, C-4), 131.24 (C-H<sub>ar</sub>, C-6), 128.47 (2C-H<sub>ar</sub>, C-3', C-5'), 127.05 (C<sub>q,ar</sub>, C-4'), 125.64 (2C-H<sub>ar</sub>, C-2', C6'), 120.27 (C<sub>q,ar</sub>, C-1), 119.19 (C-H<sub>ar</sub>, C-5), 116.01 (C-H<sub>ar</sub>, C-3), 20.58 (CH<sub>3</sub>).

Anal. Calcd. for C<sub>15</sub>H<sub>15</sub>N<sub>3</sub>SO: C: 63.13; H: 5.30; N: 14.73. Found: C: 63.12; H: 5.249; N: 14.89.



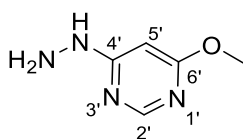
Preparation of arylhydrazones (Figure 16, box IV):

4-hydrazinyl-6-methoxypyrimidine necessary for the synthesis of the arylhydrazones **IV-a-c** and **VII-d** was prepared in a two-step approach starting from 4,6-dichloropyrimidine [89,222].

**4-chloro-6-methoxypyrimidine (E-7)**

To a cooled solution (-10 °C) of 4,6-dichloropyrimidine (**E-6**, 5 g, 33.56 mmol) in dry methanol one equivalent of sodium hydride (titrated solution in dry methanol) was added, the solution was allowed to warm to room temperature and react for 48 hours. The solvent was removed, the crude product dissolved in brine and extracted with chloroform and used without further purification.

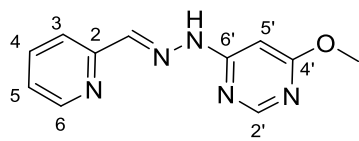
$^1\text{H-NMR}$  (500 MHz, DMSO- $d_6$ ):  $\delta$  = 8.68 (d,  $^5J(\text{H,H})$  = 0.8 Hz, 1H<sub>ar</sub>, H-2), 7.18 (d,  $^5J(\text{H,H})$  = 0.9 Hz, 1H<sub>ar</sub>, H-5), 3.96 (s, 3H, OCH<sub>3</sub>).

**4-hydrazinyl-6-methoxypyrimidine (E-8)**

To a solution of 4-chloro-6-methoxypyrimidine (2.5 g crude product) in methanol an aqueous solution of hydrazine (80 %, 6.1 mL) was added and refluxed. After evaporation of the solvent, the aqueous solution of the crude product was alkalized with sodium hydroxide and extracted with methylene chloride to give the product as an ochre powder in 60% yield.

$^1\text{H-NMR}$  (500 MHz, CDCl<sub>3</sub>):  $\delta$  = 8.26 (s, 1H<sub>ar</sub>, H-2), 6.42 (bs, 1H, NH), 6.07 (s, 1H<sub>ar</sub>, H-5), 3.92 (s, 3H, OCH<sub>3</sub>), 3.42 (bs, 2H, NH<sub>2</sub>).  $^{13}\text{C-NMR}$  (126 MHz, CDCl<sub>3</sub>):  $\delta$  = 170.72 (C<sub>q ar</sub>, C-6), 167.17 (C<sub>q ar</sub>, C-4), 157.68 (C-H<sub>ar</sub>, C-2), 84.90 (C-H<sub>ar</sub>, C-5), 53.87 (OCH<sub>3</sub>).

#### 4'-methoxy-6'-(2-(pyridin-2-ylmethylene)hydrazinyl)pyrimidine (IV-a)



The reaction of 2-pyridinecarboxaldehyde (191.1 mg, 1.78 mmol) with 4-hydrazinyl-6-methoxypyrimidine (250 mg, 1.78 mmol) resulted in brightly rosy crystals of the product in 72% yield (293 mg, 1.28 mmol).

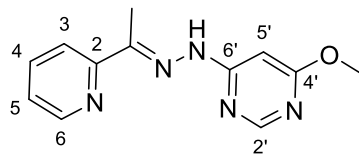
$^1\text{H-NMR}$  (300 MHz,  $\text{CDCl}_3$ ):  $\delta$  = 8.78 (bs, 1H, NH), 8.60 (d,  $^3J(\text{H,H})$  = 4.8 Hz, 1H<sub>ar</sub>, H-6), 8.38 (d,  $^5J(\text{H,H})$  = 0.6 Hz, 1H<sub>ar</sub>, H-2'), 8.00 (d,  $^3J(\text{H,H})$  = 8.0 Hz, 1H<sub>ar</sub>, H-3), 7.93 (s, 1H, C=NH), 7.75 (t,  $^3J(\text{H,H})$  = 7.3 Hz, 1H<sub>ar</sub>, H-4), 6.63 (d,  $^5J(\text{H,H})$  = 0.7 Hz, 1H<sub>ar</sub>, H-5'), 3.99 (s, 3H, OCH<sub>3</sub>).

$^{13}\text{C-NMR}$  (126 MHz, DMSO- $d_6$ ):  $\delta$  = 170.00 (C<sub>q,ar</sub>, C-4'), 162.78 (C<sub>q,ar</sub>, C-6'), 157.77 (C-H<sub>ar</sub>, C-2), 153.47 (C<sub>q,ar</sub>, C-2), 149.28 (C-H<sub>ar</sub>, C-6), 142.77 (HC=N), 136.59 (C-H<sub>ar</sub>, C-4), 123.62 (C-H<sub>ar</sub>, C-5), 119.44 (C-H<sub>ar</sub>, C-3), 85.38 (C-H<sub>ar</sub>, C-5'), 53.54 (OCH<sub>3</sub>).

Anal. Calcd. for C<sub>11</sub>H<sub>11</sub>N<sub>5</sub>O×0.75 H<sub>2</sub>O: C, 54.43; H, 5.19; N, 28.85. Found: C, 54.36; H, 4.49; N, 28.94.

ESI-MS: m/z Calcd. for [M]: 229.0964. Found: 230.0979 for [M+H]<sup>+</sup>, 252.0798 for [M+Na]<sup>+</sup>.

#### 4'-methoxy-6'-(2-(1-(pyridin-2-yl)ethylidene)hydrazinyl)pyrimidine (IV-b)



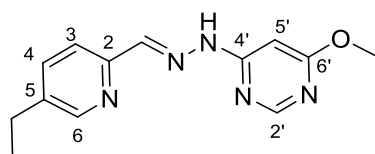
The reaction of 2-acetylpyridine (0.2 mL, 1.78 mmol) with 4-hydrazinyl-6-methoxypyrimidine (250 mg, 1.78 mmol) resulted in brightly rosy crystals of the product in 79% yield (342 mg, 1.41 mmol).

$^1\text{H-NMR}$  (500 MHz, DMSO- $d_6$ ):  $\delta$  = 10.43 (s, 1H, NH), 8.57 (ddd,  $^5J(\text{H,H})$  = 0.9 Hz,  $^4J(\text{H,H})$  = 1.7 Hz,  $^3J(\text{H,H})$  = 4.8 Hz, 1H<sub>ar</sub>, H-6), 8.37 (d,  $^5J(\text{H,H})$  = 0.9 Hz, 1H<sub>ar</sub>, H-2'), 8.15 (dt,  $^5J(\text{H,H})$  = 0.9 Hz,  $^3J(\text{H,H})$  = 8.1 Hz, 1H<sub>ar</sub>, H-3), 7.85 – 7.75 (sm, 1H<sub>ar</sub>, H-4), 7.35 (ddd,  $^4J(\text{H,H})$  = 1.1 Hz,  $^3J(\text{H,H})$  = 4.8 Hz,  $^3J(\text{H,H})$  = 7.4 Hz, 1H, H-5), 6.57 (d,  $^5J(\text{H,H})$  = 0.9 Hz, 1H, H-5'), 3.89 (s, 3H, OCH<sub>3</sub>), 2.40 (s, 3H, C=NCH<sub>3</sub>).

$^{13}\text{C-NMR}$  (126 MHz, DMSO- $d_6$ ):  $\delta$  = 170.04 (C<sub>q,ar</sub>, C-4'), 163.51 (C<sub>q,ar</sub>, C-6'), 157.53 (C-H<sub>ar</sub>, C-2'), 155.24 (C<sub>q,ar</sub>, C-2), 148.42 (C-H<sub>ar</sub>, C-6), 147.91 (C<sub>q</sub>, C=N), 136.44 (C-H<sub>ar</sub>, C-4), 123.40 (C-H<sub>ar</sub>, C-5), 119.93 (C-H<sub>ar</sub>, C-3), 86.10 (C-H<sub>ar</sub>, C-5'), 53.50 (OCH<sub>3</sub>), 11.76 (C=NCH<sub>3</sub>).

Anal. Calcd. for C<sub>12</sub>H<sub>13</sub>N<sub>5</sub>O×0.5 H<sub>2</sub>O: C, 57.13; H, 5.59; N, 27.76. Found: C, 57.23; H, 5.46; N, 27.09.

ESI-MS: m/z Calcd. for [M]: 243.1120. Found: 244.1128 for [M+H]<sup>+</sup>, 266.0953 for [M+Na]<sup>+</sup>.

**4'-[2-[(5-ethylpyridin-2-yl)methylidene]hydrazin-1-yl]-6'-methoxypyrimidine (IV-c)**

The reaction of 5-ethylpicolinaldehyde (**E-5**, 241.1 mg, 1.78 mmol) with 4-hydrazinyl-6-methoxypyrimidine (**E-8**, 250 mg, 1.78 mmol) resulted in brightly rosy crystals of the product in 63% yield (288.7 mg, 1.12 mmol).

$^1\text{H-NMR}$  (500 MHz,  $\text{DMSO-d}_6$ ):  $\delta$  = 11.45 (s, 1H, NH), 8.43 (d,  $^4J(\text{H,H}) = 1.6$  Hz, 1H<sub>ar</sub>, H-6), 8.33 (d,  $^5J(\text{H,H}) = 0.9$  Hz, 1H<sub>ar</sub>, H-2'), 8.12 (s, 1H, C=NH), 7.93 (d,  $^3J(\text{H,H}) = 8.1$  Hz, 1H<sub>ar</sub>, H-3), 7.68 (dd,  $^4J(\text{H,H}) = 2.1$  Hz,  $^3J(\text{H,H}) = 8.2$  Hz, 1H<sub>ar</sub>, H-4), 6.49 (d,  $^5J(\text{H,H}) = 0.6$  Hz, 1H<sub>ar</sub>, H-5'), 3.89 (s, 3H, OCH<sub>3</sub>), 2.64 (q,  $^3J(\text{H,H}) = 7.6$  Hz, 2H, CH<sub>2</sub>CH<sub>3</sub>), 1.20 (t,  $^3J(\text{H,H}) = 7.6$  Hz, 3H, CH<sub>2</sub>CH<sub>3</sub>).

$^{13}\text{C-NMR}$  (126 MHz,  $\text{DMSO-d}_6$ ):  $\delta$  = 169.96 (C<sub>q,ar</sub>, C-6'), 162.78 (C<sub>q,ar</sub>, C-4'), 157.74 (C-H<sub>ar</sub>, C-2'), 151.22 (C<sub>q,ar</sub>, C-2), 148.73 (C-H<sub>ar</sub>, C-6), 142.91 (C-H, HC=N), 139.16 (C<sub>q,ar</sub>, C-5), 135.87 (C-H<sub>ar</sub>, C-4), 119.11 (C-H<sub>ar</sub>, C-3), 85.26 (C-H<sub>ar</sub>, C-5'), 53.50 (OCH<sub>3</sub>), 25.15 (CH<sub>2</sub>CH<sub>3</sub>), 15.08 (CH<sub>2</sub>CH<sub>3</sub>).

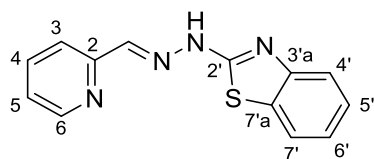
Anal. Calcd. for C<sub>13</sub>H<sub>15</sub>N<sub>5</sub>O: C, 60.69; H, 5.88; N, 27.22. Found: C, 60.32; H, 5.76; N, 27.28.

ESI-MS: m/z Calcd. for [M]: 257.1277. Found: 258.1272 for [M+H]<sup>+</sup>, 280.1074 for [M+Na]<sup>+</sup>.

Preparation of pyridinyl hydrazino-benzothiazoles (Figure 16, box V):

As a general comment on the hydrazino-benzothiazole derivatives from boxes V, VI and VII, in the  $^{13}\text{C}$  NMR spectra (especially measured by attached proton test (APT) method) some signals were not detectable. Mainly this occurred for the bridging quaternary carbons  $C-3'a$  and  $C-7'a$ , but dependent on the respective compounds also for some other signals. Those are indicated below.

**2'-(2-(pyridin-2-yl)methylene)hydrazinyl)-1',3'-benzothiazole (V-a)**



The reaction of picolinaldehyde (**E-5**, 0.144 mL, 1.513 mmol) with 2-hydrazino-benzothiazole (250 mg, 1.513 mmol) in ethanolic solution under acetic acid catalysis resulted in bright yellowish shining crystals, which

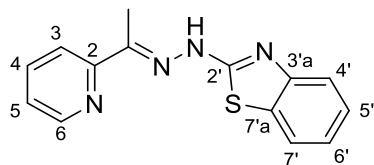
delivered the pure product in 75% yield (287.7 mg, 1.132 mmol) after recrystallization.

$^1\text{H-NMR}$  (500 MHz,  $\text{DMSO-}d_6$ ):  $\delta$  = 12.48 (bs, 1H, NH), 8.60 (ddd,  $^5J(\text{H,H}) = 1.0$  Hz,  $^4J(\text{H,H}) = 1.7$  Hz,  $^3J(\text{H,H}) = 5.0$  Hz, 1H<sub>ar</sub>, H-6), 8.14 (s, 1H, C=NH, H-7), 7.91 (d,  $^3J(\text{H,H}) = 7.9$  Hz, 1H<sub>ar</sub>, H-4'), 7.87 (m, 1H<sub>ar</sub>, H-3), 7.80 (d,  $^3J(\text{H,H}) = 7.9$  Hz, 1H<sub>ar</sub>, H-7'), 7.49 (d,  $^3J(\text{H,H}) = 5.9$  Hz, 1H<sub>ar</sub>, H-4), 7.38 (ddd,  $^4J(\text{H,H}) = 1.6$  Hz,  $^3J(\text{H,H}) = 4.9$  Hz,  $^3J(\text{H,H}) = 7.3$  Hz, 1H<sub>ar</sub>, H-5), 7.35 – 7.29 (sm, 1H<sub>ar</sub>, H-5' or H-6'), 7.17 – 7.10 (sm, 1H<sub>ar</sub>, H-6' or H-5').

$^{13}\text{C-NMR}$  (101 MHz,  $\text{DMSO-}d_6$ ):  $\delta$  = 167.07 (C<sub>q,ar</sub>, C-2'), 153.09 (C<sub>q,ar</sub>, C-2), 149.52 (C-H<sub>ar</sub>, C-6), 136.79 (C-H<sub>ar</sub>, C-4), 126.04 (C-H<sub>ar</sub>, C-5'), 123.88 (C-H<sub>ar</sub>, C-5), 121.94 (C-H<sub>ar</sub>, C-6'), 121.58 (C-H<sub>ar</sub>, C-7'), 119.39 (C-H<sub>ar</sub>, C-4'). Signals for HC=N, C-3, C-3'a and C-7'a were not detectable.

Anal. Calcd. for  $\text{C}_{13}\text{H}_{10}\text{N}_4\text{S}$ : C: 61.4; H: 3.96; N: 22.03. Found: C: 61.81; H: 3.936; N: 22.4.

Purity was additionally determined with HPLC MS to be  $\geq 95\%$  (m/z calculated for [M]: 254.31, found 255.2 for  $[\text{M} + \text{H}]^+$ ).

**2'-(2-(1-(pyridin-2-yl)ethylidene)hydrazinyl)-1',3'-benzothiazole (V-b)**

The reaction of 1-(pyridin-2-yl)ethanone (0.17 mL, 1.513 mmol) with 2-hydrazino-benzothiazole (250 mg, 1.513 mmol) in ethanolic solution under acetic acid catalysis resulted in beige precipitate, which delivered the

pure product after recrystallization. The yield was not determined. NMRs revealed the presence of acetic acid in the crystals, therefore EA analysis was adapted accordingly.

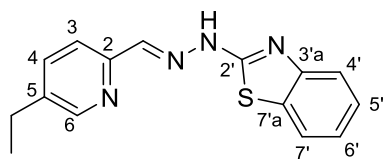
$^1\text{H-NMR}$  (500 MHz,  $\text{DMSO-}d_6$ ):  $\delta = 11.86$  (bs, N-H), 8.59 (ddd,  $^5J(\text{H,H}) = 0.9$  Hz,  $^4J(\text{H,H}) = 1.6$  Hz,  $^3J(\text{H,H}) = 4.7$  Hz, 1H<sub>ar</sub>, H-6), 8.08 (d,  $^3J(\text{H,H}) = 8.2$  Hz, 1H<sub>ar</sub>, H-4'), 7.90 – 7.83 (sm, 1H<sub>ar</sub>, H-4), 7.74 (d,  $^3J(\text{H,H}) = 7.6$  Hz, 1H<sub>ar</sub>, H-7'), 7.41 – 7.36 (sm, 2H<sub>ar</sub>, H-5, H-3), 7.33 – 7.27 (sm, 1H<sub>ar</sub>, H-5'), 7.11 (td,  $^4J(\text{H,H}) = 0.9$  Hz,  $^3J(\text{H,H}) = 7.8$  Hz, 1H<sub>ar</sub>, H-6'), 2.43 (s, 3H, CH<sub>3</sub>, H-8).

$^{13}\text{C-NMR}$  (126 MHz,  $\text{DMSO-}d_6$ ):  $\delta = 168.17$  (C<sub>q,ar</sub>, C-2'), 155.07 (C<sub>q,ar</sub>, C-2), 148.59 (C-H<sub>ar</sub>, C-6), 136.39 (C-H<sub>ar</sub>, C-4), 125.98 (C-H<sub>ar</sub>, C-5'), 123.53 (C-H<sub>ar</sub>, C-5), 121.70 (C-H<sub>ar</sub>, C-6' or C7'), 121.67 (C-H<sub>ar</sub>, C-7' or C-6'), 119.69 (C-H<sub>ar</sub>, C-4'), 12.68 (CH<sub>3</sub>) – the signals for CH<sub>3</sub>C=N, C-3, C-3'a, C-7'a were not detectable.

Anal. Calcd. for C<sub>14</sub>H<sub>12</sub>N<sub>4</sub>S×0.7 C<sub>2</sub>H<sub>4</sub>O<sub>2</sub>: C: 59.6; H: 4.8; N: 18.1. Found: C: 59.1; H: 4.9; N: 18.0.

Additionally purity was determined with HPLC MS to be  $\geq 95\%$  (m/z calculated for [M]: 268.34, found 268.8 for [M + H]<sup>+</sup>, 291.3 for [M + Na]<sup>+</sup>).

### 2'-(2-(5-ethylpyridin-2-yl)methylene)hydrazinyl)-1',3'-benzothiazole (V-c)



The reaction of 5-ethyl-picolinaldehyde (**E-5**, 200 mg, 1.48 mmol) with 2-hydrazino-benzothiazole (244.5 mg, 1.480 mmol) in ethanolic solution under acetic acid catalysis resulted in cream-colored precipitate, which

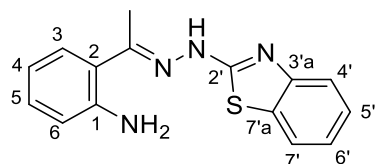
delivered the pure product in 46% yield (192.2 mg, 0.681 mmol) after recrystallization.

<sup>1</sup>H-NMR (500 MHz, DMSO-*d*<sub>6</sub>): δ = 12.41 (bs, 1H, NH), 8.46 (dd, <sup>5</sup>*J*(H,H) = 0.6 Hz, <sup>4</sup>*J*(H,H) = 2.1 Hz, 1H<sub>ar</sub>, H-6), 8.13 (s, 1H, C=NH), 7.84 (d, <sup>3</sup>*J*(H,H) = 7.9 Hz, 1H<sub>ar</sub>, H-4'), 7.79 (d, <sup>3</sup>*J*(H,H) = 7.9 Hz, 1H<sub>ar</sub>, H-7'), 7.73 (ddd, <sup>3</sup>*J*(H,H) = 0.5 Hz, <sup>3</sup>*J*(H,H) = 2.1 Hz, <sup>3</sup>*J*(H,H) = 8.2 Hz, 1H<sub>ar</sub>, H-3), 7.48 (d, <sup>3</sup>*J*(H,H) = 4.8, 1H<sub>ar</sub>, H-4), 7.31 (td, <sup>3</sup>*J*(H,H) = 1.3 Hz, <sup>3</sup>*J*(H,H) = 8.0 Hz, 1H<sub>ar</sub>, H-5' or H-6'), 7.17 – 7.10 (sm, 1H<sub>ar</sub>, H-6' or H-5'), 2.66 (q, <sup>3</sup>*J*(H,H) = 7.7 Hz, 2H, CH<sub>2</sub>CH<sub>3</sub>), 1.21 (t, <sup>3</sup>*J*(H,H) = 7.7 Hz, 3H, CH<sub>2</sub>CH<sub>3</sub>).

<sup>13</sup>C-NMR (126 MHz, DMSO-*d*<sub>6</sub>): 166.99 (C<sub>q,ar</sub>, C-2'), 150.82 (C<sub>q,ar</sub>, C-2), 148.93 (C-H<sub>ar</sub>, C-6), 139.41 (C<sub>q,ar</sub>, C-5), 135.98 (C-H<sub>ar</sub>, C-4), 125.95 (C-H<sub>ar</sub>, C-5'), 121.80 (C-H<sub>ar</sub>, C-6'), 121.49 (C-H<sub>ar</sub>, C-7'), 119.04 (C-H<sub>ar</sub>, C-4'), 25.17 (CH<sub>2</sub>CH<sub>3</sub>), 15.07 (CH<sub>2</sub>CH<sub>3</sub>) – the signals for HC=N, C-3, C-3'a, C-7'a were not visible.

Anal. Calcd. for C<sub>15</sub>H<sub>14</sub>N<sub>4</sub>S: C: 63.80; H: 5.00; N: 19.84. Found: C: 63.47; H: 4.886; N: 19.81.

### Preparation of the acetaniline hydrazino-benzothiazole 2-(1-(2-(1',3'-benzothiazol-2'-yl)hydrazine-1-ylidene)ethyl)aniline (V-d)

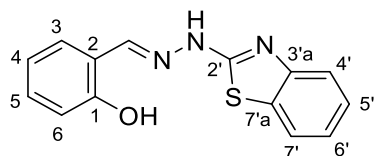


The reaction of 2-aceto-anilin (0.10 mL, 1.21 mmol) with 2-hydrazino-benzothiazole (200 mg, 1.21 mmol) in ethanolic solution under acetic acid catalysis delivered the product as a greyish brownish solid after recrystallization.

<sup>1</sup>H-NMR (500 MHz, DMSO-*d*<sub>6</sub>): δ = 11.62 (s, 1H, NH), 7.67 (d, <sup>3</sup>*J*(H,H) = 7.9 Hz, 1H<sub>ar</sub>, H-4'), 7.43 (dd, <sup>4</sup>*J*(H,H) = 1.4 Hz, <sup>3</sup>*J*(H,H) = 8.0 Hz, 1H<sub>ar</sub>, H-7'), 7.30 – 7.19 (m, 2H<sub>ar</sub>, H-3, H-5), 7.10 – 7.00 (m, 2H<sub>ar</sub>, H-5', H-6'), 6.82 (s, 2H, NH<sub>2</sub>), 6.76 (dd, <sup>4</sup>*J*(H,H) = 1.3 Hz, <sup>3</sup>*J*(H,H) = 8.2 Hz, 1H<sub>ar</sub>, H-4), 6.61 – 6.51 (sm, 1H<sub>ar</sub>, H-6), 2.43 (s, 3H, CH<sub>3</sub>).

<sup>13</sup>C-NMR (126 MHz, DMSO-*d*<sub>6</sub>): δ = 165.34 (C<sub>q,ar</sub>, C-2'), 156.54 (C<sub>q</sub>, CH<sub>3</sub>C=N), 147.38 (C<sub>q,ar</sub>, CNH<sub>2</sub>, C-1), 129.18 (C-H<sub>ar</sub>, C-5), 129.03 (C-H<sub>ar</sub>, C-5'), 126.22 (C-H<sub>ar</sub>, C-3), 121.94 (C-H<sub>ar</sub>, C-6'), 121.24 (C-H<sub>ar</sub>, C-7'), 118.07 (C<sub>q,ar</sub>, C-2), 115.96 (C-H<sub>ar</sub>, C-), 114.95 (C-H<sub>ar</sub>, C-4), 114.07 (C-H<sub>ar</sub>, C-4'), 15.67 (CH<sub>3</sub>). The signals for C-3'a and C-7'a were not detectable.

Purity of the compound was determined with HPLC MS to be ≥ 95% (m/z calculated for [M]: 282.36, found 283.1 for [M + H]<sup>+</sup>).

Preparation of hydroxyphenyl hydrazino-benzothiazoles (Figure 16, box VI):**2-((2-(1',3'-benzothiazol-2'-yl)hydrazine-1-ylidene)methyl)phenol (VI-a)**

The reaction of salicylic aldehyde (0.13 mL, 1.21 mmol) with 2-hydrazino-benzothiazole (200 mg, 1.21 mmol) in ethanolic solution under acetic acid catalysis delivered the

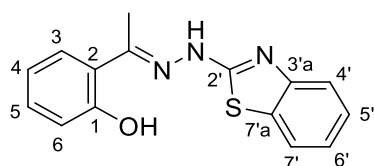
pure product as a white precipitate in 93% yield (306 mg, 1.13 mmol) after recrystallization.

$^1\text{H-NMR}$  (500 MHz,  $\text{DMSO-}d_6$ ):  $\delta$  = 12.14 (s, 1H, NH), 10.44 (s, 1H, OH), 8.45 (s, 1H, C=NH), 7.74 (d,  $^3J(\text{H,H})$  = 7.9 Hz, 1H<sub>ar</sub>, H-4'), 7.61 (d,  $^3J(\text{H,H})$  = 6.6 Hz, 1H<sub>ar</sub>, H-7'), 7.41 – 7.32 (m, 1H<sub>ar</sub>, H-3), 7.31 – 7.27 (sm, 1H<sub>ar</sub>, H-6'), 7.27 – 7.24 (sm, 1H<sub>ar</sub>, H-5'), 7.09 (td,  $^4J(\text{H,H})$  = 1.3 Hz,  $^3J(\text{H,H})$  = 7.9 Hz, 1H<sub>ar</sub>, H-5), 6.95 – 6.88 (m, 2H<sub>ar</sub>, H-6, H-4).

$^{13}\text{C-NMR}$  (126 MHz,  $\text{DMSO-}d_6$ ):  $\delta$  = 166.40 (C<sub>q,ar</sub>, C-2'), 156.59 (C<sub>q,ar</sub>, C-OH, C-1), 146.98 (HC=N), 130.80 (C-H<sub>ar</sub>, C-4), 127.71 (C-H<sub>ar</sub>, C-6), 126.15 (C-H<sub>ar</sub>, C-5'), 121.77 (C-H<sub>ar</sub>, C-7'), 121.51 (C-H<sub>ar</sub>, C-5), 119.61 (C<sub>q,ar</sub>, C-2), 119.42 (C-H<sub>ar</sub>, C-4'), 116.12 (C-H<sub>ar</sub>, C-3) – the signals for C-6', C-3'a and C-7'a were not visible.

Anal. Calcd. for C<sub>14</sub>H<sub>11</sub>N<sub>3</sub>O: C: 62.43; H: 4.12; N: 15.60. Found: C: 62.56; H: 4.086; N: 15.76.

Purity was additionally determined with HPLC MS to be  $\geq 95\%$  (m/z calculated for [M]: 269.32, found 315.2 for [M + H]<sup>+</sup>).

**2-(1-(2-(1',3'-benzothiazol-2'-yl)hydrazine-1-ylidene)ethyl)phenol (VI-b)**

The reaction of 2-hydroxyacetophenon (0.15 mL, 1.21 mmol) with 2-hydrazino-benzothiazole (200 mg, 1.21 mmol) in ethanolic solution under acetic acid catalysis delivered the pure product as a yellow precipitate in 92% yield (315 mg, 1.11 mmol) after recrystallization.

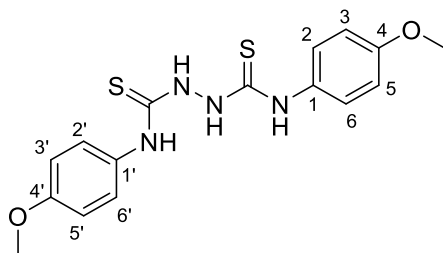
$^1\text{H-NMR}$  (500 MHz,  $\text{DMSO-}d_6$ ):  $\delta$  = 12.52 (bs, 1H, NH), 7.66 (d,  $^3J(\text{H,H})$  = 7.7 Hz, 1H<sub>ar</sub>, H-7'), 7.59 (dd,  $^4J(\text{H,H})$  = 1.0 Hz,  $^3J(\text{H,H})$  = 7.8 Hz, 1H<sub>ar</sub>, H-4'), 7.30 – 7.24 (m, 2H<sub>ar</sub>, H-5', H-6'), 7.19 (d,  $^3J(\text{H,H})$  = 7.8 Hz, 1H<sub>ar</sub>, H-3), 7.06 (t,  $^3J(\text{H,H})$  = 7.5 Hz, 1H<sub>ar</sub>, H-5), 6.93 – 6.87 (m, 2H<sub>ar</sub>, H-4, H-6), 6.50 (bs, 1H, OH), 2.50 (s, 3H, CH<sub>3</sub>).

$^{13}\text{C-NMR}$  (126 MHz,  $\text{DMSO-}d_6$ ):  $\delta$  = 165.12 (C<sub>q,ar</sub>, C-2'), 159.60 (C<sub>q,ar</sub>, C-OH, C-1), 158.23 (C<sub>q,ar</sub>, C-3'a), 141.17 (C<sub>q</sub>, CH<sub>3</sub>C=N), 130.58 (C-H<sub>ar</sub>, C-5), 128.40 (C-H<sub>ar</sub>, C-3), 126.66 (C-H<sub>ar</sub>, C-5'), 123.72 (C<sub>q,ar</sub>, C-7'a), 122.45 (C-H<sub>ar</sub>, C-6'), 121.62 (C-H<sub>ar</sub>, C-7'), 119.91 (C<sub>q,ar</sub>, C-2), 118.72 (C-H<sub>ar</sub>, C-4), 116.70 (C-H<sub>ar</sub>, C-4'), 112.35 (C-H<sub>ar</sub>, C-6), 14.41 (CH<sub>3</sub>).

Anal. Calcd. for C<sub>15</sub>H<sub>13</sub>N<sub>3</sub>SO $\times$ 1.25 H<sub>2</sub>O: C: 58.9; H: 5.11; N: 13.74. Found: C: 58.7; H: 4.728; N: 13.85.

Preparation of combined structures (Figure 16, box VII):

***N,N*-bis(4-methoxyphenyl)hydrazine-1,2-bis(carbothioamide) (VII-a)**



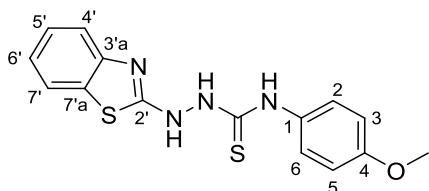
The reaction of 4-methoxyphenylisothiocyanate (413.1 mg, 2.5 mmol) with hydrazine (0.06 mL 80% aqueous, 1.25 mmol) in ethanolic solution delivered the pure product as a white solid in 69% yield (310 mg, 0.856 mmol) after recrystallization.

$^1\text{H-NMR}$  (500 MHz,  $\text{DMSO-}d_6$ ):  $\delta$  = 9.69 (s, 2H, 2 NH), 9.52 (s, 2H, 2 NH), 7.38 (d,  $^3J(\text{H,H})$  = 8.8 Hz, 4H<sub>ar</sub>, H-3, H-3', H-5, H-5'), 6.93 – 6.86 (m, 4H<sub>ar</sub>, H-2, H-2', H-6, H-6'), 3.75 (s, 6H, 2 OCH<sub>3</sub>).

$^{13}\text{C-NMR}$  (126 MHz,  $\text{DMSO-}d_6$ ):  $\delta$  = 156.82 (2C<sub>q,ar</sub>, C-4, C-4'), 132.11 (2C<sub>q,ar</sub>, C-1, C-1'), 126.77 (4C-H<sub>ar</sub>, (even though with very low intensity) C-2, C-2', C-6, C-6'), 113.48 (4C-H<sub>ar</sub>, C-3, C-3', C-5, C-5'), 55.35 (2 OCH<sub>3</sub>). – for the quaternary C=S no signal was visible in APT test, the signal for C-2, C-2', C-6 and C-6' had a remarkably low intensity.

Anal. Calcd. for C<sub>16</sub>H<sub>18</sub>N<sub>4</sub>S<sub>2</sub>O<sub>2</sub>: C: 53.02; H: 5.01; N: 15.46. Found: C: 53.18; H: 5.047; N: 15.66.

**3-[(1',3'-benzothiazol-2'yl)amino]-1-(4-methoxyphenyl)thiourea (VII-b)**



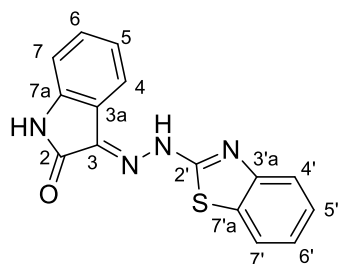
The reaction of *N*-(4-methoxyphenyl)hydrazinecarbothioamide **C-1** (250 mg, 1.513 mmol) with 2-hydrazinobenzothiazole (250 mg, 1.513 mmol) in ethanolic solution delivered the pure product as a yellow solid in 75% yield (357.2 mg, 1.139 mmol) after recrystallization.

$^1\text{H-NMR}$  (500 MHz,  $\text{DMSO-}d_6$ ):  $\delta$  = 13.38 (s, 1H, N-H), 7.66 (s, 1H, N-H), 7.60 (dd,  $^3J(\text{H,H})$  = 1.3 Hz,  $^3J(\text{H,H})$  = 8.2 Hz, 1H<sub>ar</sub>, H-4'), 7.37 – 7.31 (sm, 1H<sub>ar</sub>, H-5'), 7.30 – 7.25 (sm, 2H<sub>ar</sub>, H-3, H-5), 7.19 (dd,  $^3J(\text{H,H})$  = 1.4 Hz,  $^3J(\text{H,H})$  = 7.7 Hz, 1H<sub>ar</sub>, H-7'), 7.10 – 7.06 (sm, 2H<sub>ar</sub>, H-2, H-6), 6.93 (td,  $^3J(\text{H,H})$  = 1.4 Hz,  $^3J(\text{H,H})$  = 7.7 Hz, 1H<sub>ar</sub>, H-6'), 3.82 (s, 3H, OCH<sub>3</sub>). For one NH no signal was visible.

$^{13}\text{C-NMR}$  (101 MHz,  $\text{DMSO-}d_6$ ):  $\delta$  = 165.69 (C<sub>q,ar</sub>, C=S), 159.89 (C<sub>q,ar</sub>, C-2'), 148.39 (C<sub>q,ar</sub>, C-4), 139.48 (C<sub>q,ar</sub>, C-3'a), 133.49 (C-H<sub>ar</sub>, C-5'), 130.64 (C-H<sub>ar</sub>, C-6'), 129.73 (2C-H<sub>ar</sub>, C-2, C-6), 124.55 (C<sub>q,ar</sub>, C-7'a), 124.48 (C<sub>q,ar</sub>, C-1), 123.29 (C-H<sub>ar</sub>, C-7'), 119.64 (C-H<sub>ar</sub>, C-4'), 114.78 (2C-H<sub>ar</sub>, C-3, C-5), 55.56 (OCH<sub>3</sub>).

Anal. Calcd. for C<sub>15</sub>H<sub>14</sub>N<sub>4</sub>S<sub>2</sub>O: C: 54.52; H: 4.27; N: 16.96. Found: C: 54.26; H: 4.082; N: 16.7.



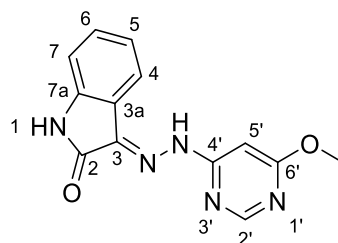
**3-(2-(1',3'-benzothiazol-2'-yl)hydrazine-1-ylidene)-2,3-dihydro-indol-2-one (VII-c)**

The reaction of isatin (222.6 mg, 1.513 mmol) with 2-hydrazino-benzothiazole (250 mg, 1.513 mmol) in ethanolic solution under acetic acid catalysis delivered the pure product as a yellow precipitate after recrystallization (The yield was not determined).

$^1\text{H-NMR}$  (500 MHz,  $\text{DMSO-}d_6$ ):  $\delta = 13.38$  (s, 1H, N-H), 11.24 (s, 1H, N-H), 7.94 (d,  $^3J(\text{H,H}) = 7.6$  Hz, 1H<sub>ar</sub>, H-4'), 7.67 (d,  $^3J(\text{H,H}) = 7.6$  Hz, 1H<sub>ar</sub>, H-7'), 7.55 (d,  $^3J(\text{H,H}) = 7.3$  Hz, 1H<sub>ar</sub>, H-7), 7.44 – 7.39 (sm, 1H<sub>ar</sub>, H-6' or H-5'), 7.39 – 7.34 (sm, 1H<sub>ar</sub>, H-5' or H-6'), 7.30 – 7.25 (m, 1H<sub>ar</sub>, H-4), 7.10 (t,  $^3J(\text{H,H}) = 7.7$  Hz, 1H<sub>ar</sub>, H-6), 6.97 (d,  $^3J(\text{H,H}) = 7.9$  Hz, 1H<sub>ar</sub>, H-5).

$^{13}\text{C-NMR}$  (126 MHz,  $\text{DMSO-}d_6$ ):  $\delta = 141.64$  (C<sub>q,ar</sub>, C-7a), 130.85 (C-H<sub>ar</sub>, C-6), 126.36 (C-H<sub>ar</sub>, C-5'), 123.29 (C-H<sub>ar</sub>, C-6'), 122.43 (C-H<sub>ar</sub>, C-5), 121.93 (C-H<sub>ar</sub>, C-7'), 120.48 (C-H<sub>ar</sub>, C-4), 120.01 (C-H<sub>ar</sub>, C-4'), 119.74 (C<sub>q,ar</sub>, C-3a), 111.09 (C-H<sub>ar</sub>, C-7). Signals for C-3, C-3a', and C-7a' were not visible in the APT test.

Purity of the compound was determined with HPLC MS to be  $\geq 95\%$  (m/z calculated for [M]: 294.33, found 295.2 for [M + H]<sup>+</sup>).

**3-(2'-(6'-methoxypyrimidin-4'-yl)hydrazono)inulin-2-one (VII-d)**

4-hydrazinyl-6-methoxypyrimidine (**E-8**, 150 mg, 1.04 mmol) was then reacted with isatin (152.7 mg, 1.04 mmol) in ethanolic solution under acetic acid catalysis. The reaction delivered the pure product as a yellow powder after column chromatography and recrystallization in 24% yield (68 mg, 0.248 mmol).

$^1\text{H-NMR}$  (500 MHz,  $\text{DMSO-}d_6$ ):  $\delta = 11.09$  (bs, 1H, N-H), 10.70 (s, 1H, N-H), 8.51 (s, 1H<sub>ar</sub>, H-2'), 8.11 (d,  $^3J(\text{H,H}) = 7.9$  Hz, 1H<sub>ar</sub>, H-7), 7.35 (td,  $^4J(\text{H,H}) = 0.9$  Hz,  $^3J(\text{H,H}) = 7.7$  Hz, 1H<sub>ar</sub>, H-6), 7.04 (td,  $^4J(\text{H,H}) = 0.9$  Hz,  $^3J(\text{H,H}) = 7.6$  Hz, 1H<sub>ar</sub>, H-5), 6.89 (d,  $^3J(\text{H,H}) = 7.9$  Hz, 1H<sub>ar</sub>, H-4), 6.63 (s, 1H<sub>ar</sub>, H-5'), 3.93 (s, 3H, OCH<sub>3</sub>).

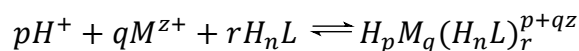
$^{13}\text{C-NMR}$  (126 MHz,  $\text{DMSO-}d_6$ ):  $\delta = 170.22$  (C<sub>q,ar</sub>, C-6'), 164.64 (C<sub>q</sub>, C=O), 163.06 (C<sub>q,ar</sub>, C-4'), 158.15 (C-H<sub>ar</sub>, C-2'), 143.07 (C<sub>q</sub>, C-7a), 135.81 (C<sub>q,ar</sub>, C-3), 131.72 (C-H<sub>ar</sub>, C-6), 125.67 (C-H<sub>ar</sub>, C-5), 121.49 (C-H<sub>ar</sub>, C-4), 120.00 (C<sub>q,ar</sub>, C-3a), 110.92 (C-H<sub>ar</sub>, C-7), 87.83 (C-H<sub>ar</sub>, C-5'), 53.90 (OCH<sub>3</sub>).

Anal. Calcd. for C<sub>13</sub>H<sub>11</sub>N<sub>5</sub>O×H<sub>2</sub>O: C: 54.35; H: 4.56; N: 24.38. Found: C: 54.85; H: 4.517; N: 23.26.

Additionally purity was determined with HPLC MS to be  $\geq 95\%$  (m/z calculated for [M]: 269.26, found 270.0 for [M + H]<sup>+</sup>).

## 6.2. UV-Vis spectrophotometric measurements for complex stability evaluation

The interaction of metal ions and ligands can be quantified by means of stability constants  $\beta_{p,q,r}$  that give information about the thermodynamic stability of metal complexes [352,353]. In a system containing a metal ion  $M^{z+}$  and a ligand  $H_nL$ , the following solution equilibrium can be formulated:



The stoichiometric coefficients for the metal ion ( $q$ ) and the ligand ( $r$ ) are higher or equal to zero, while the coefficient  $p$  can be positive for protons, but can also take negative values for hydroxide ions [353]. According to the law of mass action the stability constant  $\beta_{p,q,r}$  can be expressed as the quotient of the activities of the participating species  $\{X_i\}$ , which is defined as the product of their activity coefficients  $f_i$  with their concentrations  $[X_i]$ :

$$\beta_{p,q,r} = \frac{\{H_pM_q(H_nL)_r^{p+qz}\}}{\{H^+\}^p\{M^{z+}\}^q\{H_nL\}^r} = \frac{f_{H_pM_q(H_nL)_r^{p+qz}}}{f_{H^+}^p \cdot f_{M^{z+}}^q \cdot f_{H_nL}^r} \cdot \frac{[H_pM_q(H_nL)_r^{p+qz}]}{[H^+]^p[M^{z+}]^q[H_nL]^r}$$

The excess of a low-valent electrolyte salt ensures constant activity coefficients for all ions and molecules in the system under investigation. This allows the incorporation of activity coefficients into the stability constant and therefore the approximately usage of concentrations instead of activities [352–354]. Accordingly, an ionic strength of 0.20 M was adjusted using KCl salt in the samples.

Spectrophotometric titrations were performed on samples of the ligands alone or in the presence of  $FeCl_3$  or  $CuCl_2$ . The applied metal-to-ligand ratios were 1:1, 1:2 and 1:3. Generally the concentration of the ligand was set to 50  $\mu$ M. Due to its lower water solubility ligand **Q-4** is an exception to this general procedure. Here a more diluted sample preparation was required; therefore titrations with this ligand were performed at 10  $\mu$ M ligand concentrations. The initial pH of the samples was 2, the initial volume 10.00 mL. pH values were determined using an *Orion 710A* pH-meter equipped with a *Metrohm* combined electrode (type 6.0234.100). The electrode system was calibrated to the pH scale by means of blank titrations (strong acid vs. strong base; HCl vs. KOH) according to the method suggested by Irving *et al.* [355]. Samples were deoxygenated by bubbling purified argon for *ca.* 10 min prior to the measurements. Defined volumes of a 0.10 M carbonate-free KOH solution

containing 0.10 M KCl were applied to the sample using a *Metrohm 665 Dosimat* burette until a pH of 11.5 was reached. The reaction vial was thermostated to  $25.0 \pm 0.1$  °C and kept under argon atmosphere.

In case of ligand **IV-b** additional samples were prepared for the 1:1 Fe (III) to ligand ratio at lower pH values. In this individual samples KCl was partially or completely replaced by HCl, and pH values in the range between 0.7 and 2.0 were calculated from the HCl content.

In the evaluation of the equilibrium model  $pH^+ + qM^{z+} + rH_nL \rightleftharpoons H_pM_q(H_nL)_r^{p+qz}$  for the calculation of the stability constants  $\beta_{p,q,r}$  it is good practice to analyze the two subsystems, in which one or the other stoichiometric coefficient is set to zero.  $\beta_{p,q,0}$ , in which r is zero, describes the acid-base equilibria for the metal ion,  $\beta_{p,0,r}$  the one for the free ligand. Therefore from the latter system, the ligand's pK<sub>a</sub> values can be determined. In case of the metal hydroxido species, literature data was used [356].

Spectral changes upon addition of the base were recorded in the wavelength interval between 200 and 800 nm using a *Hewlett Packard 8452A* diode array spectrophotometer. Quartz glass cuvettes with path lengths (*l*) of 1 or 2 cm were used (Hellma), depending on the molar absorptivity ( $\epsilon$ ) of the applied ligand samples. During one titration spectra of approximately 30 samples were measured.

According to the Lambert-Beer law the absorption *A* of the sample (*s*) at a wavelength ( $\lambda$ ) is composed of the additive contributions of each single species  $X_i$  that is present in the solution [353]:

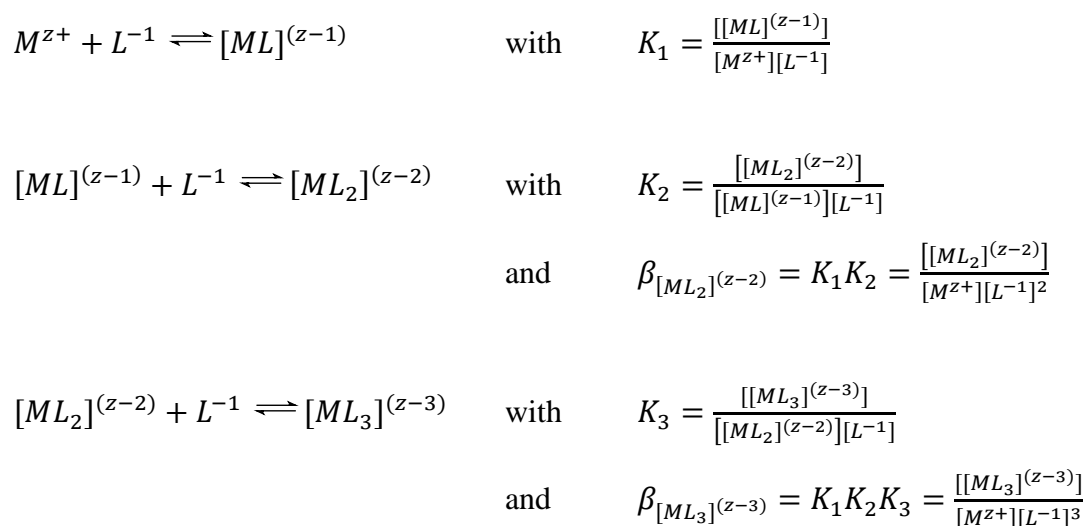
$$A_{s,\lambda} = \sum_{i=1}^N A_{i,s,\lambda} = l \cdot \sum_{i=1}^N \epsilon_{i,\lambda} \cdot c_{i,s}$$

With the help of the program PSEQUAD the molar absorbance spectra of the individual species  $X_i$  were calculated on the basis of deconvolution of the measured spectra. This is done in two steps by first solving the matrices of data describing the equilibrium system through the mass-balance equations at the applied pH values for the unknown free concentrations. The second step includes refinement and minimizing steps in order to obtain the formation constants  $\beta_{p,q,r}$  and molar absorptivity values  $\epsilon_i$  that best fit to the measured data and the

applied equilibrium model [357]. These calculations were done by Professor *Éva A. Enyedy* (Department of Inorganic and Analytical Chemistry, University of Szeged, Hungary).

With the help of the computer program MEDUSA [358] the calculated data can be used to predict further chemical equilibrium and distribution diagrams at given conditions.

$\beta_{p,q,r}$  is the overall stability constant, which is also called cumulative stability constant, since it can be formulated as the product of stepwise stability constants [359]. For simplicity reasons the following considerations are given for an example system of a ligand like **Q-1**, which coordinates to the metal ion in its deprotonated form  $L^{-1}$ . With iron<sup>III</sup> ( $z = 3$ ) three putative complexes can be formed, which are described by the following equations:



Concentrations and distributions of the different species can be calculated based on the total metal ion concentration  $[M^{z+}]_{\Sigma}$ :

$$[M^{z+}]_{\Sigma} = [M^{z+}] + [ML]^{(z-1)} + [ML_2]^{(z-2)} + [ML_3]^{(z-3)}$$

applying the above listed equilibria this can be written as:

$$[M^{z+}]_{\Sigma} = [M^{z+}] \cdot \{1 + K_1[L] + K_1 \cdot K_2[L]^2 + K_1 \cdot K_2 \cdot K_3[L]^3\} = [M^{z+}] \cdot \xi$$

the expression within the curly brackets can be summarized in  $\xi$  and is defined as the reciprocal fraction of a species, which was not converted into another one. Applying these formulas, the free metal ion concentration can be described as

$$[M^{z+}] = \frac{[M^{z+}]_{\Sigma}}{\xi}$$

Accordingly, the concentrations of the other species can be formulated as

$$[[ML]^{(z-1)}] = \frac{[M^{z+}]_{\Sigma}}{\xi} \cdot K_1 [L]$$

$$[[ML_2]^{(z-2)}] = \frac{[M^{z+}]_{\Sigma}}{\xi} \cdot K_1 \cdot K_2 [L]^2$$

$$[[ML_3]^{(z-3)}] = \frac{[M^{z+}]_{\Sigma}}{\xi} \cdot K_1 \cdot K_2 \cdot K_3 [L]^3$$

These basic relations are incorporated in the two applied programs (PSEQUAD and MEDUSA).

### 6.3. Electrochemical Studies

#### 6.3.1. Cyclic voltammetry

The thermodynamics and kinetics of redox reactions, which take place at the interface of an electrode and an ionic conductor, can be investigated with dynamic electroanalytical methods, such as cyclic voltammetry. The interaction of electrical energy and chemical change within the observed heterogeneous electron transfer reactions causes voltammograms with characteristic shapes. The unequivocal positions of the voltammetric waves on the potential scale are characteristic for the individual electrochemical properties of redox systems, like a virtual fingerprint. Therefore the technique has been labelled “electrochemical spectroscopy” [360–362].

The experimental setup is built by an electrochemical cell consisting of three electrodes as shown in Figure 77 A. Potentials of the working electrode are given against a non-polarized reference electrode. In order to protect the reference electrode against large currents, an additional auxiliary electrode is used [362]. The electrochemical cell is connected to a potentiostat with voltage scan generator and recorder. A linear potential ramp is applied to the working electrode with a constant sweep rate  $= \frac{dE}{dt}$ .

After reaching the switching potential  $E_{\lambda}$  the direction of the potential ramp is reversed and the potential returns linearly to its initial value, thus forming a triangular voltage as depicted in Figure 77 B.

The system utilized in this thesis consisted of a PC controlled electrochemical measurement system (*EF 451*, Szeged, Hungary) with a glassy carbon disc electrode as working electrode, a platinum electrode as auxiliary electrode and a Ag/AgCl/KCl (1 M) reference electrode. Electrochemical potentials were converted into the normal hydrogen electrode (NHE) scale by addition of 0.236 V [363].

The water jacket of the electrochemical cell (see Figure 77 A) ensured a constant temperature of  $25.0 \pm 0.1$  °C. Due to low solubility in aqueous solution, samples containing either 1.0 mM metal ion or 1 mM ligand were prepared in a 90% (v/v) DMSO-water mixture. 10 mM of *tert*-butylammonium chloride (TBACl) was used as a supporting electrolyte and a sweep rate of  $v = 100$  mV/s was applied in the range of  $-1.5$  to  $+1.2$  V.

Measurements were performed under argon atmosphere after purging the samples for 15 min with argon.

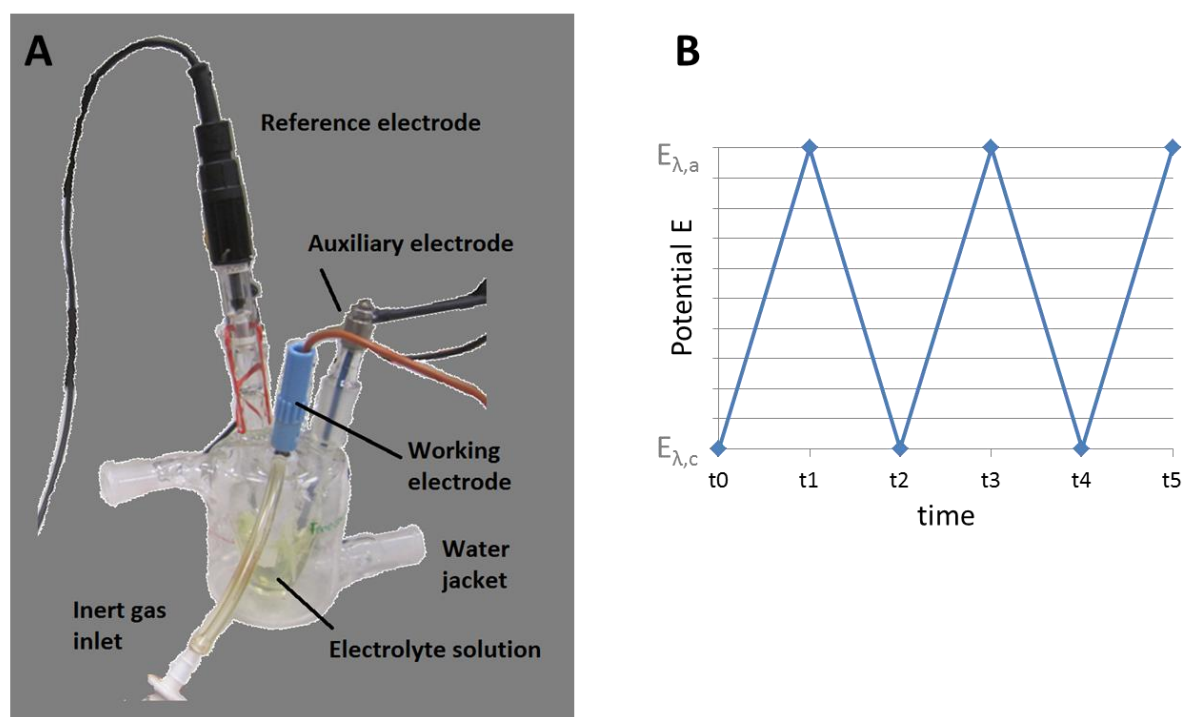
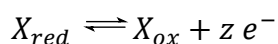


**Figure 77:** Experimental setup of CV measurements A: thermostated reaction vial with an Ag/AgCl (1M KCl) reference electrode, a Pt-reference electrode and a Glassy Carbon disc electrode as a working electrode. CVs were performed in 90% (v/v) DMSO with TBACl (10 mM) as supporting electrolyte. B: time course of the triangular voltage applied in the three electrode system.

Ferrocene in 90 % (v/v) DMSO-water was used as an external standard to reconcile the electrochemical system ( $E_{1/2} = +0.428 \pm 0.012$  V). Figure 78 shows a representative voltammogram of the applied standard.

At the initial potential (A) no electrochemical processes take place, yet [361]. Changing the potential (from A to B), only capacitive currents flow, which are caused by the formation of the Helmholtz double layer without charge transfer between electrode and electrolyte [362]. As soon as the electrochemical double layer is formed, the oxidation takes place (B), and a Faradaic current occurs based on the heterogeneous charge transfer at the phase boundary [362].



The current  $I$  flowing as a result of this reaction with the transfer of  $z$  electrons is “diffusion controlled”: It is proportional to the concentration gradient of the produced oxidized species  $X_{ox}$  at the electrode surface ( $x=0$ ):

$$I = zFA \cdot D_{[X_{ox}]} \left( \frac{\partial [X_{ox}]}{\partial x} \right)_{x=0} = j_{[X_{red}]} \cdot zFA$$

with  $F$  being the Faraday constant,  $A$  being the electrode surface and  $D$  being the diffusion coefficient. The charge flux at this reaction  $j_{[X]}$  is proportional to the concentration gradient at the electrode surface [362]:

$$j_{[X_{red}]} = -D_{[X_{red}]} \left( \frac{\partial [X_{red}]}{\partial x} \right)_{x=0} = D_{[X_{ox}]} \left( \frac{\partial [X_{ox}]}{\partial x} \right)_{x=0}$$

Therefore the current can be expressed as

$$I = j_{[X_{red}]} \cdot zFA.$$

The oxidation of the reduced species takes place, with its peak in position (C) in Figure 78. As a consequence of the occurring reaction, the concentration of the reduced species at the electrode surface decreases following the Nernst equation [361]:

$$E = E^{\circ} - \frac{RT}{zF} \cdot \ln \frac{[X_{red}]}{[X_{ox}]}$$

This decrease in concentration results in a decrease of the diffusion dependent current, as seen in the voltammogram from points (C) to (D). A slight increase in the current might be observed from point (D) to the anodic switching potential  $E_{\lambda, \text{anodic}}$ , which is reached at point (E) in Figure 78. This might indicate a new redox process – in aqueous solutions at 1.23 V against NHE formation of  $O_2$  might be observed for example.

Reversing the sweep after the switching potential causes an inversion of the Helmholtz double layer, resulting in capacitive currents [361,362]. Is the double layer established, as in point F in Figure 78, the diffusion controlled reduction of the oxidized species starts with its maximum resulting in the peak current at position G Figure 78. Due to a decrease in concentration of the oxidized species at the electrode surface, the current decreases again from (G) to (H). The cycle is continued to the cathodic switching potential at (J), and repeated from there.

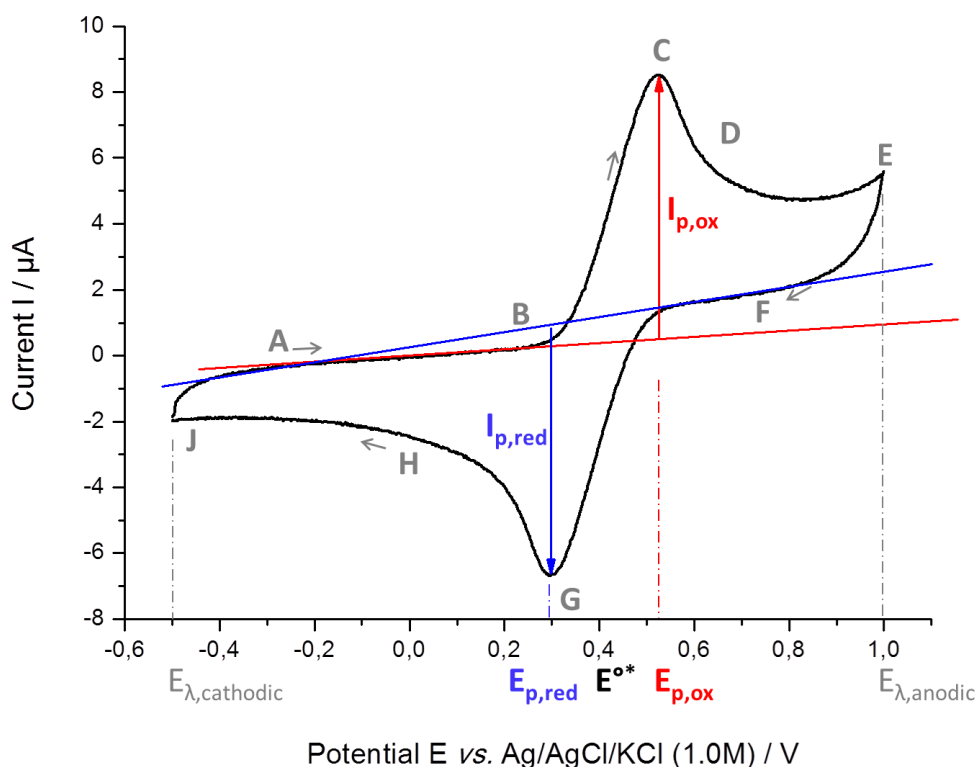


**Figure 78:** Representative voltammogram of a 1.0 mM Ferrocene solution in 90% (v/v) DMSO, supplemented with 10 mM TBACl at a sweep rate of  $\nu = 100$  mV/s in the range of  $-0.5$  to  $+1.0$  V,  $E_{\lambda,\text{cathodic}}$ ,  $E_{\lambda,\text{anodic}}$ : switching potentials;  $E_{p,\text{red}}$ ,  $E_{p,\text{ox}}$ : peak potentials,  $I_{p,\text{red}}$ ,  $I_{p,\text{ox}}$ : peak currents.

Two factors influence the current at the working electrode, namely the heterogeneous charge transfer (as defined in the equation describing  $j_{(X)}$ ) and the transport of mass, that builds up a concentration gradient at the electrode surface [362]. In the described voltammogram, the current is diffusion controlled, that means the charge transfer occurs at such a high rate, that a dynamic equilibrium is established at the phase boundary and the Nernst equation is satisfied. This is the case for reversible systems [362]. On the contrary, in some cases the rate of the charge transfer is very slow, so that only one of the heterogeneous reactions (oxidation or



reduction) can be measured. In that cases the current depends on this rate and is charge-transfer controlled. These reactions are irreversible and the Nernst equation does not describe these processes [362]. A third case can be distinguished, in which charge-transfer and diffusion influence the measured current. In these reactions, which are termed “quasi-reversible” the Nernst equation is approximately satisfied [362].

Correlating the described kinetics with observed experimental parameters, diagnostic criteria could be identified for the characterization of electrochemical systems. For example the ratio of anodic to cathodic peak currents has been found to be close to 1 for reversible processes [360]. Also the half-peak potentials of a reversible process should have a distance of  $\Delta E = 58 \text{ mV}$  [361].

### 6.3.2. Oxidation of ascorbic acid (ASC) and glutathione (GSH)

The redox activity of compounds can also be investigated by monitoring reactions with biologically relevant antioxidants. At pH 7.4 two powerful intracellular reducing agents are glutathione (GSH) and ascorbate (ASC), with formal potential of the GSSG/GSH and the dehydro-L-ascorbic acid/ASC redox pairs are  $-0.26 \text{ V}$  and  $+0.05 \text{ V}$ , respectively [255,256]. The changes in characteristic regions of the compounds' spectra (especially those of metal complexes) that occur upon reaction with the antioxidants were followed over time [89,263]. In order to address the reversibility of the observed reactions, hydrogen peroxide was added at the end of the reaction with the antioxidants to re-oxidize the reduced products [89]. UV-Vis spectrophotometric measurements were performed under aseptic conditions using a Hewlett Packard 8452A diode array spectrophotometer and a special, tightly closed tandem cuvette (Hellma Tandem Cell, 238-QS, path length: 1 cm, Figure 79).



**Figure 79:** Tandem Cuvette used for GSH and ASC oxidation assay.

The reagents were separated until the reaction was triggered. The pH of the solutions was adjusted to 7.40 by 50 mM HEPES and an ionic strength of 0.1 M (KCl) was applied at  $25.0 \pm 0.1$  °C. In case of the **IVa**-Fe system, a pH of 5.45 was adjusted by 50 mM MES buffer. One of the isolated pockets contained the reducing agent (ASC or GSH) at ten times higher concentrations than that of the metal ions. The other pocket contained the ligand in the presence of equimolar amounts of metal ions. The used concentrations were 25  $\mu$ M in case of the **IVa**-Cu (II) system, 50  $\mu$ M for the **IVa**-Fe (III) system, and 100  $\mu$ M for the **Q-1**, **Q-2**, **Q-3** and **Q-4** systems with both metal ions. Both isolated pockets of the cuvette were completely deoxygenated by carefully bubbling a stream of argon for 10 min before mixing the reactants. Spectra were recorded before and immediately after mixing, and changes were followed for up to 90 min. At the end of the measurements *cc.* H<sub>2</sub>O<sub>2</sub> (35%, 50  $\mu$ L to 1.4 mL) was added to the samples.

**7. List of Abbreviations**

6PG $\delta$ L	6-phosphoglucono- $\delta$ -lactone
ABC	ATP-binding-cassette
ADP	Adenosine diphosphate
Akt1	threonine-protein kinase (PKB)
ASK1	apoptosis signal-regulating kinase-1
ATCC	American tissue culture collection
ATP	Adenosine triphosphate
Bad	Bcl-2-associated death promoter
Bax	Bcl-2-associated X protein
BCRP	Breast Cancer Resistance Protein
bs	NMR signal, broad singlet
Cat	catalase
CDK2	Cyclin-dependent kinase 2
CHO	Chinese Hamster ovary
CP	ceruloplasmin
C <sub>q</sub>	NMR signal, quaternary carbon
C <sub>q,ar</sub>	NMR signal, quaternary aromatic carbon
CS	collateral sensitivity
CTR1	copper transporter
d	NMR signal, duplet
DCF	Dichlorofluorescein
DCFDA	2'7'-Dichlorofluoresceindiacetate
DCF-H	Dichlorofluorescin
dd	NMR signal, duplet of duplets
ddd	NMR signal, duplet of duplets of duplets
DMEM	Dulbecco's Modified Eagle Medium
DMSO	dimethyl sulfoxide

DMT1	divalent metal transporter
DNA	Deoxyribonucleic acid
dt	NMR signal, duplet of triplets
DTP	Developmental Therapeutics Program
DTT	dithiothreitol
ECAR	extracellular acidification rates
FACS	Fluorescence-activated cell sorting
FBS	fetal bovine serum
FPN1	ferroportin
G6P	glucose-6-phosphate
G6PDH	glucose-6-phosphate dehydrogenase
GPx	glutathione peroxidase
GPx	glutathione peroxidase
GR	glutathione reductase
GRX	glutaredoxin
GSH	reduced glutathione
GS-SG	oxidized glutathione
GST $\pi$	Glutathione S-transferase $\pi$
HIF-1 $\alpha$	Hypoxia-inducible factor 1-alpha
HSAB	hard and soft acids and bases
IKK	I $\kappa$ B-kinase
IRE-IRP	iron-response element and iron-regulatory protein (1/2)
ISC	iron sulfur cluster
I $\kappa$ B	inhibitor of NF $\kappa$ B
J	NMR signal, coupling constant
JNK	c-Jun N-terminal kinase
Keap1	Kelch-like ECH-associated protein 1
m	NMR signal, multiplet
MCX-I	mitochondrial complex I

MDR	Multidrug Resistance
MRP1	Multidrug resistance-associated protein 1
MTFR	mitotransferrin
mTOR	mammalian target of rapamycin
MTT	3-(4,5-dimethylthiazol-2-yl)-2,5-diphenyl tetrazolium bromide
NAC	<i>N</i> -acetylcysteine
NADP <sup>+</sup>	oxidized nicotinamide adenine dinucleotide phosphate
NADPH	reduced nicotinamide adenine dinucleotide phosphate
NCI	National Cancer Institute
NDRG1	N-myc downstream-regulated gene 1
NFκB	nuclear factor κB
Nrf2	Nuclear factor (erythroid-derived 2)-like 2
OX	oxidases
PBS	phosphate buffered saline
PDK1	3'-phosphoinositide-dependent kinase-1
PG	Plumbagin
P-gp	P-glycoprotein
PI3K	phosphatidylinositol-3-kinase
PI3K/AKT/mTOR	Phosphatidylinositol-4,5-bisphosphate 3-kinase / Protein kinase B (PKB) / mammalian target of rapamycin
PKC	protein kinase C
PKD	protein kinase D
PTEN	phosphatidylinositol-3,4,5-trisphosphate 3-phosphatase
pyr	pyruvate
q	NMR signal, quartet
ROS	reactive oxygen species
RPMI	Roswell Park Memorial Institute medium,
RR	Ribonucleotide reductase
s	NMR signal, singlet

sm	NMR signal, symmetrical multiplet
SNP	single-nucleotide polymorphism
SOD	superoxide dismutase
SR	Selectivity ratio
STEAP3	six transmembrane epithelial antigen of the prostate 3 (ferrireductase)
t	NMR signal, triplet
TBACl	<i>tert</i> -butylammonium chloride
<sup>t</sup> BHP	<i>tert</i> -butyl hydroperoxide
td	NMR signal, triplet of duplets
tet-off	tetracycline-repressible
Tf	Transferrin
TfR	transferrin receptor
TPx	thioredoxin peroxidase
Trx	thioredoxin
Trx-(SH) <sub>2</sub>	reduced thioredoxin
TrxR	thioredoxin reductase
Trx-S <sub>2</sub>	oxidized thioredoxin
TSC	thiosemicarbazone

**8. Bibliography**

- [1] P. Chiba, G.F. Ecker, Inhibitors of ABC-type drug efflux pumps: an overview of the current patent situation, *Expert Opin. Ther. Pat.* 14 (2004) 499–508. doi:10.1517/13543776.14.4.499.
- [2] P. Boyle, B. Levin, International Agency for Research on Cancer., *World cancer report 2008 2008*, IARC Press, Lyon, 2008. <http://site.ebrary.com/id/10306279> (accessed November 18, 2014).
- [3] M.M. Gottesman, T. Fojo, S.E. Bates, MULTIDRUG RESISTANCE IN CANCER: ROLE OF ATP-DEPENDENT TRANSPORTERS, *Nat. Rev. Cancer.* 2 (2002) 48–58. doi:10.1038/nrc706.
- [4] K. Aktories, U. Förstermann, F. Hofmann, K. Starke, *Allgemeine und spezielle Pharmakologie und Toxikologie*, 9th ed., Elsevier, 2005.
- [5] M.M. Gottesman, J. Ludwig, D. Xia, G. Szakacs, Defeating Drug Resistance in Cancer, *Discov. Med.* 6 (2009) 18–23.
- [6] L.A. Garraway, P.A. Jänne, Circumventing Cancer Drug Resistance in the Era of Personalized Medicine, *Cancer Discov.* 2 (2012) 214–226. doi:10.1158/2159-8290.CD-12-0012.
- [7] C. Bock, T. Lengauer, Managing drug resistance in cancer: lessons from HIV therapy, *Nat. Rev. Cancer.* 12 (2012) 494–501. doi:10.1038/nrc3297.
- [8] G.J. Schuurhuis, H.J. Broxterman, J.H. de Lange, H.M. Pinedo, T.H. van Heijningen, C.M. Kuiper, et al., Early multidrug resistance, defined by changes in intracellular doxorubicin distribution, independent of P-glycoprotein., *Br. J. Cancer.* 64 (1991) 857–861.
- [9] G. Szakács, J.K. Paterson, J.A. Ludwig, C. Booth-Genthe, M.M. Gottesman, Targeting multidrug resistance in cancer, *Nat. Rev. Drug Discov.* 5 (2006) 219–234. doi:10.1038/nrd1984.
- [10] B. Marquez, F. Van Bambeke, ABC multidrug transporters: target for modulation of drug pharmacokinetics and drug-drug interactions, *Curr. Drug Targets.* 12 (2011) 600–620.
- [11] O.H. Warburg, The Classic: The Chemical Constitution of Respiration Ferment, *Clin. Orthop. Relat. Res.* 468 (2010) 2833–2839. doi:10.1007/s11999-010-1534-y.
- [12] R.C. Lyon, J.S. Cohen, P.J. Faustino, F. Megnin, C.E. Myers, Glucose Metabolism in Drug-sensitive and Drug-resistant Human Breast Cancer Cells Monitored by Magnetic Resonance Spectroscopy, *Cancer Res.* 48 (1988) 870–877.
- [13] M.-E. Harper, A. Antoniou, E. Villalobos-Menuey, A. Russo, R. Trauger, M. Vendemelio, et al., Characterization of a novel metabolic strategy used by drug-resistant tumor cells, *FASEB J. Off. Publ. Fed. Am. Soc. Exp. Biol.* 16 (2002) 1550–1557. doi:10.1096/fj.02-0541com.
- [14] H.J. Broxterman, H.M. Pinedo, C.M. Kuiper, L.C. Kaptein, G.J. Schuurhuis, J. Lankelma, Induction by verapamil of a rapid increase in ATP consumption in multidrug-resistant tumor cells., *FASEB J.* 2 (1988) 2278–2282.

- [15] H.J. Broxterman, H.M. Pinedo, C.M. Kuiper, G.J. Schuurhuis, J. Lankelma, Glycolysis in P-glycoprotein-overexpressing human tumor cell lines Effects of resistance-modifying agents, *FEBS Lett.* 247 (1989) 405–410. doi:10.1016/0014-5793(89)81380-8.
- [16] E. Landwojtowicz, P. Nervi, A. Seelig, Real-Time Monitoring of P-Glycoprotein Activation in Living Cells <sup>†</sup>, *Biochemistry (Mosc.)*. 41 (2002) 8050–8057. doi:10.1021/bi025720s.
- [17] E. Gatlik-Landwojtowicz, P. Äänismaa, A. Seelig, The Rate of P-Glycoprotein Activation Depends on the Metabolic State of the Cell <sup>†</sup>, *Biochemistry (Mosc.)*. 43 (2004) 14840–14851. doi:10.1021/bi048761s.
- [18] P.J. Thornalley, N. Rabbani, Glyoxalase in tumorigenesis and multidrug resistance, *Semin. Cell Dev. Biol.* 22 (2011) 318–325. doi:10.1016/j.semcdb.2011.02.006.
- [19] G.L. Semenza, HIF-1 mediates metabolic responses to intratumoral hypoxia and oncogenic mutations, *J. Clin. Invest.* 123 (2013) 3664–3671. doi:10.1172/JCI67230.
- [20] B. Zhivotovsky, S. Orrenius, The Warburg Effect returns to the cancer stage, *Semin. Cancer Biol.* 19 (2009) 1–3. doi:10.1016/j.semcancer.2008.12.003.
- [21] H.A. Burris, Overcoming acquired resistance to anticancer therapy: focus on the PI3K/AKT/mTOR pathway, *Cancer Chemother. Pharmacol.* 71 (2013) 829–842. doi:10.1007/s00280-012-2043-3.
- [22] M. Wartenberg, F.C. Ling, M. Müschen, F. Klein, H. Acker, M. Gassmann, et al., Regulation of the multidrug resistance transporter P-glycoprotein in multicellular tumor spheroids by hypoxia-inducible factor (HIF-1) and reactive oxygen species, *FASEB J.* 17 (2003) 503–505.
- [23] S. Doublier, D.C. Belisario, M. Polimeni, L. Annaratone, C. Riganti, E. Allia, et al., HIF-1 activation induces doxorubicin resistance in MCF7 3-D spheroids via P-glycoprotein expression: a potential model of the chemo-resistance of invasive micropapillary carcinoma of the breast, *BMC Cancer.* 12 (2012) 4.
- [24] E. Wang, M.D. Lee, K.W. Dunn, Lysosomal accumulation of drugs in drug-sensitive MES-SA but not multidrug-resistant MES-SA/Dx5 uterine sarcoma cells, *J. Cell. Physiol.* 184 (2000) 263–274. doi:10.1002/1097-4652(200008)184:2<263::AID-JCP15>3.0.CO;2-F.
- [25] T. Yamagishi, S. Sahni, D.M. Sharp, A. Arvind, P.J. Jansson, D.R. Richardson, P-glycoprotein Mediates Drug Resistance via a Novel Mechanism Involving Lysosomal Sequestration, *J. Biol. Chem.* 288 (2013) 31761–31771. doi:10.1074/jbc.M113.514091.
- [26] M. Dean, A. Rzhetsky, R. Allikmets, The Human ATP-Binding Cassette (ABC) Transporter Superfamily, *Genome Res.* 11 (2001) 1156–1166. doi:10.1101/gr.184901.
- [27] K. Dano, Active outward transport of daunomycin in resistant Ehrlich ascites tumor cells, *Biochim. Biophys. Acta.* 323 (1973) 466–483.
- [28] R.L. Juliano, V. Ling, A surface glycoprotein modulating drug permeability in Chinese hamster ovary cell mutants, *Biochim. Biophys. Acta.* 455 (1976) 152–162.



- [29] S.P. Cole, H.F. Downes, S.E. Mirski, D.J. Clements, Alterations in glutathione and glutathione-related enzymes in a multidrug-resistant small cell lung cancer cell line, *Mol. Pharmacol.* 37 (1990) 192–197.
- [30] S.P. Cole, G. Bhardwaj, J.H. Gerlach, J.E. Mackie, C.E. Grant, K.C. Almquist, et al., Overexpression of a transporter gene in a multidrug-resistant human lung cancer cell line, *Science*. 258 (1992) 1650–1654.
- [31] L.A. Doyle, W. Yang, L.V. Abruzzo, T. Krognann, Y. Gao, A.K. Rishi, et al., A multidrug resistance transporter from human MCF-7 breast cancer cells, *Proc. Natl. Acad. Sci.* 95 (1998) 15665–15670. doi:10.1073/pnas.95.26.15665.
- [32] G.A. Altenberg, Structure of multidrug-resistance proteins of the ATP-binding cassette (ABC) superfamily, *Curr. Med. Chem.-Anti-Cancer Agents*. 4 (2004) 53–62.
- [33] I.D. Kerr, P.M. Jones, A.M. George, Multidrug efflux pumps: The structures of prokaryotic ATP-binding cassette transporter efflux pumps and implications for our understanding of eukaryotic P-glycoproteins and homologues: The structure of eukaryotic ABC multidrug pumps, *FEBS J.* 277 (2010) 550–563. doi:10.1111/j.1742-4658.2009.07486.x.
- [34] K. Wong, S.J. Bridson, N.D. Holliday, I.D. Kerr, Plasma membrane dynamics and tetrameric organisation of ABCG2 transporters in mammalian cells revealed by single particle imaging techniques, *Biochim. Biophys. Acta BBA - Mol. Cell Res.* 1863 (2016) 19–29. doi:10.1016/j.bbamcr.2015.10.002.
- [35] M. Yu, A. Ocana, I.F. Tannock, Reversal of ATP-binding cassette drug transporter activity to modulate chemoresistance: why has it failed to provide clinical benefit?, *Cancer Metastasis Rev.* 32 (2013) 211–227. doi:10.1007/s10555-012-9402-8.
- [36] L. ChemAxon, Instant J Chem / MarvinSketch, ChemAxon Ltd., Budapest, Hungary, 2012. <http://www.chemaxon.com>.
- [37] A. Tamaki, C. Ierano, G. Szakács, R.W. Robey, S.E. Bates, The controversial role of ABC transporters in clinical oncology, *Essays Biochem.* 50 (2011) 209–232. doi:10.1042/bse0500209.
- [38] X. Declèves, S. Bihorel, M. Debray, S. Yousif, G. Camenisch, J.-M. Scherrmann, ABC transporters and the accumulation of imatinib and its active metabolite CGP74588 in rat C6 glioma cells, *Pharmacol. Res.* 57 (2008) 214–222. doi:10.1016/j.phrs.2008.01.006.
- [39] E. Bakos, R. Evers, E. Sinkó, A. Váradi, P. Borst, B. Sarkadi, Interactions of the human multidrug resistance proteins MRP1 and MRP2 with organic anions, *Mol. Pharmacol.* 57 (2000) 760–768.
- [40] S.V. Ambudkar, S. Dey, C.A. Hrycyna, M. Ramachandra, I. Pastan, M.M. Gottesman, Biochemical, cellular, and pharmacological aspects of the multidrug transporter, *Annu. Rev. Pharmacol. Toxicol.* 39 (1999) 361–398.

- [41] M.D. Hall, M.D. Handley, M.M. Gottesman, Is resistance useless? Multidrug resistance and collateral sensitivity, *Trends Pharmacol. Sci.* 30 (2009) 546–556. doi:10.1016/j.tips.2009.07.003.
- [42] G. Szakács, M.D. Hall, M.M. Gottesman, A. Boumendjel, R. Kachadourian, B.J. Day, et al., Targeting the Achilles Heel of Multidrug-Resistant Cancer by Exploiting the Fitness Cost of Resistance, *Chem. Rev.* 114 (2014) 5753–5774. doi:10.1021/cr4006236.
- [43] S.G. Aller, J. Yu, A. Ward, Y. Weng, S. Chittaboina, R. Zhuo, et al., Structure of P-Glycoprotein Reveals a Molecular Basis for Poly-Specific Drug Binding, *Science*. 323 (2009) 1718–1722. doi:10.1126/science.1168750.
- [44] R. Callaghan, R.C. Ford, I.D. Kerr, The translocation mechanism of P-glycoprotein, *FEBS Lett.* 580 (2006) 1056–1063. doi:10.1016/j.febslet.2005.11.083.
- [45] C. Van Der Does, R. Tampé, How do ABC transporters drive transport?, *Biol. Chem.* 385 (2004). doi:10.1515/BC.2004.121.
- [46] P.D.W. Eckford, F.J. Sharom, ABC Efflux Pump-Based Resistance to Chemotherapy Drugs, *Chem. Rev.* 109 (2009) 2989–3011. doi:10.1021/cr9000226.
- [47] T. Tsuruo, H. Iida, S. Tsukagoshi, Y. Sakurai, Overcoming of vincristine resistance in P388 leukemia in vivo and in vitro through enhanced cytotoxicity of vincristine and vinblastine by verapamil, *Cancer Res.* 41 (1981) 1967–1972.
- [48] W. Klinkhammer, H. Müller, C. Globisch, I.K. Pajeva, M. Wiese, Synthesis and biological evaluation of a small molecule library of 3rd generation multidrug resistance modulators, *Bioorg. Med. Chem.* 17 (2009) 2524–2535. doi:10.1016/j.bmc.2009.01.072.
- [49] P. Mistry, A.J. Stewart, W. Dangerfield, S. Okiji, C. Liddle, D. Bootle, et al., In Vitro and in Vivo Reversal of P-Glycoprotein-mediated Multidrug Resistance by a Novel Potent Modulator, XR9576, *Cancer Res.* 61 (2001) 749–758.
- [50] O. Polgar, S.E. Bates, ABC transporters in the balance: is there a role in multidrug resistance?, *Biochem. Soc. Trans.* 33 (2005) 241–246.
- [51] G. Szakács, G.K. Chen, M.M. Gottesman, The molecular mysteries underlying P-glycoprotein-mediated multidrug resistance, *Cancer Biol. Ther.* 3 (2004) 382–384.
- [52] M. Falasca, K.J. Linton, Investigational ABC transporter inhibitors, *Expert Opin. Investig. Drugs.* 21 (2012) 657–666. doi:10.1517/13543784.2012.679339.
- [53] L. Amiri-Kordestani, A. Basseville, K. Kurdziel, A.T. Fojo, S.E. Bates, Targeting MDR in breast and lung cancer: Discriminating its potential importance from the failure of drug resistance reversal studies, *Drug Resist. Updat.* 15 (2012) 50–61. doi:10.1016/j.drug.2012.02.002.
- [54] K. Juvale, M. Wiese, 4-Substituted-2-phenylquinazolines as inhibitors of BCRP, *Bioorg. Med. Chem. Lett.* 22 (2012) 6766–6769. doi:10.1016/j.bmcl.2012.08.024.

- [55] K. Juvale, V.F.S. Pape, M. Wiese, Investigation of chalcones and benzochalcones as inhibitors of breast cancer resistance protein, *Bioorg. Med. Chem.* 20 (2012) 346–355. doi:10.1016/j.bmc.2011.10.074.
- [56] K. Juvale, K. Stefan, M. Wiese, Synthesis and biological evaluation of flavones and benzoflavones as inhibitors of BCRP/ABCG2, *Eur. J. Med. Chem.* 67 (2013) 115–126. doi:10.1016/j.ejmech.2013.06.035.
- [57] J.D. Allen, A. van Loevezijn, J.M. Lakhai, M. van der Valk, O. van Tellingen, G. Reid, et al., Potent and Specific Inhibition of the Breast Cancer Resistance Protein Multidrug Transporter in Vitro and in Mouse Intestine by a Novel Analogue of Fumitremorgin C 1 This work was supported in part by grant NKI 97-1433 from the Dutch Cancer Society (to A. H. S.). Synthesis investigations by A. v. L. and G-J. K. were supported by the Netherlands Research Council for Chemical Sciences (NWO/CW) and the Netherlands Technology Foundation (STW).1, *Mol. Cancer Ther.* 1 (2002) 417–425.
- [58] I. Ivnitiski-Steele, R.S. Larson, D.M. Lovato, H.M. Khawaja, S.S. Winter, T.I. Oprea, et al., High-Throughput Flow Cytometry to Detect Selective Inhibitors of ABCB1, ABCC1, and ABCG2 Transporters, *ASSAY Drug Dev. Technol.* 6 (2008) 263–276. doi:10.1089/adt.2007.107.
- [59] P. Matsson, J.M. Pedersen, U. Norinder, C.A.S. Bergström, P. Artursson, Identification of Novel Specific and General Inhibitors of the Three Major Human ATP-Binding Cassette Transporters P-gp, BCRP and MRP2 Among Registered Drugs, *Pharm. Res.* 26 (2009) 1816–1831. doi:10.1007/s11095-009-9896-0.
- [60] Z. Shi, A.K. Tiwari, S. Shukla, R.W. Robey, S. Singh, I.-W. Kim, et al., Sildenafil Reverses ABCB1- and ABCG2-Mediated Chemotherapeutic Drug Resistance, *Cancer Res.* 71 (2011) 3029–3041. doi:10.1158/0008-5472.CAN-10-3820.
- [61] S. Shukla, C.-P. Wu, S.V. Ambudkar, Development of inhibitors of ATP-binding cassette drug transporters – present status and challenges, *Expert Opin. Drug Metab. Toxicol.* 4 (2008) 205–223. doi:10.1517/17425255.4.2.205.
- [62] K. Maeno, A. Nakajima, G. Conseil, A. Rothnie, R.G. Deeley, S.P.C. Cole, Molecular Basis for Reduced Estrone Sulfate Transport and Altered Modulator Sensitivity of Transmembrane Helix (TM) 6 and TM17 Mutants of Multidrug Resistance Protein 1 (ABCC1), *Drug Metab. Dispos.* 37 (2009) 1411–1420. doi:10.1124/dmd.109.026633.
- [63] C.-P. Wu, A.M. Calcagno, S.V. Ambudkar, Reversal of ABC drug transporter-mediated multidrug resistance in cancer cells: evaluation of current strategies, *Curr. Mol. Pharmacol.* 1 (2008) 93.
- [64] S.C. Köhler, M. Wiese, HM30181 Derivatives as Novel Potent and Selective Inhibitors of the Breast Cancer Resistance Protein (BCRP/ABCG2), *J. Med. Chem.* (2015). doi:10.1021/acs.jmedchem.5b00188.

- [65] W. Szybalski, V. Bryson, GENETIC STUDIES ON MICROBIAL CROSS RESISTANCE TO TOXIC AGENTS I. , Cross Resistance of *Escherichia coli* to Fifteen Antibiotics, *J. Bacteriol.* 64 (1952) 489–499.
- [66] K.M. Pluchino, M.D. Hall, A.S. Goldsborough, R. Callaghan, M.M. Gottesman, Collateral sensitivity as a strategy against cancer multidrug resistance, *Drug Resist. Updat.* 15 (2012) 98–105. doi:10.1016/j.drug.2012.03.002.
- [67] K.M. Marks, E.S. Park, A. Arefolov, K. Russo, K. Ishihara, J.E. Ring, et al., The Selectivity of Austocystin D Arises from Cell-Line-Specific Drug Activation by Cytochrome P450 Enzymes, *J. Nat. Prod.* 74 (2011) 567–573. doi:10.1021/np100429s.
- [68] S.P.C. Cole, R.G. Deeley, Transport of glutathione and glutathione conjugates by MRP1, *Trends Pharmacol. Sci.* 27 (2006) 438–446. doi:10.1016/j.tips.2006.06.008.
- [69] Z. Benderra, A. Trussardi, H. Morjani, A.M. Villa, S.M. Doglia, M. Manfait, Regulation of cellular glutathione modulates nuclear accumulation of daunorubicin in human MCF7 cells overexpressing multidrug resistance associated protein, *Eur. J. Cancer Oxf. Engl.* 1990. 36 (2000) 428–434.
- [70] N.T. Bech-Hansen, J.E. Till, V. Ling, Pleiotropic phenotype of colchicine-resistant CHO cells: Cross-resistance and collateral sensitivity, *J. Cell. Physiol.* 88 (1976) 23–31.
- [71] R. Callaghan, J.R. Riordan, Collateral sensitivity of multidrug resistant cells to narcotic analgesics is due to effects on the plasma membrane, *Biochim. Biophys. Acta.* 1236 (1995) 155–162.
- [72] R. Callaghan, G. Berridge, D.R. Ferry, C.F. Higgins, The functional purification of P-glycoprotein is dependent on maintenance of a lipid–protein interface, *Biochim. Biophys. Acta BBA - Biomembr.* 1328 (1997) 109–124. doi:10.1016/S0005-2736(97)00079-5.
- [73] D.Y. Alakhova, A.V. Kabanov, Pluronic and MDR Reversal: An Update, *Mol. Pharm.* 11 (2014) 2566–2578. doi:10.1021/mp500298q.
- [74] C. Alemán, J.-P. Annereau, X.-J. Liang, C.O. Cardarelli, B. Taylor, J.J. Yin, et al., P-glycoprotein, expressed in multidrug resistant cells, is not responsible for alterations in membrane fluidity or membrane potential, *Cancer Res.* 63 (2003) 3084–3091.
- [75] A.V. Kabanov, E.V. Batrakova, V.Y. Alakhov, An essential relationship between ATP depletion and chemosensitizing activity of Pluronic block copolymers, *J. Control. Release Off. J. Control. Release Soc.* 91 (2003) 75–83.
- [76] D.Y. Alakhova, N.Y. Rapoport, E.V. Batrakova, A.A. Timoshin, S. Li, D. Nicholls, et al., Differential metabolic responses to pluronic in MDR and non-MDR cells: A novel pathway for chemosensitization of drug resistant cancers, *J. Controlled Release.* 142 (2010) 89–100. doi:10.1016/j.jconrel.2009.09.026.

- [77] J. Bentley, D.M. Quinn, R.S. Pitman, J.R. Warr, G.L. Kellett, The human KB multidrug-resistant cell line KB-C1 is hypersensitive to inhibitors of glycosylation, *Cancer Lett.* 115 (1997) 221–227.
- [78] S.E. Bell, D.M. Quinn, G.L. Kellett, J.R. Warr, 2-Deoxy-D-glucose preferentially kills multidrug-resistant human KB carcinoma cell lines by apoptosis., *Br. J. Cancer.* 78 (1998) 1464–1470.
- [79] J.W. Polli, S.A. Wring, J.E. Humphreys, L. Huang, J.B. Morgan, L.O. Webster, et al., Rational use of in vitro P-glycoprotein assays in drug discovery, *J. Pharmacol. Exp. Ther.* 299 (2001) 620–628.
- [80] J.R. Warr, F. Brewer, M. Anderson, J. Fergusson, Verapamil hypersensitivity of vincristine resistant Chinese hamster ovary cell lines, *Cell Biol. Int. Rep.* 10 (1986) 389–399. doi:10.1016/0309-1651(86)90011-1.
- [81] D.F. Cano-Gauci, J.R. Riordan, Action of calcium antagonists on multidrug resistant cells. Specific cytotoxicity independent of increased cancer drug accumulation, *Biochem. Pharmacol.* 36 (1987) 2115–2123.
- [82] J. Karwatsky, M.C. Lincoln, E. Georges, A mechanism for P-glycoprotein-mediated apoptosis as revealed by verapamil hypersensitivity, *Biochemistry (Mosc.)*. 42 (2003) 12163–12173.
- [83] R.-M. Laberge, R. Ambadipudi, E. Georges, P-glycoprotein (ABCB1) modulates collateral sensitivity of a multidrug resistant cell line to verapamil, *Arch. Biochem. Biophys.* 491 (2009) 53–60. doi:10.1016/j.abb.2009.09.012.
- [84] A.S. Goldsborough, M.D. Handley, A.E. Dulcey, K.M. Pluchino, P. Kannan, K.R. Brimacombe, et al., Collateral Sensitivity of Multidrug-Resistant Cells to the Orphan Drug Tiopronin, *J. Med. Chem.* 54 (2011) 4987–4997. doi:10.1021/jm2001663.
- [85] M.D. Hall, T.S. Marshall, A.D.T. Kwit, L.M.M. Jenkins, A.E. Dulcey, J.P. Madigan, et al., Inhibition of Glutathione Peroxidase Mediates the Collateral Sensitivity of Multidrug-Resistant Cells to Tiopronin, *J. Biol. Chem.* (2014) jbc.M114.581702. doi:10.1074/jbc.M114.581702.
- [86] M. Whitnall, J. Howard, P. Ponka, D.R. Richardson, A class of iron chelators with a wide spectrum of potent antitumor activity that overcomes resistance to chemotherapeutics, *Proc. Natl. Acad. Sci.* 103 (2006) 14901–14906.
- [87] D.B. Lovejoy, P.J. Jansson, U.T. Brunk, J. Wong, P. Ponka, D.R. Richardson, Antitumor Activity of Metal-Chelating Compound Dp44mT Is Mediated by Formation of a Redox-Active Copper Complex That Accumulates in Lysosomes, *Cancer Res.* 71 (2011) 5871–5880. doi:10.1158/0008-5472.CAN-11-1218.
- [88] A.M. Merlot, D.S. Kalinowski, D.R. Richardson, Novel Chelators for Cancer Treatment: Where Are We Now?, *Antioxid. Redox Signal.* 18 (2013) 973–1006. doi:10.1089/ars.2012.4540.

- [89] V.F.S. Pape, D. Türk, P. Szabó, M. Wiese, E.A. Enyedy, G. Szakács, Synthesis and characterization of the anticancer and metal binding properties of novel pyrimidinylhydrazone derivatives, *J. Inorg. Biochem.* 144 (2015) 18–30. doi:10.1016/j.jinorgbio.2014.12.015.
- [90] P.J. Jansson, T. Yamagishi, A. Arvind, N. Seebacher, E. Gutierrez, A. Stacy, et al., Di-2-pyridylketone 4,4-Dimethyl-3-thiosemicarbazone (Dp44mT) Overcomes Multidrug-Resistance by a Novel Mechanism Involving the Hijacking of Lysosomal P-Glycoprotein (Pgp)., *J. Biol. Chem.* 290 (2015) 9588–9603. doi:10.1074/jbc.M114.631283.
- [91] J.H. Wu, S.L. Mao, S.X. Liao, Y.H. Yi, C.Q. Lan, Z.W. Su, Desmosdumotin B: a new special flavone from *Desmos dumosus*, *Chin. Chem. Lett.* 12 (2001) 49–50.
- [92] K. Nakagawa-Goto, K.F. Bastow, J.-H. Wu, H. Tokuda, K.-H. Lee, Total synthesis and bioactivity of unique flavone desmosdumotin B and its analogs, *Bioorg. Med. Chem. Lett.* 15 (2005) 3016–3019. doi:10.1016/j.bmcl.2005.04.070.
- [93] K. Nakagawa-Goto, K.F. Bastow, T.-H. Chen, S.L. Morris-Natschke, K.-H. Lee, Antitumor Agents 260. New Desmosdumotin B Analogues with Improved In Vitro Anticancer Activity, *J. Med. Chem.* 51 (2008) 3297–3303. doi:10.1021/jm701208v.
- [94] K. Nakagawa-Goto, P.-C. Chang, C.-Y. Lai, H.-Y. Hung, T.-H. Chen, P.-C. Wu, et al., Antitumor Agents. 280. Multidrug Resistance-Selective Desmosdumotin B Analogues, *J. Med. Chem.* 53 (2010) 6699–6705. doi:10.1021/jm100846r.
- [95] G. Szakács, J.-P. Annereau, S. Lababidi, U. Shankavaram, A. Arciello, K.J. Bussey, et al., Predicting drug sensitivity and resistance: profiling ABC transporter genes in cancer cells, *Cancer Cell.* 6 (2004) 129–137.
- [96] W.C. Reinhold, M. Sunshine, H. Liu, S. Varma, K.W. Kohn, J. Morris, et al., CellMiner: A Web-Based Suite of Genomic and Pharmacologic Tools to Explore Transcript and Drug Patterns in the NCI-60 Cell Line Set, *Cancer Res.* 72 (2012) 3499–3511. doi:10.1158/0008-5472.CAN-12-1370.
- [97] R.H. Shoemaker, The NCI60 human tumour cell line anticancer drug screen, *Nat. Rev. Cancer.* 6 (2006) 813–823. doi:10.1038/nrc1951.
- [98] D. Türk, M.D. Hall, B.F. Chu, J.A. Ludwig, H.M. Fales, M.M. Gottesman, et al., Identification of Compounds Selectively Killing Multidrug-Resistant Cancer Cells, *Cancer Res.* 69 (2009) 8293–8301. doi:10.1158/0008-5472.CAN-09-2422.
- [99] M. Liscovitch, D. Ravid, A case study in misidentification of cancer cell lines: MCF-7/AdrR cells (re-designated NCI/ADR-RES) are derived from OVCAR-8 human ovarian carcinoma cells, *Cancer Lett.* 245 (2007) 350–352. doi:10.1016/j.canlet.2006.01.013.
- [100] J.A. Ludwig, G. Szakács, S.E. Martin, B.F. Chu, C. Cardarelli, Z.E. Sauna, et al., Selective Toxicity of NSC73306 in MDR1-Positive Cells as a New Strategy to Circumvent Multidrug Resistance in Cancer, *Cancer Res.* 66 (2006) 4808–4815. doi:10.1158/0008-5472.CAN-05-3322.

- [101] Y.N. Chen, L.A. Mickley, A.M. Schwartz, E.M. Acton, J.L. Hwang, A.T. Fojo, Characterization of adriamycin-resistant human breast cancer cells which display overexpression of a novel resistance-related membrane protein., *J. Biol. Chem.* 265 (1990) 10073–10080.
- [102] M.D. Hall, N.K. Salam, J.L. Hellawell, H.M. Fales, C.B. Kensler, J.A. Ludwig, et al., Synthesis, Activity, and Pharmacophore Development for Isatin- $\beta$ -thiosemicarbazones with Selective Activity toward Multidrug-Resistant Cells, *J. Med. Chem.* 52 (2009) 3191–3204. doi:10.1021/jm800861c.
- [103] M.D. Hall, K.R. Brimacombe, M.S. Varonka, K.M. Pluchino, J.K. Monda, J. Li, et al., Synthesis and Structure–Activity Evaluation of Isatin- $\beta$ -thiosemicarbazones with Improved Selective Activity toward Multidrug-Resistant Cells Expressing P-Glycoprotein, *J. Med. Chem.* 54 (2011) 5878–5889. doi:10.1021/jm2006047.
- [104] D.S. Kalinowski, D.R. Richardson, The Evolution of Iron Chelators for the Treatment of Iron Overload Disease and Cancer, *Pharmacol. Rev.* 57 (2005) 547–583. doi:10.1124/pr.57.4.2.
- [105] A. Budimir, Metal ions, Alzheimer's disease and chelation therapy, *Acta Pharm.* 61 (2011) 1–14. doi:10.2478/v10007-011-0006-6.
- [106] H. Eklund, U. Uhlin, M. Färnegårdh, D.T. Logan, P. Nordlund, Structure and function of the radical enzyme ribonucleotide reductase, *Prog. Biophys. Mol. Biol.* 77 (2001) 177–268. doi:10.1016/S0079-6107(01)00014-1.
- [107] N.T.V. Le, D.R. Richardson, The role of iron in cell cycle progression and the proliferation of neoplastic cells, *Biochim. Biophys. Acta BBA - Rev. Cancer.* 1603 (2002) 31–46. doi:10.1016/S0304-419X(02)00068-9.
- [108] W. Kaim, B. Schwederski, *Bioinorganic Chemistry: Inorganic Elements in the Chemistry of Life - An Introduction and Guide*, 1st ed., Wiley, West Sussex, England, 1994.
- [109] J.A. Jacobsen, J.L. Fullagar, M.T. Miller, S.M. Cohen, Identifying Chelators for Metalloprotein Inhibitors Using a Fragment-Based Approach, *J. Med. Chem.* 54 (2011) 591–602. doi:10.1021/jm101266s.
- [110] R. McRae, P. Bagchi, S. Sumalekshmy, C.J. Fahrni, In Situ Imaging of Metals in Cells and Tissues, *Chem. Rev.* 109 (2009) 4780–4827. doi:10.1021/cr900223a.
- [111] S.V. Torti, F.M. Torti, Ironing Out Cancer, *Cancer Res.* 71 (2011) 1511–1514. doi:10.1158/0008-5472.CAN-10-3614.
- [112] G.Y.L. Lui, Z. Kovacevic, V. Richardson, A.M. Merlot, D.S. Kalinowski, D.R. Richardson, Targeting cancer by binding iron: Dissecting cellular signaling pathways, *Oncotarget.* 5 (2015). <http://www.impactjournals.com/oncotarget/index.php?journal=oncotarget&page=article&op=view&path%5B%5D=4349> (accessed July 20, 2015).
- [113] A. Gupte, R.J. Mumper, Elevated copper and oxidative stress in cancer cells as a target for cancer treatment, *Cancer Treat. Rev.* 35 (2009) 32–46. doi:10.1016/j.ctrv.2008.07.004.

- [114] H. Tapiero, D.M. Townsend, K.D. Tew, Trace elements in human physiology and pathology. Copper, *Biomed. Pharmacother.* 57 (2003) 386–398. doi:10.1016/S0753-3322(03)00012-X.
- [115] D.J.R. Lane, T.M. Mills, N.H. Shafie, A.M. Merlot, R. Saleh Moussa, D.S. Kalinowski, et al., Expanding horizons in iron chelation and the treatment of cancer: Role of iron in the regulation of ER stress and the epithelial–mesenchymal transition, *Biochim. Biophys. Acta BBA - Rev. Cancer.* 1845 (2014) 166–181. doi:10.1016/j.bbcan.2014.01.005.
- [116] U. Jungwirth, C.R. Kowol, B.K. Keppler, C.G. Hartinger, W. Berger, P. Heffeter, Anticancer Activity of Metal Complexes: Involvement of Redox Processes, *Antioxid. Redox Signal.* 15 (2011) 1085–1127. doi:10.1089/ars.2010.3663.
- [117] M. Valko, H. Morris, M.T.D. Cronin, Metals, toxicity and oxidative stress, *Curr. Med. Chem.* 12 (2005) 1161–1208.
- [118] E.J. Martinez-Finley, S. Chakraborty, S.J.B. Fretham, M. Aschner, Cellular transport and homeostasis of essential and nonessential metals, *Metallomics.* 4 (2012) 593. doi:10.1039/c2mt00185c.
- [119] M.L.-H. Huang, D.J.R. Lane, D.R. Richardson, Mitochondrial Mayhem: The Mitochondrion as a Modulator of Iron Metabolism and Its Role in Disease, *Antioxid. Redox Signal.* 15 (2011) 3003–3019. doi:10.1089/ars.2011.3921.
- [120] D.J.R. Lane, A.M. Merlot, M.L.-H. Huang, D.-H. Bae, P.J. Jansson, S. Sahni, et al., Cellular iron uptake, trafficking and metabolism: Key molecules and mechanisms and their roles in disease, *Biochim. Biophys. Acta BBA - Mol. Cell Res.* 1853 (2015) 1130–1144. doi:10.1016/j.bbamcr.2015.01.021.
- [121] D.R. Richardson, D.S. Kalinowski, S. Lau, P.J. Jansson, D.B. Lovejoy, Cancer cell iron metabolism and the development of potent iron chelators as anti-tumour agents, *Biochim. Biophys. Acta BBA - Gen. Subj.* 1790 (2009) 702–717. doi:10.1016/j.bbagen.2008.04.003.
- [122] J. Wang, K. Pantopoulos, Regulation of cellular iron metabolism, *Biochem. J.* 434 (2011) 365–381. doi:10.1042/BJ20101825.
- [123] Y. Yu, D.S. Kalinowski, Z. Kovacevic, A.R. Siafakas, P.J. Jansson, C. Stefani, et al., Thiosemicarbazones from the Old to New: Iron Chelators That Are More Than Just Ribonucleotide Reductase Inhibitors, *J. Med. Chem.* 52 (2009) 5271–5294. doi:10.1021/jm900552r.
- [124] C. Santini, M. Pellei, V. Gandin, M. Porchia, F. Tisato, C. Marzano, Advances in Copper Complexes as Anticancer Agents, *Chem. Rev.* 114 (2014) 815–862. doi:10.1021/cr400135x.
- [125] M. Shvartsman, Z.I. Cabantchik, Intracellular iron trafficking: role of cytosolic ligands, *BioMetals.* 25 (2012) 711–723. doi:10.1007/s10534-012-9529-7.
- [126] H. Fieten, P.A.J. Leegwater, A.L. Watson, J. Rothuizen, Canine models of copper toxicosis for understanding mammalian copper metabolism, *Mamm. Genome.* 23 (2012) 62–75. doi:10.1007/s00335-011-9378-7.



- [127] Y. Hatori, S. Clasen, N.M. Hasan, A.N. Barry, S. Lutsenko, Functional Partnership of the Copper Export Machinery and Glutathione Balance in Human Cells, *J. Biol. Chem.* 287 (2012) 26678–26687. doi:10.1074/jbc.M112.381178.
- [128] C.M. Nutting, C.M.L. van Herpen, A.B. Miah, S.A. Bhide, J.-P. Machiels, J. Buter, et al., Phase II study of 3-AP Triapine in patients with recurrent or metastatic head and neck squamous cell carcinoma, *Ann. Oncol.* 20 (2009) 1275–1279. doi:10.1093/annonc/mdn775.
- [129] C.R. Kowol, R. Berger, R. Eichinger, A. Roller, M.A. Jakupec, P.P. Schmidt, et al., Gallium(III) and Iron(III) Complexes of  $\alpha$ -N-Heterocyclic Thiosemicarbazones: Synthesis, Characterization, Cytotoxicity, and Interaction with Ribonucleotide Reductase, *J. Med. Chem.* 50 (2007) 1254–1265. doi:10.1021/jm0612618.
- [130] Y. Yu, J. Wong, D.B. Lovejoy, D.S. Kalinowski, D.R. Richardson, Chelators at the Cancer Coalface: Desferrioxamine to Triapine and Beyond, *Clin. Cancer Res.* 12 (2006) 6876–6883. doi:10.1158/1078-0432.CCR-06-1954.
- [131] F. Saletta, Y.S. Rahmanto, A.R. Sifakas, D.R. Richardson, Cellular Iron Depletion and the Mechanisms Involved in the Iron-dependent Regulation of the Growth Arrest and DNA Damage Family of Genes, *J. Biol. Chem.* 286 (2011) 35396–35406. doi:10.1074/jbc.M111.273060.
- [132] D. Fu, D.R. Richardson, Iron chelation and regulation of the cell cycle: 2 mechanisms of posttranscriptional regulation of the universal cyclin-dependent kinase inhibitor p21CIP1/WAF1 by iron depletion, *Blood.* 110 (2007) 752–761. doi:10.1182/blood-2007-03-076737.
- [133] Z. Kovacevic, S. Chikhani, D.B. Lovejoy, D.R. Richardson, Novel Thiosemicarbazone Iron Chelators Induce Up-Regulation and Phosphorylation of the Metastasis Suppressor N-myc Down-Stream Regulated Gene 1: A New Strategy for the Treatment of Pancreatic Cancer, *Mol. Pharmacol.* 80 (2011) 598–609. doi:10.1124/mol.111.073627.
- [134] J. Yuan, D.B. Lovejoy, D.R. Richardson, Novel Di-2-Pyridyl-Derived Iron Chelators with Marked and Selective Anti-Tumor Activity: In Vitro and In Vivo Assessment, *Blood.* 104 (2004) 1450–1458. doi:10.1182/blood-2004-03-0868.
- [135] C.R. Kowol, P. Heffeter, W. Miklos, L. Gille, R. Trondl, L. Cappellacci, et al., Mechanisms underlying reductant-induced reactive oxygen species formation by anticancer copper(II) compounds, *J. Biol. Inorg. Chem.* 17 (2012) 409–423. doi:10.1007/s00775-011-0864-x.
- [136] A. Gaál, G. Orgován, Z. Polgári, A. Réti, V.G. Mihucz, S. Bősze, et al., Complex forming competition and in-vitro toxicity studies on the applicability of di-2-pyridylketone-4,4,-dimethyl-3-thiosemicarbazone (Dp44mT) as a metal chelator, *J. Inorg. Biochem.* 130 (2014) 52–58. doi:10.1016/j.jinorgbio.2013.09.016.
- [137] A. Kellett, O. Howe, M. O'Connor, M. McCann, B.S. Creaven, S. McClean, et al., Radical-induced DNA damage by cytotoxic square-planar copper(II) complexes incorporating o-

- phthalate and 1,10-phenanthroline or 2,2'-dipyridyl, *Free Radic. Biol. Med.* 53 (2012) 564–576. doi:10.1016/j.freeradbiomed.2012.05.034.
- [138] R. Buchtík, Z. Trávníček, J. Vančo, R. Herchel, Z. Dvořák, Synthesis, characterization, DNA interaction and cleavage, and in vitro cytotoxicity of copper(II) mixed-ligand complexes with 2-phenyl-3-hydroxy-4(1H)-quinolinone, *Dalton Trans.* 40 (2011) 9404–9412. doi:10.1039/C1DT10674K.
- [139] S.S. Bhat, A.A. Kumbhar, H. Heptullah, A.A. Khan, V.V. Gobre, S.P. Gejji, et al., Synthesis, Electronic Structure, DNA and Protein Binding, DNA Cleavage, and Anticancer Activity of Fluorophore-Labeled Copper(II) Complexes, *Inorg. Chem.* 50 (2011) 545–558. doi:10.1021/ic101534n.
- [140] J. Luis García-Giménez, M. González-Álvarez, M. Liu-González, B. Macías, J. Borrás, G. Alzuet, Toward the development of metal-based synthetic nucleases: DNA binding and oxidative DNA cleavage of a mixed copper(II) complex with N-(9H-purin-6-yl)benzenesulfonamide and 1,10-phenanthroline. Antitumor activity in human Caco-2 cells and Jurkat T lymphocytes. Evaluation of p53 and Bcl-2 proteins in the apoptotic mechanism, *J. Inorg. Biochem.* 103 (2009) 923–934. doi:10.1016/j.jinorgbio.2009.04.003.
- [141] D. Senthil Raja, N.S.P. Bhuvanesh, K. Natarajan, Effect of N(4)-Phenyl Substitution in 2-Oxo-1,2-dihydroquinoline-3-carbaldehyde Semicarbazones on the Structure, DNA/Protein Interaction, and Antioxidative and Cytotoxic Activity of Cu(II) Complexes, *Inorg. Chem.* 50 (2011) 12852–12866. doi:10.1021/ic2020308.
- [142] S. Rajalakshmi, T. Weyhermüller, A.J. Freddy, H.R. Vasanthi, B.U. Nair, Anomalous behavior of pentacoordinate copper complexes of dimethylphenanthroline and derivatives of terpyridine ligands: Studies on DNA binding, cleavage and apoptotic activity, *Eur. J. Med. Chem.* 46 (2011) 608–617. doi:10.1016/j.ejmech.2010.11.041.
- [143] A. Barve, A. Kumbhar, M. Bhat, B. Joshi, R. Butcher, U. Sonawane, et al., Mixed-Ligand Copper(II) Maltolate Complexes: Synthesis, Characterization, DNA Binding and Cleavage, and Cytotoxicity, *Inorg. Chem.* 48 (2009) 9120–9132. doi:10.1021/ic9004642.
- [144] O.F. Ikotun, E.M. Higbee, W. Ouellette, R.P. Doyle, Pyrophosphate-bridged complexes with picomolar toxicity, *J. Inorg. Biochem.* 103 (2009) 1254–1264. doi:10.1016/j.jinorgbio.2009.07.010.
- [145] K.G. Daniel, P. Gupta, R.H. Harbach, W.C. Guida, Q.P. Dou, Organic copper complexes as a new class of proteasome inhibitors and apoptosis inducers in human cancer cells, *Biochem. Pharmacol.* 67 (2004) 1139–1151. doi:10.1016/j.bcp.2003.10.031.
- [146] Y. Xiao, D. Chen, X. Zhang, Q. Cui, Y. Fan, C. Bi, et al., Molecular study on copper-mediated tumor proteasome inhibition and cell death, *Int. J. Oncol.* 37 (2010) 81–87.

- [147] J.B. Baell, G.A. Holloway, New Substructure Filters for Removal of Pan Assay Interference Compounds (PAINS) from Screening Libraries and for Their Exclusion in Bioassays, *J. Med. Chem.* 53 (2010) 2719–2740. doi:10.1021/jm901137j.
- [148] J. Baell, M.A. Walters, Chemistry: Chemical con artists foil drug discovery, *Nat. News.* 513 (2014) 481. doi:10.1038/513481a.
- [149] J.A. Lee, M.T. Uhlik, C.M. Moxham, D. Tomandl, D.J. Sall, Modern Phenotypic Drug Discovery Is a Viable, Neoclassic Pharma Strategy, *J. Med. Chem.* 55 (2012) 4527–4538. doi:10.1021/jm201649s.
- [150] J. Kotz, Phenotypic screening, take two, *SciBX Sci.-Bus. Exch.* 5 (2012). doi:10.1038/scibx.2012.380.
- [151] O. Sorg, Oxidative stress: a theoretical model or a biological reality?, *C. R. Biol.* 327 (2004) 649–662. doi:10.1016/j.crvi.2004.05.007.
- [152] G.-Y. Liou, P. Storz, Reactive oxygen species in cancer, *Free Radic. Res.* 44 (2010) 479–496. doi:10.3109/10715761003667554.
- [153] W. Lopaczynski, S.H. Zeisel, Antioxidants, programmed cell death, and cancer, *Nutr. Res.* 21 (2001) 295–307.
- [154] A.J. Nappi, E. Vass, Comparative studies of enhanced iron-mediated production of hydroxyl radical by glutathione, cysteine, ascorbic acid, and selected catechols, *Biochim. Biophys. Acta.* 1336 (1997) 295–302.
- [155] M. Valko, C.J. Rhodes, J. Moncol, M. Izakovic, M. Mazur, Free radicals, metals and antioxidants in oxidative stress-induced cancer, *Chem. Biol. Interact.* 160 (2006) 1–40. doi:10.1016/j.cbi.2005.12.009.
- [156] B. Enyedi, P. Várnai, M. Geiszt, Redox state of the endoplasmic reticulum is controlled by Ero 1L- $\alpha$  and intraluminal calcium, *Antioxid. Redox Signal.* 13 (2010) 721–729.
- [157] M. Carocho, I.C.F.R. Ferreira, A review on antioxidants, prooxidants and related controversy: Natural and synthetic compounds, screening and analysis methodologies and future perspectives, *Food Chem. Toxicol.* 51 (2013) 15–25. doi:10.1016/j.fct.2012.09.021.
- [158] M. Landriscina, F. Maddalena, G. Laudiero, F. Esposito, Adaptation to oxidative stress, chemoresistance, and cell survival, *Antioxid. Redox Signal.* 11 (2009) 2701–2716.
- [159] M.P. Murphy, A. Holmgren, N.-G. Larsson, B. Halliwell, C.J. Chang, B. Kalyanaraman, et al., Unraveling the Biological Roles of Reactive Oxygen Species, *Cell Metab.* 13 (2011) 361–366. doi:10.1016/j.cmet.2011.03.010.
- [160] K. Jomova, M. Valko, Advances in metal-induced oxidative stress and human disease, *Toxicology.* 283 (2011) 65–87. doi:10.1016/j.tox.2011.03.001.
- [161] K. Jomova, S. Baros, M. Valko, Redox active metal-induced oxidative stress in biological systems, *Transit. Met. Chem.* 37 (2012) 127–134. doi:10.1007/s11243-012-9583-6.

- [162] A.P. Fernandes, A. Holmgren, Glutaredoxins: Glutathione-Dependent Redox Enzymes with Functions Far Beyond a Simple Thioredoxin Backup System, *Antioxid. Redox Signal.* 6 (2004) 63–74. doi:10.1089/152308604771978354.
- [163] H.-J. Choi, S.-J. Kim, P. Mukhopadhyay, S. Cho, J.-R. Woo, G. Storz, et al., Structural basis of the redox switch in the OxyR transcription factor, *Cell.* 105 (2001) 103–113.
- [164] H.E. Seifried, D.E. Anderson, E.I. Fisher, J.A. Milner, A review of the interaction among dietary antioxidants and reactive oxygen species, *J. Nutr. Biochem.* 18 (2007) 567–579. doi:10.1016/j.jnutbio.2006.10.007.
- [165] M. Gutscher, A.-L. Pauleau, L. Marty, T. Brach, G.H. Wabnitz, Y. Samstag, et al., Real-time imaging of the intracellular glutathione redox potential, *Nat. Methods.* 5 (2008) 553–559. doi:10.1038/nmeth.1212.
- [166] D. Trachootham, W. Lu, M.A. Ogasawara, N.R.-D. Valle, P. Huang, Redox Regulation of Cell Survival, *Antioxid. Redox Signal.* 10 (2008) 1343–1374. doi:10.1089/ars.2007.1957.
- [167] M.T. Kuo, Redox Regulation of Multidrug Resistance in Cancer Chemotherapy: Molecular Mechanisms and Therapeutic Opportunities, *Antioxid. Redox Signal.* 11 (2009) 99–133. doi:10.1089/ars.2008.2095.
- [168] S. Ueda, H. Masutani, H. Nakamura, T. Tanaka, M. Ueno, J. Yodoi, Redox control of cell death, *Antioxid. Redox Signal.* 4 (2002) 405–414.
- [169] X. Wang, C.R. Campos, J.C. Peart, L.K. Smith, J.L. Boni, R.E. Cannon, et al., Nrf2 Upregulates ATP Binding Cassette Transporter Expression and Activity at the Blood–Brain and Blood–Spinal Cord Barriers, *J. Neurosci.* 34 (2014) 8585–8593. doi:10.1523/JNEUROSCI.2935-13.2014.
- [170] C.M. Beaufort, J.C.A. Helmijr, A.M. Piskorz, M. Hoogstraat, K. Ruigrok-Ritstier, N. Besselink, et al., Ovarian Cancer Cell Line Panel (OCCP): Clinical Importance of In Vitro Morphological Subtypes, *PLoS ONE.* 9 (2014) e103988. doi:10.1371/journal.pone.0103988.
- [171] W.G. Harker, B.I. Sikic, Multidrug (Pleiotropic) Resistance in Doxorubicin-selected Variants of the Human Sarcoma Cell Line MES-SA, *Cancer Res.* 45 (1985) 4091–4096.
- [172] D.-W. Shen, C. Cardarelli, J. Hwang, M. Cornwell, N. Richert, S. Ishii, et al., Multiple drug-resistant human KB carcinoma cells independently selected for high-level resistance to colchicine, adriamycin, or vinblastine show changes in expression of specific proteins., *J. Biol. Chem.* 261 (1986) 7762–7770.
- [173] J. Wang, L.-S. Tai, C.-H. Tzang, W.F. Fong, X.-Y. Guan, M. Yang, 1p31, 7q21 and 18q21 chromosomal aberrations and candidate genes in acquired vinblastine resistance of human cervical carcinoma KB cells, *Oncol. Rep.* 19 (2008) 1155–1164.
- [174] D. Türk, M.D. Hall, B.F. Chu, J.A. Ludwig, H.M. Fales, M.M. Gottesman, et al., Identification of Compounds Selectively Killing Multidrug-Resistant Cancer Cells, *Cancer Res.* (2009). doi:10.1158/0008-5472.CAN-09-2422.

- [175] G. Maggiora, M. Vogt, D. Stumpfe, J. Bajorath, *Molecular Similarity in Medicinal Chemistry*, *J. Med. Chem.* 57 (2014) 3186–3204. doi:10.1021/jm401411z.
- [176] M.D. Hall, N.K. Salam, J.L. Hellawell, H.M. Fales, C.B. Kensler, J.A. Ludwig, et al., Synthesis, activity, and pharmacophore development for isatin-beta-thiosemicarbazones with selective activity toward multidrug-resistant cells, *J. Med. Chem.* 52 (2009) 3191–3204. doi:10.1021/jm800861c.
- [177] P. Heffeter, A. Popovic-Bijelic, P. Saiko, R. Dornetshuber, U. Jungwirth, N. Voevodskaya, et al., Ribonucleotide reductase as one important target of [Tris(1,10-phenanthroline)lanthanum(III)] trithiocyanate (KP772), *Curr. Cancer Drug Targets.* 9 (2009) 595–607.
- [178] F.A. Hart, F.P. Laming, Complexes of 1,10-phenanthroline with lanthanide chlorides and thiocyanates, *J. Inorg. Nucl. Chem.* 26 (1964) 579–585. doi:10.1016/0022-1902(64)80291-8.
- [179] G.A. Lawrance, *Introduction to Coordination Chemistry*, 1st edition, Wiley, 2011.
- [180] R.W. Brockman, J.R. Thomson, M.J. Bell, H.E. Skipper, Observations on the Antileukemic Activity of Pyridine-2-carboxaldehyde Thiosemicarbazone and Thiocarbohydrazone, *Cancer Res.* 16 (1956) 167–170.
- [181] G. Rappa, A. Lorico, M.-C. Liu, G.D. Kruh, A.H. Cory, J.G. Cory, et al., Overexpression of the Multidrug Resistance Genes *mdr1*, *mdr3*, and *mrp* in L1210 Leukemia Cells Resistant to Inhibitors of Ribonucleotide Reductase, *Biochem. Pharmacol.* 54 (1997) 649–655.
- [182] W. Miklos, K. Pelivan, C.R. Kowol, C. Pirker, R. Dornetshuber-Fleiss, M. Spitzwieser, et al., Triapine-mediated ABCB1 induction via PKC induces widespread therapy unresponsiveness but is not underlying acquired triapine resistance, *Cancer Lett.* 361 (2015) 112–120. doi:10.1016/j.canlet.2015.02.049.
- [183] C.R. Kowol, R. Trondl, P. Heffeter, V.B. Arion, M.A. Jakupec, A. Roller, et al., Impact of Metal Coordination on Cytotoxicity of 3-Aminopyridine-2-carboxaldehyde Thiosemicarbazone (Triapine) and Novel Insights into Terminal Dimethylation, *J. Med. Chem.* 52 (2009) 5032–5043. doi:10.1021/jm900528d.
- [184] P.V. Bernhardt, P.C. Sharpe, M. Islam, D.B. Lovejoy, D.S. Kalinowski, D.R. Richardson, Iron Chelators of the Dipyridylketone Thiosemicarbazone Class: Precomplexation and Transmetalation Effects on Anticancer Activity, *J. Med. Chem.* 52 (2009) 407–415. doi:10.1021/jm801012z.
- [185] D.R. Richardson, P.C. Sharpe, D.B. Lovejoy, D. Senaratne, D.S. Kalinowski, M. Islam, et al., Dipyridyl Thiosemicarbazone Chelators with Potent and Selective Antitumor Activity Form Iron Complexes with Redox Activity, *J. Med. Chem.* 49 (2006) 6510–6521. doi:10.1021/jm0606342.
- [186] I.H. Hall, N.J. Peaty, J.R. Henry, J. Easmon, G. Heinisch, G. Pürstinger, Investigations on the mechanism of action of the novel antitumor agents 2-benzothiazolyl, 2-benzoxazolyl, and 2-

- benzimidazolyl hydrazones derived from 2-acetylpyridine, *Arch. Pharm. (Weinheim)*. 332 (1999) 115–123.
- [187] K.J. Schaper, J.K. Seydel, M. Rosenfeld, J. Kazda, Development of inhibitors of mycobacterial ribonucleotide reductase, *Lepr. Rev.* 57 Suppl 3 (1986) 254–264.
- [188] I. Machado, M. Fernández, L. Becco, B. Garat, R.F. Brissos, N. Zabarska, et al., New metal complexes of NNO tridentate ligands: Effect of metal center and co-ligand on biological activity, *Inorganica Chim. Acta*. 420 (2014) 39–46. doi:10.1016/j.ica.2013.10.022.
- [189] M. Calinescu, E. Ion, R. Georgescu, T. Negreanu-prjol, Synthesis and spectroscopic, antibacterial and antifungal studies on copper (II) complexes with 2-benzothiazolyl hydrazones, *Rev Roum Chim.* 53 (2008) 911–919.
- [190] J.K. Seydel, K.-J. Schaper, B. Clement, S. Rüscher-Gerdes, N. Reiling, S. Ehlers, Pharmaceutical compositions for treating infections with drug resistant mycobacteria, WO2011/047814, n.d.
- [191] J.G. Cory, D.L. Downes, A.H. Cory, K.J. Schaper, J.K. Seydel, Substituted 2-acetylpyridine- $\alpha$ -(N)-heterylhydrazones as inhibitors of ribonucleotide reductase activity and L1210 cell growth, *Anticancer Res.* 14 (1994) 875–879.
- [192] M.T. Cocco, C. Congiu, V. Lilliu, V. Onnis, Synthesis and in vitro antitumoral activity of new hydrazinopyrimidine-5-carbonitrile derivatives, *Bioorg. Med. Chem.* 14 (2006) 366–372. doi:10.1016/j.bmc.2005.08.012.
- [193] M.A. Gaston, L.R.S. Dias, A.C.C. Freitas, A.L.P. Miranda, E.J. Barreiro, Synthesis and analgesic properties of new 4-arylhydrazone 1-H pyrazole [3, 4-b] pyridine derivatives, *Pharm. Acta Helv.* 71 (1996) 213–219.
- [194] L. Savini, L. Chiasserini, A. Gaeta, C. Pellerano, Synthesis and anti-tubercular evaluation of 4-quinolylhydrazones, *Bioorg. Med. Chem.* 10 (2002) 2193–2198.
- [195] M.A. Soares, J.A. Lessa, I.C. Mendes, J.G. Da Silva, R.G. dos Santos, L.B. Salum, et al., N4-Phenyl-substituted 2-acetylpyridine thiosemicarbazones: Cytotoxicity against human tumor cells, structure–activity relationship studies and investigation on the mechanism of action, *Bioorg. Med. Chem.* 20 (2012) 3396–3409. doi:10.1016/j.bmc.2012.04.027.
- [196] J.A. Lessa, I.C. Mendes, P.R.O. da Silva, M.A. Soares, R.G. dos Santos, N.L. Speziali, et al., 2-Acetylpyridine thiosemicarbazones: Cytotoxic activity in nanomolar doses against malignant gliomas, *Eur. J. Med. Chem.* 45 (2010) 5671–5677. doi:10.1016/j.ejmech.2010.09.021.
- [197] É.A. Enyedy, N.V. Nagy, É. Zsigó, C.R. Kowol, V.B. Arion, B.K. Keppler, et al., Comparative Solution Equilibrium Study of the Interactions of Copper(II), Iron(II) and Zinc(II) with Triapine (3-Aminopyridine-2-carbaldehyde Thiosemicarbazone) and Related Ligands, *Eur. J. Inorg. Chem.* 2010 (2010) 1717–1728. doi:10.1002/ejic.200901174.
- [198] I. Đilović, M. Rubčić, V. Vrdoljak, S.K. Pavelić, M. Kralj, I. Piantanida, et al., Novel thiosemicarbazone derivatives as potential antitumor agents: Synthesis, physicochemical and

- structural properties, DNA interactions and antiproliferative activity, *Bioorg. Med. Chem.* 16 (2008) 5189–5198. doi:10.1016/j.bmc.2008.03.006.
- [199] V. Vrdoljak, M. Cindrić, D. Milić, D. Matković-Čalogović, P. Novak, B. Kamenar, Synthesis of five new molybdenum(VI) thiosemicarbazone complexes. Crystal structures of salicylaldehyde and 3-methoxy-salicylaldehyde 4-methylthiosemicarbazones and their molybdenum(VI) complexes, *Polyhedron*. 24 (2005) 1717–1726. doi:10.1016/j.poly.2005.05.002.
- [200] G. Tamasi, L. Chiasserini, L. Savini, A. Segà, R. Cini, Structural study of ribonucleotide reductase inhibitor hydrazones. Synthesis and X-ray diffraction analysis of a copper(II)-benzoylpyridine-2-quinolinyl hydrazone complex, *J. Inorg. Biochem.* 99 (2005) 1347–1359. doi:10.1016/j.jinorgbio.2005.03.009.
- [201] C.R. Kowol, R. Trondl, V.B. Arion, M.A. Jakupec, I. Lichtscheidl, B.K. Keppler, Fluorescence properties and cellular distribution of the investigational anticancer drug Triapine (3-aminopyridine-2-carboxaldehyde thiosemicarbazone) and its zinc(ii) complex, *Dalton Trans.* 39 (2010) 704. doi:10.1039/b919119b.
- [202] D.X. West, J.J. Ingram III, N.M. Kozub, G.A. Bain, A.E. Liberta, Copper (II) complexes of 2-formyl-, 2-acetyl- and 2-benzoyl-pyridine N (4)-phenyl-, N (4)-o-methoxyphenyl-, N (4)-p-methoxy-phenyl- and N (4)-p-nitrophenylthiosemicarbazones, *Transit. Met. Chem.* 21 (1996) 213–218.
- [203] J. Easmon, G. Pürstinger, K.-S. Thies, G. Heinisch, J. Hofmann, Synthesis, Structure–Activity Relationships, and Antitumor Studies of 2-Benzoxazolyl Hydrazones Derived from Alpha-(*N*)-acyl Heteroaromatics, *J. Med. Chem.* 49 (2006) 6343–6350. doi:10.1021/jm060232u.
- [204] P. Sengupta, R. Dinda, S. Ghosh, Ruthenium(II) complexes of NSO donor ligands in the form of ring-substituted 4-phenyl-thiosemicarbazones of salicylaldehyde and *o*-hydroxyacetophenone, *Transit. Met. Chem.* 27 (2002) 665–667. doi:10.1023/A:1019800729485.
- [205] E.B. Seena, M.R.P. Kurup, Spectral and structural studies of mono- and binuclear copper(II) complexes of salicylaldehyde N(4)-substituted thiosemicarbazones, *Polyhedron*. 26 (2007) 829–836. doi:10.1016/j.poly.2006.09.040.
- [206] P. Bindu, M.R.P. Kurup, T.R. Satyakeerty, Epr, cyclic voltammetric and biological activities of copper(II) complexes of salicylaldehyde N(4)-substituted thiosemicarbazone and heterocyclic bases, *Polyhedron*. 18 (1998) 321–331. doi:10.1016/S0277-5387(98)00166-1.
- [207] E. Pahontu, V. Fala, A. Gulea, D. Poirier, V. Tapcov, T. Rosu, Synthesis and Characterization of Some New Cu(II), Ni(II) and Zn(II) Complexes with Salicylidene Thiosemicarbazones: Antibacterial, Antifungal and in Vitro Antileukemia Activity, *Molecules*. 18 (2013) 8812–8836. doi:10.3390/molecules18088812.

- [208] V. Mahalingam, N. Chitrapriya, F.R. Fronczek, K. Natarajan, New Ru(II)–DMSO complexes of ON/SN chelates: Synthesis, behavior of Schiff bases towards hydrolytic cleavage of CN bond, electrochemistry and biological activities, *Polyhedron*. 29 (2010) 3363–3371. doi:10.1016/j.poly.2010.09.019.
- [209] Saswati, R. Dinda, C.S. Schmiesing, E. Sinn, Y.P. Patil, M. Nethaji, et al., Mixed-ligand nickel(II) thiosemicarbazone complexes: Synthesis, characterization and biological evaluation, *Polyhedron*. 50 (2013) 354–363. doi:10.1016/j.poly.2012.11.031.
- [210] M. Cindrić, M. Rubčić, The Rare Examples of Thiosemicarbazonato Chromium(III) Complexes: Crystal Structures of [Cr(Hsal 4-Metsc)<sub>2</sub>]Cl·CH<sub>3</sub>OH and [Cr(Hsal 4-Phtsc)<sub>2</sub>]Cl, *Croat. Chem. Acta*. 85 (2012) 505–513. doi:10.5562/cca2153.
- [211] V. Vrdoljak, D. Milić, M. Cindrić, D. Matković-Čalogović, D. Cinčić, Synthesis of novel molybdenum(V) complexes: Structural characterization of two thiosemicarbazonato complexes [MoOC12{C<sub>6</sub>H<sub>4</sub>(O)CH:NNHC:SNHC6H<sub>5</sub>}] and [MoOC12{C<sub>10</sub>H<sub>6</sub>(O)CH:NNHC:SNHC6H<sub>5</sub>}]·CH<sub>3</sub>CN, and two oxohalomolybdates NH<sub>4</sub>[MoOC14(CH<sub>3</sub>CN)] and [C<sub>5</sub>H<sub>5</sub>NH]<sub>2</sub>[MoOC15]·CH<sub>2</sub>Cl<sub>2</sub>, *Polyhedron*. 26 (2007) 3363–3372. doi:10.1016/j.poly.2007.03.028.
- [212] M. Cindrić, M. Uzelac, D. Cinčić, I. Halasz, G. Pavlović, T. Hrenar, et al., Three routes to nickel(II) salicylaldehyde 4-phenyl and 4-methylthiosemicarbazonato complexes: mechanochemical, electrochemical and conventional approach, *CrystEngComm*. 14 (2012) 3039–3045. doi:10.1039/C2CE06611D.
- [213] V.V. Bon, S.I. Orysyk, V.I. Pekhnyo, S.V. Volkov, Square-planar 1:2 Ni(II) and Pd(II) complexes with different coordination mode of salicylaldehyde (4)-phenylthiosemicarbazone: Synthesis, structure and spectral properties, *J. Mol. Struct.* 984 (2010) 15–22. doi:10.1016/j.molstruc.2010.08.046.
- [214] M. Mohan, M.P. Gupta, L. Chandra, N.K. Jha, Synthesis, characterization and antitumour properties of some metal(II) complexes of 2-pyridinecarboxaldehyde 2'-pyridylhydrazone and related compounds, *Inorganica Chim. Acta*. 151 (1988) 61–68. doi:10.1016/S0020-1693(00)83485-4.
- [215] G. Vantomme, N. Hafezi, J.-M. Lehn, A light-induced reversible phase separation and its coupling to a dynamic library of imines, *Chem. Sci.* 5 (2014) 1475–1483. doi:10.1039/C3SC53130A.
- [216] S.-Q. Wu, Y.-T. Wang, A.-L. Cui, H.-Z. Kou, Toward Higher Nuclearity: Tetranuclear Cobalt(II) Metallogrid Exhibiting Spin Crossover, *Inorg. Chem.* 53 (2014) 2613–2618. doi:10.1021/ic402971a.
- [217] M.F. Primik, S. Göschl, M.A. Jakupec, A. Roller, B.K. Keppler, V.B. Arion, Structure–Activity Relationships of Highly Cytotoxic Copper(II) Complexes with Modified Indolo[3,2-c]quinoline Ligands, *Inorg. Chem.* 49 (2010) 11084–11095. doi:10.1021/ic101633z.



- [218] E. Ion, M. Calinescu, A. Emandi, V. Badea, D. Negoiu, Copper (II) Complex Compounds with Mixed Hydrazone Ligands, *Rev. Chim.-Buchar.-Orig. Ed.-.* 59 (2008) 12.
- [219] S.R. Girish, V.K. Revankar, V.B. Mahale, Oxomolybdenum (V) complexes of 2-benzothiazolyl hydrazones, *Transit. Met. Chem.* 21 (1996) 401–405.
- [220] M. Călinescu, E. Ion, A.-M. Stadler, Studies on nickel (II) complex compounds with 2-benzothiazolyl hydrazones, *Rev Roum Chim.* 53 (2008) 903–909.
- [221] N.S. Youssef, E. El-Zahany, A.M.A. El-Seidy, A. Caselli, S. Fantauzzi, S. Cenini, Synthesis and characterisation of new Schiff base metal complexes and their use as catalysts for olefin cyclopropanation, *Inorganica Chim. Acta.* 362 (2009) 2006–2014. doi:10.1016/j.ica.2008.09.012.
- [222] J.K. Seydel, K.-J. Schaper, Substituierte 2-Acylpyridin- $\alpha$ -(N)-hetarylhydrazone sowie diese enthaltende Arzneimittel, DE3716131A1, 1987.
- [223] P.S. Kalsi, B.R. Chhabra, J. Singh, R. Vig, Selective Oxidation of Primary Allylic Alcohols to  $\alpha\beta$ -Unsaturated Aldehydes, *Synlett.* 1992 (1992) 425–426. doi:10.1055/s-1992-21368.
- [224] K.C. Agrawal, P.D. Mooney, A.C. Sartorelli, Potential antitumor agents. 13. 4-Methyl-5-amino-1-formylisoquinoline thiosemicarbazone, *J. Med. Chem.* 19 (1976) 970–972.
- [225] B.R. Chhabra, K. Hayano, T. Ohtsuka, H. Shirahama, T. Matsumoto, Selective oxidation of allylic methyls in medium ring compounds, *Chem. Lett.* 10 (1981) 1703–1706.
- [226] Y. Tagawa, K. Yamashita, Y. Higuchi, Y. Goto, IMPROVED OXIDATION OF ACTIVE METHYL GROUP OF N-HETEROAROMATIC COMPOUNDS BY SELENIUM DIOXIDE IN, *Heterocycles.* 60 (2003) 953–957.
- [227] D.L. Klayman, J.F. Bartosevich, T.S. Griffin, C.J. Mason, J.P. Scovill, 2-Acetylpyridine thiosemicarbazones. 1. A new class of potential antimalarial agents, *J. Med. Chem.* 22 (1979) 855–862.
- [228] A.S. Dobek, D.L. Klayman, E.T. Dickson, J.P. Scovill, E.C. Tramont, Inhibition of clinically significant bacterial organisms in vitro by 2-acetylpyridine thiosemicarbazones., *Antimicrob. Agents Chemother.* 18 (1980) 27–36. doi:10.1128/AAC.18.1.27.
- [229] X. Mei, P. Wang, A. Caracoti, P. Mingo, V. Boyd, R. Murray, et al., Hydrazone, hydrazine and thiosemicarbazone derivatives as antifungal agents, Google Patents, 2001. <http://www.google.com/patents/US6329378> (accessed September 29, 2014).
- [230] S.A. Thompson, L. Wheat, N.A. Brown, P.B. Wingrove, G.V. Pillai, P.J. Whiting, et al., Salicylidene salicylhydrazide, a selective inhibitor of  $\beta$  1-containing GABA<sub>A</sub> receptors, *Br. J. Pharmacol.* 142 (2004) 97–106. doi:10.1038/sj.bjp.0705689.
- [231] K. Krishnan, K. Prathiba, V. Jayaprakash, A. Basu, N. Mishra, B. Zhou, et al., Synthesis and ribonucleotide reductase inhibitory activity of thiosemicarbazones, *Bioorg. Med. Chem. Lett.* 18 (2008) 6248–6250. doi:10.1016/j.bmcl.2008.09.097.

- [232] A. Shaikh Kabber, M.A. Bassar, N.A. Mote, Synthesis and Antimicrobial Activity of Some Schiff Bases from Benzothiazoles, *Asian J. Chem.* 13 (2001) 496–500.
- [233] J. Easmon, G. Heinisch, J. Hofmann, T. Langer, H. Grunicke, J. Fink, et al., Thiazolyl and benzothiazolyl hydrazones derived from  $\alpha$ -(N)-acetylpyridines and diazines: synthesis, antiproliferative activity and CoMFA studies, *Eur. J. Med. Chem.* 32 (1997) 397–408. doi:10.1016/S0223-5234(97)81677-7.
- [234] E.B. Lindgren, M.A. de Brito, T.R.A. Vasconcelos, M.O. de Moraes, R.C. Montenegro, J.D. Yoneda, et al., Synthesis and anticancer activity of (E)-2-benzothiazole hydrazones, *Eur. J. Med. Chem.* 86 (2014) 12–16. doi:10.1016/j.ejmech.2014.08.039.
- [235] D. Gupta-Ostermann, J. Bajorath, The “SAR Matrix” method and its extensions for applications in medicinal chemistry and chemogenomics, *F1000Research*. (2014). doi:10.12688/f1000research.4185.2.
- [236] K.L. Rinehart, Antitumor compounds from tunicates, *Med. Res. Rev.* 20 (2000) 1–27. doi:10.1002/(SICI)1098-1128(200001)20:1<1::AID-MED1>3.0.CO;2-A.
- [237] C.M. Rath, B. Janto, J. Earl, A. Ahmed, F.Z. Hu, L. Hiller, et al., Meta-omic Characterization of the Marine Invertebrate Microbial Consortium That Produces the Chemotherapeutic Natural Product ET-743, *ACS Chem. Biol.* 6 (2011) 1244–1256. doi:10.1021/cb200244t.
- [238] E.L. Cooper, D. Yao, Diving for drugs: tunicate anticancer compounds, *Drug Discov. Today*. 17 (2012) 636–648. doi:10.1016/j.drudis.2012.02.006.
- [239] R.G. Pearson, Hard and Soft Acids and Bases, *J. Am. Chem. Soc.* 85 (1963) 3533–3539. doi:10.1021/ja00905a001.
- [240] R.G. Pearson, Acids and bases, *Science*. 151 (1966) 172–177. doi:10.1126/science.151.3707.172.
- [241] K.L. Haas, K.J. Franz, Application of Metal Coordination Chemistry To Explore and Manipulate Cell Biology, *Chem. Rev.* 109 (2009) 4921–4960. doi:10.1021/cr900134a.
- [242] É.A. Enyedy, É. Zsigó, N.V. Nagy, C.R. Kowol, A. Roller, B.K. Keppler, et al., Complex-Formation Ability of Salicylaldehyde Thiosemicarbazone towards ZnII, CuII, FeII, FeIII and GaIII Ions, *Eur. J. Inorg. Chem.* 2012 (2012) 4036–4047. doi:10.1002/ejic.201200360.
- [243] P.J. Jansson, C.L. Hawkins, D.B. Lovejoy, D.R. Richardson, The iron complex of Dp44mT is redox-active and induces hydroxyl radical formation: An EPR study, *J. Inorg. Biochem.* 104 (2010) 1224–1228. doi:10.1016/j.jinorgbio.2010.07.012.
- [244] E.M. Becker, D.B. Lovejoy, J.M. Greer, R. Watts, D.R. Richardson, Identification of the dipyrindyl ketone isonicotinoyl hydrazone (PKIH) analogues as potent iron chelators and anti-tumour agents, *Br. J. Pharmacol.* 138 (2003) 819–830. doi:10.1038/sj.bjp.0705089.
- [245] Y. 'ning Song, H. Xu, W. Chen, P. Zhan, X. Liu, 8-Hydroxyquinoline: a privileged structure with a broad-ranging pharmacological potential, *MedChemComm.* 6 (2015) 61–74. doi:10.1039/C4MD00284A.

- [246] G.S. Bajwa, K.E. Hartman, M.M. Joullié, Antimalarials. 1. Heterocyclic analogs of N-substituted naphthalenebisoxazines, *J. Med. Chem.* 16 (1973) 134–138.
- [247] É.A. Enyedy, O. Dömötör, E. Varga, T. Kiss, R. Trondl, C.G. Hartinger, et al., Comparative solution equilibrium studies of anticancer gallium(III) complexes of 8-hydroxyquinoline and hydroxy(thio)pyrone ligands, *J. Inorg. Biochem.* 117 (2012) 189–197. doi:10.1016/j.jinorgbio.2012.08.005.
- [248] Royal Society of Chemistry, SCQuery, The IUPAC Stability Constants Database, Academic Software, 2005.
- [249] R.J. Motekaitis, R.M. Smith, A.E. Martell, Critically Selected Stability Constants of Metal Complexes Database, College Station, TX, USA, 1997.
- [250] T.D. Turnquist, E.B. Sandell, Stability constants of iron(III)-8-hydroxyquinoline complexes, *Anal. Chim. Acta.* 42 (1968) 239–245. doi:10.1016/S0003-2670(01)80304-4.
- [251] G. Chen, Tris(quinolin-8-olato- $\kappa^2 N, O$ )iron(III) methanol solvate, *Acta Crystallogr. Sect. E Struct. Rep. Online.* 62 (2006) m3383–m3384. doi:10.1107/S1600536806048653.
- [252] R.C. Hoy, R.H. Morriss, The crystal structure of the form of anhydrous copper 8-hydroxyquinolate, *Acta Crystallogr.* 22 (1967) 476–482.
- [253] R.M. Smith, A.E. Martell, R.J. Motekaitis, NIST critically selected stability constants of metal complexes database, National Institute of Standards and Technology, U.S. Dept. of Commerce, Gaithersburg, MD, 2004. <http://trove.nla.gov.au/work/20880716>.
- [254] S. Tardito, A. Barilli, I. Bassanetti, M. Tegoni, O. Bussolati, R. Franchi-Gazzola, et al., Copper-Dependent Cytotoxicity of 8-Hydroxyquinoline Derivatives Correlates with Their Hydrophobicity and Does Not Require Caspase Activation, *J. Med. Chem.* 55 (2012) 10448–10459. doi:10.1021/jm301053a.
- [255] F.Q. Schafer, G.R. Buettner, Redox environment of the cell as viewed through the redox state of the glutathione disulfide/glutathione couple, *Free Radic. Biol. Med.* 30 (2001) 1191–1212.
- [256] C.G. Hartinger, S. Zorbas-Seifried, M.A. Jakupec, B. Kynast, H. Zorbas, B.K. Keppler, From bench to bedside – preclinical and early clinical development of the anticancer agent indazolium trans-[tetrachlorobis(1H-indazole)ruthenate(III)] (KP1019 or FFC14A), *J. Inorg. Biochem.* 100 (2006) 891–904. doi:10.1016/j.jinorgbio.2006.02.013.
- [257] R.T. Dean, P. Nicholson, The action of nine chelators on iron-dependent radical damage, *Free Radic. Res.* 20 (1994) 83–101.
- [258] R.J. Bergeron, J. Wiegand, J.S. McManis, J. Bussenius, R.E. Smith, W.R. Weimar, Methoxylation of Desazadesferrithiocin Analogues: Enhanced Iron Clearing Efficiency, *J. Med. Chem.* 46 (2003) 1470–1477. doi:10.1021/jm020412d.
- [259] T.B. Chaston, D.B. Lovejoy, R.N. Watts, D.R. Richardson, Examination of the Antiproliferative Activity of Iron Chelators Multiple Cellular Targets and the Different

- Mechanism of Action of Triapine Compared with Desferrioxamine and the Potent Pyridoxal Isonicotinoyl Hydrazone Analogue 311, *Clin. Cancer Res.* 9 (2003) 402–414.
- [260] P.V. Bernhardt, L.M. Caldwell, T.B. Chaston, P. Chin, D.R. Richardson, Cytotoxic iron chelators: characterization of the structure, solution chemistry and redox activity of ligands and iron complexes of the di-2-pyridyl ketone isonicotinoyl hydrazone (HPKIH) analogues, *JBIC J. Biol. Inorg. Chem.* 8 (2003) 866–880. doi:10.1007/s00775-003-0486-z.
- [261] T.B. Chaston, D.R. Richardson, Interactions of the pyridine-2-carboxaldehyde isonicotinoyl hydrazone class of chelators with iron and DNA: implications for toxicity in the treatment of iron overload disease, *J. Biol. Inorg. Chem.* 8 (2003) 427–438. doi:10.1007/s00775-002-0434-3.
- [262] B. Song, N. Aebischer, C. Orvig, Reduction of [VO<sub>2</sub>(ma)<sub>2</sub>]<sup>-</sup> and [VO<sub>2</sub>(ema)<sub>2</sub>]<sup>-</sup> by Ascorbic Acid and Glutathione: Kinetic Studies of Pro-Drugs for the Enhancement of Insulin Action†, *Inorg. Chem.* 41 (2002) 1357–1364. doi:10.1021/ic0111684.
- [263] T. Jakusch, É.A. Enyedy, K. Kozma, Z. Paár, A. Bényei, T. Kiss, Vanadate complexes of 3-hydroxy-1,2-dimethyl-pyridinone: Speciation, structure and redox properties, *Inorganica Chim. Acta.* 420 (2014) 92–102. doi:10.1016/j.ica.2013.12.034.
- [264] J.J. Ruiz, A. Aldaz, M. Dominguez, Mechanism of L-ascorbic acid oxidation and dehydro-L-ascorbic acid reduction on a mercury electrode. I. Acid medium, *Can. J. Chem.* 55 (1977) 2799–2806. doi:10.1139/v77-389.
- [265] C. Kerksick, D. Willoughby, The Antioxidant Role of Glutathione and N-Acetyl-Cysteine Supplements and Exercise-Induced Oxidative Stress, *J. Int. Soc. Sports Nutr.* 2 (2005) 38–44. doi:10.1186/1550-2783-2-2-38.
- [266] B. Noszál, D. Visky, M. Kraszni, Population, Acid–Base, and Redox Properties of *N*-Acetylcysteine Conformers, *J. Med. Chem.* 43 (2000) 2176–2182. doi:10.1021/jm9909600.
- [267] J.P. Baumberger, J.J. Jürgensen, K. Bardwell, The coupled redox potential of the lactate-enzyme-pyruvate system, *J. Gen. Physiol.* 16 (1933) 961.
- [268] W.W. Cleland, Dithiothreitol, a New Protective Reagent for SH Groups\*, *Biochemistry (Mosc.)*. 3 (1964) 480–482. doi:10.1021/bi00892a002.
- [269] A. Seo, J.L. Jackson, J.V. Schuster, D. Vardar-Ulu, Using UV-absorbance of intrinsic dithiothreitol (DTT) during RP-HPLC as a measure of experimental redox potential in vitro, *Anal. Bioanal. Chem.* 405 (2013) 6379–6384. doi:10.1007/s00216-013-7063-2.
- [270] W. Jakubowski, 2,7-DICHLOROFLUORESCIN OXIDATION AND REACTIVE OXYGEN SPECIES: WHAT DOES IT MEASURE?, *Cell Biol. Int.* 24 (2000) 757–760. doi:10.1006/cbir.2000.0556.
- [271] E. Eruslanov, S. Kusmartsev, Identification of ROS Using Oxidized DCFDA and Flow-Cytometry, in: D. Armstrong (Ed.), *Adv. Protoc. Oxidative Stress II*, Humana Press, Totowa,

- NJ, 2010: pp. 57–72. [http://link.springer.com/10.1007/978-1-60761-411-1\\_4](http://link.springer.com/10.1007/978-1-60761-411-1_4) (accessed November 3, 2014).
- [272] C.P. LeBel, H. Ischiropoulos, S.C. Bondy, Evaluation of the probe 2', 7'-dichlorofluorescein as an indicator of reactive oxygen species formation and oxidative stress, *Chem. Res. Toxicol.* 5 (1992) 227–231.
- [273] J. Procházková, L. Kubala, H. Kotasová, I. Gudernová, Z. Šrámková, M. Pekarová, et al., ABC transporters affect the detection of intracellular oxidants by fluorescent probes, *Free Radic. Res.* 45 (2011) 779–787. doi:10.3109/10715762.2011.579120.
- [274] M. Wartenberg, E. Hoffmann, H. Schwindt, F. Grünheck, J. Petros, J.R.S. Arnold, et al., Reactive oxygen species-linked regulation of the multidrug resistance transporter P-glycoprotein in Nox-1 overexpressing prostate tumor spheroids, *FEBS Lett.* 579 (2005) 4541–4549. doi:10.1016/j.febslet.2005.06.078.
- [275] W.A. Morgan, B. Kaler, P.H. Bach, The role of reactive oxygen species in adriamycin and menadione-induced glomerular toxicity, *Toxicol. Lett.* 94 (1998) 209–215.
- [276] Y. Cai, J. Lu, Z. Miao, L. Lin, J. Ding, others, Reactive oxygen species contribute to cell killing and P-glycoprotein downregulation by salvicine in multidrug resistant K562/A02 cells, *Cancer Biol. Ther.* 6 (2007) 1794.
- [277] Y. Jing, J. Dai, R.M. Chalmers-Redman, W.G. Tatton, S. Waxman, Arsenic trioxide selectively induces acute promyelocytic leukemia cell apoptosis via a hydrogen peroxide-dependent pathway, *Blood.* 94 (1999) 2102–2111.
- [278] B.-Y. You, Y.-H. Wang, M.-L. Kuo, Role of reactive oxygen species in cupric 8-quinolinoxide-induced genotoxic effect, *Mutat. Res. Toxicol. Environ. Mutagen.* 491 (2001) 45–56.
- [279] H.-R. Lu, Reactive Oxygen Species Elicit Apoptosis by Concurrently Disrupting Topoisomerase II and DNA-Dependent Protein Kinase, *Mol. Pharmacol.* 68 (2005) 983–994. doi:10.1124/mol.105.011544.
- [280] J. Yi, J. Yang, R. He, F. Gao, H. Sang, X. Tang, et al., Emodin enhances arsenic trioxide-induced apoptosis via generation of reactive oxygen species and inhibition of survival signaling, *Cancer Res.* 64 (2004) 108–116.
- [281] T. Atsumi, S. Fujisawa, K. Tonosaki, Relationship between intracellular ROS production and membrane mobility in curcumin-and tetrahydrocurcumin-treated human gingival fibroblasts and human submandibular gland carcinoma cells, *Oral Dis.* 11 (2005) 236–242.
- [282] L.K. Chin, J.Q. Yu, Y. Fu, T. Yu, A.Q. Liu, K.Q. Luo, Production of reactive oxygen species in endothelial cells under different pulsatile shear stresses and glucose concentrations, *Lab. Chip.* 11 (2011) 1856. doi:10.1039/c0lc00651c.
- [283] T. Ohashi, A. Mizutani, A. Murakami, S. Kojo, T. Ishii, S. Taketani, Rapid oxidation of dichlorodihydrofluorescein with heme and hemoproteins: formation of the fluorescein is independent of the generation of reactive oxygen species, *FEBS Lett.* 511 (2002) 21–27.

- [284] Z.-F. Chen, M.-X. Tan, L.-M. Liu, Y.-C. Liu, H.-S. Wang, B. Yang, et al., Cytotoxicity of the traditional chinese medicine (TCM) plumbagin in its copper chemistry, *Dalton Trans. Camb. Engl.* 2003. (2009) 10824–10833. doi:10.1039/b910133k.
- [285] S. Nazeem, A.S. Azmi, S. Hanif, A. Ahmad, R.M. Mohammad, S.M. Hadi, et al., Plumbagin induces cell death through a copper-redox cycle mechanism in human cancer cells, *Mutagenesis*. 24 (2009) 413–418. doi:10.1093/mutage/geb023.
- [286] J.-H. Lee, J.-H. Yeon, H. Kim, W. Roh, J. Chae, H.-O. Park, et al., The Natural Anticancer Agent Plumbagin Induces Potent Cytotoxicity in MCF-7 Human Breast Cancer Cells by Inhibiting a PI-5 Kinase for ROS Generation, *PLoS ONE*. 7 (2012) e45023. doi:10.1371/journal.pone.0045023.
- [287] K.S. Kumar, S. Nazeem, A. Azmi, S. Hanif, Reactive Oxygen-Dependent DNA Damage Resulting from the Oxidation of Plumbagin by a Copper-redox Cycle Mechanism: Implications for its Anti-cancer Properties, *Austral-Asian J. Cancer*. 7 (2008) 65–72.
- [288] A. Gomes, E. Fernandes, J.L.F.C. Lima, Fluorescence probes used for detection of reactive oxygen species, *J. Biochem. Biophys. Methods*. 65 (2005) 45–80. doi:10.1016/j.jbbm.2005.10.003.
- [289] B. Kalyanaraman, V. Darley-Usmar, K.J.A. Davies, P.A. Dennery, H.J. Forman, M.B. Grisham, et al., Measuring reactive oxygen and nitrogen species with fluorescent probes: challenges and limitations, *Free Radic. Biol. Med.* 52 (2012) 1–6. doi:10.1016/j.freeradbiomed.2011.09.030.
- [290] H. Zhu, G.L. Bannenberg, P. Moldéus, H.G. Shertzer, Oxidation pathways for the intracellular probe 2',7'-dichlorofluorescein, *Arch. Toxicol.* 68 (1994) 582–587. doi:10.1007/s002040050118.
- [291] M.J. Burkitt, P. Wardman, Cytochrome c Is a Potent Catalyst of Dichlorofluorescein Oxidation: Implications for the Role of Reactive Oxygen Species in Apoptosis, *Biochem. Biophys. Res. Commun.* 282 (2001) 329–333. doi:10.1006/bbrc.2001.4578.
- [292] C.F. Chignell, R.H. Sik, A photochemical study of cells loaded with 2',7'-dichlorofluorescein: implications for the detection of reactive oxygen species generated during UVA irradiation, *Free Radic. Biol. Med.* 34 (2003) 1029–1034. doi:10.1016/S0891-5849(03)00022-4.
- [293] P. Wardman, Fluorescent and luminescent probes for measurement of oxidative and nitrosative species in cells and tissues: Progress, pitfalls, and prospects, *Free Radic. Biol. Med.* 43 (2007) 995–1022. doi:10.1016/j.freeradbiomed.2007.06.026.
- [294] M.B. Grisham, Methods to detect hydrogen peroxide in living cells: Possibilities and pitfalls, *Comp. Biochem. Physiol. A. Mol. Integr. Physiol.* 165 (2013) 429–438. doi:10.1016/j.cbpa.2013.02.003.
- [295] V.V. Belousov, A.F. Fradkov, K.A. Lukyanov, D.B. Staroverov, K.S. Shakhbazov, A.V. Terskikh, et al., Genetically encoded fluorescent indicator for intracellular hydrogen peroxide, *Nat. Methods*. 3 (2006) 281–286. doi:10.1038/nmeth866.

- [296] J.B. Lim, H.D. Sikes, Use of a genetically encoded hydrogen peroxide sensor for whole cell screening of enzyme activity, *Protein Eng. Des. Sel. PEDS.* 28 (2015) 79–83. doi:10.1093/protein/gzv003.
- [297] K.N. Markvicheva, D.S. Bilan, N.M. Mishina, A.Y. Gorokhovatsky, L.M. Vinokurov, S. Lukyanov, et al., A genetically encoded sensor for H<sub>2</sub>O<sub>2</sub> with expanded dynamic range, *Bioorg. Med. Chem.* 19 (2011) 1079–1084. doi:10.1016/j.bmc.2010.07.014.
- [298] J. Weller, K.M. Kizina, K. Can, G. Bao, M. Müller, Response properties of the genetically encoded optical H<sub>2</sub>O<sub>2</sub> sensor HyPer, *Free Radic. Biol. Med.* 76 (2014) 227–241. doi:10.1016/j.freeradbiomed.2014.07.045.
- [299] A. Hernández-Barrera, A. Velarde-Buendía, I. Zepeda, F. Sanchez, C. Quinto, R. Sánchez-Lopez, et al., Hyper, a Hydrogen Peroxide Sensor, Indicates the Sensitivity of the Arabidopsis Root Elongation Zone to Aluminum Treatment, *Sensors.* 15 (2015) 855–867. doi:10.3390/s150100855.
- [300] A.J. Meyer, T.P. Dick, Fluorescent Protein-Based Redox Probes, *Antioxid. Redox Signal.* 13 (2010) 621–650. doi:10.1089/ars.2009.2948.
- [301] FuGENE® HD Transfection Reagent, (n.d.). <https://worldwide.promega.com/products/reporter-assays-and-transfection/transfection-reagents/fugene-hd-ultimate-transfection-performance/fugene-hd-transfection-reagent/> (accessed July 7, 2015).
- [302] M. Wartenberg, M. Richter, A. Datchev, S. Günther, N. Milosevic, M.M. Bekhite, et al., Glycolytic pyruvate regulates P-Glycoprotein expression in multicellular tumor spheroids via modulation of the intracellular redox state, *J. Cell. Biochem.* (2009) n/a–n/a. doi:10.1002/jcb.22422.
- [303] M. Wartenberg, Down-regulation of Intrinsic P-glycoprotein Expression in Multicellular Prostate Tumor Spheroids by Reactive Oxygen Species, *J. Biol. Chem.* 276 (2001) 17420–17428. doi:10.1074/jbc.M100141200.
- [304] M. Bakker, J. Renes, A. Groenhuijzen, P. Visser, H. Timmer-Bosscha, M. Müller, et al., Mechanisms for high methoxymorpholino doxorubicin cytotoxicity in doxorubicin-resistant tumor cell lines, *Int. J. Cancer.* 73 (1997) 362–366. doi:10.1002/(SICI)1097-0215(19971104)73:3<362::AID-IJC10>3.0.CO;2-F.
- [305] L. Mátés, M.K.L. Chuah, E. Belay, B. Jerchow, N. Manoj, A. Acosta-Sanchez, et al., Molecular evolution of a novel hyperactive Sleeping Beauty transposase enables robust stable gene transfer in vertebrates, *Nat. Genet.* 41 (2009) 753–761. doi:10.1038/ng.343.
- [306] G. Szakács, C. Ozvegy, E. Bakos, B. Sarkadi, A. Váradi, Transition-state formation in ATPase-negative mutants of human MDR1 protein, *Biochem. Biophys. Res. Commun.* 276 (2000) 1314–1319. doi:10.1006/bbrc.2000.3576.

- [307] K.R. Brimacombe, M.D. Hall, D.S. Auld, J. Inglese, C.P. Austin, M.M. Gottesman, et al., A Dual-Fluorescence High-Throughput Cell Line System for Probing Multidrug Resistance, *Assay Drug Dev. Technol.* 7 (2009) 233–249. doi:10.1089/adt.2008.165.
- [308] Common Stock Solutions, Buffers, and Media, *Curr. Protoc. Neurosci.* (1997). <http://onlinelibrary.wiley.com/doi/10.1002/0471142301.nsa02as00/full> (accessed May 21, 2015).
- [309] R.J. Geraghty, A. Capes-Davis, J.M. Davis, J. Downward, R.I. Freshney, I. Knezevic, et al., Guidelines for the use of cell lines in biomedical research, *Br. J. Cancer.* 111 (2014) 1021–1046. doi:10.1038/bjc.2014.166.
- [310] H.G. Drexler, C.C. Uphoff, Mycoplasma contamination of cell cultures: Incidence, sources, effects, detection, elimination, prevention, *Cytotechnology.* 39 (2002) 75–90. doi:10.1023/A:1022913015916.
- [311] A. Downes, T.P. Blunt, On the Influence of Light upon Protoplasm, *Proc. R. Soc. Lond.* 28 (1878) 199–212. doi:10.1098/rspl.1878.0109.
- [312] C.J. Miller, H.S. Kassem, S.D. Pepper, Y. Hey, T.H. Ward, G.P. Margison, Mycoplasma infection significantly alters microarray gene expression profiles, *BioTechniques.* 35 (2003) 812–815.
- [313] MycoAlert™ Mycoplasma Detection Kit, (n.d.). <http://www.lonza.com/products-services/bio-research/cell-culture-products/mycoplasma-detection-and-removal/mycoalert-mycoplasma-detection-kit.aspx> (accessed July 5, 2015).
- [314] E. Aldecoa-Otalora, W.B. Langdon, P. Cunningham, M.J. Arno, Unexpected presence of mycoplasma probes on human microarrays, *BioTechniques.* 47 (2009) 1013–1016.
- [315] T. Mosmann, Rapid colorimetric assay for cellular growth and survival: application to proliferation and cytotoxicity assays, *J. Immunol. Methods.* 65 (1983) 55–63.
- [316] M.V. Berridge, A.S. Tan, K.D. McCoy, R. Wang, others, The biochemical and cellular basis of cell proliferation assays that use tetrazolium salts, *Biochemica.* 4 (1996) 15–19.
- [317] T.L. Riss, R.A. Moravec, A.L. Niles, H.A. Benink, T.J. Worzella, L. Minor, Cell Viability Assays, in: G.S. Sittampalam, N. Gal-Edd, M. Arkin, D. Auld, C. Austin, B. Bejcek, et al. (Eds.), *Assay Guid. Man., Eli Lilly & Company and the National Center for Advancing Translational Sciences, Bethesda (MD), 2004.* <http://www.ncbi.nlm.nih.gov/books/NBK144065/> (accessed May 21, 2015).
- [318] F. Denizot, R. Lang, Rapid colorimetric assay for cell growth and survival. Modifications to the tetrazolium dye procedure giving improved sensitivity and reliability, *J. Immunol. Methods.* 89 (1986) 271–277.
- [319] T. Bernas, J. Dobrucki, Mitochondrial and nonmitochondrial reduction of MTT: Interaction of MTT with TMRE, JC-1, and NAO mitochondrial fluorescent probes, *Cytometry.* 47 (2002) 236–242. doi:10.1002/cyto.10080.



- [320] M.V. Berridge, A.S. Tan, Characterization of the Cellular Reduction of 3-(4,5-dimethylthiazol-2-yl)-2,5-diphenyltetrazolium bromide (MTT): Subcellular Localization, Substrate Dependence, and Involvement of Mitochondrial Electron Transport in MTT Reduction, *Arch. Biochem. Biophys.* 303 (1993) 474–482. doi:10.1006/abbi.1993.1311.
- [321] Y. Liu, D.A. Peterson, H. Kimura, D. Schubert, Mechanism of Cellular 3-(4,5-Dimethylthiazol-2-yl)-2,5-Diphenyltetrazolium Bromide (MTT) Reduction, *J. Neurochem.* 69 (1997) 581–593. doi:10.1046/j.1471-4159.1997.69020581.x.
- [322] H. Mueller, M.U. Kassack, M. Wiese, Comparison of the Usefulness of the MTT, ATP, and Calcein Assays to Predict the Potency of Cytotoxic Agents in Various Human Cancer Cell Lines, *J. Biomol. Screen.* 9 (2004) 506–515. doi:10.1177/1087057104265386.
- [323] T. Riss, M. O'Brien, R. Moravec, others, Choosing the right cell-based assay for your research, *Cell Notes.* 6 (2003) 6.
- [324] R. Hamid, Y. Rotshteyn, L. Rabadi, R. Parikh, P. Bullock, Comparison of alamar blue and MTT assays for high through-put screening, *Toxicol. In Vitro.* 18 (2004) 703–710. doi:10.1016/j.tiv.2004.03.012.
- [325] S. Al-Nasiry, N. Geusens, M. Hanssens, C. Luyten, R. Pijnenborg, The use of Alamar Blue assay for quantitative analysis of viability, migration and invasion of choriocarcinoma cells, *Hum. Reprod.* 22 (2007) 1304–1309. doi:10.1093/humrep/dem011.
- [326] J. O'Brien, I. Wilson, T. Orton, F. Pognan, Investigation of the Alamar Blue (resazurin) fluorescent dye for the assessment of mammalian cell cytotoxicity, *Eur. J. Biochem.* 267 (2000) 5421–5426.
- [327] G.R. Nakayama, M.C. Caton, M.P. Nova, Z. Parandoosh, Assessment of the Alamar Blue assay for cellular growth and viability in vitro, *J. Immunol. Methods.* 204 (1997) 205–208.
- [328] C. Mo, R. Yamagata, A. Pan, J. Reddy, N. Hazari, G. Duke, Development of a high-throughput Alamar blue assay for the determination of influenza virus infectious dose, serum antiviral neutralization titer and virus ca/ts phenotype, *J. Virol. Methods.* 150 (2008) 63–69. doi:10.1016/j.jviromet.2008.03.006.
- [329] S.A. Ahmed, R.M. Gogal, J.E. Walsh, A new rapid and simple non-radioactive assay to monitor and determine the proliferation of lymphocytes: an alternative to [3H]thymidine incorporation assay, *J. Immunol. Methods.* 170 (1994) 211–224.
- [330] S.N. Rampersad, Multiple Applications of Alamar Blue as an Indicator of Metabolic Function and Cellular Health in Cell Viability Bioassays, *Sensors.* 12 (2012) 12347–12360. doi:10.3390/s120912347.
- [331] G. Elliott, J. McGrath, E. Crockett-Torabi, Green Fluorescent Protein: A Novel Viability Assay for Cryobiological Applications, *Cryobiology.* 40 (2000) 360–369. doi:10.1006/cryo.2000.2258.

- [332] C. Baumstark-Khan, M. Palm, J. Wehner, M. Okabe, M. Ikawa, G. Horneck, Green Fluorescent Protein (GFP) as a Marker for Cell Viability After UV Irradiation, *J. Fluoresc.* 9 (1999) 37–43. doi:10.1023/A:1020583623407.
- [333] G.U. Nienhaus, The Green Fluorescent Protein: A Key Tool to Study Chemical Processes in Living Cells, *Angew. Chem. Int. Ed.* 47 (2008) 8992–8994. doi:10.1002/anie.200804998.
- [334] M. Chalfie, Y. Tu, G. Euskirchen, W.W. Ward, D.C. Prasher, Green fluorescent protein as a marker for gene expression, *Science.* 263 (1994) 802–805.
- [335] R.E. Campbell, O. Tour, A.E. Palmer, P.A. Steinbach, G.S. Baird, D.A. Zacharias, et al., A monomeric red fluorescent protein, *Proc. Natl. Acad. Sci. U. S. A.* 99 (2002) 7877–7882. doi:10.1073/pnas.082243699.
- [336] N.C. Shaner, R.E. Campbell, P.A. Steinbach, B.N.G. Giepmans, A.E. Palmer, R.Y. Tsien, Improved monomeric red, orange and yellow fluorescent proteins derived from *Discosoma* sp. red fluorescent protein, *Nat. Biotechnol.* 22 (2004) 1567–1572. doi:10.1038/nbt1037.
- [337] M.Z. Lin, M.R. McKeown, H.-L. Ng, T.A. Aguilera, N.C. Shaner, R.E. Campbell, et al., Autofluorescent Proteins with Excitation in the Optical Window for Intravital Imaging in Mammals, *Chem. Biol.* 16 (2009) 1169–1179. doi:10.1016/j.chembiol.2009.10.009.
- [338] M.A. Wall, M. Socolich, R. Ranganathan, The structural basis for red fluorescence in the tetrameric GFP homolog DsRed, *Nat. Struct. Mol. Biol.* 7 (2000) 1133–1138. doi:10.1038/81992.
- [339] H. Mizuno, A. Sawano, P. Eli, H. Hama, A. Miyawaki, Red Fluorescent Protein from *Discosoma* as a Fusion Tag and a Partner for Fluorescence Resonance Energy Transfer†, *Biochemistry (Mosc.)* 40 (2001) 2502–2510. doi:10.1021/bi002263b.
- [340] I. GraphPad Software, GraphPad Prism, GraphPad Software, Inc., 2007. [www.graphpad.com](http://www.graphpad.com).
- [341] Z. Holló, L. Homolya, C.W. Davis, B. Sarkadi, Calcein accumulation as a fluorometric functional assay of the multidrug transporter, *Biochim. Biophys. Acta BBA - Biomembr.* 1191 (1994) 384–388. doi:10.1016/0005-2736(94)90190-2.
- [342] L. Homolya, M. Holló, M. Müller, E.B. Mechetner, B. Sarkadi, A new method for a quantitative assessment of P-glycoprotein-related multidrug resistance in tumour cells., *Br. J. Cancer.* 73 (1996) 849–855.
- [343] Attune® Acoustic Focusing Cytometer User Guide (PN 4453328 Rev F) - cms\_082577.pdf, (n.d.).  
[https://www3.appliedbiosystems.com/cms/groups/mcb\\_support/documents/generaldocuments/cms\\_082577.pdf](https://www3.appliedbiosystems.com/cms/groups/mcb_support/documents/generaldocuments/cms_082577.pdf) (accessed July 5, 2015).
- [344] Routine Cloning Using Top10 Competent Cells, (n.d.).  
<http://www.lifetechnologies.com/hu/en/home/references/protocols/cloning/competent-cells-protocol/routine-cloning-using-top10-competent-cells.html> (accessed July 6, 2015).

- [345] W.-T. Chan, C.S. Verma, D.P. Lane, S.K.-E. Gan, A comparison and optimization of methods and factors affecting the transformation of *Escherichia coli*, *Biosci. Rep.* 33 (2013). doi:10.1042/BSR20130098.
- [346] G. Bertani, STUDIES ON LYSOGENESIS I. : The Mode of Phage Liberation by Lysogenic *Escherichia coli*, *J. Bacteriol.* 62 (1951) 293.
- [347] Evrogen HyPer: Summary, (n.d.). <http://www.evrogen.com/products/HyPer/HyPer.shtml> (accessed July 6, 2015).
- [348] QIAprep Spin Miniprep Kit - QIAGEN, (n.d.). <https://www.qiagen.com/hu/shop/sample-technologies/dna-sample-technologies/plasmid-dna/qiaprep-spin-miniprep-kit> (accessed July 6, 2015).
- [349] H.C. Birnboim, J. Doly, A rapid alkaline extraction procedure for screening recombinant plasmid DNA., *Nucleic Acids Res.* 7 (1979) 1513.
- [350] nanodrop\_2000\_user\_manual.pdf, (n.d.). [http://www.mlz-garching.de/files/nanodrop\\_2000\\_user\\_manual.pdf](http://www.mlz-garching.de/files/nanodrop_2000_user_manual.pdf) (accessed July 5, 2015).
- [351] S.R. Gallagher, P.R. Desjardins, Quantitation of DNA and RNA with absorption and fluorescence spectroscopy, *Curr. Protoc. Mol. Biol.* Ed. Frederick M Ausubel Al. Appendix 3 (2006) Appendix 3D. doi:10.1002/0471142727.mba03ds76.
- [352] R.S. Tobias, The determination of stability constants of complex inorganic species in aqueous solutions, *J. Chem. Educ.* 35 (1958) 592. doi:10.1021/ed035p592.
- [353] D.J. Leggett, *Computational Methods for the Determination of Formation Constants*, Springer Science & Business Media, 2013.
- [354] L.-O. Öhman, Experimental determination of stability constants of aqueous complexes, *Chem. Geol.* 151 (1998) 41–50. doi:10.1016/S0009-2541(98)00069-2.
- [355] H.M. Irving, M.G. Miles, L.D. Pettit, A study of some problems in determining the stoichiometric proton dissociation constants of complexes by potentiometric titrations using a glass electrode, *Anal. Chim. Acta.* 38 (1967) 475–488. doi:10.1016/S0003-2670(01)80616-4.
- [356] C.F. Baes, R.E. Mesmer, *The Hydrolysis of Cations*, Wiley, New York, 1976.
- [357] L. Zékány, I. Nagypál, in: D.J. Leggett (Ed.), *Comput. Methods Determ. Form. Constants*, 1985: pp. 291–353.
- [358] I. Puigdomenech, *MEDUSA (Make Equilibrium Diagrams Using Sophisticated Algorithms)*, Inorganic Chemistry Royal Institute of Technology, Stockholm, Sweden, 2009. <https://www.kth.se/en/che/medusa>.
- [359] R. Martens-Menzel, *Physikalische Chemie in der Analytik: eine Einführung in die Grundlagen mit Anwendungsbeispielen*, 2., aktualisierte Aufl, Vieweg + Teubner, Wiesbaden, 2011.
- [360] R.S. Nicholson, I. Shain, Theory of Stationary Electrode Polarography. Single Scan and Cyclic Methods Applied to Reversible, Irreversible, and Kinetic Systems., *Anal. Chem.* 36 (1964) 706–723. doi:10.1021/ac60210a007.

- [361] B. Speiser, Elektroanalytische Methoden II: cyclische voltammetrie, Chem. Unserer Zeit. 15 (1981) 62–67.
- [362] J. Heinze, Cyclic Voltammetry—“Electrochemical Spectroscopy”. New Analytical Methods (25), Angew. Chem. Int. Ed. Engl. 23 (1984) 831–847. doi:10.1002/anie.198408313.
- [363] A.J. Bard, L.R. Faulkner, Electrochemical Methods—Fundamentals and Applications, John Wiley & Sons, New York, 2000.

**9. Appendix**

**Table A1.** Predicted physicochemical properties and measured biological data (IC<sub>50</sub> values in  $\mu\text{M}$ ) of isatin  $\beta$ -TSCs \_\_\_\_\_ page 222

**Table A2.** Predicted physicochemical properties and measured biological data (IC<sub>50</sub> values in  $\mu\text{M}$ ) of pyridinecarbaldehyde TSCs \_\_\_\_\_ page 223

**Table A3.** Predicted physicochemical properties and measured biological data (IC<sub>50</sub> values in  $\mu\text{M}$ ) of salicylaldehyde TSCs and an aniline derivative \_\_\_\_\_ page 225

**Table A4.** Predicted physicochemical properties and measured biological data (IC<sub>50</sub> values in  $\mu\text{M}$ ) of arylhydrazones \_\_\_\_\_ page 226

**Table A5.** Predicted physicochemical properties and measured biological data (IC<sub>50</sub> values in  $\mu\text{M}$ ) of hydrazinobenzothiazoles \_\_\_\_\_ page 227

**Table A1.** Predicted physicochemical properties and measured biological data (IC<sub>50</sub> values in  $\mu$ M) of isatin  $\beta$ -TSCs

Compound code	MW / g/mol	logD	TPSA	calc pKa	calc pKb	IC <sub>50</sub> (MES- SA)	IC <sub>50</sub> (MES- SA/Dx5)	IC <sub>50</sub> (MES- SA_ mCh)	IC <sub>50</sub> (MES- SA/Dx5 _mCh)	IC <sub>50</sub> (KB-3-1)	IC <sub>50</sub> (KB-V1)	IC <sub>50</sub> (A2780)	IC <sub>50</sub> (A2780 adr)
<b>I-a</b> (NSC73306)	326.37	3.01	74.75	9.28	-1.48	6.10 $\pm$ 0.942	3.59 $\pm$ 1.01	12.06 $\pm$ 3.32	4.15 $\pm$ 0.895	7.82 $\pm$ 2.06	3.78 $\pm$ 0.433	7.49 $\pm$ 0.297	4.84 $\pm$ 1.21
<b>I-b</b>	410.37	4.44	83.98	9.31	-2.38	6.14 $\pm$ 2.41	2.78 $\pm$ 1.21	8.14 $\pm$ 2.34	2.52 $\pm$ 0.862	6.56 $\pm$ 2.69	3.92 $\pm$ 0.642	3.39 $\pm$ 0.932	3.77 $\pm$ 1.34
<b>I-c</b>	310.37	3.68	65.52	9.33	-1.23	5.33 $\pm$ 1.43	3.27 $\pm$ 0.751	11.31 $\pm$ 2.53	3.27 $\pm$ 0.850	4.44 $\pm$ 1.47	4.00 $\pm$ 0.618	9.70 $\pm$ 1.50	8.75 $\pm$ 1.94
<b>I-d</b>	341.35	3.11	108.66	9.17	-1.91	9.17 $\pm$ 3.64	4.74 $\pm$ 1.10	15.76 $\pm$ 7.57	7.55 $\pm$ 6.73	8.196 $\pm$ 1.52	4.58 $\pm$ 0.900	25.70 $\pm$ 6.92	8.78 $\pm$ 2.35
<b>I-e</b>	364.35	4.04	65.52	9.22	-2.14	2.06 $\pm$ 0.360	1.40 $\pm$ 0.349	3.34 $\pm$ 0.694	1.95 $\pm$ 0.905				

**Table A2.** Predicted physicochemical properties and measured biological data (IC<sub>50</sub> values in μM) of pyridinecarbaldehyde TSCs:

Compound code	MW / g/mol	logD	TPSA	calc pKa	calc pKb	IC <sub>50</sub> (MES- SA)	IC <sub>50</sub> (MES- SA/Dx5)	IC <sub>50</sub> (MES- SA_ mCh)	IC <sub>50</sub> (MES- SA/Dx5 _mCh)	IC <sub>50</sub> (KB-3-1)	IC <sub>50</sub> (KB-V1)	IC <sub>50</sub> (A2780)	IC <sub>50</sub> (A2780 adr)
triapine	195.25	0.29	89.32	11.67	4.95			1.305 ± 0.396	2.523 ± 0.802				
<b>II-a</b>	256.33	3.36	49.31	9.44	3.05			0.715 ± 0.153	0.585 ± 0.161				
<b>II-c</b>	300.38	2.76	58.54	9.4	2.88	0.340 ± 0.056	0.0142 ± 0.0023	0.252 ± 0.117	0.0635 ± 0.0311	0.951 ± 0.900	1.75 ± 2.38	0.0457 ± 0.00064	0.0306 ± 0.0139
<b>II-d</b>	300.38	3.33	58.54	9.4	3.77			4.715 ± 0.323	4.22 ± 0.479				
<b>II-e</b>	314.41	4.16	58.54	9.4	3.43	0.423 ± 0.0812	0.0718 ± 0.0388	0.096 ± 0.022	0.0559 ± 0.00126				
<b>II-f</b>	270.35	3.87	49.31	9.46	3.05	0.396 ± 0.184	0.0762 ± 0.0230	0.794 ± 0.244	0.766 ± 0.710	0.744 ± 0.135	0.915 ± 0.252	0.0480 ± 0.00214	0.0635 ± 0.0045
<b>II-g</b>	284.38	3.43	49.31	9.46	2.88	0.0163 ± 0.0086	0.00178 ± 0.00054	0.0654 ± 0.0798	0.0294 ± 0.0166	0.0404 ± 0.0169	0.0360 ± 0.0149	0.0172 ± 0.00578	0.0210 ± 0.0054
<b>II-h</b>	284.38	3.43	49.31	9.4	2.88			0.0317 ± 0.00281	0.0632 ± 0.0167				
<b>II-i</b>	284.38	3.43	49.31	9.43	2.88			0.0299 ± 0.00631	0.0922 ± 0.0330				

Table A2. continued

Compound code	MW / g/mol	logD	TPSA	calc pKa	calc pKb	IC <sub>50</sub> (MES- SA)	IC <sub>50</sub> (MES- SA/Dx5)	IC <sub>50</sub> (MES- SA_ mCh)	IC <sub>50</sub> (MES- SA/Dx5 _mCh)	IC <sub>50</sub> (KB-3-1)	IC <sub>50</sub> (KB-V1)	IC <sub>50</sub> (A2780)	IC <sub>50</sub> (A2780 adr)
<b>II-j</b>	301.32	3.3	92.45	9.25	3.05	2.70 ± 0.88	1.83 ± 0.469	2.74 ± 1.43	2.74 ± 0.0786	1.05 ± 0.274	1.99 ± 1.02	0.666 ± 0.277	1.37 ± 0.192
<b>II-k</b>	329.38	4.26	92.45	9.25	3.43	10.88 ± 2.19	8.02 ± 4.70	10.47 ± 1.17	11.05 ± 1.98	8.03 ± 0.91	8.93 ± 0.96	no fit possible	
<b>II-l</b>	324.32	4.24	49.31	9.31	3.05			0.849 ± 0.125	0.720 ± 0.201				
<b>II-m</b>	338.35	3.79	49.31	9.31	2.88			9.59 ± 1.32	11.72 ± 0.2123				
<b>II-n</b>	324.32	4.23	49.31	9.09	3.05			0.125 ± 0.0364	0.159 ± 0.0928				
<b>II-o</b>	338.35	3.79	49.31	9.09	2.88			0.0332 ± 0.00659	0.161 ± 0.0845				
<b>II-q</b>	314.41	2.74	71.67	9.40	6.10	10.67 ± 2.36	8.02 ± 1.49	18.48 ± 1.14	17.66 ± 5.47	20.58 ± 6.29	22.26 ± 1.40	4.35 ± 0.683	4.87 ± 0.527



**Table A3.** Predicted physicochemical properties and measured biological data (IC<sub>50</sub> values in μM) of salicylaldehyde TSCs and an aniline derivative:

Compound code	MW / g/mol	logD	TPSA	calc pKa	calc pKb	IC <sub>50</sub> (MES- SA)	IC <sub>50</sub> (MES- SA/Dx5)	IC <sub>50</sub> (MES- SA_ mCh)	IC <sub>50</sub> (MES- SA/Dx5 _mCh)	IC <sub>50</sub> (KB-3-1)	IC <sub>50</sub> (KB-V1)	IC <sub>50</sub> (A2780)	IC <sub>50</sub> (A2780 adr)
<b>III-a</b>	271.34	3.58	56.65	8.68	1.91			14.04 ± 9.61	6.45 ± 5.81				
<b>III-b</b>	301.36	3.42	65.88	8.67	1.71	3.91 ± 0.969	3.50 ± 0.672	2.67 ± 0.689	1.85 ± 0.177	5.02 ± 0.320	4.87 ± 1.63	5.47 ± 0.707	6.95 ± 0.826
<b>III-c</b>	285.36	4.09	56.65	8.68	1.99	3.97 ± 1.47	5.36 ± 2.09	1.44 ± 0.249	1.87 ± 0.468	3.36 ± 0.395	3.69 ± 1.06	5.15 ± 1.04	6.01 ± 0.788
<b>III-d</b>	299.39	3.94	56.65	8.63	1.74			10.86 ± 2.64	3.46 ± 1.93				
<b>III-e</b>	339.34	4.46	56.65	8.65	0.97			5.07 ± 1.86	4.08 ± 1.50				
<b>III-f</b>	384.33	3.41	99.79	6.40	0.35			16.36 ± 3.38	11.92 ± 1.66				
<b>III-g</b>	384.33	3.41	99.79	6.40	0.35			21.13 ± 2.86	13.88 ± 1.65				

**Table A4.** Predicted physicochemical properties and measured biological data (IC<sub>50</sub> values in μM) of arylhydrazones.

Compound code	MW / g/mol	logD	TPSA	calc pKa	calc pKb	IC <sub>50</sub> (MES-SA)	IC <sub>50</sub> (MES-SA/Dx5)	IC <sub>50</sub> (MES-SA_mCh)	IC <sub>50</sub> (MES-SA/Dx5_mCh)	IC <sub>50</sub> (KB-3-1)	IC <sub>50</sub> (KB-V1)	IC <sub>50</sub> (A2780)	IC <sub>50</sub> (A2780 adr)
<b>IV-a</b>	229.24	2.36	72.29	11.57	3.50	2.82 ± 0.535	2.49 ± 0.552	2.45 ± 0.813	2.71 ± 0.96	1.95 ± 0.294	2.83 ± 0.382	1.73 ± 0.0560	1.95 ± 0.0934
<b>IV-b</b>	243.26	1.92	72.29	11.18	3.43	0.265 ± 0.0785	0.0953 ± 0.0289	0.261 ± 0.0603	0.22 ± 0.0044	0.358 ± 0.0490	0.494 ± 0.0798	0.144 ± 0.0337	0.0272 ± 0.00756
<b>IV-c</b>	257.29	3.32	72.29	11.65	3.71	1.55 ± 0.285	1.11 ± 0.198	2.33 ± 0.388	2.11 ± 0.72	1.23 ± 0.0257	1.57 ± 0.238	1.30 ± 0.169	0.630 ± 0.0962
<b>IV-d</b>	212.25	1.98	50.17	12.66	4.34			0.102 ± 0.0869	0.0591 ± 0.0071				
<b>IV-e</b>	248.28	4.00	50.17	12.95	4.04			0.820 ± 0.286	0.435 ± 0.109				
<b>IV-f</b>	262.31	3.55	50.17	12.59	3.97			0.483 ± 0.987	0.382 ± 0.186				
<b>IV-g</b>	262.31	4.49	50.17	13.03	4.74			0.559 ± 0.146	0.397 ± 0.0371				
<b>IV-h</b>	276.34	4.00	50.17	12.71	4.67			0.298 ± 0.0672	0.294 ± 0.0153				
<b>VII-d</b>	269.26	2.15	88.5	8.73	3.21			Not toxic			Not toxic		

**Table A5.** Predicted physicochemical properties and measured biological data (IC<sub>50</sub> values in  $\mu\text{M}$ ) of pyridinyl hydrazinobenzothiazoles and an acetanilide derivative

Compound code	MW / g/mol	logD	TPSA	calc pKa	calc pKb	IC <sub>50</sub> (MES- SA)	IC <sub>50</sub> (MES- SA/Dx5)	IC <sub>50</sub> (MES- SA_ mCh)	IC <sub>50</sub> (MES- SA/Dx5 _mCh)	IC <sub>50</sub> (KB-3-1)	IC <sub>50</sub> (KB-V1)	IC <sub>50</sub> (A2780)	IC <sub>50</sub> (A2780 adr)
<b>V-a</b>	254.31	4.05	50.17	8.80	3.88	1.42 $\pm 0.223$	1.02 $\pm 0.154$	2.70 $\pm 0.258$	3.36 $\pm 1.36$	0.646 $\pm 0.066$	0.840 $\pm 0.194$	0.587 $\pm 0.0867$	0.455 $\pm 0.111$
<b>V-b</b>	268.34	3.58	50.17	8.37	3.68	0.201 $\pm 0.0856$	0.0142 $\pm 0.00193$	0.252 $\pm 0.0714$	0.104 $\pm 0.0224$	0.344 $\pm 0.0353$	0.279 $\pm 0.0480$	0.0944 $\pm 0.0330$	0.0312 $\pm 0.00886$
<b>V-c</b>	282.36	5.00	50.17	8.90	4.14	3.24 $\pm 0.0548$	1.85 $\pm 0.0391$	4.26 $\pm 0.054$	3.83 $\pm 1.47$	0.612 $\pm 0.116$	1.14 $\pm 0.0804$	0.814 $\pm 0.0446$	0.619 $\pm 0.185$
<b>V-d</b>	282.36	1.59	63.3	5.48	13.86	45.58 $\pm 8.81$	28.00 $\pm 4.22$	46.16 $\pm 9.10$	19.01 $\pm 2.87$				
<b>VII-c</b>	294.33	2.47	66.38	5.73	2.30			Not toxic					

**Table A5.** Predicted physicochemical properties and measured biological data (IC<sub>50</sub> values in μM) of hydroxyphenyl hydrazinobenzothiazoles

Compound code	MW / g/mol	logD	TPSA	calc pKa	calc pKb	IC <sub>50</sub> (MES- SA)	IC <sub>50</sub> (MES- SA/Dx5)	IC <sub>50</sub> (MES- SA_ mCh)	IC <sub>50</sub> (MES- SA/Dx5 _mCh)	IC <sub>50</sub> (KB-3-1)	IC <sub>50</sub> (KB-V1)	IC <sub>50</sub> (A2780)	IC <sub>50</sub> (A2780 adr)
<b>VI-a</b>	269.32	4.20	57.51	8.61	4.76	24.68 ± 8.55	10.45 ± 4.60	23.18 ± 11.39	4.55 ± 1.89	18.07 ± 9.94	11.73 ± 1.23	3.16 ± 0.630	6.01 ± 1.43
<b>VI-b</b>	283.35	4.07	57.51	8.57	4.56	12.51 ± 1.67	5.52 ± 1.77	21.61 ± 3.23	11.64 ± 4.76	14.29 ± 3.65	12.07 ± 3.51	8.74 ± 2.80	9.95 ± 1.33
<b>VI-c</b>	299.35	4.09	66.74	9.04	4.55			14.91 ± 7.89	11.57 ± 8.55				
<b>VI-d</b>	313.37	3.95	66.74	8.93	4.35			50.67 ± 9.37	15.37 ± 6.58				
<b>VI-e</b>	283.35	4.70	57.51	8.92	4.83			89.10 ± 27.50	15.60 ± 8.05				
<b>VI-f</b>	314.32	3.21	100.65	6.38	4.02			4.07 ± 1.59	1.99 ± 0.714				
<b>VI-g</b>	283.35	4.36	46.51	10.09	4.80			Not toxic	Not toxic				

### 10. Acknowledgement

I would like to thank my supervisor, *Professor Dr. M. Wiese*, for giving me the opportunity to work on such an interesting topic. During the time of my PhD he was constantly available for thorough and fruitful discussions, and I want to thank him for his helpful comments and his constructive criticism. I appreciate the trust he had in me and the freedom he provided, to develop my own thoughts about the project. Furthermore I would like to thank him for the opportunity to foster a collaboration with *Dr. Gergely Szakács* at the Hungarian Academy of Sciences and for providing the framework to spend a significant part of my PhD time in his laboratory.

My unofficial second supervisor *Dr. Gergely Szakács* I would like to thank for hospitably accepting me as a member of his work group and for teaching me to ask the right questions, and to find suitable methods that might lead to answers (or further questions). I am grateful for the uncountable opportunities he provided for me, to follow the path of my ideas on the project and for his support in building up the network that was necessary to do so. I learned a lot during the time I spent in his laboratory and not least through his unfatiguing critical proof-reading of paper drafts, he helped to improve my scientific writing skills. I want to thank him for very fruitful and inspiring discussions and the confidence he had in me.

I would like to thank *Professor Dr. G. Bendas*, for his willingness to take the co-referendum, for very nice and fruitful discussions and for making the teaching in the first semester a pleasant experience.

*Professor Dr. U. Jaehde* I would like to thank for taking part in the committee, for his supervision in the BIGS DrugS graduate school and for the opportunity to perform work that involved the handling of cytostatic agents in his laboratory.

I would like to thank *Professor Dr. A. Meyer* for taking part in the committee.

Having mentioned a network that was established in the scope of the project, I would foremost like to thank our collaborator *Professor Dr. Éva A. Enyedy* from the University of Szeged for her kind hospitality and for giving me the opportunity to work in her laboratory. She gave me a deeper insight into the work of a bioinorganic chemist. I would like to

especially thank her for her help in data analysis, as well as in fixing technical issues in the laboratory. I would like to furthermore thank her husband *Dominik Hollender*, as well as her group members *Dr. Orsolya Dömötör* and *Katalin Tóth Szűcsné* for technical support in the laboratory.

I am extremely grateful to *Dr. Miklós Geiszt* for thorough, helpful and fruitful discussions about ROS related issues of the project and for providing the HyPerC and HyPerC121s plasmids.

My former colleague *Zsuzsanna Nagy* I would like to thank for supervising me with the DNA work that was necessary for the preparation of stably transfected cells, and *Nóra Kucsma* and *Áron Szepesi* for the lentiviral transfection of MES-SA and MES-SA/Dx5 cells.

I am grateful for help in programming issues and for fruitful discussions I had with *Dr. Anna Lovrics* and *Judit Sessler*, and further discussions with *Dr. Anna Brozik*. Also, I want to thank my colleagues *Szilárd Tóth* and *Dr. Dóra Türk* for the help I have obtained with FACS measurements and especially *Szilárd* for his support and contribution in creating the corresponding figure. I am grateful to them and to *András Füredi* for their kind and uncomplicated collaboration in common projects. I would like to thank them, as well as my further office members *Mihaly Cserepes*, *Anna Küllői*, *Tímea Windt*, *Lilla Hámori*, *Veronika Nagy* and *Dániel Kiss*, as well as *Zsófia Rakvács* and *Ágnes Bilecz* for a very nice and stimulating working atmosphere. As a special office member I would like to thank *Krisztina Mohos* for being an angel in ordering and organizational issues. As her German “counterpart”, I would also like to thank *Tatjana Müller* for support in organizational issues in Bonn.

For their friendship, technical assistance in the cellular laboratory, very nice conversations, an amazing optimism and a constant believe in me, I would like to thank *Rozália Soós*, *Elvira Komlósi*, *Ibolya Kurko*, *Iris Jusen* and *Dieter Baumert*.

I would like to take the opportunity, to also thank my colleagues from the work group of *Professor Dr. M. Wiese*, who provided a nice working atmosphere. I especially want to thank *Dr. Mathias Weigt* for his help with computational problems and for sharing data he collected from a crystal structure database. I want to thank *Dr. Kapil Juvale*, *Dr. Martin Koch*, *Dr. Svenja Wieschrath*, *Jennifer Gallus*, *Stefanie Kraege* and my former office members *Dr. Kerstin Steggemann* and *Matthias Christlieb* for nice conversations on scientific and non-scientific issues. I am grateful to *Dr. Katja Sterz* for initial support in the cellular laboratory.

Many people contributed to the analysis of synthesized compounds. For the measurement of NMR spectra I would like to thank *Sabine Terhart-Krabbe* and *Orsolya Egyed Lejtoviczné*. Furthermore, I would like to thank *Herrmann Passgang* for the measurement of combustion analysis and *Pál Szabó* for conducting LC-MS measurements. Additionally, I would like to thank my “Wahlpflichtstudenten” *Sarah Hopp*, *Christian Müller* and *Roland Pietz* for support in the synthesis of presented compounds.

I would like to take the opportunity to thank all those friends who were there for me, and accompanied me on my way as a PhD student.

I would like to express my gratitude to *Dr. Flóra Szeri* for her critical proof-reading of excerpts from the manuscript of this thesis, for her honesty and very helpful comments, for always being there for me, for cheering me up in difficult times, for never stopping to believe in me, for making me climb up mountains and simply for being herself. I would like to thank *Kriszta Kerekes* for cheerful conversations, and for the motivation and support I obtained from her, *Alasdair*, *Flóra* and *Mesi* in overlooking and overcoming some of the stones on the way.

I would like to thank *Dr. Anja Voreck*, as well as *Oleg Pogrebnyak* and *Andrea László* (and their mothers) for their friendship, their support and believe in me. I am grateful to *Anne Thomas*, with whom I could share the ups and downs of the writing process in regular updates; I want to sincerely thank her for the mutual motivation. In the long list of people I am grateful to, I also have to mention my long-time friends *Dr. Julia Siebert-Krümpelmann*, *Mareike Gammel* and *Nadine Witte*, who frequently lent me an ear and cheered me up.

I am extremely grateful to the choir *Wave of Joy*, for being like a big second family, for the opportunity to sing with you that always cheered me up and put a smile (back) into my face, even in times, when I could only join via skype. I am happy that I met some very good friends in this choir, and I thank you (especially *Rolf Rau* and *Andrea Schulze*, *Anette* and *Volker Schade*, *Anette* and *Reiner Viebahn*, *Dr. Elke Mannigel*, *Elfriede Szymczak*, *Ulrike Kemper* and many more) for your smiles and hugs, for supporting and motivating me and for constantly believing in me.

Nicht zuletzt möchte ich mich ganz herzlich bei meinen Eltern bedanken, die immer für mich da waren und mich in meinen Entscheidungen stets unterstützt haben. Durch Eure Unterstützung, Eure Liebe und Euren Glauben an mich bin ich heute, wer ich bin. Ohne Euch wären weder mein Chemie-Studium, noch diese Arbeit möglich gewesen.

## *11. Verfassererklärung*

Ich erkläre, dass ich die vorgelegte Arbeit persönlich, selbständig und ohne Benutzung anderer als der angegebenen Hilfsmittel verfasst habe. Die vorgelegte oder eine ähnliche Arbeit wurden vorher nicht anderweitig als Dissertation eingereicht.

Auszüge der Arbeit wurden in den Fachzeitschriften „Journal of Inorganic Biochemistry“ und „European Journal of Medicinal Chemistry“ veröffentlicht.

Bonn, 18.12.2015

Veronika F.S. Pape



**12. List of Publications**Publications related to the thesis

---

Pape VFS, Türk D, Szabó P, Wiese M, Enyedy EA, Szakács G. Synthesis and characterization of the anticancer and metal binding properties of novel pyrimidinylhydrazone derivatives. *J Inorg Biochem.* 2015;144:18–30.

Pape VFS, Tóth S, Füredi A, Szebényi K, Lovrics A, Szabó P, et al. Design, synthesis and biological evaluation of thiosemicarbazones, hydrazinobenzothiazoles and arylhydrazones as anticancer agents with a potential to overcome multidrug resistance. *Eur J Med Chem.* 2016;117:335–54.

Szakács G, Füredi A, Tóth S, Pape VFS, Türk D, Soós T, Ferenczi-Palkó R, Fülöp F, Szatmári I, Dormán G. „MDR-reversing 8-hydroxy-quinoline derivatives” P16 00234, 2016.

Publications not related to the thesis

---

Juvale K, Pape VFS, Wiese M. Investigation of chalcones and benzochalcones as inhibitors of breast cancer resistance protein. *Bioorg. Med. Chem.* 2012;20:346–55.

Toth PM, Naruhn S, Pape VFS, Dörr SMA, Klebe G, Müller R, et al. Development of Improved PPAR $\beta/\delta$  Inhibitors. *ChemMedChem.* 2012;7:159–70.

Naruhn S, Toth PM, Adhikary T, Kaddatz K, Pape V, Dorr S, et al. High-Affinity Peroxisome Proliferator-Activated Receptor  $\beta/\delta$  -Specific Ligands with Pure Antagonistic or Inverse Agonistic Properties. *Mol. Pharmacol.* 2011;80:828–38.

Diederich W, Doerr S, Kaddatz K, Klebe G, Mueller R, Naruhn S, et al. Verbindungen Als Ppar Beta/Delta Inhibitoren Für Die Behandlung Von Ppar Beta/Delta-Vermittelten Erkrankungen „compounds as PPAR beta/delta inhibitors for treating PPAR beta/delta-mediated diseases“ WO2012/168345A1, 2012. Available from: <http://depatisnet.dpma.de/DepatisNet/depatisnet?action=bibdat&docid=WO002012168345A1>

### 13. Conference Presentations

2012: Poster at *4th FEBS Special meeting, ATP-Binding Cassette (ABC) Proteins: From Multidrug Resistance to Genetic Diseases*, Innsbruck, Austria:

**Design, synthesis, testing and functional characterization of novel MDR selective compounds targeting resistant cancer**

Veronika F.S. Pape, Michael Wiese, Gergely Szakács

2013: Poster at *Multi-Drug Efflux Systems - Gordon Research Conference*, Ventura, USA:

**Hitting where it hurts – compounds targeting MDR cells.**

Szilárd Tóth, András Füredi, Veronika Pape, Eszter Kanta, Antónia Síkhegyi, Dóra Türk, Gergely Szakács

Poster at *MRIC - Redox Modulation of Health and Disease*, Erlangen, Germany:

**Chelators as anticancer agents with potential to overcome multidrug resistance**

Veronika F.S. Pape, Éva A. Enyedy, Gabriella M. Bognár, Szilárd Tóth, András Füredi, Dóra Türk, Michael Wiese, Gergely Szakács

Posters at *Role of MDR proteins in pharmacokinetics and toxicology*, Ryn, Poland:

**Targeting the Achilles heel – application of a myth?**

Veronika F.S. Pape, Szilárd Tóth, András Füredi, Dóra Türk, Michael Wiese, Gergely Szakács

**In search for molecules that selectively kill MDR cancer cells by exploiting the function of P-glycoprotein**

Szilárd Tóth, András Füredi, Eszter Kanta, Antónia Síkhegyi, Veronika F.S. Pape, Dóra Türk, Gergely Szakács

2014: Poster at *EuroBIC - 12th European Biological Inorganic Chemistry Conference*, Zürich, Switzerland:

**Investigating the impact of ROS on the toxicity of Plumbagin and its copper complexes**

Veronika F.S. Pape, Éva A. Enyedy, Anna Lovrics, Zsuzsanna Nagy, Nóra Kucsma, Áron Szepesi, Miklós Geiszt, Michael Wiese, Gergely Szakács

- 2015: Oral presentation at 5<sup>th</sup> Gárdos György Szimpózium, Mátraháza, Hungary:  
**Daganatsejtek rezisztenciája – Az MDR szelektivitás a kémiai szempontból**  
*(Resistance of tumor cells – MDR selectivity from a chemical viewpoint)*